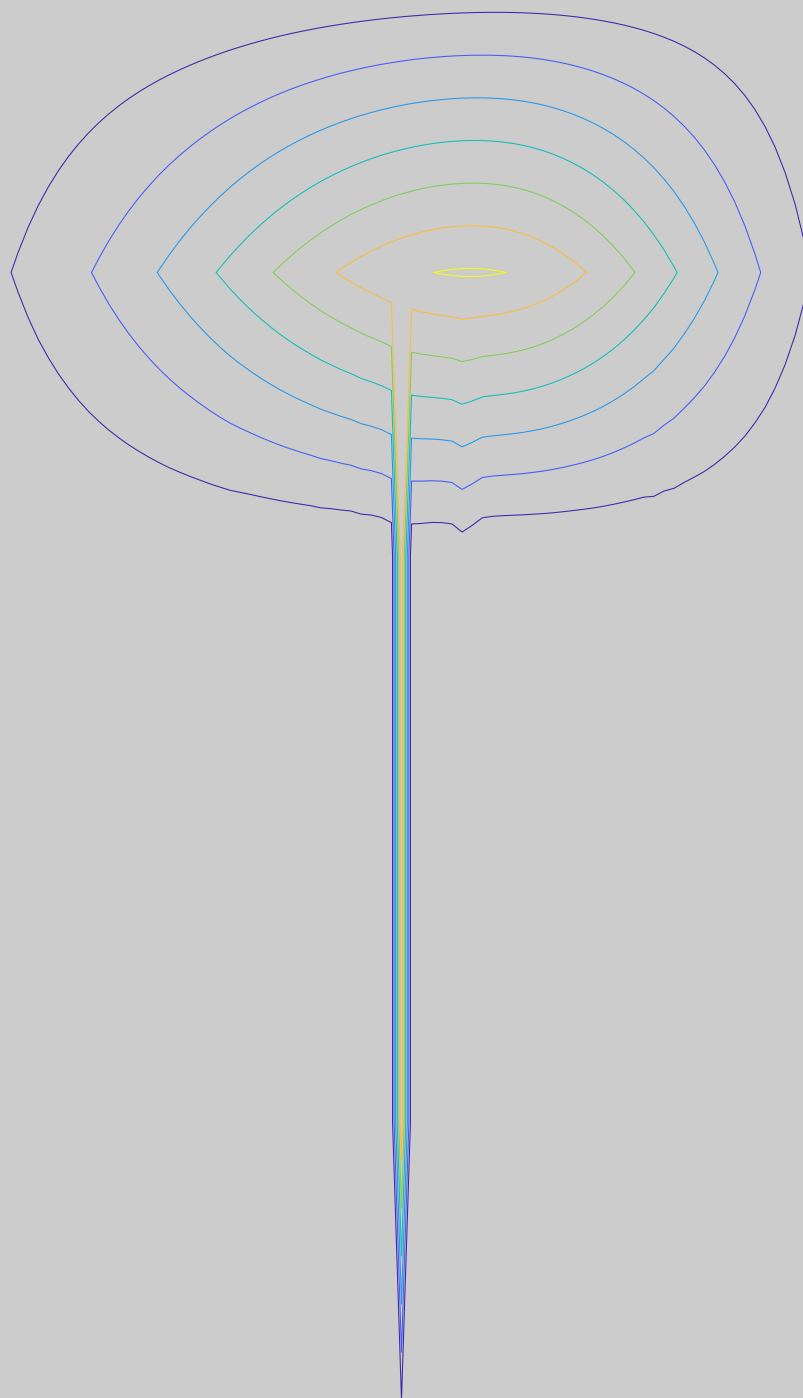


# Hybrid Models for Vibration Monitoring

## Dynamic Substructuring and Modal Expansion for Industrial Sensor Systems



Samuel Strobel



Technische Universität München  
TUM School of Engineering and Design

# Hybrid Models for Vibration Monitoring

## *Dynamic Substructuring and Modal Expansion for Industrial Sensor Systems*

**Samuel Thomas Strobel**

Vollständiger Abdruck der von der TUM School of Engineering and Design der Technischen Universität München zur Erlangung eines

**Doktors der Ingenieurwissenschaften (Dr.-Ing.)**

genehmigten Dissertation.

**Vorsitz:** Prof. Dr.-Ing. Rüdiger Daub

**Prüfer der Dissertation:**

1. Prof. dr.ir. Daniel J. Rixen
2. Assoc. Prof. dr. Gregor Čepou

Die Dissertation wurde am 1. Juni 2023 bei der Technischen Universität München eingereicht und durch die TUM School of Engineering and Design am 9. Oktober 2023 angenommen.



## Danksagung

Die Möglichkeit zu dieser Arbeit bekam ich von 2017 bis 2020 durch die Zusammenarbeit des Lehrstuhls für Angewandte Mechanik der Technischen Universität München mit der zentralen Forschungsabteilung der Siemens AG in Erlangen. Siemens finanzierte das Projekt. Für das hierfür entgegengebrachte Vertrauen möchte ich mich bei den Kollegen beiderseits als allererstes herzlich bedanken.

Prof. dr. ir. Daniel J. Rixen hat mich als Doktorvater nicht nur auf fachlicher und menschlicher Ebene unterstützt, sondern hat an seinem Lehrstuhl ein unvergleichliches Umfeld geschaffen, das die Forschung in einem spaßvollen und respektvollen Umgang lebt, wie ich sie sonst nirgends gesehen habe. Die Atmosphäre am Lehrstuhl mit dem “AM-Standard” war eine hervorragende Basis für die Arbeit an diesem spannenden Thema.

Bei allen Lehrstuhlkollegen möchte ich mich daher für die Zeit auf fachlicher, musikalischer, sportlicher und freundschaftlicher Ebene bedanken. Besonders werden mir hier die Diskussionen und Konferenzaufenthalte mit meinem Bürokollegen Johannes Maierhofer in Erinnerung bleiben. Dr.-Ing. habil. Thomas Thümmel sorgte dafür, dass ich für den Prüfstand am Lehrstuhl ein extra Labor bekam. Hier fehlte es an nichts, vielen Dank.

Dr.-Ing. Uwe Linnert schuf mir bei Siemens die Möglichkeiten und Freiheiten für Forschung im industriellen Umfeld. Ohne sein Vertrauen und seine Offenheit wäre diese Arbeit nicht möglich gewesen.

Der Ausgleich für viele Höhen und Tiefen meiner Promotionszeit fand meistens auf dem Rad statt. Besonders möchte ich mich hier bei Dr.-Ing. Franz-Josef Streit bedanken, mit dem ich als Diskussionspartner während seiner eigenen Promotion und als Teamkollege auf dem Rad über viele Berge gefahren bin.

Abschließend möchte ich mich bei meiner Frau Nikola bedanken.

Du hast mir für diese Arbeit wertvollste Unterstützung und das selbstloseste Verständnis entgegengebracht.

Danke!

Erlangen, den 12. Dezember 2023

*Samuel Strobel*

## Abstract

Vibration monitoring is an essential element of research in digitalization and automation. With respect to rotating machinery, constrained devices based on integrated Micro-Electro-Mechanical sensor technology (MEMS), typically provide acceleration-based health information. These sensor systems are usually connected to the industrial internet via wireless transmission technology. Here, the problem occurs. Wireless transmission standards require measurement positions at the housing - far away from the fault origin. Accurate and precise, quantitative fault diagnosis demands a dynamic, adaptive description of the holistic, mechanical transfer paths between fault sources and sensor system position. These can be influenced by internal support stiffnesses between rotor and housing, boundary conditions and specific operational conditions. In this thesis, hybrid and exclusively experimental approaches are presented which address this issue. For the application of these methods, an exemplary MEMS sensor is characterized with respect to frequency response linearity and temperature sensitivity.

The experimental technique is proposed for monitoring of structures with low flexibility. A virtual accelerometer is placed inside a roller bearing based on coupled frequency response and transmissibility functions. The performance of this technique is validated on an industrial centrifugal pump test rig with an exemplary roller bearing fault and a MEMS sensor system. Therefore, several bearing fault diagnosis methods are evaluated and recommendations are given with respect to restrictions of MEMS accelerometer technology.

The hybrid approach contains a combination of numerical and experimental modeling methods and also suits high-flexible structures. An industrial blower is utilized as exemplary application. Therefore, a numerical modeling technique for rotor systems with overhung impellers is presented. The rotor is created and validated based on a one-dimensional Timoshenko beam with an analogous stiffness model at the impeller aiming to reach minimum degrees of freedom (DoF). This model is coupled with the machine housing utilizing Lagrange Multiplier frequency-based substructuring (LM-FBS) and virtual point transformation (VPT) techniques.

Interface dynamics at the virtual bearing DoF are implemented by the System Equivalent Model Mixing (SEMM) modal expansion framework. In the context of SEMM-based modal expansion, a novel, iterative approach is presented for the integration of operational conditions at the entire speed range. Filtering effects of the Moore-Penrose pseudoinverse are utilized to find virtual unbalance forces at the rotor. The iterative updating process is exclusively based on operational output measurements by a minimal sensor set-up containing two triaxial accelerometers. Unphysical force-peaks are eliminated based on an adaptive force shaping procedure. This technique is based on an iterative cubic spline fit on the force spectral envelope. Finally, the entire methodology is validated by frequency response functions and operational measurements with two different unbalance scenarios at the blower test rig. The final adaption to varying boundary conditions with a same approach but solely based on the monitoring accelerometer at the housing demonstrates further force estimation enhancement. Even an exemplary unbalance force estimation scenario with a final MEMS sensor system could be achieved successfully.

---

## Zusammenfassung

Vibrationsbasierte Zustandsüberwachung ist ein essenzieller Bestandteil im Forschungsbereich der Digitalisierung und Automatisierung. Ressourcenbeschränkte Sensorlösungen basierend auf Mikro-Elektro-Mechanischen Systemen (MEMS) können hierbei die wesentlichen Zustandsinformationen erfassen. Im Hinblick auf rotierende Maschinen betrifft das zumeist Informationen über die Beschleunigung am Gehäuse. Die zugrundeliegenden Sensorsysteme sind mittels drahtlosen Kommunikationsschnittstellen mit dem industriellen Internet verbunden. Die Messposition am Gehäuse ist dabei ein Problem, da sie für die drahtlose Kommunikationsmöglichkeit unbedingt erforderlich ist, aber zumeist weit vom Ort des Schadens am Rotor entfernt liegt. Deshalb benötigt die genaue, präzise und quantitative Zustandsüberwachung eine ganzheitliche Beschreibung der mechanischen Transferpfade zwischen den Fehlerquellen und der Messposition am Gehäuse. Die Transferfunktionen können durch interne Kopplungssteifigkeiten als auch durch Rand- oder Betriebsbedingungen beeinflusst werden. Diese Arbeit schlägt hierfür zwei Lösungsansätze vor, welche an zwei industriellen Beispielen evaluiert werden. Für deren Validierung wird ein beispielhafter MEMS-Beschleunigungssensor hinsichtlich Übertragungslinearität und Temperaturempfindlichkeit charakterisiert.

Ein Ansatz für die Zustandsüberwachung, der ausschließlich auf experimenteller Modellierung basiert, betrachtet ein Anwendungsbeispiel mit geringer interner Flexibilität. Hierbei wird ein virtueller Beschleunigungsaufnehmer basierend auf gekoppelten Transmissibilitäten und Admittanzen im Inneren eines Wälzlagers platziert. Die Validierung der Methode erfolgt mithilfe eines beispielhaften Wälzlagerschadens in einem Kreiselpumpenprüfstand und einem MEMS-Sensorsystem. Hierfür werden Techniken zur Lagerdiagnose spezifisch für die MEMS-Sensorik evaluiert.

Der hybride Ansatz besteht aus einer Kombination von numerischer und experimenteller Modellierung, welche auch für hochflexible Strukturen geeignet ist. Die Methodenentwicklung erfolgt an einem industriellen Lüfterprüfstand. Für dessen Rotor, welcher eines weit verbreiteten Typs mit überhängendem Impeller entspricht, wird eine numerische Modellierungstechnik mit dem Ziel entwickelt, minimale Freiheitsgradanzahl zu erreichen. Der Rotor besteht aus einem eindimensionalen Timoshenko-Balken mit einem Ersatzsteifigkeitsmodell am Übergang Welle-Impeller und wird mit dem Maschinengehäuse mithilfe der Lagrange Multiplikatorbasierten Substrukturierung und virtueller Punkt-Transformation gekoppelt.

Die Schnittstellendynamik wird im Nachhinein mithilfe der modalen Expansionstechnik System Equivalent Model Mixing (SEMM) implementiert. Im Rahmen dieser Expansionstechnik entsteht ein neuer, iterativer Ansatz, mit welchem strukturdynamische Änderungen durch die Betriebsbedingungen der Maschine erfasst werden können. Dabei filtert die Moore-Penrose Pseudoinverse virtuelle Unwuchtkräfte aus dem hybriden Modell und den Betriebsmessungen. Diese werden mithilfe eines minimalen Sensor-Setups bestehend aus zwei triaxialen Beschleunigungsaufnehmern erfasst. Unphysikalische Kraftspitzen können dabei auf der Basis iterativer, adaptiver, kubischer Spline-Fits entfernt werden. Die Validierung der gesamten Methodik erfolgt durch Frequenzübertragungsfunktionen und Betriebsmessungen bei zwei verschiedenen Unwuchtszenarien am Lüfterprüfstand. Eine finale Adaption an veränderte Randbedingungen mit einem einzigen Sensor sowie mit einem exemplarischen MEMS-Sensorsystem liefert mit derselben Methodik eine gute Approximation der Unwucht am Rotor.



# Contents

|          |   |           |
|----------|---|-----------|
| <b>1</b> | <b>Introduction</b>   | <b>5</b>  |
| 1.1      | Classification of Vibration Monitoring . . . . .                  | 5         |
| 1.1.1    | Signal-Based Monitoring . . . . .                                 | 6         |
| 1.1.2    | Model-Based Monitoring . . . . .                                  | 9         |
| 1.2      | Research Questions and Objectives . . . . .                       | 10        |
| 1.3      | Scientific Contribution . . . . .                                 | 11        |
| 1.4      | Structure of the Thesis . . . . .                                 | 11        |
| <br>     |   |           |
| <b>I</b> | <b>Vibration Monitoring Fundamentals</b>                          | <b>15</b> |
| <br>     |   |           |
| <b>2</b> | <b>Structural Dynamics for Monitoring Applications</b>            | <b>17</b> |
| 2.1      | Representation Domains for Hybrid Dynamic Models . . . . .        | 17        |
| 2.1.1    | Physical Domain . . . . .   | 18        |
| 2.1.2    | Modal Domain Representation . . . . .                             | 19        |
| 2.1.3    | State-Space Domain Representation . . . . .                       | 20        |
| 2.1.4    | Time Domain Representation . . . . .                              | 22        |
| 2.1.5    | Frequency Domain Representation . . . . .                         | 22        |
| 2.1.6    | Summary . . . . .   | 23        |
| 2.2      | Lagrange Multiplier Frequency-Based Substructuring . . . . .      | 23        |
| 2.2.1    | Substructure Coupling . . . . .                                   | 24        |
| 2.2.2    | Substructure Decoupling . . . . .                                 | 26        |
| 2.3      | Virtual Point Transformation . . . . .                            | 27        |
| 2.3.1    | Displacement Transformation . . . . .                             | 28        |
| 2.3.2    | Force Transformation . . . . .                                    | 30        |
| 2.3.3    | Virtual Point Coupling . . . . .                                  | 31        |
| 2.3.4    | Virtual Point Quality Indicators . . . . .                        | 32        |
| 2.4      | System Equivalent Model Mixing (SEMM) . . . . .                   | 36        |
| 2.4.1    | Basic SEMM . . . . .  | 37        |
| 2.4.2    | Fully Extended Interface SEMM . . . . .                           | 40        |
| 2.4.3    | Extended Equilibrium SEMM . . . . .                               | 42        |
| 2.4.4    | Extended Compatibility SEMM . . . . .                             | 43        |
| <br>     |   |           |
| <b>3</b> | <b>Vibration Monitoring Methods</b>                               | <b>45</b> |
| 3.1      | State-Space Observer Approach . . . . .                           | 45        |
| 3.2      | Kalman Filter . . . . .   | 46        |
| 3.3      | Frequency Modulated Fault Extraction of Rotor Unbalance . . . . . | 49        |
| 3.4      | Amplitude Modulated Fault Diagnosis of Roller Bearings . . . . .  | 49        |
| 3.4.1    | Statistical Indicators . . . . .                                  | 51        |
| 3.4.2    | Envelope Analysis . . . . .                                       | 51        |
| 3.4.3    | Optimal Filter Design . . . . .                                   | 53        |

|            |   |            |
|------------|---|------------|
| 3.4.4      | Concluding Signal-Based Condition Indicator . . . . .                         | 62         |
| 3.4.5      | Summary . . . . .   | 63         |
| <b>4</b>   | <b>Test Rig Characterization</b>  | <b>65</b>  |
| 4.1        | Blower Test Rig . . . . .   | 65         |
| 4.1.1      | Housing Dynamics and Their Influence on Unbalance Monitoring . . . . .        | 66         |
| 4.1.2      | Modal Analysis . . . . .  | 72         |
| 4.1.3      | Transfer Function Reciprocity . . . . .                                       | 74         |
| 4.1.4      | Summary . . . . .   | 75         |
| 4.2        | Pump Test Rig . . . . .   | 76         |
| 4.2.1      | Transfer Function Reproducibility . . . . .                                   | 80         |
| 4.2.2      | Operational Output Reproducibility . . . . .                                  | 81         |
| 4.2.3      | Temperature Influence . . . . .   | 82         |
| 4.2.4      | Summary . . . . .   | 83         |
| <b>II</b>  | <b>Hybrid Dynamic Substructuring and Modal Expansion</b>                      | <b>85</b>  |
| <b>5</b>   | <b>Hybrid Dynamic Modeling</b>  | <b>87</b>  |
| 5.1        | Rotor Modeling . . . . .  | 87         |
| 5.1.1      | Reference Simulation . . . . .  | 88         |
| 5.1.2      | Reduced Simulation . . . . .  | 89         |
| 5.1.3      | Experimental Rotor Validation . . . . .                                       | 95         |
| 5.1.4      | Summary . . . . .   | 98         |
| 5.2        | Frequency-Based Model Mixing . . . . .  | 98         |
| 5.2.1      | Housing Model Estimation . . . . .  | 99         |
| 5.2.2      | SEMM-Based Modal Expansion . . . . .  | 105        |
| 5.2.3      | Results . . . . .   | 108        |
| 5.3        | Summary . . . . .   | 112        |
| <b>6</b>   | <b>Iterative SEMM-Based Model Adaption</b>                                    | <b>113</b> |
| 6.1        | Model Adaption to Operating Conditions . . . . .                              | 113        |
| 6.1.1      | Operational Force Estimation . . . . .  | 119        |
| 6.1.2      | Adaptive Force Shaping . . . . .  | 126        |
| 6.2        | Model Adaption to Varying Boundary Conditions . . . . .                       | 128        |
| 6.3        | Summary . . . . .   | 131        |
| <b>III</b> | <b>Industrial Applications</b>  | <b>133</b> |
| <b>7</b>   | <b>Application of a Final Sensor System</b>                                   | <b>135</b> |
| 7.1        | Experimental Sensor Characterization . . . . .                                | 135        |
| 7.1.1      | Frequency Response Linearity Evaluation . . . . .                             | 135        |
| 7.1.2      | Temperature Sensitivity Characterization . . . . .                            | 139        |
| 7.1.3      | Summary . . . . .   | 142        |
| 7.2        | Virtual Sensing for Bearing Fault Diagnosis . . . . .                         | 142        |
| 7.2.1      | Virtual Sensing and Validation . . . . .                                      | 142        |
| 7.2.2      | Concluding Summary . . . . .  | 148        |
| 7.3        | Application of an Industrial Sensor System to the Blower SEMM Model . . . . . | 148        |

---

|  |            |
|--|------------|
| <b>8 Conclusion and Perspective</b>  | <b>153</b> |
| 8.1 Concluding Summary . . . . .   | 153        |
| 8.2 Recommendations and Future Work . . . . .  | 155        |
| <b>A Impeller Specific Parameters for Geometrical Moments of Inertia Calculation</b> | <b>159</b> |
| A.1 Rotor Blades with Constant Cross-Sectional Area . . . . .                        | 159        |
| A.2 Rotor Blades with Varying Cross-Sectional Area . . . . .                         | 160        |
| A.3 Flow Guiding Coverage . . . . .  | 161        |
| <b>B Adaptive Force Shaping Conditions</b>   | <b>163</b> |
| <b>Bibliography</b>  | <b>167</b> |



# Nomenclature

## Roman Symbols

|     |   |     |                               |
|-----|---|-----|-------------------------------|
| $c$ | damping constant                        | $w$ | whirl movement                |
| $c$ | quefrequency                            | $A$ | amplitude                     |
| $f$ | frequency                               | $C$ | Cepstrum                      |
| $k$ | stiffness                               | $E$ | Expected value                |
| $k$ | kurtosis                                | $F$ | excitation force              |
| $l$ | intrinsic mode function residual signal | $I$ | condition Indicator           |
| $m$ | mass                                    | $I$ | geometrical moment of inertia |
| $s$ | intrinsic mode function start signal    | $T$ | time period                   |
| $t$ | time                                    | $X$ | signal                        |

## Boldface Roman Symbols

|     |  |     |                                     |
|-----|--|-----|-------------------------------------|
| $e$ | state error vector                     | $D$ | direct link matrix                  |
| $f$ | force vector                           | $F$ | filter matrix                       |
| $f$ | filter vector                          | $G$ | gyroscopic matrix                   |
| $g$ | interface gap force vector             | $H$ | feedback matrix                     |
| $m$ | virtual load vector                    | $I$ | identity matrix                     |
| $q$ | virtual displacement / rotation vector | $K$ | stiffness matrix                    |
| $q$ | coordinate vector                      | $K$ | Kalman gain matrix                  |
| $r$ | residual load vector                   | $M$ | mass matrix                         |
| $u$ | displacement / rotation vector         | $P$ | Boolean matrix                      |
| $v$ | measurement noise vector               | $P$ | Covariance matrix                   |
| $v$ | state input vector                     | $Q$ | state error covariance matrix       |
| $w$ | weighting vector                       | $R$ | interface displacement modes matrix |
| $w$ | state uncertainty vector               | $R$ | measurement error covariance matrix |
| $x$ | state vector                           | $R$ | modal reduction matrix              |
| $y$ | state output vector                    | $S$ | impact sequence vector              |
| $A$ | state transition matrix                | $T$ | transmissibility matrix             |
| $A$ | acceleration matrix                    | $U$ | displacement / rotation matrix      |
| $B$ | state influence matrix                 | $X$ | signal matrix                       |
| $B$ | signed Boolean matrix                  | $Y$ | transfer function matrix            |
| $C$ | damping matrix                         | $Z$ | dynamic stiffness matrix            |
| $C$ | output gain matrix                     |     |                                     |

## Greek Symbols

|                        |                   |           |                                      |
|------------------------|-------------------|-----------|--------------------------------------|
| $\boldsymbol{\eta}(t)$ | modal coordinates | $\rho$    | specific impact / sensor consistency |
| $\mu$                  | residual          | $\varrho$ | deviation                            |
| $\varepsilon$          | eccentricity      | $\theta$  | damping ratio                        |
| $\phi$                 | eigenmode         | $\tau$    | time increment                       |
| $\psi$                 | rotation          | $\omega$  | circular frequency                   |
| $\sigma$               | error             | $\Omega$  | angular excitation frequency         |
| $\varsigma$            | singular value    |           |                                      |

## Boldface Greek Symbols

|                        |  |                     |                            |
|------------------------|--|---------------------|----------------------------|
| $\boldsymbol{\lambda}$ | interface force vector                     | $\boldsymbol{\Psi}$ | amplitude and phase vector |
| $\boldsymbol{\rho}$    | overall impact / sensor consistency vector | $\boldsymbol{\chi}$ | reciprocity matrix         |
| $\boldsymbol{\Phi}$    | mode shape matrix                          |                     |                            |

## Operators

|                 |                        |                      |                                       |
|-----------------|------------------------|----------------------|---------------------------------------|
| $\tilde{\star}$ | filtered               | $\bar{\star}$        | mean value                            |
| $\dot{\star}$   | time derivative        | $\star^+$            | Moore–Penrose inverse (pseudoinverse) |
| $\ddot{\star}$  | second time derivative | $\star^T$            | transpose                             |
| $\hat{\star}$   | observed estimate      | $\star^H$            | complex conjugate transpose           |
| $\star^{-1}$    | inverse                | $\mathcal{F}(\star)$ | Fourier transformation                |

## Subscripts

|               |                      |
|---------------|----------------------|
| $\star_c$     | compatibility        |
| $\star_{CPW}$ | cepstrum prewhitened |
| $\star_e$     | equilibrium          |

## Superscripts

|                  |                         |
|------------------|-------------------------|
| $\star^{approx}$ | approximated            |
| $\star^{est}$    | estimated               |
| $\star^-$        | a priori state estimate |

## Abbreviations

|        |   |
|--------|---|
| ADC    | analog-to-digital converter                               |
| DoF    | degree(s) of freedom                                      |
| EMD    | Empirical Mode Decomposition                              |
| FBS    | frequency-based substructuring                            |
| FE     | finite element  |
| FEM    | finite element method                                     |
| FIR    | finite impulse response                                   |
| FRF    | frequency response function                               |
| IDM    | interface displacement mode                               |
| IMF    | intrinsic mode function                                   |
| LM-FBS | Lagrange Multiplier FBS                                   |
| MEMS   | Micro-Electro-Mechanical System                           |
| MOMEDA | Multipoint Optimal Minimum Entropy Deconvolution Adjusted |
| RMS    | root mean square value                                    |
| RUL    | remaining useful lifetime                                 |
| SEMM   | System Equivalent Model Mixing                            |
| VP     | virtual point   |
| VPT    | virtual point transformation                              |



## Chapter 1

# Introduction

Vibrations are omnipresent. They can occur in an audible, visible, tactile manner or are just hidden as in most instances of daily life. Mechanical vibrations are beautiful in music, but can be annoying and cause great harm. We can observe vibrations from various point of views in all engineering disciplines. Interdisciplinary orientated, they can be transformed between different domain representations (see Sec. 2.1). In the age of digitalization and automation, these dynamics are contemplated as data packets with specific resolution and size. Another point of view is the analog signal form of vibration. Here, vibrations are enclosed in dynamic current and voltage signals. In most cases, the signal chain is established by a transducer that physically converts the mechanical vibration into an analog voltage signal, where a superordinate sensor system is responsible for pre-processing, digitalization and post-processing.

All these observations are based on inputs excitations and output responses of a mechanical system. This thesis proposes a framework that brings together the inputs and outputs of all representations described above and describes the correlation between these inputs and outputs for industrial condition monitoring applications.

We focus on mechanical vibrations of rotating machinery and build a bridge to digital observation. Therefore, novel modeling and transducer techniques are applied and evolved.

## 1.1 Classification of Vibration Monitoring

Emerging techniques in the past already pursued holistic approaches to vibration-based monitoring solutions, especially within industrial applications, where unexpected failures can cause serious damages or long downtimes. Most vibration-based industrial condition monitoring systems solely use information from sensor data. Within this thesis, we call these solutions *signal-* or *data-*based systems. Research is very applied in this context and focuses on applications with far-reaching consequences. The centrifugal pump is a predestined example in this context. Pumps and blowers are essential elements in a wide range of industrial use cases like power plants and fluid supply solutions. In this case, monitoring systems need to detect mechanical, hydraulic and peripheral disturbances. We can list a multitude of examples concerning these disturbances: unbalance, rotor-stator rubbing, bent or warped shafts, misalignment, bearing or sealing faults, gas in pumping medium, dry run, cavitation pulsation, etc. are common representatives [19, 25, 38, 76]. State-of-the-art methods related to data-based approaches often use machine learning [26, 124] or deep learning techniques [123] for automatic classification of these faults. We will come back to the faults, but first discuss common strategies to guarantee machine health.

To begin with the field of vibration monitoring, we look back into the past. Initially, the first vibration-based monitoring system was established by Rathbone in the year 1939 [106].

Within his paper named “Vibration Tolerance”, he created a chart which characterized the machine condition based on vibration amplitude and frequency. Hence, a new research topic was opened, although systematic condition monitoring started with the invention of FFT (Fast Fourier Transformation) analyzers in the 1970s [105]. Since these years, much has evolved. Today, a distinction is made between three strategies [105]:

1. **Run-to-Break Operation.** This type of handling the machine state is a kind of brute-force method, where an application operates until it breaks down, so that the operator can benefit of a maximum of operating hours without downtime. However, this strategy is only applicable if such a machine operates totally independent of its surroundings e.g., other components or machines. Otherwise a sudden breakdown has the potential to shut down an assembly line or even the entire production.
2. **Preventive Maintenance at Regular Service Intervals.** As a contrast to run-to-break operation and to prevent incalculable risks, regular service intervals are defined which must be shorter than the expected machine live. The interval time is calculated based on statistical evaluations so that less than 1-2 % of the machines fail in the defined time. In practice, worst case assumption are made, with the result that most of the regarded machines can work two- or threefold longer than the assumed time interval would suggest [92]. This drastically reduces endurance, but the operator is on the safe side. A solution to get as close as possible to the optimum maintenance interval is described in the following point.
3. **Condition-Based Maintenance.** This maintenance technique is based on condition monitoring or on its extension, the condition-based diagnosis. When a proper diagnosis is made, the remaining useful lifetime (RUL) can be predicted. As a consequence, service intervals can be saved and the machine live can be exhausted to a maximum while ensuring that no damage is caused. Prerequisite is a condition monitoring algorithm built on an accurate and precise model description of the entire observed system. This leads to the need for hybrid dynamic models that support such monitoring approaches with a powerful machine description to push maintenance intervals close to their optimum. *Hybrid* in this occasion means a combination of numerical simulation, experimental testing and measured data at operation. The demand for these models which are commonly designated as *Digital Twins* will be discussed in Sec. 1.2.

### 1.1.1 Signal-Based Monitoring

Within this thesis, methods for condition-based diagnosis are developed in the context of vibration-based maintenance. Therefore, we start with the measurement of mechanical vibrations. Mechanical states can be captured by different sensors. They are either characterized by *displacement*, *velocity*, or *acceleration* sensors in order to describe the state variables, namely the displacement  $\mathbf{u}$  and its time-derivatives  $\dot{\mathbf{u}}$  and  $\ddot{\mathbf{u}}$  in the time-dependent mechanical equation of motion

$$\mathbf{M}\ddot{\mathbf{u}}(t) + \mathbf{C}\dot{\mathbf{u}}(t) + \mathbf{K}\mathbf{u}(t) = \mathbf{f}(t); \quad \mathbf{u} \in \mathbb{R}^n. \quad (1.1)$$

It contains the mass, damping and stiffness within the matrices  $\mathbf{M}$ ,  $\mathbf{C}$  and  $\mathbf{K}$  in a discretized description of the physical state with  $n$  degrees of freedom (DoF).

Meaningfully, an appropriate sensor is selected, based on the final application. Resting upon the characteristic vibration fingerprint and structural dynamic properties, some sensor types are more suitable than others. Nowadays, accelerometers are established for most

applications. Though, there are some fields where displacement or velocity transducers are favorable. Especially in monitoring systems according to standards such as DIN ISO 20816 [39], which are based on vibration velocity, appropriate transducers are occasionally used.

**Velocity sensors** are mostly based on a seismically suspended magnet within a coil attached to the housing. A big disadvantage of these sensors is the low bandwidth. Their bandwidth is usually representative between 10 Hz and 1 kHz. Due to that reason, common standards, as well as the DIN ISO 20816, set their vibration amplitude limits within this range. Another application for displacement and velocity transducers are light, slightly dampened structures. In these cases, laser vibrometers are predestined because of their ability to measure vibration without adding sensor mass to the structure. In Sec. 7.1, an exemplary scenario for that application is shown. The focus for what concerns measurements within this thesis lies on accelerations.

**Accelerometers** are in most cases the mean of choice when it comes to high bandwidth, high sensitivity and low sensor mass. All examples from literature within this section are based on acceleration signals. High-performance accelerometers are mostly based on a piezoelectric principle [105]. The integrated piezoelectric crystal generates an electric charge which is proportional to pressure applied to the crystal. This pressure is generated by a seismic mass inside the sensor. An integrated circuit converts the charge to voltage utilizing an amplifier. Of course, this voltage signal is analog. Before sampling for digitalization, analog filtering is required to minimize effects such as noise, aliasing, and disturbances. Subsequently, the signal is discretised by an appropriate analog-to-digital converter (ADC) and post-processed by the measurement system. This entire measurement chain can be very expensive, although in research and development applications, piezoelectric sensor types are indispensable due to their unrivaled performance.

In this thesis, we focus on faults in rotating machinery. Most of the implied rotor systems are supported by roller bearings. Their health is of big interest for industrial use cases. A standard was created specifically for this purpose. Therefore, the VDI3832 guideline [140] regards collective vibration level over a period of time or spectral analyses of the signal envelope. Further established methods for monitoring these components referring to [21, 28] are *Empirical Mode Decomposition*, *Multipoint Optimal Minimum Entropy Deconvolution Adjusted (MOMEDA)* filtering and combinations with Fourier and Hilbert transformation. These methods are evaluated in more detail referring to the test environment in Sec. 3.4. Further studies showed successful bearing fault detection utilizing *Winger-Ville distribution* [13] or *Wavelet transformation* [14, 97]. Due to different kinematics-defining components of the roller bearings (see Fig. 3.2), some methods are more expedient than others. Wavelet transformation [97] and envelope analysis using Hilbert and Fourier transformation [44] for instance, are well established in detecting outer race defects. On the other hand, inner race and ball defects are better captured by Wavelet transformation due to the fine resolution in high frequency range of the technique [135]. The upper mentioned Empirical Mode Decomposition (EMD) was initially presented in [129]. It also builds on envelope analysis and uses so-called Intrinsic Mode Functions (IMF) as pre-filtering of the vibration signal. We observe it in Sec. 3.4.3. Particularly, the EMD works especially well as a self-adapting signal handling technique for non-stationary processes [41, 150]. Thereupon, Peng explores an enhancement of this fault diagnosis method [98]. Here, the raw acceleration signal is separated into slim bands utilizing wavelet packet transformation as pre-processor. Subsequently, the standard procedure of Empirical Mode Decomposition is performed on these bands to parse the signal into IMFs. Afterwards, again the envelope spectral analysis is applied. Improvements of this method, when comparing it for example with wavelet-based spectrograms, are better resolu-

tion in the time and frequency domain representation, although some ripple in the resulting post-processed signals are caused by drawbacks concerning fault identification. Though, computing efficiency increases.

Of course, these methods were already combined and automated in various manner. In this context, envelope analysis was applied in [77] to automatically find frequency bands in which the bearing fault information can be captured. The underlying approach is led by a wavelet-supported spectral kurtosis calculation. This statistical indicator (definition see Sec. 3.4.1) is combined with a wavelet transformation to find a proper filtering technique for the vibration signal. The subsequent envelope analysis successfully extracts the bearing fault information.

Although roller bearing defects play an important role in researching new condition monitoring methods, there is also a need for techniques that monitor rotor faults that can cause bearing defects over time. Previous work has shown in [71] that an overload caused by rotor unbalance can damage the bearings and also the entire machine. Even gearboxes are examples which often require high reliability without maintenance, where bearings are not the only vulnerable parts. Despite of a declining market due to increasing electrification, gearboxes need condition-based preservation [149]. Moreover, effects at interaction of components within the entire system including motor and gearbox led to extensive research findings [19]. In this context, again the Empirical Mode Decomposition method helped to detect gearbox-specific faults such as tooth cracks [44].

To sum up, we can imagine that all mentioned fault detection algorithms are based on similar physical occurrences. Effectively, they express themselves within the vibration signal either in a frequency modulated manner or within an amplitude modulated form. In the flow chart of Fig. 1.1 this classification is made. All mentioned signal-based methods are based on amplitude modulated signal analysis except the unbalance monitoring of Korkua et al. [71] which is attributable to frequency modulation.

Most of the previously presented signal analysis work is based on high performance piezoelectric sensor technology as described above. Although, all methods within this thesis are developed for industrial sensor systems. Industrial requirements often go hand in hand with costs.

**Micro-Electro-Mechanical (MEMS) accelerometers** can be the cost-effective solution to this problem. These transducers including a signal condition unit cost about 10 % or less compared to piezoelectric accelerometers [3] but can reach high accuracy even in advanced, industrial applications [2]. They consist of polysilicon structures atop silicon wafers which are manufactured by surface micro machine processes. The structure contains a spring-mass system which oscillates with the applied dynamic force. Structure deflection is measured using differential capacitors, which are composed of electrodes fixed to the moving mass and electrode counterparts at the surrounding sensor structure. The differential capacitor is unbalanced by a mass deflecting force with the result of an acceleration proportional sensor output amplitude [127].

Note, the signal chain is extremely shortened when talking about digital MEMS accelerometers. After the presented transducer principle, all signal processing steps are integrated in the sensor chip. Hence, the dynamic capacitance is transformed into a voltage signal, filtered and digitalized directly on the sensor unit. The digital output values are usually collected by a microprocessor. When adding a wireless communication unit and low-power energy supply, we have a so-called *constrained device* or *wireless sensor node*. The short analogue path already triggered the application to wireless communication units in the past [148]. These sensor

nodes can be meshed within a big sensor network depending on the wireless communication method. Generalized, it is called *sensor system* within this thesis.

In the past, MEMS sensor technology was already recognized as highly promising for the future, especially for fault diagnostic due to its cost effectiveness, low power consumption, integrability and reliability [71]. It is proven that piezoelectric accelerometers are substitutable by MEMS sensors in vibration measurements applications especially in the low frequency range [84]. Often, MEMS sensors imply drawbacks such as low sensitivity, unsatisfactory noise performance or resolution. A study for structural health monitoring has shown that these effects are improvable [67]. A further issue, namely temperature sensitivity can also be handled [40]. By utilizing MEMS accelerometers, various fault examples such as bowed shafts, unbalances and bearing faults were already successfully diagnosed [122]. In detail, MEMS sensor systems were used, for example, on centrifugal pumps to detect cavitation, impeller damage and dry run [38]. A further helpful advantage is that these integrated sensor systems enable on-shaft vibration measurements to detect base looseness, unbalance and misalignment in rotordynamics [43, 93, 101]. Especially, orbit measurements can be carried out particularly well as demonstrated in [64].

## Conclusion

Condition-based maintenance is the method of choice in the data-driven world. MEMS vibration sensor systems are already established in various condition monitoring applications due to several advantages such as cost effectiveness, low power consumption and integrability. However, referring to the sensors, only the signal processing part was discussed. Note, monitoring of dynamic mechanical phenomena requires a holistic approach as aforementioned the beginning of this section.

### 1.1.2 Model-Based Monitoring

Accurate and precise diagnosis of faults under varying boundary conditions requires deep knowledge about the system. This is only sustainable utilizing a signal-based approach when sufficient amount and quality of data according to all possible operating scenarios is available. In most applications, this requirement is not fulfilled. In these cases, signal-based techniques can just *detect* faults.

We must distinguish between *fault detection* and *fault diagnosis*. Fault detection shows that the disturbance happened, but only diagnosis can find the fault cause, location and quantity [61]. When deeper fault information is required, model-based fault diagnosis is preferable. Usually, input and output values are required to set up a reliable model [60]. Generally, the model serves as a tool to *predict* output values when fed with new, unknown data.

When the model and failure modes are exactly defined, signal-based fault detection can be used for preselection. In case the measurand exceeds defined vibration limits, the fault type is found based on specific signal characteristics. Building on that prior knowledge, the model-based algorithm can finally quantify the fault dimension by an optimization calculation [114, 130]. Here, the required models are usually created by numerical simulations.

Another big advantage of model-based techniques is the reconstruction of inaccessible degrees of freedom (DoF) in the observed application. These DoF can be gathered as virtual sensors. Virtual sensors are really helpful, if there are application-specific requirements for physical sensor positions which are not suitable with respect to fault quantification. Kullaa [75] showed that the virtual sensor should be still placed near to a physical transducer. In this scenario, virtual sensing can even work with experimental models when the transfer paths between the virtual sensor, the fault source and the physical sensor are well understood. A virtual sensing

approach will be evaluated in Sec 7.2.1 of this thesis.

Since understanding model-based methods usually requires some insight into the algorithms, two related state-of-the-art methods will be presented, namely the state-space observer approach (see Sec. 3.1) and the Kalman filter (see Sec. 3.2).

## 1.2 Research Questions and Objectives

Accurate and precise predictive maintenance is still a challenge in recent development processes. Current research strongly focuses on machine learning approaches and deep learning based techniques which typically require enormous amounts of data to train the underlying models. The contradiction is obvious. Within the development phase, there is often not enough or even no operational data available. Learning approaches need huge datasets accurately representing the required healthy and faulty machine states. Even if a prototype or pilot system exists, tremendous manual effort is needed to implement all types of faults which are to be identified and quantified.

Moreover, imagine that the fault diagnosis algorithm was trained for a component (rotating machine) at a locomotive A. Will the same algorithm detect and quantify these faults at locomotive B with the same accuracy and precision? What happens if the bogie of locomotive B changed to significantly differing stiffness and damping properties?

The algorithm will only perform in case of these changes are captured in the training data sets.

Imagine a second example. The new component was perfectly numerically simulated including all conceivable fault scenarios<sup>1</sup>. Imagine that this component is now mounted inside the locomotive and someone uses that component as rack for heavy wedges. In order to hang these wedges, an extra stiff rack is mounted on the component. As a consequence, the entire system's dynamics change. The fault specific acceleration amplitude can be halved compared with the original healthy state. What if this acceleration complies with an unbalance which will continuously destroy the bearings? Probably nobody will notice. These changes of boundary conditions at varying peripheries are usually not captured.

Another problem comes up when the diagnosis is based on wireless sensor systems. These nodes have to be placed at the outside housing due to its shielding effect in order to guarantee a robust data connection. The fault occurs usually at the rotor system - far away from that measurement position. Nevertheless, the diagnosis algorithm needs to address the entire system, including the disturbances due to transfer paths between fault and measurement position to capture the holistic system states.

Within this thesis, hybrid modeling approaches are pursued to solve the discussed issues of a MEMS-based sensor system. Drawbacks of single approaches either based on operational data or numerical simulations are handled by such hybrid techniques<sup>2</sup>.

The presented methodology for model description contains a minimum amount of DoF to be compatible with constrained devices based on MEMS accelerometers. Finally, the presented method must be retrofittable since monitoring solutions are sometimes needed at already widely deployed systems.

When looking at all domain representations (see Sec. 2.1), a bundle of techniques for setting up models is already established. With respect to numerical modeling, the type, location and connection of finite elements must be well considered in order to find a minimum DoF set. In

<sup>1</sup>Note, this is not the typical industrial use-case, since 3D-models including all material properties are not always provided by the subcontractors.

<sup>2</sup>Note, an exclusively experimental testing strategy can also fail when not all substructures of the component are physically available.

the field of experimental testing, the interface dynamics are difficult to capture. We deal with these dynamics by mixing hybrid models based on the Lagrange Multiplier frequency-based substructuring (LM-FBS) technique with the modal expansion framework System Equivalent Model Mixing (SEMM). The operational conditions are captured by a modal expansion technique. The signal-based part for feeding the models focuses on the MEMS restrictions and researches for the best suitable fault identification method. Finally, the entire diagnosis is realized based on a single, triaxial accelerometer at the housing.

Therefore, the objective of this thesis is formulated as:

*Method development for a holistic, hybrid adaptive modeling strategy which allows quantitative fault diagnosis of rotating machinery by industrial, constrained sensor systems.*

### 1.3 Scientific Contribution

In this thesis, novel methods within the scope of hybrid dynamic models for vibration monitoring are contributed by the author:

- A modeling approach for rotor types widely used in industrial pump and blower applications is developed. The basic idea, which is also published in [72], focuses on a minimum degrees of freedom set and can therefore be seen as a model reduction technique.
- The effect of orthotropic elastic rotor support on unbalance monitoring is initially described in publication [73].
- A SEMM-based modal expansion strategy is created for the implementation of interface dynamics between rotor and housing of rotating machinery. The results are published in [74]. Here, a simple numerical housing approach is utilized in combination with the rotor model of [72]. The implementation of rotor support dynamics is further increased by coupling an experimental housing model with the upper mentioned rotor (see Sec. 5.2.1 and 5.2.2)
- Operational conditions are introduced into hybrid dynamic models utilizing a novel, iterative, SEMM-based modal expansion scheme (see Chap. 6).
- All proposed methods are successfully validated with application to an industrial use-case based on a Micro-Electro-Mechanical sensor system (MEMS) in Chap. 7.

### 1.4 Structure of the Thesis

At the beginning of this thesis, vibration monitoring strategies were presented. These were classified into signal-based methods and model-based approaches. In the context of signal-based fault diagnosis, we distinguish between amplitude-modulated signals and their frequency-modulated counterparts. The model-based component builds on the theory of structural dynamics which can be formulated in different domain representations. They are described in Chap. 2, in the beginning of Part I. Here, the main theory of this thesis is outlined within the Lagrange Multiplier frequency-based substructuring method in combination with the virtual point transformation (VPT) and the SEMM-based modal expansion.

Afterwards, we come back to the signal-based monitoring methods and their classification into frequency modulation (unbalance identification in Sec. 3.3) and amplitude modulation

(roller bearing fault identification in Sec. 3.4).

In Chap. 4, two test rigs of industrial applications are characterized for subsequent method development - namely a blower for locomotive motor cooling and a centrifugal pump which is responsible for circulating the oil within the cooling circuit of a traction transformer.

Subsequently, Part II describes the entire modeling strategy. All models have been calculated using MATLAB<sup>®</sup><sup>3</sup>. Part II starts with Chap. 5 which shows the overall modeling approach with respect to a hybrid dynamic model, assembled by a numerical rotor and a machine housing (numerically and experimentally modeled). This approach and its subsequent extension is solely shown on the blower test rig. The combination of the numerical rotor and the experimental housing is further pursued by modal expansion in Sec. 5.2.2. This expanded, hybrid model is then adapted in Chap. 6. Here, structural dynamic changes due to operational conditions are implemented for the entire rotational speed range. The model is validated based on two exemplary unbalances in Sec 6.1.1. Here, unphysical spikes occur which are filtered out based on an iterative, adaptive cubic spline fit within the force spectrum in Sec 6.1.2. A similar technique is subsequently applied on a scenario with changed boundary conditions.

Chap. 7 introduces the industrial sensor system applications of the final Part III. An exemplary sensor system is presented and evaluated. Here, we characterize a MEMS accelerometer concerning amplitude response linearity and temperature sensitivity. The same sensor is then applied to a virtual sensing approach at the pump test rig concerning roller bearing fault quantification. Furthermore, it is also applied to the hybrid dynamic model which is the outcome of Chap. 6. This exemplary case study is outlined in Sec. 7.3.

The entire thesis can also be classified into methods and applications. This structure is graphically shown in Fig. 1.1.

---

<sup>3</sup>Version 9.13.0.2049777

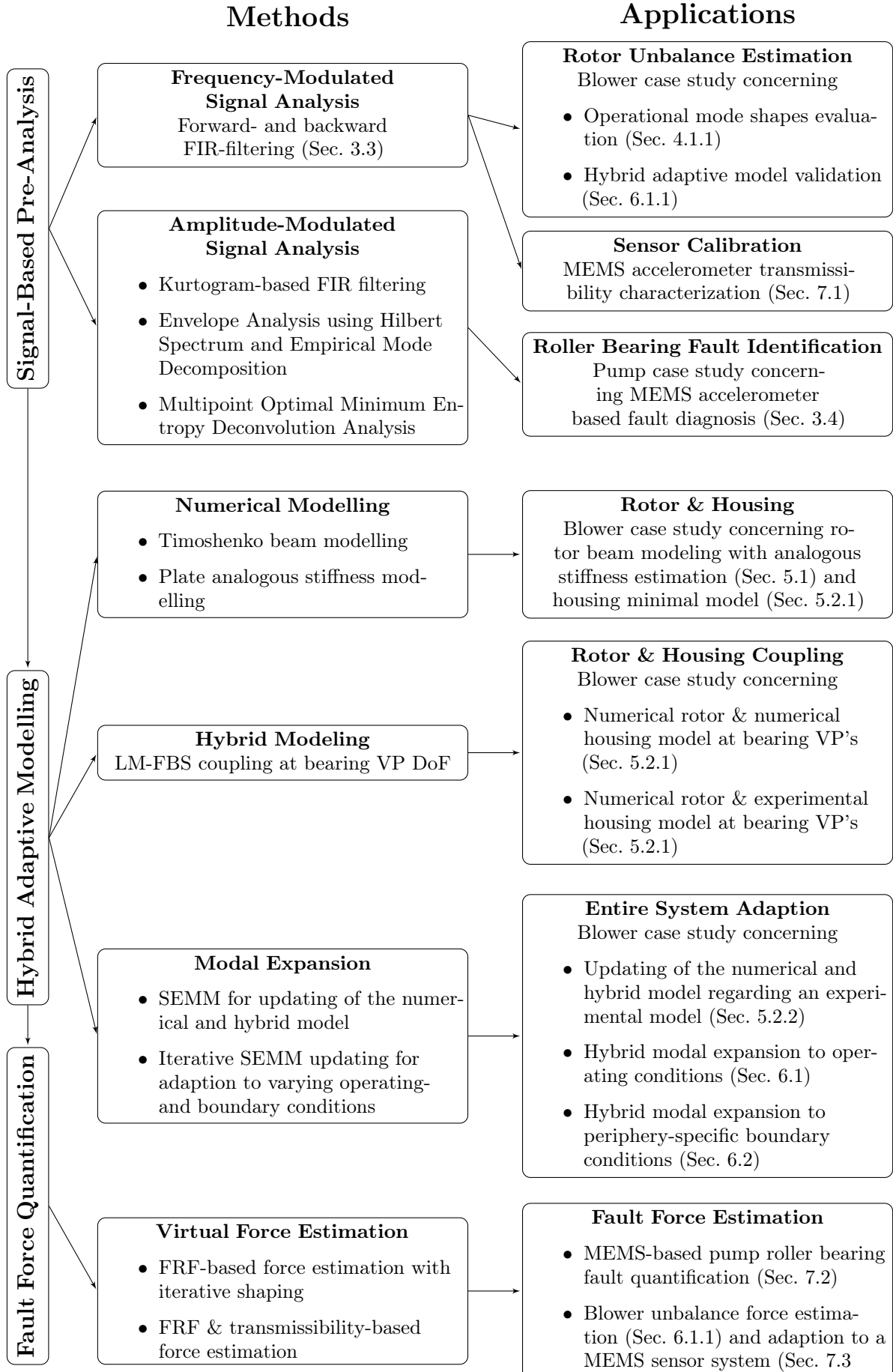


Figure 1.1: Flow chart with methods and applications to a blower- and a pump test rig.



## Part I

# Vibration Monitoring Fundamentals



## Chapter 2

# Structural Dynamics for Monitoring Applications

In the era of ephemeral words for digitalization scopes such as the *Internet of Things (IoT)*, the *Digital Twin* or the *Industrial Metaverse*, we must not forget that we talk about physical relationships, when bringing sensor data into cloud solutions. These laws are old. Many innovations in the field of structural dynamics build on Isaac Newton's *Principia Mathematica* [91]. Even vibration-based monitoring solutions can not exist without Newton's laws, when they are based on physical relations. His fundamental theory of mechanics builds on three laws: *The Law of Inertia*, *The Law of Acceleration* and *The Law of Action and Reaction*. Within structural dynamics for monitoring applications, the second law has high impact. It is translated from the Latin language as follows:

*“A change in motion is proportional to the motive force impressed and takes place along the straight line in which that force is impressed.”* [30, 100]

Within this thesis, solutions are developed which should best describe relations between an interaction of forces and the change of motion of the entire system as a result of these forces. The focus lies on rotating machinery with forces acting on the rotor system. The dynamic *state* and therefore relationships between these forces and their responses can be formulated in different domains.

## 2.1 Representation Domains for Hybrid Dynamic Models

A major decision within hybrid modeling is the choice of representation domain. Essentially, the physical domain can be divided into five different representations which are most relevant in structural dynamics. Generally, we can transform them into each other. The chosen classification into five representations is based on [139]. Here, they are categorized into the *physical domain*, *modal domain*, *state-space domain*, *time domain* and *frequency domain*. These representations can be alternatively classified according to [5]. Here, they are divided into a *spatial description* which implies the physical and modal domain, a *spectral description* which contains the time domain and the frequency domain and the *state description* which comprises the state-space domain and the Laplace domain. Our chosen classification does not contain the Laplace representation, but this representation is not utilized within this thesis anyway. Starting from Newton's second law, we define the continuous mechanical equation of motion as *physical domain*. All five chosen representations are discretized approximations of the physical domain. Hence, we specify them as *physical domain*, *modal domain*, *state-space domain*, *time domain* and *frequency domain*. An overview over the chosen classification is given in Fig. 2.1.

## Physical Domain

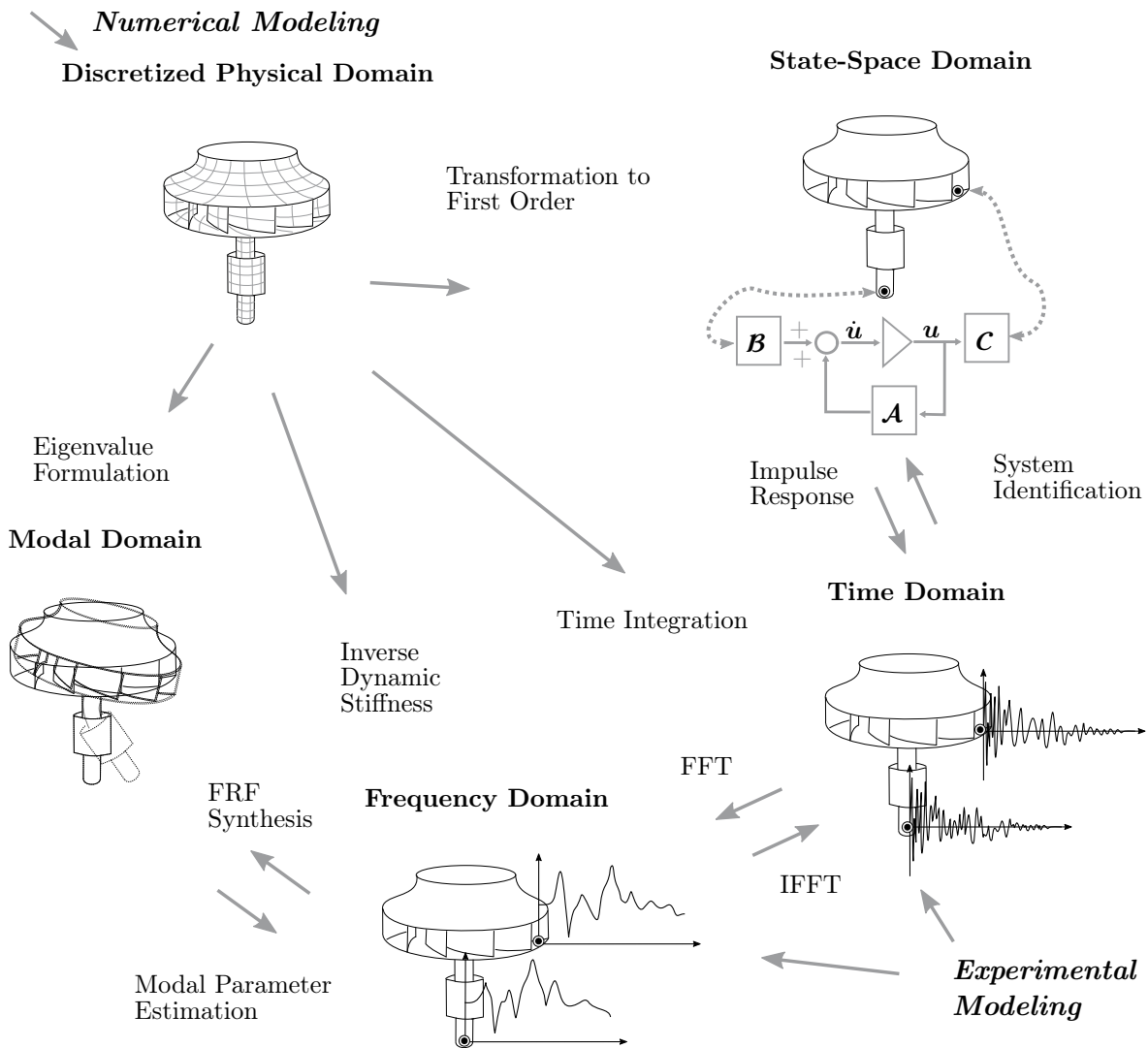


**Figure 2.1:** Visualization of five representations of structural dynamic models inspired by [139]. Some transformation possibilities are delineated to show the versatility between these domains. Dynamic models can be created in a numerical or experimental manner. These typical starting points are depicted in the top left and bottom right corners of the figure.

### 2.1.1 Physical Domain

The physical domain describes the continuous equilibrium between the system's internal forces based on inertia, velocity-proportional damping and elasticity in this thesis. The discretized physical domain can also be called *physical* since the relation between these internal forces is directly readable from the system matrices with displacements  $\mathbf{u}(t)$  or their time derivatives and an external load  $\mathbf{f}(t)$  on the equation's right hand side. Usually, this discretization is based on a numerical simulation using finite elements (FE). Based on the formulation of Newton's second law, the discretized balance of forces is written as:

$$\mathbf{M}\ddot{\mathbf{u}}(t) + \mathbf{C}\dot{\mathbf{u}}(t) + \mathbf{K}\mathbf{u}(t) = \mathbf{f}(t); \quad \mathbf{u} \in \mathbb{R}^n. \quad (2.1)$$

Here, the mass matrix  $\mathbf{M}$ , the damping matrix  $\mathbf{C}$  and the stiffness matrix  $\mathbf{K}$  are defined for a linearized system. When discretized, the forces are vectors that are non-linear functions of  $\ddot{\mathbf{u}}(t)$ ,  $\dot{\mathbf{u}}(t)$  and  $\mathbf{u}$  and can no longer be expressed using constant matrices. As the presented techniques are further based on measurements which require a time-invariant system, nonlinear behavior is not considered within this thesis. In order to be comprehensive,  $\mathbf{G}$  should be added to the velocity-proportional term as further system matrix. Note,  $\mathbf{G}$  depends on the rotational speed and therefore applies only to the rotating component<sup>1</sup>. We define a dimension of  $n$  degrees of freedom for the displacements  $\mathbf{u}(t)$  and external loads  $\mathbf{f}(t)$ . In principle, a node of a finite element is usually associated to a maximum of six DoF. In this case,  $\mathbf{u}(t)$  would imply three displacements which are associated with the forces and three rotations correlated with three external moments on the right hand side of Eq. (2.1). When observing a complex system by FE analysis, we usually need a fine mesh with a huge amount of DoF. This leads to big computational effort and can be reduced by modal reduction techniques. Although this is not part of this thesis, it is briefly described in the next section for the sake of completeness.

### 2.1.2 Modal Domain Representation

When looking at modal shapes, mainly global behavior is observed. These mode shapes often rather represent dynamic properties in the lower frequency range. As the same amount of modes in the physical domain representation can be calculated as there are DoF utilizing the finite element method (FEM), the local resonances at higher frequencies are often not of interest. Hence, the modal domain representation is suitable to reduce the model size. For more information and an overview over model reduction techniques, also in the modal domain representation, please find [17].

Generally, there are  $n$  eigenmodes  $\phi$  (natural vibration modes) in a system of  $n$  DoF computable. When damping is neglected, the inertia forces are balanced with the elastic forces and can be written as an eigenvalue problem referring to [49]:

$$(\mathbf{K} - \omega_k^2 \mathbf{M}) \phi_k = 0; \quad k = 1, \dots, n. \quad (2.2)$$

with the eigenfrequencies  $\omega_k$  of the mode shape  $k$ . The eigenmodes  $\phi$  are written in columns of the mode shape matrix  $\Phi$ :

$$\Phi = [\phi_1, \phi_2, \dots, \phi_n]. \quad (2.3)$$

The modes can be scaled to be mass-normalized,  $\mathbf{M}$ - and  $\mathbf{K}$ -orthogonal and sorted by increasing eigenfrequency  $\omega_k$  so that

$$\Phi^T \mathbf{M} \Phi = \mathbf{I} \quad \text{and} \quad \Phi^T \mathbf{K} \Phi = \text{diag}(\omega_1^2, \dots, \omega_n^2). \quad (2.4)$$

A set of modal coordinates,  $\boldsymbol{\eta}(t)$  now replaces the displacements  $\mathbf{u}$ . They represent either the amplitude of the full space of modes  $n$  or a subspace of the first modes  $k = 1, \dots, m$  in case of model reduction intentions. This kind of model reduction is called *modal truncation*. The underlying reduction matrix is defined as

$$\mathcal{R} = [\phi_1, \dots, \phi_m]. \quad (2.5)$$

---

<sup>1</sup>Essentially, the gyroscopic effect is large at high rotational speeds and specific rotor geometries and will be neglected here. For more information about these rotordynamics, please find [48].

Therefore, the response  $\mathbf{u}$  can be assembled back, using the principle of mode superposition as

$$\mathbf{u}(t) = \sum_{k=1}^n \phi_k \eta_k = \Phi \boldsymbol{\eta}(t) \quad (2.6)$$

or approximated by  $m$  out of  $n$  modes in case of the truncated model:

$$\mathbf{u}(t) \approx \sum_{k=1}^m \phi_k \eta_k = \mathcal{R} \boldsymbol{\eta}(t); \quad \boldsymbol{\eta} \in \mathcal{R}^m. \quad (2.7)$$

Now, an equivalent representation to the discretized physical domain representation via the force equilibrium is built:

$$\mathbf{M} \mathcal{R} \ddot{\boldsymbol{\eta}} + \mathbf{C} \mathcal{R} \dot{\boldsymbol{\eta}} + \mathbf{K} \mathcal{R} \boldsymbol{\eta} = \mathbf{f}(t) + \mathbf{r}(t). \quad (2.8)$$

Since there are now less unknowns to represent the DoF than there are equilibrium equations to solve, there is in general always a residual force (captured by  $\mathbf{r}(t)$ ), whatever the solution for  $\boldsymbol{\eta}$ . A „best choice“ for  $\boldsymbol{\eta}$  is then for instance to ensure that the residual force is zero in the representation subspace, i.e. that it does not produce any work in that space:  $\mathcal{R}^T \mathbf{r} = 0$ . That can be seen as applying the principle of virtual work in case the solution is constraint to satisfy Eq. (2.7) and is often referred to as the *Rayleigh-Ritz method* [49]. Therefore, Eq. (2.8) is pre-multiplied with  $\mathcal{R}^T$  resulting  $\mathcal{R}^T \mathbf{r} = 0$ :

$$\mathbf{M}_m \ddot{\boldsymbol{\eta}} + \mathbf{C}_m \dot{\boldsymbol{\eta}} + \mathbf{K}_m \boldsymbol{\eta} = \mathbf{f}_m(t). \quad (2.9)$$

For further details, please find [5, 139]. Generally, the modal domain representation is not utilized for the presented methods in this thesis. In order to build up an experimental model in the modal domain representation, a huge bundle of sensors is needed for proper mode shape representation of complex structures. The modal domain representation seems not to be a suitable solution as we choose an approach based on substructures and a small amount of measurement DoF.

### 2.1.3 State-Space Domain Representation

The state-space formulation is usually widely used in control and in signal processing applications. After successful application of the state-space approach in structural dynamic system identification and substructuring by Su and Juan [126], further research with respect to experimental substructuring techniques was expedited by Sjövall and Abrahamsson [118–120]. They showed several advantages of this formulation, especially concerning robustness and convergence properties [121] with respect to model identification. Furthermore, the state-space domain representation is suitable to represent structural dynamic models in cases of strong damping (see Sec. 3.3 in [49] for details). An overview over possible substructuring applications in the state-space domain representation is given by Gibanca in [50].

A basic property of the state-space domain representation is the first-order form. The second order ordinary differential equation of Eq. (2.1) is transformed to the first order **ABCD** equation of motion. Therefore, the state vector  $\mathbf{x}$  is introduced:

$$\mathbf{x}(t) \hat{=} \begin{bmatrix} \mathbf{u}(t) \\ \dot{\mathbf{u}}(t) \end{bmatrix} \quad (2.10)$$

which contains the displacements and its first time derivative. The external loads are written as input vector

$$\mathbf{v}(t) \hat{=} \mathbf{f}(t). \quad (2.11)$$

The state transition matrix  $\mathbf{A}$  and the state influence matrix  $\mathbf{B}$  contain the mass, stiffness and damping matrices in the following notation:

$$\mathbf{A} \hat{=} \begin{bmatrix} \mathbf{0} & \mathbf{I} \\ -\mathbf{M}^{-1}\mathbf{K} & -\mathbf{M}^{-1}\mathbf{C} \end{bmatrix}; \quad \mathbf{B} \hat{=} \begin{bmatrix} \mathbf{0} \\ -\mathbf{M}^{-1}\mathbf{P}_f \end{bmatrix}. \quad (2.12)$$

The output gain matrix  $\mathbf{C}$  and the direct link matrix  $\mathbf{D}$  supplement the first order representation utilizing the  $n \times n$  Boolean matrices  $\mathbf{P}_f$ ,  $\mathbf{P}_d$  and  $\mathbf{P}_v$  which are responsible for selection of a subset of input force or output displacements and their first time derivative. Note that they do not necessarily have to be Boolean. For a second order dynamic system as the mechanical equation of motion,  $\mathbf{D}$  is zero. Hence,  $\mathbf{C}$  and  $\mathbf{D}$  are defined as

$$\mathbf{C} \hat{=} \begin{bmatrix} \mathbf{P}_d & \mathbf{0} \\ \mathbf{0} & \mathbf{P}_v \end{bmatrix}; \quad \mathbf{D} \hat{=} \begin{bmatrix} \mathbf{0} \\ \mathbf{0} \end{bmatrix}. \quad (2.13)$$

Now, the equation of motion is split into a form describing the internal dynamics  $\dot{\mathbf{x}}(t)$ :

$$\dot{\mathbf{x}}(t) = \mathbf{A}\mathbf{x}(t) + \mathbf{B}\mathbf{v}(t) \quad (2.14)$$

and the output  $\mathbf{y}(t)$ :

$$\mathbf{y}(t) = \mathbf{C}\mathbf{x}(t) + \mathbf{D}\mathbf{v}(t) \quad (2.15)$$

which also contains all displacements and their first time derivative at certain DoF. These DoF are selected by  $\mathbf{P}_f$ ,  $\mathbf{P}_d$  and  $\mathbf{P}_v$ . In case they are  $n \times n$  identity matrices, all loads  $\mathbf{f}$  are chosen for the input vector  $\mathbf{v}$ . In this case, all displacements  $\mathbf{u}$  and velocities  $\dot{\mathbf{u}}$  are considered by the output vector  $\mathbf{y}$  as well. The relations are:

$$\mathbf{f}(t) \hat{=} \mathbf{P}_f \mathbf{v}(t); \quad \mathbf{u}(t) \hat{=} \begin{bmatrix} \mathbf{P}_d & \mathbf{0} \end{bmatrix} \mathbf{y}(t); \quad \dot{\mathbf{u}}(t) \hat{=} \begin{bmatrix} \mathbf{0} & \mathbf{P}_v \end{bmatrix} \mathbf{y}(t). \quad (2.16)$$

Note, the system's dimension is now  $2n \times 2n$ . Although, the equation of motion has changed to first order now. In Fig. 2.2, an exemplary state-space loop of a coupled rotor system is depicted. Here, the exciting loads during operation at the rotor (blue) are described by  $\mathbf{v}_{in}$ . For example, the output variables  $\mathbf{y}_{out}$  can be used to determine the input variables  $\mathbf{v}_{in}$  with a monitoring system on the housing. Therefore, these operational forces can be found based on the sensor values and the state-space matrices  $\mathbf{A}$ ,  $\mathbf{B}$  and  $\mathbf{C}$ .

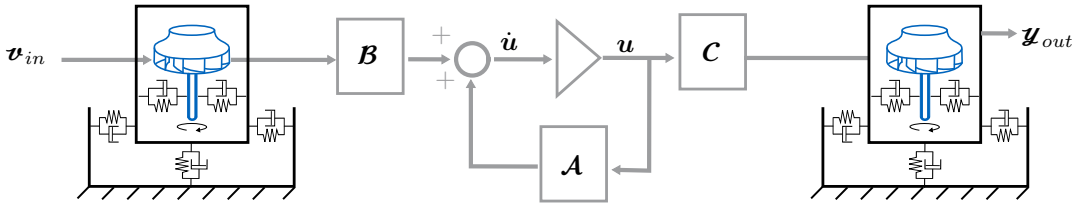


**Figure 2.2:** State-space loop of an exemplary rotor system with input load vector  $\mathbf{v}_{in}$  at the rotor. The output displacements and velocities at the housing are represented by  $\mathbf{y}_{out}$ .

### 2.1.4 Time Domain Representation

The time domain representation suits for a bundle of modeling problems. Even for monitoring applications and for structures with high damping, the representation can be utilized. In particular, nonlinear systems or components excited by impact-like forces can be reasonably described in the time domain representation.

However, we can determine a time domain representation model with more or less computationally efficient methods. Starting from a numerical model - for example in the physical domain representation, the time representation can be reached by a Newmark time-stepping scheme. This technique, as well as a launch from the modal domain representation using a bundle of modes to capture high-frequency content, would be inefficient examples.

On the other hand, impulse response functions (IRFs) are well suited for constrained devices. A quick solution for operating in the time representation would be the inverse Fourier transform of frequency response functions  $\mathbf{Y}(\omega)$ . We will have a closer look at these functions in Sec. 2.1.5. However, applying the inverse Fourier transform, we get the linear harmonic response of motion in the time domain representation based on the Duhamel convolution integral:

$$\mathbf{u}(t) = \mathbf{Y}(t) \cdot \mathbf{f}(t) = \int_{\tau=0}^t \mathbf{Y}(\tau) \cdot \mathbf{f}(t - \tau) d\tau. \quad (2.17)$$

Here, the IRF matrix  $\mathbf{Y}(t)$  describes the relation between input force impulses  $\mathbf{f}(t = 0)$  and output displacements  $\mathbf{u}(t)$  in a time sequence  $\tau$ .

For further details and typical applications, please find [110–112, 136]. Impulse response determination by impact measurements were considered in [78, 138]. Actually, the time domain representation formulation is only indirectly utilized within this thesis. We focus on the frequency domain representation and use the inverse Fourier transform to estimate operational forces in the time domain representation based on coupled frequency response functions and operational displacements.

### 2.1.5 Frequency Domain Representation

The equation of motion Eq. (2.1) in the physical domain representation can be transformed into the frequency domain representation by Fourier transformation of the displacements  $\mathbf{u}(t)$  and its time-derivatives  $\dot{\mathbf{u}}(t)$  and  $\ddot{\mathbf{u}}(t)$ . Therefore, these vectors are a function of the excitation circular frequency  $\omega$  using

$$\mathbf{u}(t) = \int_{-\infty}^{\infty} \mathbf{u}(\omega) e^{-j\omega t} d\omega. \quad (2.18)$$

When applying the relations  $\dot{\mathbf{u}}(\omega) = j\omega\mathbf{u}(\omega)$  and  $\ddot{\mathbf{u}}(\omega) = -\omega^2\mathbf{u}(\omega)$ , the linear harmonic response of motion gets the form:

$$[-\omega^2\mathbf{M} + j\omega\mathbf{C} + \mathbf{K}] \mathbf{u}(\omega) = \mathbf{f}(\omega). \quad (2.19)$$

The content of the left-hand side angular brackets is summarized by the dynamic stiffness matrix  $\mathbf{Z}(\omega)$ :

$$\mathbf{Z}(\omega)\mathbf{u}(\omega) = \mathbf{f}(\omega). \quad (2.20)$$

When taking the inverse of the dynamic stiffness matrix, we get the admittance matrix  $\mathbf{Y}(\omega)$  as

$$\mathbf{Y}(\omega) = (\mathbf{Z}(\omega))^{-1}; \quad \mathbf{Y}, \mathbf{Z} \in \mathbb{C}^{n \times n}; \quad (2.21)$$

which describes the transfer function in the frequency domain representation. The admittance matrix contains  $n$  DoF complex-valued frequency response functions (FRFs) of the dynamic system in the form of

$$Y_{ij}(\omega) = \frac{u_i(\omega)}{f_j(\omega)}. \quad (2.22)$$

Here,  $i$  and  $j$  feature the DoF of responses  $u$  to excitations  $f$ . The name *admittance* generally stands for the displacements  $\mathbf{u}$  or their time derivatives  $\dot{\mathbf{u}}$  and  $\ddot{\mathbf{u}}$  in response to the excitation load  $\mathbf{f}$ . In case of displacements, it is called *receptance* and in the cases of velocities or accelerations, it is designated as *mobility* or *accelerance*.

Now, a bridge to experimental testing is built. Usually, the elements of  $\mathbf{Y}(\omega)$  are determined by FRF measurements. Therefore, the accelerance description is valued as commonest representation of the admittance due to popular response measurements by accelerometers. When coupling these experimental accelerations with FE models, they usually have to be converted into receptances due to the displacement-dependent dynamic stiffness  $\mathbf{Z}(\omega)$ . As we will primarily operate in the frequency domain representation within this thesis, henceforth the circular frequency  $\omega$  is omitted at the admittance notation for clarity reasons.

### 2.1.6 Summary

The five presented domain representations of structural dynamic system representation serve as a framework for hybrid modeling techniques. All variants describe the relation between an input load and the structure's response based on their mechanical properties inside the system matrices, their internal displacements and their time-derivatives. These relations are most visible in the physical domain representation. Hence, this description is favorable within FE-modeling techniques. Of course, the representation of a dynamic system can be written in the time domain representation, but also in the frequency domain representation by Fourier transformation of the time representation. Restructuring of the system matrices for the state-space domain representation is advantageous for model-based monitoring as we see directly the correlation between inputs and outputs. This confirms the state-space as a common representation for control systems. Furthermore, the system can be written as a superposition of mode shapes in the modal domain representation which is preferable within some model reduction techniques, but not for the presented monitoring methods. Due to best suitability with experimental determined transfer functions, the frequency domain representation will be the method of choice for the presented techniques within this thesis. All subsequently explained methods are written in the frequency domain representation.

## 2.2 Lagrange Multiplier Frequency-Based Substructuring

The frequency domain representation was introduced as preferred representation for dynamic modeling within vibration monitoring (Sec. 2.1.5). In this section, a classical, frequency-based approach for system assembling based on substructures is shown. The substructuring technique is helpful especially in the context of hybrid models since numerical and experimental models can thus be combined. Most content is based on [139], unless otherwise noted. The classical frequency-based substructuring theory was initially established by Jetmundsen et al. in [63]. De Klerk et al. reformulated the method with respect to the interface forces between substructures in [36]. These interface forces were defined as *Lagrange Multipliers*. A general overview over the dynamic substructuring methods in terms of Lagrange Multiplier frequency-based substructuring (LM-FBS) is given in [35].

### 2.2.1 Substructure Coupling

The coupling and decoupling procedure will be presented on an example based on two substructures A and B. Therefore,  $\omega$  is omitted from the notation since all matrices depend on frequency. Based on Eq. (2.22), we write for the displacement responses:

$$\mathbf{u} = \mathbf{Y}(\mathbf{f} + \mathbf{g}). \quad (2.23)$$

Compared with Eq. (2.22), there is an additional load vector  $\mathbf{g}$ , which describes the contact forces and moments between A and B.  $\mathbf{u}_2^A$  and  $\mathbf{u}_2^B$  collect all interface DoF, whereby  $\mathbf{u}_1^A$  and  $\mathbf{u}_3^B$  belong to DoF of the structures where the response is known before or should be calculated after coupling. The vectors within Eq. (2.23) for  $n$  DoF are defined as follows:

$$\mathbf{u} = \begin{bmatrix} \mathbf{u}_1^A \\ \mathbf{u}_2^A \\ \mathbf{u}_2^B \\ \mathbf{u}_3^B \end{bmatrix}, \quad \mathbf{f} = \begin{bmatrix} \mathbf{f}_1^A \\ \mathbf{f}_2^A \\ \mathbf{f}_2^B \\ \mathbf{f}_3^B \end{bmatrix}, \quad \mathbf{g} = \begin{bmatrix} \mathbf{0} \\ \mathbf{g}_2^A \\ \mathbf{g}_2^B \\ \mathbf{0} \end{bmatrix}, \quad \text{with } \mathbf{u}, \mathbf{f}, \mathbf{g} \in \mathbb{R}^n. \quad (2.24)$$

The exemplary coupling scheme is depicted in Fig. 2.3. In this figure, the rotor A is coupled

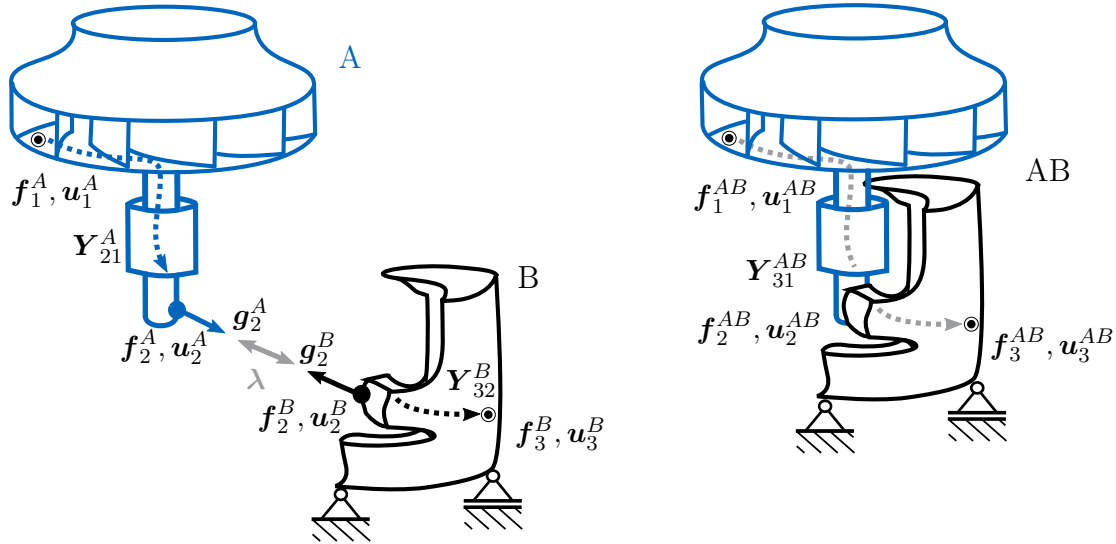


**Figure 2.3:** Exemplary coupling scheme of two substructures. The rotor (substructure A) is coupled with a sliced motor housing (substructure B) at the lower bearing seat ( $\mathbf{f}_2, \mathbf{u}_2$ ).

with a sliced motor B at the bearing seat. Hereby, the rotor is excited by a force  $\mathbf{f}_1^A$  at the impeller. This force results in a displacement  $\mathbf{u}_1^A$  at the same DoF. At this location and direction, there is the so-called *driving-point* FRF  $\mathbf{Y}_{11}^A$ . The rotor transmits the excitation via its transfer function  $\mathbf{Y}_{21}^A$  to the interface DoF at the bearing seat. Here, the load results in a displacement  $\mathbf{u}_2^A$ . Normally, we would get a displacement gap  $\delta$  between  $\mathbf{u}_2^A$  and  $\mathbf{u}_2^B$  now. In order to prohibit that gap, the *compatibility condition* is introduced. This term ensures  $\mathbf{u}_2^A$  and  $\mathbf{u}_2^B$  to be equal:

$$\delta = \mathbf{u}_2^B - \mathbf{u}_2^A = \mathbf{0}, \quad \delta \hat{=} \mathbf{B}_c \mathbf{u} = \mathbf{0}, \quad \text{with } \mathbf{B}_c = [\mathbf{0} \quad -\mathbf{I} \quad \mathbf{I} \quad \mathbf{0}]. \quad (2.25)$$

To close the gap, the force  $\lambda$  is introduced. System B is represented by a motor housing in our example. It is sliced for better visibility of the coupling point. At the interface of substructure

B, the load  $\mathbf{g}_2^B$  reacts to  $\mathbf{g}_2^A$ . In order to reach force equilibrium, the *equilibrium condition* must be fulfilled:

$$\mathbf{g}_2^A = -\mathbf{g}_2^B = \boldsymbol{\lambda}, \quad \mathbf{g} \hat{=} -\mathbf{B}_e^T \boldsymbol{\lambda} = \mathbf{0}, \quad \text{with } \mathbf{B}_e = \begin{bmatrix} \mathbf{0} & -\mathbf{I} & \mathbf{I} & \mathbf{0} \end{bmatrix}. \quad (2.26)$$

$\mathbf{B}_c$  and  $\mathbf{B}_e$  are signed Boolean matrices, which allow the selection of interface DoF. In our example,  $\mathbf{B}_c$  and  $\mathbf{B}_e$  are equal, but they can differ from each other especially when it comes to real measurements, where the amount of excitations differs from the measured acceleration response DoF. When enforcing both conditions within the coupling procedure, the *dual formulation* is performed. The dual assembly is preferred within experimental testing [36]. In this case, the Boolean matrices have one row per interface compatibility condition for  $\mathbf{B}_c$  and one column per interface equilibrium condition for  $\mathbf{B}_e$ . In Eq. (2.26), the Lagrange Multiplier  $\boldsymbol{\lambda}$  is introduced. The Lagrange Multiplier represents a virtual force or moment and is responsible for the cohesion of the substructures as already shown in Fig. 2.3 (gray double arrow).

Now, the example is further discussed. Due to the excitation at the interface, we get  $\mathbf{Y}_{32}^B$  as FRF between the input DoF two and the output DoF three. Here, reaction  $\mathbf{u}_3^B$  is observable. After coupling, the system AB shows new dynamics as marked on the right side of Fig. 2.3. When coupling or decoupling substructures, they must be excited at all interface DoF. All responses have to be measured at all interface DoF as well. Thus,  $\mathbf{Y}$  is occupied in block-matrix form. In the presented example, it is assembled as follows:

$$\mathbf{Y} = \begin{bmatrix} \mathbf{Y}_{11}^A & \mathbf{Y}_{12}^A & 0 & 0 \\ \mathbf{Y}_{21}^A & \mathbf{Y}_{22}^A & 0 & 0 \\ 0 & 0 & \mathbf{Y}_{22}^B & \mathbf{Y}_{23}^B \\ 0 & 0 & \mathbf{Y}_{32}^B & \mathbf{Y}_{33}^B \end{bmatrix}. \quad (2.27)$$

The uncoupled linear harmonic response of motion is thus expressed as:

$$\mathbf{u} = \mathbf{Y}(\mathbf{f} + \mathbf{g}) \quad \rightarrow \quad \begin{bmatrix} \mathbf{u}_1^A \\ \mathbf{u}_2^A \\ \mathbf{u}_2^B \\ \mathbf{u}_3^B \end{bmatrix} = \begin{bmatrix} \mathbf{Y}_{11}^A & \mathbf{Y}_{12}^A & \mathbf{0} & \mathbf{0} \\ \mathbf{Y}_{21}^A & \mathbf{Y}_{22}^A & \mathbf{0} & \mathbf{0} \\ \mathbf{0} & \mathbf{0} & \mathbf{Y}_{22}^B & \mathbf{Y}_{23}^B \\ \mathbf{0} & \mathbf{0} & \mathbf{Y}_{32}^B & \mathbf{Y}_{33}^B \end{bmatrix} \left( \begin{bmatrix} \mathbf{f}_1^A \\ \mathbf{f}_2^A \\ \mathbf{f}_2^B \\ \mathbf{f}_3^B \end{bmatrix} + \begin{bmatrix} \mathbf{0} \\ \mathbf{g}_2^A \\ \mathbf{g}_2^B \\ \mathbf{0} \end{bmatrix} \right). \quad (2.28)$$

To replace the interface load  $\mathbf{g}$  in Eq. (2.28), we write for the linear harmonic response of motion using the equilibrium condition:

$$\mathbf{u} = \mathbf{Y}(\mathbf{f} - \mathbf{B}_e^T \boldsymbol{\lambda}) \quad \text{with} \quad \mathbf{g} = -\mathbf{B}_e^T \boldsymbol{\lambda} = \begin{bmatrix} \mathbf{0} \\ \boldsymbol{\lambda} \\ -\boldsymbol{\lambda} \\ \mathbf{0} \end{bmatrix}. \quad (2.29)$$

Take the linear harmonic response of motion with satisfied force equilibrium from Eq. (2.29), and insert it into the compatibility condition as follows:

$$\mathbf{B}_c \mathbf{Y}(\mathbf{f} - \mathbf{B}_e^T \boldsymbol{\lambda}) = \mathbf{0} \quad \text{with} \quad \mathbf{B}_c \mathbf{u} = \mathbf{0} \quad \text{and} \quad \mathbf{u} = \mathbf{Y}(\mathbf{f} - \mathbf{B}_e^T \boldsymbol{\lambda}). \quad (2.30)$$

Hence, we solve for the Lagrange Multiplier:

$$\boldsymbol{\lambda} = (\mathbf{B}_c \mathbf{Y} \mathbf{B}_e^T)^{-1} \mathbf{B}_c \mathbf{Y} \mathbf{f}. \quad (2.31)$$

Now, we go back to the dynamic equation Eq. (2.29) and insert the Lagrange Multiplier  $\lambda$ . Thus, the general formulation of the coupled system response is written as:

$$\mathbf{u} = \underbrace{\mathbf{Y}\mathbf{f}}_{\mathbf{u}_{\text{uncoupled}}} - \underbrace{\mathbf{Y}\mathbf{B}_e^T (\mathbf{B}_c\mathbf{Y}\mathbf{B}_e^T)^{-1} \mathbf{B}_c\mathbf{Y}\mathbf{f}}_{\mathbf{u}_{\text{coupling}}}. \quad (2.32)$$

It essentially consists of a difference between the uncoupled responses and the new coupling term. The interface force  $\lambda$  closes the interface gap, which is produced by the uncoupled responses. The dual assembled FRF matrix is therefore defined as:

$$\mathbf{Y}^{AB} = \mathbf{Y} - \underbrace{\mathbf{Y}\mathbf{B}_e^T (\mathbf{B}_c\mathbf{Y}\mathbf{B}_e^T)^{-1} \mathbf{B}_c\mathbf{Y}}_{\substack{\text{interface stiffness} \\ \lambda}}. \quad (2.33)$$

In the coupled admittance formulation, the interface stiffness

$$\mathbf{Z}_{\text{int}} = (\mathbf{B}_c\mathbf{Y}\mathbf{B}_e^T)^{-1}, \quad (2.34)$$

can be extracted which must be invertible. Hence, proper conditioning of  $\mathbf{Z}_{\text{int}}$  is mandatory. This can lead to problems in case of experimental testing.  $\mathbf{B}_c$  and  $\mathbf{B}_e$  help to choose the best combination of measured DoF to enhance the conditioning of the interface stiffness. A lot of research is being done in this field [132, 141].

The LM-FBS algorithm in Eq. (2.33) serves as a framework for coupling any number of substructures with almost arbitrary DoF. Though, note that after the coupling procedure, all rows and columns according to the interface DoF have the same entries. ( $\mathbf{u}_2^A = \mathbf{u}_2^B$  and  $\mathbf{f}_2^A = \mathbf{f}_2^B$  referring to the presented example). These sub-matrices can be removed in order to reduce the system dimension since they do not contain extra information.

## 2.2.2 Substructure Decoupling

In some scenarios, only information about the entire system is available and one component should be changed. In this case, a decoupling technique is helpful. Imagine that the motor housing of the presented example in Fig. 2.3 gets a new design from different material and measurements only can be performed at the old, built-in machine. For the old and the new housing, simulation data is available including the entire FRF matrices. Thus, we aim to decouple the old substructure B from AB like  $\mathbf{AB} - \mathbf{B} = \mathbf{A}$  before coupling the new system B with A again. A related example was investigated in [15].

The basic procedure is delineated, focusing on the dual formulation as within the coupling technique. Generally, the method strongly resembles, but the compatibility condition (Eq. (2.25)) is formulated reversely. The initial equations of motion are written as

$$\mathbf{u}^{AB} = \mathbf{Y}^{AB} (\mathbf{f}^{AB} + \mathbf{g}^{AB}) \quad (2.35)$$

and

$$\mathbf{u}^B = -\mathbf{Y}^B \mathbf{g}^B \quad (2.36)$$

with the negatively set contact force  $\mathbf{g}^B$  in the system response linear harmonic response of system B. Similar to Eq. (2.28), the equation is formulated as:

$$\begin{bmatrix} \mathbf{u}_1^{AB} \\ \mathbf{u}_2^{AB} \\ \mathbf{u}_3^{AB} \\ \mathbf{u}_2^B \\ \mathbf{u}_3^B \end{bmatrix} = \begin{bmatrix} \mathbf{Y}_{11}^{AB} & \mathbf{Y}_{12}^{AB} & \mathbf{Y}_{13}^{AB} & \mathbf{0} & \mathbf{0} \\ \mathbf{Y}_{21}^{AB} & \mathbf{Y}_{22}^{AB} & \mathbf{Y}_{23}^{AB} & \mathbf{0} & \mathbf{0} \\ \mathbf{Y}_{31}^{AB} & \mathbf{Y}_{32}^{AB} & \mathbf{Y}_{33}^{AB} & \mathbf{0} & \mathbf{0} \\ \mathbf{0} & \mathbf{0} & \mathbf{0} & -\mathbf{Y}_{22}^B & -\mathbf{Y}_{23}^B \\ \mathbf{0} & \mathbf{0} & \mathbf{0} & -\mathbf{Y}_{32}^B & -\mathbf{Y}_{33}^B \end{bmatrix} \left( \begin{bmatrix} \mathbf{f}_1^{AB} \\ \mathbf{f}_2^{AB} \\ \mathbf{0} \\ \mathbf{0} \\ \mathbf{0} \end{bmatrix} + \begin{bmatrix} \mathbf{0} \\ \mathbf{g}_2^{AB} \\ \mathbf{0} \\ \mathbf{g}_2^B \\ \mathbf{0} \end{bmatrix} \right). \quad (2.37)$$

The negative contact force  $\mathbf{g}^B$  is considered by the negative admittances in Eq. (2.37) due to the removal of B. Now, a similar starting situation as within the coupling procedure before performing the LM-FBS algorithm is observed. This algorithm is essentially the same except of  $\mathbf{Y}$  and the Boolean matrices for compatibility and equilibrium. These are defined as:

$$\mathbf{B}_c = [\mathbf{0} \quad -\mathbf{I} \quad \mathbf{0} \quad \mathbf{I} \quad \mathbf{0}] \quad \text{and} \quad \mathbf{B}_e = [\mathbf{0} \quad -\mathbf{I} \quad \mathbf{0} \quad \mathbf{I} \quad \mathbf{0}]. \quad (2.38)$$

Note, the system dimension further increases compared with the coupling procedure since the entire system and substructure B are written in block-matrix form. Here, all DoF of B also appear in AB and are therefore doubled. Thus, the substructure A can be identified by extracting B using the same LM-FBS algorithm as in Eq. (2.33):

$$\mathbf{Y}^A = \mathbf{Y} - \mathbf{Y}\mathbf{B}_e^T (\mathbf{B}_c\mathbf{Y}\mathbf{B}_e^T)^{-1} \mathbf{B}_c\mathbf{Y}. \quad (2.39)$$

The basic difference can be read from:

$$\mathbf{Y} = \begin{bmatrix} \mathbf{Y}^A & \mathbf{0} \\ \mathbf{0} & \mathbf{Y}^B \end{bmatrix} \quad \text{coupling A and B: } \mathbf{A} + \mathbf{B} = \mathbf{AB} \quad (2.40)$$

and

$$\mathbf{Y} = \begin{bmatrix} \mathbf{Y}^{AB} & \mathbf{0} \\ \mathbf{0} & -\mathbf{Y}^B \end{bmatrix} \quad \text{decoupling B from AB: } \mathbf{A} = \mathbf{AB} - \mathbf{B}. \quad (2.41)$$

For practical recommendations in experimental frequency-based substructuring, please find [133]. Further details concerning the decoupling procedure are described in [34, 142]. A deeper insight into the conditioning problem at the interfaces is given in [115, 134]. In some cases, the decoupling can be enhanced by extending the interface for the compatibility and equilibrium conditions at so-called *internal* DoF, which are not part of the interfaces. This technique will play a more important role at the different SEMM methods in Sec 5.2 and Chap 6 of this thesis.

## 2.3 Virtual Point Transformation

Frequency-based substructuring within experimental testing applications requires proper FRF measurements at the interface DoF. These FRFs are usually based on impact force excitations and acceleration measurements by piezoelectric sensors. There is ongoing research utilizing rotation sensors in order to characterize the interfaces [22, 23]. State-of-the-art interface rotation and displacement modeling is established by a filtered coordinate transformation. This convention is called *virtual point transformation* (VPT) due to the fact that these points are mostly not accessible by sensors and therefore designated as *virtual*. The VPT reduces an

overdetermined set of excitations and responses around the interfaces to six DoF, which fully describe the coupling point by three displacements  $\mathbf{u}_X, \mathbf{u}_Y, \mathbf{u}_Z$ , three rotations  $\mathbf{q}_{\psi_X}, \mathbf{q}_{\psi_Y}, \mathbf{q}_{\psi_Z}$  and the correlating excitations. This technique assumes maximum stiffness in the area of sensor and actuator sets so that the dynamic of the structure(s) can be referred to as rigid body motion. The following passage describes the VPT methodology based on [139] and [89]. A basic requirement for the selection of excitation and response DoF is the ability to represent all six rigid body modes. Therefore, the excitation and measurement points should be well distributed over the structure. A well imaginable reason for this specification is the demand for controllability and observability of the underlying dynamic system. Of course, this would work best, if the system were a rigid body. We will come back to that issue later. In general, maximum information can be reached by well distributed actuator and sensor DoF. Start from the linear harmonic response of motion

$$\mathbf{u} = \mathbf{Y}(\mathbf{f} + \mathbf{g}) \quad \text{with} \quad \mathbf{u} \in \mathbb{R}^n \quad (2.42)$$

regarding only non-collocated DoF  $n$ . As introduced in the presented example of Sec. 2.2, two systems A and B (see Fig. 2.3) are coupled. Now, the focus lies on the interface admittances  $\mathbf{Y}_{22}^A$  and  $\mathbf{Y}_{22}^B$ . Previously, these interface DoF were assumed to be well-accessible for excitation and measurement. Imagine a rotating machine where the coupling point is a non-accessible bearing. These six interface DoF inside this bearing should be found in order to couple A and B properly. These interface dynamics are found by a set of non-collocated inputs and outputs. The therefore measured accelerations are characterized by the displacements  $\mathbf{u}^k$  and the applied excitation forces by  $\mathbf{f}^h$ . An exemplary scenario is depicted in Fig. 2.4. Here, a VPT is performed at the lower bearing seat of a rotor to find three displacements  $\mathbf{q}_X^v, \mathbf{q}_Y^v, \mathbf{q}_Z^v$  and three rotations  $\mathbf{q}_{\psi_X}^v, \mathbf{q}_{\psi_Y}^v, \mathbf{q}_{\psi_Z}^v$  and the related loads  $\mathbf{m}$  at the virtual point  $v$  (orange).

### 2.3.1 Displacement Transformation

The virtual point displacements  $\mathbf{q}$  are written in the columns of a  $n \times m$  *Interface Displacement Mode* (IDM) matrix. The IDM matrix complies with a frequency-independent mode shape matrix (see brace in Eq. (2.44)). By means of the IDM matrix, the virtual displacements  $\mathbf{q} \in m$  can be found by a reduction of the set of  $n > m$  non-collocated outputs. The correlation between these matrices is defined as

$$\mathbf{u} = \mathbf{R}_u \mathbf{q} + \boldsymbol{\mu}. \quad (2.43)$$

Here, the overdetermined system of measured outputs  $\mathbf{u}$  is reduced to the virtual point displacements and rotations  $\mathbf{q}$  by the IDM matrix  $\mathbf{R}_u$ . Note that only rigid body modes are considered as IDMs in this case, but also more advanced IDMs could be used to determine the system. Due to the reduction process, a residual  $\boldsymbol{\mu}$  appears. Eq. (2.43) is written for a triaxial accelerometer<sup>2</sup>:

$$\begin{bmatrix} u_x^k \\ u_y^k \\ u_z^k \end{bmatrix} = \underbrace{\begin{bmatrix} e_{x,X}^k & e_{x,Y}^k & e_{x,Z}^k \\ e_{y,X}^k & e_{y,Y}^k & e_{y,Z}^k \\ e_{z,X}^k & e_{z,Y}^k & e_{z,Z}^k \end{bmatrix} \begin{bmatrix} 1 & 0 & 0 & 0 & r_Z^k & -r_Y^k \\ 0 & 1 & 0 & -r_Z^k & 0 & r_X^k \\ 0 & 0 & 1 & r_Y^k & -r_X^k & 0 \end{bmatrix}}_{\mathbf{R}_u^{kv} = \mathbf{E}^k \mathbf{r}^k} \begin{bmatrix} q_X^v \\ q_Y^v \\ q_Z^v \\ q_{\psi_X}^v \\ q_{\psi_Y}^v \\ q_{\psi_Z}^v \end{bmatrix} + \begin{bmatrix} \mu_x^k \\ \mu_y^k \\ \mu_z^k \end{bmatrix}. \quad (2.44)$$

<sup>2</sup>Even when writing about accelerometers, we always regard the displacements  $u$  after twofold integration of the acceleration.

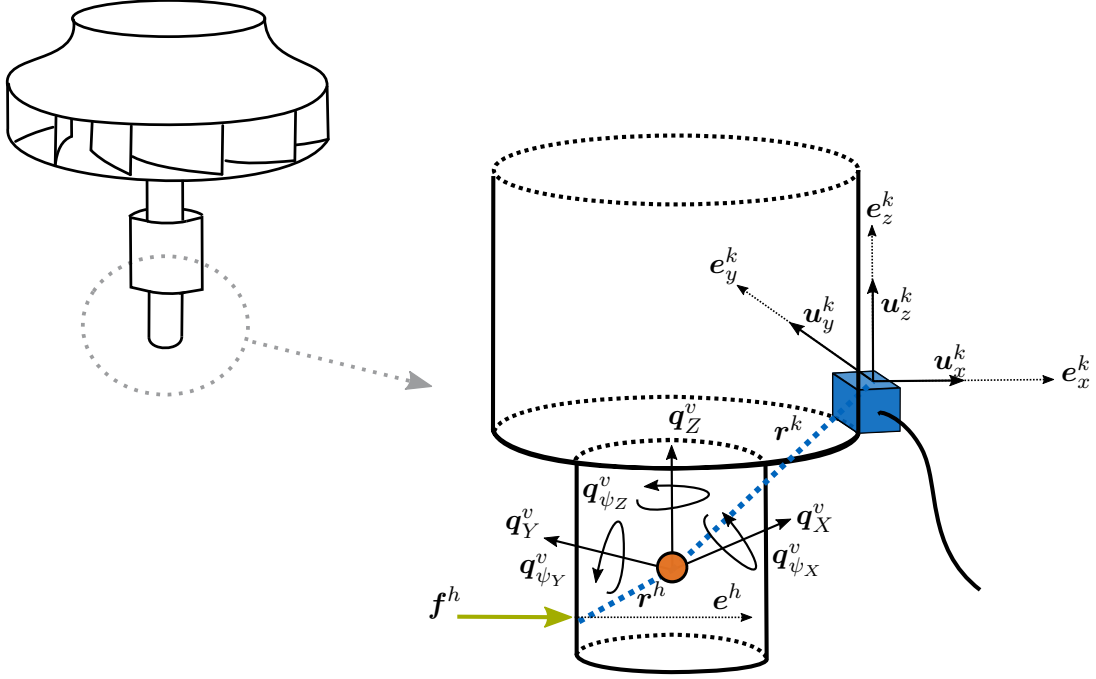


**Figure 2.4:** Visualization of the virtual point spatial transformation at the lower bearing seat of a rotor. The virtual point (orange) is characterized by three displacements  $q_X^v, q_Y^v, q_Z^v$ , three rotations  $q_{\psi_X}^v, q_{\psi_Y}^v, q_{\psi_Z}^v$  and the related loads  $\mathbf{m}$  (not delineated). An exemplary acceleration sensor  $k$  (blue,  $k \geq 3$ ) is shown to visualize the measured displacements  $u_x^k, u_y^k, u_z^k$  in appropriated directions  $e$ . This sensor is placed at a distance of  $r^k$  from the virtual point. An exemplary impact force  $f^h$  (green,  $h \geq 9$ ) excites the structure at the lower bearing seat,  $r^h$ .

Here,  $R_u^{kv}$  stands for the IDM matrix of a triaxial accelerometer  $k$  which contributes to the virtual point  $v$ . All sensor axes orientations are caught by  $E^k = [e_x^k e_y^k e_z^k]$ . Furthermore, the relative position vector between all sensors and the VP are defined by  $r^k$ .

According to an overdetermined system, at least three triaxial sensors are needed. Therefore, the general definition of  $R_u$  by  $R_u^{kv}$  is written in block-matrix form as follows:

$$R_u = \begin{bmatrix} R^{1,1} \\ R^{2,1} \\ R^{3,1} \\ & R^{4,2} \\ & R^{5,2} \\ & R^{6,2} \\ & \ddots \\ & & R^{N_k, N_v} \end{bmatrix}. \quad (2.45)$$

We go back to Eq. (2.43). Essentially, the virtual point displacements and rotations  $\mathbf{q}$  are of interest. The equation is pre-multiplied with  $R_u^T$ , enforcing  $R_u^T \boldsymbol{\mu} = 0$ :

$$R_u^T \mathbf{u} = R_u^T R_u \mathbf{q} + R_u^T \boldsymbol{\mu} \quad (2.46)$$

Solving for  $\mathbf{q}$ , we get

$$\mathbf{q} = \underbrace{(R_u^T R_u)^{-1} R_u^T}_{R_u^+ = T_u} \mathbf{u} = T_u \mathbf{u}. \quad (2.47)$$

$\mathbf{R}_u^+$  is the Moore-Penrose pseudo-inverse of  $\mathbf{R}_u$ . This matrix multiplication is tantamount to filtering on the virtual point displacements. It is equivalent to a transformation matrix  $\mathbf{T}_u$ . By this filtering process, the residual  $\boldsymbol{\mu}$  is eliminated. For a detailed view on the filtering effect,  $\mathbf{q}$  is inserted into Eq. (2.43) [133]. Thus, the filtered displacements is written as:

$$\tilde{\mathbf{u}} = \mathbf{R}_u \underbrace{(\mathbf{R}_u^T \mathbf{R}_u)^{-1} \mathbf{R}_u^T}_{\mathbf{R}_u^+ = \mathbf{T}_u} \mathbf{u} = \mathbf{R}_u \mathbf{T}_u \mathbf{u}. \quad (2.48)$$

The filtering process can also be considered as least-squares minimization. Therefore, the measured displacements are explicitly computable from  $\mathbf{q}$ , assuming an ideally stiff structure. For practical considerations and more information - especially about the assembly of the interface deformation modes, please find [51, 55].

### 2.3.2 Force Transformation

When deriving six virtual loads  $\mathbf{m}$  at the virtual point, the forces and moments can not be calculated in both ways as it was the case with the displacements. Only the determination of  $\mathbf{m}$  based on a set of loads  $\mathbf{f}$  is possible. When the set of force excitation DoF is collocated with the sensor DoF, we get an IDM matrix for  $\mathbf{f}$  with structure similar to the displacements. Hence, the correlation between all excitations and the virtual loads does not contain a residuum anymore. We can imagine, that different combinations of forces can generate the same virtual moment. Though, all virtual loads  $\mathbf{m}$  can be determined explicitly by excitations  $\mathbf{f}$ . The following relationship applies:

$$\mathbf{m} = \mathbf{R}_f^T \mathbf{f}. \quad (2.49)$$

The IDM matrix  $\mathbf{R}^{hv}$  of an excitation  $h$  for a virtual point  $v$  can be assembled by the product of the distance  $\mathbf{r}^h$  and the orientation  $\mathbf{e}^h$ . Note,  $\mathbf{r}^h$  describes the distance between a single load and the virtual point and  $\mathbf{e}^h$  stands for the excitation orientation of  $f$ . Hence, the virtual point loads are written as:

$$\begin{bmatrix} m_X^v \\ m_Y^v \\ m_Z^v \\ m_{\psi_X}^v \\ m_{\psi_Y}^v \\ m_{\psi_Z}^v \end{bmatrix} = \underbrace{\begin{bmatrix} 1 & 0 & 0 \\ 0 & 1 & 0 \\ 0 & 0 & 1 \\ 0 & -r_Z^h & r_Y^h \\ r_Z^h & 0 & -r_X^h \\ -r_Y^h & r_X^h & 0 \end{bmatrix}}_{\mathbf{R}_f^{hv} = \mathbf{r}^h \mathbf{e}^h} \begin{bmatrix} \mathbf{e}_X^{hT} \\ \mathbf{e}_Y^{hT} \\ \mathbf{e}_Z^{hT} \end{bmatrix} \mathbf{f}^h. \quad (2.50)$$

Generally, an overdetermined system is favorable - also for the virtual loads determination. Here, we define  $p > m$  excitation DoF. Usually, at least nine DoF  $p$  are a good choice. The sub-matrices  $\mathbf{R}^{hv}$  are written in block diagonal form in order to assemble  $\mathbf{R}_f$  for the



The virtual displacements are defined as

$$\mathbf{q} = \mathbf{T}_u \mathbf{u} \quad \rightarrow \quad \begin{bmatrix} \mathbf{q}_1^A \\ \mathbf{q}_2^A \\ \mathbf{q}_2^B \\ \mathbf{q}_3^B \end{bmatrix} = \begin{bmatrix} \mathbf{I} & \mathbf{0} & \mathbf{0} & \mathbf{0} \\ \mathbf{0} & \mathbf{T}_u^A & \mathbf{0} & \mathbf{0} \\ \mathbf{0} & \mathbf{0} & \mathbf{T}_u^B & \mathbf{0} \\ \mathbf{0} & \mathbf{0} & \mathbf{0} & \mathbf{I} \end{bmatrix} \begin{bmatrix} \mathbf{u}_1^A \\ \mathbf{u}_2^A \\ \mathbf{u}_2^B \\ \mathbf{u}_3^B \end{bmatrix}. \quad (2.57)$$

Just as with the standard LM-FBS coupling, we can combine the compatibility condition with the equilibrium condition as within Eq. (2.32) and get for the coupled response:

$$\mathbf{u} = \mathbf{Y} \mathbf{f} - \mathbf{Y} \mathbf{T}_f^T \mathbf{B}^T (\mathbf{B} \mathbf{T}_u \mathbf{Y} \mathbf{T}_f^T \mathbf{B}^T)^{-1} \mathbf{B} \mathbf{T}_u \mathbf{Y} \mathbf{f} \quad (2.58)$$

This equation can be further explained similarly to the standard LM-FBS algorithm referring to [139]:

$$\mathbf{u} = \underbrace{\mathbf{Y} \mathbf{f}}_{\substack{\text{uncoupled} \\ \text{response}}} - \underbrace{\mathbf{Y} \mathbf{T}_f^T \mathbf{B}^T}_{\substack{\text{response to} \\ \text{VP force } \lambda}} \underbrace{(\mathbf{B} \underbrace{\mathbf{T}_u \mathbf{Y} \mathbf{T}_f^T}_{\substack{\text{VP admittance} \\ \mathbf{Y}_{qm}}} \mathbf{B}^T)^{-1}}_{\substack{\text{VP interface} \\ \text{admittance}}} \underbrace{\mathbf{B} \mathbf{T}_u \mathbf{Y} \mathbf{f}}_{\mathbf{q}_{\text{interface gap}}}. \quad (2.59)$$

Finally, the coupled admittances are obtained by

$$\mathbf{Y}^{AB} = \mathbf{Y} - \mathbf{Y} \mathbf{T}_f^T \mathbf{B}^T (\mathbf{B} \mathbf{T}_u \mathbf{Y} \mathbf{T}_f^T \mathbf{B}^T)^{-1} \mathbf{B} \mathbf{T}_u \mathbf{Y} \quad \text{with} \quad \mathbf{u} = \mathbf{Y}^{AB} \mathbf{f}. \quad (2.60)$$

According to [133], the virtual point admittance  $\mathbf{Y}_{qm}$  is found:

$$\mathbf{Y}_{qm} = \mathbf{T}_u \mathbf{Y} \mathbf{T}_f^T \quad (2.61)$$

with the virtual point displacements

$$\mathbf{q} = \mathbf{Y}_{qm} \mathbf{m} - \mathbf{Y}_{qm} \mathbf{B}^T (\mathbf{B} \mathbf{Y}_{qm} \mathbf{B}^T)^{-1} \mathbf{B} \mathbf{Y}_{qm} \mathbf{m}. \quad (2.62)$$

### 2.3.4 Virtual Point Quality Indicators

It is very important to check, how well the applied excitations and response measurements describe the virtual point DoF. This can be evaluated by several quality indicators [133]:

- Passivity,
- Observability,
- Consistency,
  - Global (overall) consistency concerning all sensors / excitations,
  - Specific consistency observing the sensor / excitation DoF,
- Reciprocity.

These criteria are briefly discussed in the following paragraphs.

### Passivity

The passivity indicator observes the energy within the driving point system. It only regards the diagonal terms and therefore the driving point FRF at the virtual point  $\mathbf{Y}_{ii}$ . When the system acts passive, no energy is stored. Passivity can also be an indicator for stability. Although passivity and stability are related, they are slightly different. Note that the system can be non-passive, and still be stable if there is enough damping inside. The passivity indicator is formulated observing the phase:

$$\angle \mathbf{Y}_{ii} \begin{cases} \in [-180, 0] & \text{in case of receptance FRFs} \\ \in [-90, 90] & \text{in case of mobility FRFs} \\ \in [0, 180] & \text{in case of accelerance FRFs} \end{cases} \quad \text{with } \mathbf{Y}_{ii} \in \mathbf{Y}_{qm} \quad (2.63)$$

### Observability

Observability can be schematically imagined in the way that a certain virtual point movement needs sensors at all anti-nodes of the surrounding body in order to be able to represent the entire virtual point dynamics adequately. When evaluating the VPT observability before performing measurements, the spatial transformation grade can be observed by the square matrix  $\mathbf{S}$  [94]:

$$\mathbf{S} = (\mathbf{R}^T \mathbf{R}) \quad (2.64)$$

As this matrix must be inverted in Eq. (2.47) and Eq. (2.52), it must be well conditioned. This condition number of  $\mathbf{S}$  is defined as

$$\kappa(\mathbf{S}) = \frac{\varsigma_{max}(\mathbf{S})}{\varsigma_{min}(\mathbf{S})} \quad (2.65)$$

The higher  $\kappa$  the worse the conditioning. Here,  $\varsigma_{min}(\mathbf{S})$  and  $\varsigma_{max}(\mathbf{S})$  are the smallest and largest singular values, respectively eigenvalues of  $\mathbf{S}$ . In order to reach good conditioning,  $\mathbf{S}$  should be full rank and contain no linear dependence. Otherwise,  $\kappa$  becomes infinity and the virtual point DoF can not be fully described by the chosen excitation and sensor positions. A rough guideline for the condition number is  $\kappa < 10^5$  [133]. Practically, we can imagine that the sensor positions and directions must be well distributed around the virtual point.

### Sensor Consistency

The sensor consistency was initially introduced as rigidity of the virtual point interface [37]. Some characteristics are shown here. For subsequent explanations based on [139] let us introduce the filter matrix  $\mathbf{F}$ :

$$\mathbf{F} \hat{=} \mathbf{R}_u \mathbf{T}_u \hat{=} \mathbf{R}_u \mathbf{R}_u^+ \quad \text{filtering the displacements} \quad \tilde{\mathbf{u}} = \mathbf{F} \mathbf{u}. \quad (2.66)$$

$\mathbf{F}$  filters a set of  $n$  measured DoF to a set of virtual point rigid body modes  $m$ . Note that this is a rank reduction of the space of  $\mathbf{u}$ :  $\text{rank}(n) > \text{rank}(m)$ . When looking back to Eq. (2.48),  $\mathbf{u}_{1,2}$  can be observed based on a certain load case some distance away from the virtual point. The exemplary load case would be an excitation  $\mathbf{f}_2$  which induces a response  $\mathbf{u}_{1,2}$  at the virtual point 1. The load 2 can contain one or more excitations around the virtual point. Transferred to this case, Eq. (2.66) means for the unfiltered sensor responses:

$$\mathbf{u}_{1,f_2} = \mathbf{Y}_{12} \mathbf{f}_2. \quad (2.67)$$

and for the filtered responses:

$$\tilde{\mathbf{u}}_{1,f_2} = \mathbf{F}_{11} \mathbf{Y}_{12} \mathbf{f}_2. \quad (2.68)$$

utilizing the filter function at the virtual point 1, reducing the space of  $\mathbf{u}$  ( $n$  measured displacements) to  $m$  virtual point rigid body motions.

### Overall Sensor Consistency

The overall sensor consistency assessment criterion compares the unfiltered responses  $\mathbf{u}$  with the filtered ones  $\tilde{\mathbf{u}}$ . Here, the overall sensor consistency evaluates these values at the entire frequency range by

$$\rho_{\mathbf{u}_{1,2}}(\omega) = \frac{\|\tilde{\mathbf{u}}_{1,2}(\omega)\|}{\|\mathbf{u}_{1,2}(\omega)\|} \quad (2.69)$$

It essentially evaluates the amplitude of both DoF sets. When the amplitude does not change due to the filtering process, all virtual point responses are perfectly described by the surrounding sensors. In this case, the overall sensor consistency  $\rho(\omega) = 1$ . In the worst case, this value becomes zero. Bad positioning, calibration or alignment of a single sensor decreases the overall sensor consistency. If the consistency drops at a specific frequency, this can be reasoned by a flexible interface displacement mode. [139].

### Specific Sensor Consistency

The specific sensor consistency is based on a variation of the spectral coherence function. It is evaluated based on [139] and is formulated for two complex vectors  $\mathbf{a}$  and  $\mathbf{b}$  as:

$$\text{coh}(\mathbf{a}, \mathbf{b}) = \frac{(\mathbf{a} + \mathbf{b})(\mathbf{a}^H + \mathbf{b}^H)}{2(\mathbf{a}\mathbf{a}^H + \mathbf{b}\mathbf{b}^H)} \quad \mathbf{a}, \mathbf{b} \in \mathbb{C} \quad \rightarrow \quad \begin{cases} 0 & \text{in case of } \mathbf{a} = -\mathbf{b} \\ \frac{1}{2} & \text{in case of } \mathbf{a} \perp \mathbf{b} \\ 1 & \text{in case of } \mathbf{a} = \mathbf{b} \end{cases} \quad (2.70)$$

This indicator can also be seen as the Modal Assurance Criterion (MAC) value between all sensor DoF and the virtual point DoF [4, 137]. Usually, the MAC value is utilized for the degree of consistency among modal vectors but this consistency criterion can also be applied to the observed FRFs within the VPT framework.

In the presented example, it is defined for every sensor channel  $u_i$  and the excitation force  $\mathbf{f}_2$  as

$$\rho_{u_{i,2}} = \text{coh}(\tilde{\mathbf{u}}_{i,2}(\omega), \mathbf{u}_{i,2}(\omega)) \quad (2.71)$$

The specific sensor consistency is a powerful tool for identification of sensor DoF which contribute poorly to the VPT. If bad channels are dropped based on the specific consistency, the overall consistency can directly show possibly enhancements on the entire transformation ability.

### Force Consistency

Usually, the force excitations within VPT measurements are performed utilizing an impact hammer. Hence, the quality indicator described subsequently is also called *impact* consistency. This criterion is very important to distinguish between proper and poor impacts - similar to the sensor channels. Again, we observe a set of filtered and unfiltered DoF. In this case, the measured and filtered forces  $f_j \in \mathbf{f}_1$  according to a virtual point 1, which produce a

response  $\mathbf{u}_2$  at the surrounding sensors. Therefore, a weighting vector  $\mathbf{w}$  is introduced to get a weighted scalar  $y_2$  as a linear combination of the responses around the virtual point:

$$y_2 = \mathbf{w}_2^T \mathbf{u}_2 \quad \text{with} \quad \mathbf{w} \in \mathbb{R}^{n_2} \quad (2.72)$$

The weighting vector  $\mathbf{w}$  just selects and assembles some responses of  $\mathbf{u}_2$ . Therefore, the linear combination for the summed filtered responses including the force filtering matrix  $\mathbf{F}$ :

$$\mathbf{F} \hat{=} \mathbf{R}_f \mathbf{T}_f \hat{=} \mathbf{R}_f \mathbf{R}_f^+ \quad (2.73)$$

is written as:

$$\tilde{\mathbf{y}}_{2,1} = \mathbf{w}_2^T \mathbf{Y}_{2,1} \mathbf{F}_{11}. \quad (2.74)$$

Here,  $\mathbf{F}_{11}$  filters the impacts at the interface to an equivalent load combination at the virtual point. Note that the weighting vector  $\mathbf{w}$  here only consists of ones.

#### *Overall Impact Consistency*

The overall impact consistency, is defined by the norm of filtered and unfiltered responses similar to the sensors. Though, in this case, the responses are filtered by the forces. This indicator shows how well the full set of forces  $\mathbf{f}_1$  is represented by the six virtual point DoF.

$$\rho_{f_{1,2}}(\omega) = \frac{\|\tilde{\mathbf{y}}_{2,1}^T(\omega)\|}{\|\mathbf{y}_{2,1}^T(\omega)\|} \quad (2.75)$$

#### *Specific Impact Consistency*

The specific impact consistency criterion is closely related to the previously introduced sensor quality indicator (see Eq. (2.71)). Here, just the responses due to unfiltered and filtered forces for each impact  $j$  are regarded. Therefore, the specific consistency indicator is defined based on the spectral coherence (Eq. (2.70)) as:

$$\rho_{f_{j,2}} = coh(\tilde{\mathbf{y}}_{2,j}(\omega), \mathbf{y}_{2,j}(\omega)) \quad \text{with} \quad f_j \in \mathbf{f}_1. \quad (2.76)$$

#### **Virtual Point Reciprocity**

A big advantage of the virtual point excitations and responses is the collocation of input and output DoF. Therefore, the reciprocity can be raised as quality assessment criterion for the VPT. The reciprocity states that the impact and sensor DoF of two FRFs are permutable. Define  $i$  to be located at the virtual point and  $j$  to be a reference DoF at the presented coupled structure. The quality of the reciprocity can be evaluated by the coherence between the admittances  $\mathbf{Y}_{ij}$  and  $\mathbf{Y}_{ji}$ :

$$\chi(\omega)_{ij} = coh(\mathbf{Y}_{ij}(\omega), \mathbf{Y}_{ji}(\omega)) \quad \text{with} \quad \mathbf{Y}_{ij}, \mathbf{Y}_{ji} \in \mathbf{Y}_{qm}. \quad (2.77)$$

Note,  $i = j$  and  $\chi = 1$  at the diagonal entries of  $\mathbf{Y}_{qm}$  [139]. The reciprocity criterion is generally useful in terms of linearity verification. A hint for linearity generally exists, if two admittances  $\mathbf{Y}_{ij}$  and  $\mathbf{Y}_{ji}$  have the same magnitude. In this case, the system shows reciprocity and can be approximated by a model with linear damping and a symmetric damping matrix [24, 146]. Even if reciprocity is not given, the system can be linear. Non-collocated impact and sensor locations, insufficient stiffness at these locations, and geometric errors often result in poor reciprocity at the virtual point, even when the system is linear. Apart from the VPT, note that reciprocity is often assumed if excitation forces are estimated based on measured responses. This is prerequisite in Sec. 6.1.1.

## 2.4 System Equivalent Model Mixing (SEMM)

The Lagrange Multiplier frequency-based substructuring technique was previously introduced to couple or decouple dynamic models especially with respect to experimental sub-models. This method can be extended to problems where dynamic information of different, entire systems is available. For example, numerical simulations are usually noiseless and can capture detailed information at any DoF of interest. Though, these numerical solutions are afflicted with more or less coarse structural dynamic assumptions.

On the other hand, experimental models keep the reality concerning these dynamics - often on a smaller subset DoF. Now, it is obvious that a blend of both models would be beneficial. We can think even further and imagine applications, where numerical models are coupled with experimental substructures within the development process and some dynamic information about the entire system is available later on. A mix of all these information can be done with some restrictions utilizing expansion techniques as *Guyan expansion*, *IRS technique*, *Dynamic stiffness expansion*, *Hurty Craig-Bampton method* and the *SEREP/VIKING technique* [69]. Even the virtual point transformation can be regarded as expansion technique [137]. Modal expansion uses information from the model (e.g., modes) to extend the measurement to unmeasured DoF. For details concerning these expansion methods, please find [11, 32, 59]. Another approach would be *model updating*, where parameters of the numerical model are tuned so that the simulation result match the measurement, then the model is used to evaluate responses at unmeasured DoF. In this thesis, the focus is set on an expansion method based on the LM-FBS algorithm. This technique is called *System Equivalent Model Mixing (SEMM)*. The big advantage of SEMM compared to the aforementioned expansion techniques is the persistence of internal DoF which are not affected by all admixed models. These internal DoF are required for virtual sensing inside the machine according to fault quantification within condition monitoring. Note that SEMM is equivalent to SEREP if the two mixed models have the same number of modes [99]. This section gives an overview over the SEMM framework referring to [69]. Essentially, SEMM is implemented in four extension levels. There are two extreme cases

- Basic SEMM,
- Fully Extended Interface SEMM

and the two cases in between:

- Extended Equilibrium SEMM and the
- Extended Compatibility SEMM.

The two intermediate cases refer to the force equilibrium and displacement compatibility conditions in the LM-FBS algorithm. In order to explain SEMM, a set of model types is introduced:

$\mathbf{Y}^S$ : Start model or model that inadequately describes the structural dynamics of the system. It is improved by the expansion technique and can be numerical, experimental or hybrid in nature.

$\mathbf{Y}^R$ : Removed model, which is an extracted part of  $\mathbf{Y}^S$ . In case of removing the start model at the boundaries  $b$ :  $\mathbf{Y}_{bb}^R = \mathbf{Y}_{bb}^S$ .

$\mathbf{Y}^E$ : Experimental model, which contains the desired dynamics and which is expanded to the DoF of  $\mathbf{Y}^S$ . Its DoF are equal to  $\mathbf{Y}^R$ .

$\mathbf{Y}^\delta$ : The delta model is introduced as an intermediate stage for better explanation.

$\mathbf{Y}^{\text{SEMM}}$ : The SEMM model has the same, full rank as  $\mathbf{Y}^{\text{S}}$  but implies the dynamics of  $\mathbf{Y}^{\text{E}}$ .

The essential task of SEMM is to exchange the dynamics at the interface DoF which belong to  $\mathbf{Y}^{\text{R}}$  and  $\mathbf{Y}^{\text{E}}$ , respectively and expand the information to all remaining, internal DoF. The dynamics of  $\mathbf{Y}^{\text{R}}$  is exchanged by  $\mathbf{Y}^{\text{E}}$  and the difference is expanded to the internal DoF. This can be visualized as a scenario when some springs are removed from a coupled system and new, different springs are added instead. The entire dynamics change due to that modification since these changes affect all internal DoF which are indirectly connected to the modified interface dynamics. An exemplary scenario is depicted in Fig. 2.5.

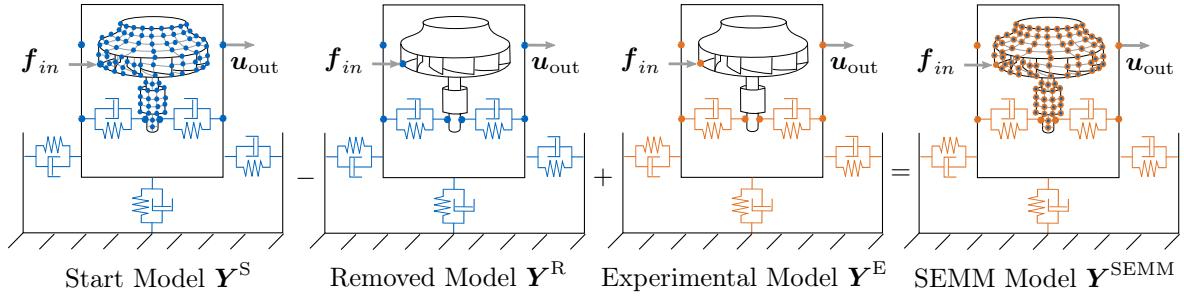


**Figure 2.5:** SEMM operating principle. An exemplary rotor is excited at the impeller ( $\mathbf{f}_{in}$ ) whereby the response of interest ( $\mathbf{u}_{out}$ ) is located at the housing. The start model  $\mathbf{Y}^{\text{S}}$  (blue) contains all intriguing DoF (internal and interface DoF) whereby the removed model  $\mathbf{Y}^{\text{R}}$  only implies a small subset of interface DoF, where dynamics are replaced by the experimental model  $\mathbf{Y}^{\text{E}}$  (orange). All interface DoF are subsequently expanded to the surrounding internal DoF by decoupling the removed model and coupling the experimental model. The resulting SEMM model  $\mathbf{Y}^{\text{SEMM}}$  essentially contains the dynamics of the small experimental model, but still includes the same complete set of DoF as the initial start model.

$\mathbf{Y}^{\text{S}}$  and  $\mathbf{Y}^{\text{SEMM}}$  have the same, global dimension  $g$ . The experimental model  $\mathbf{Y}^{\text{E}}$  has *boundary* dimension  $b$  since it appears only on a boundary subset DoF of  $\mathbf{Y}^{\text{S}}$ .  $\mathbf{Y}^{\text{S}}$  is divided into these shared boundary DoF  $b$  and into unique internal DoF  $i$  appearing only in the space of  $\mathbf{Y}^{\text{S}}$ . Particularly the start model is assembled as follows:

$$\mathbf{Y}_{gg}^{\text{S}} = \begin{bmatrix} \mathbf{Y}_{ii} & \mathbf{Y}_{ib} \\ \mathbf{Y}_{bi} & \mathbf{Y}_{bb} \end{bmatrix}^{\text{S}}, \quad \mathbf{Y}_{gb}^{\text{S}} = \begin{bmatrix} \mathbf{Y}_{ib} \\ \mathbf{Y}_{bb} \end{bmatrix}^{\text{S}} \quad \text{and} \quad \mathbf{Y}_{bg}^{\text{S}} = [\mathbf{Y}_{bi} \quad \mathbf{Y}_{bb}]^{\text{S}}. \quad (2.78)$$

Note, the sub-admittances  $\mathbf{Y}_{ii}$ ,  $\mathbf{Y}_{ib}$ ,  $\mathbf{Y}_{bi}$ ,  $\mathbf{Y}_{bb}$  do not necessarily have to be symmetric. They can also appear as  $\mathbf{Y}_{i_u i_f}$ ,  $\mathbf{Y}_{i_u b_f}$ ,  $\mathbf{Y}_{b_u i_f}$ ,  $\mathbf{Y}_{b_u b_f}$  if there are different amounts of excitation forces  $f$  and response displacements  $u$  within the internal and boundary DoF.

### 2.4.1 Basic SEMM

We start from the LM-FBS algorithm (see Eq. (2.33)) where two systems to be coupled or decoupled are written in block matrix form in  $\mathbf{Y}$ :

$$\mathbf{Y}_{\text{coupled / decoupled}} = \mathbf{Y} - \mathbf{Y} \mathbf{B}_e^T (\mathbf{B}_c \mathbf{Y} \mathbf{B}_e^T)^{-1} \mathbf{B}_c \mathbf{Y} \quad (2.79)$$

The coupling or decoupling depends on the chosen boundary DoF through the Boolean matrices  $\mathbf{B}_c$  and  $\mathbf{B}_e$  and the structure of the admittance matrix  $\mathbf{Y}$ :

$$\mathbf{Y} = \begin{bmatrix} \mathbf{Y}^A & \mathbf{0} \\ \mathbf{0} & \mathbf{Y}^B \end{bmatrix} \quad \text{coupling A and B: } A + B = AB \quad (2.80)$$

and

$$\mathbf{Y} = \begin{bmatrix} \mathbf{Y}^{AB} & \mathbf{0} \\ \mathbf{0} & -\mathbf{Y}^B \end{bmatrix} \quad \text{decoupling B from AB: } A = AB - B. \quad (2.81)$$

This basic principle can also be found in the SEMM equations where A and B can be for example a start model and an experimental model. In SEMM notation, A and B are not written in block matrix form in  $\mathbf{Y}$ . They are sorted directly by the boundary and internal DoF, since the DoF of B are always a subset of A, even though they are physically two different models. Moreover, both coupling and decoupling are included in the SEMM equations. First, the basic SEMM method will be explained. It is defined as follows:

$$\mathbf{Y}_{\text{basic}}^{\text{SEMM}} = \mathbf{Y}_{gg}^S - \mathbf{Y}_{gb}^S \left( \mathbf{Y}_{bb}^S - \mathbf{Y}_{bb}^\delta \right)^{-1} \mathbf{Y}_{bg}^S \quad (2.82)$$

with the delta model

$$\mathbf{Y}_{bb, \text{basic}}^\delta = \mathbf{Y}_{bb}^R - \underbrace{\mathbf{Y}_{bb}^R \left( \mathbf{Y}_{bb}^R - \mathbf{Y}_{bb}^E \right)^{-1} \mathbf{Y}_{bb}^R}_{\text{Interface Reduction}}. \quad (2.83)$$

The understand how Eq. (2.82)) produces a transfer function that is improved by the experimental information in  $\mathbf{Y}_{bb}^E$ , the delta model is inserted into the SEMM equation (2.82) using  $\mathbf{Y}_{bb}^R = \mathbf{Y}_{bb}^S$  because the reduction happens at the boundaries (see Eq. (2.87)):

$$\mathbf{Y}_{\text{basic}}^{\text{SEMM}} = \mathbf{Y}_{gg}^S - \mathbf{Y}_{gb}^S \left( \mathbf{Y}_{bb}^S - \mathbf{Y}_{bb}^S + \mathbf{Y}_{bb}^S \left( \mathbf{Y}_{bb}^S - \mathbf{Y}_{bb}^E \right)^{-1} \mathbf{Y}_{bb}^S \right)^{-1} \mathbf{Y}_{gb}^S. \quad (2.84)$$

Simplified:

$$\mathbf{Y}_{\text{basic}}^{\text{SEMM}} = \mathbf{Y}_{gg}^S - \mathbf{Y}_{gb}^S \left( \mathbf{Y}_{bb}^S \left( \mathbf{Y}_{bb}^S - \mathbf{Y}_{bb}^E \right)^{-1} \mathbf{Y}_{bb}^S \right)^{-1} \mathbf{Y}_{gb}^S \quad (2.85)$$

and resolved:

$$\mathbf{Y}_{\text{basic}}^{\text{SEMM}} = \mathbf{Y}_{gg}^S - \mathbf{Y}_{gb}^S \left( \mathbf{Y}_{bb}^S \right)^{-1} \left( \mathbf{Y}_{bb}^S - \mathbf{Y}_{bb}^E \right) \left( \mathbf{Y}_{bb}^S \right)^{-1} \mathbf{Y}_{gb}^S. \quad (2.86)$$

If we resolve it further, a reduction on the interface at the boundary DoF is striking:

$$\mathbf{Y}_{\text{basic}}^{\text{SEMM}} = \underbrace{\mathbf{Y}_{gg}^S - \mathbf{Y}_{gb}^S \left( \mathbf{Y}_{bb}^S \right)^{-1} \mathbf{Y}_{bg}^S}_{\text{Condensation}} + \underbrace{\mathbf{Y}_{gb}^S \left( \mathbf{Y}_{bb}^S \right)^{-1} \mathbf{Y}_{bb}^E \left( \mathbf{Y}_{bb}^S \right)^{-1} \mathbf{Y}_{bg}^S}_{\text{Expansion}} \quad (2.87)$$

Eq. (2.87) can be written in a different matrix form according to the initially explained internal DoF  $i$  and boundary DoF  $b$ . This is equal to Eq. (2.86):

$$\mathbf{Y}_{\text{basic}}^{\text{SEMM}} = \mathbf{Y}_{gg}^S - \begin{bmatrix} \mathbf{Y}_{ib} \\ \mathbf{Y}_{bb} \end{bmatrix}^S \left( \mathbf{Y}_{bb}^S \right)^{-1} \left( \mathbf{Y}_{bb}^S - \mathbf{Y}_{bb}^E \right) \left( \mathbf{Y}_{bb}^S \right)^{-1} \begin{bmatrix} \mathbf{Y}_{bi} & \mathbf{Y}_{bb} \end{bmatrix}^S. \quad (2.88)$$

Subsequently, the condensation and expansion will be explained and interpreted. Note that the superscript  $S$  for the start model is omitted from all of the following equations related to the *condensation* for clarity. The condensed part in Eq. (2.87) can be interpreted as the

dynamics of the start system when the boundary DoF are fixed, as explained subsequently: The global displacements are now regarded concerning the condensation<sup>3</sup>:

$$\begin{bmatrix} \mathbf{Y}_{ii} & \mathbf{Y}_{ib} \\ \mathbf{Y}_{bi} & \mathbf{Y}_{bb} \end{bmatrix} \begin{bmatrix} \mathbf{f}_i \\ \mathbf{f}_b + \tilde{\mathbf{f}}_b \end{bmatrix} = \begin{bmatrix} \tilde{\mathbf{u}}_i \\ \tilde{\mathbf{u}}_b = \mathbf{0} \end{bmatrix}. \quad (2.89)$$

It can also be written as:

$$\mathbf{Y}_{gg}\mathbf{f}_g + \mathbf{Y}_{gb}\tilde{\mathbf{f}}_b = \tilde{\mathbf{u}}_g. \quad (2.90)$$

For an admittance matrix, the condensation computes the admittance at the boundary DoF when the boundary displacements are fixed ( $\tilde{\mathbf{u}}_b = \mathbf{0}$  in the second line of Eq. (2.89)). Here, the boundary forces are extended by  $\tilde{\mathbf{f}}_b$  which is needed to fix the boundary displacements:

$$\mathbf{Y}_{bi}\mathbf{f}_i + \mathbf{Y}_{bb}(\mathbf{f}_b + \tilde{\mathbf{f}}_b) = \mathbf{0}. \quad (2.91)$$

We can solve Eq. (2.91) for this additional force  $\tilde{\mathbf{f}}_b$ :

$$\tilde{\mathbf{f}}_b = -\mathbf{Y}_{bb}^{-1}(\mathbf{Y}_{bi}\mathbf{f}_i + \mathbf{Y}_{bb}\mathbf{f}_b) = -\mathbf{Y}_{bb}^{-1}\mathbf{Y}_{bg}\mathbf{f}_g \quad (2.92)$$

and insert it into Eq. (2.90) to get the global, condensed displacements:

$$\mathbf{Y}_{gg}\mathbf{f}_g - \mathbf{Y}_{gb}\mathbf{Y}_{bb}^{-1}\mathbf{Y}_{bg}\mathbf{f}_g = \tilde{\mathbf{u}}_g. \quad (2.93)$$

Now, we can see exactly the condensation in Eq. (2.87):

$$(\mathbf{Y}_{gg} - \mathbf{Y}_{gb}\mathbf{Y}_{bb}^{-1}\mathbf{Y}_{bg})\mathbf{f}_g = \tilde{\mathbf{u}}_g. \quad (2.94)$$

This can be interpreted as a condensation of the admittance matrix on the boundary DoF and understood in a dual form (stiffness and admittance). In case of a stiffness matrix, the condensation computes the stiffness on the boundaries when the internal DoF are left free. Now, the *expansion* step will be explained:

Additional responses due to a motion of  $\mathbf{u}_b$  are added by the expansion step. These additional responses are obtained by the experimental measurements in  $\mathbf{Y}_{bb}^E$ .

The mathematical formulation of the expansion can be understood when regarding Eq. (2.87) from right to left considering an applied force  $\mathbf{f}_g^S$ . This is visualized in Fig. 2.6 and will now be explained.

The applied force  $\mathbf{f}_g^S$  creates a set of displacements  $\mathbf{u}_b^S$  on the boundaries:

$$\mathbf{u}_b^S = \mathbf{Y}_{bg}^S\mathbf{f}_g^S. \quad (2.95)$$

These same boundary displacements  $\mathbf{u}_b^S$  could have been produced by a fictitious boundary force  $\mathbf{f}_b^S$  on the boundaries:

$$\mathbf{f}_b^S = (\mathbf{Y}_{bb}^S)^{-1}\mathbf{u}_b^S. \quad (2.96)$$

Based on that force  $\mathbf{f}_b^S$  on the boundaries, the experimental admittances predict a set of displacements  $\mathbf{u}_b^E$ :

$$\mathbf{u}_b^E = \mathbf{Y}_{bb}^E\mathbf{f}_b^S. \quad (2.97)$$

---

<sup>3</sup>The following interpretations are based on a discussion between Prof. dr.ir. Daniel J. Rixen and the author of this thesis.

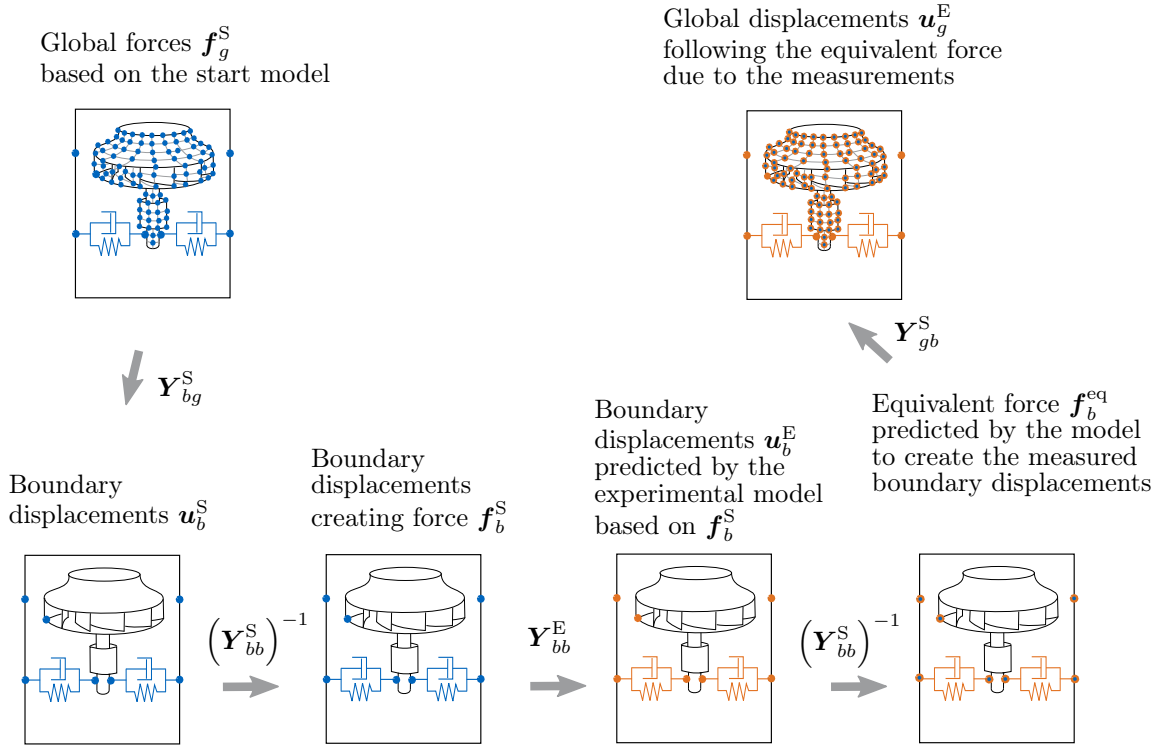


**Figure 2.6:** Basic SEMM expansion scheme starting from the global forces of a start model and ending with the expanded global displacements of an experimental model.

To produce this boundary displacements  $\mathbf{u}_b^E$ , the model would predict an equivalent force  $\mathbf{f}_b^{\text{eq}}$

$$\mathbf{f}_b^{\text{eq}} = (\mathbf{Y}_{bb}^S)^{-1} \mathbf{u}_b^E. \quad (2.98)$$

Finally, this equivalent boundary force on the boundaries would create inside the system an expanded displacement  $\mathbf{u}_g^E$

$$\mathbf{u}_g^E = \mathbf{Y}_{gb}^S \mathbf{f}_b^{\text{eq}} \quad (2.99)$$

of all global DoF due to the forces  $\mathbf{f}_b^{\text{eq}}$  needed on the boundaries to obtain the displacements  $\mathbf{u}_b^E$  that the experiments predict at the boundaries.

The upper mentioned reduction on the interface DoF can cause issues in form of fixed interface modes ending up in spurious peaks inside the FRFs. This might occur due to the reason that the boundary DoF are put to zero within the condensation. The expansion step can only modify the behavior of the system due to the motion of the boundary DoF, but can not influence (or correct) the modes of the system fixed on them. In order to deal with it, the decoupling step can be extended either for the compatibility or for the equilibrium condition. Alternatively, the decoupling can be expanded to all internal DoF within the fully extended interface SEMM.

### 2.4.2 Fully Extended Interface SEMM

This option implies full interface extension to all global DoF and represents the counterpart of the basic SEMM. The compact formulation writes:

$$\mathbf{Y}_{\text{fully ext}}^{\text{SEMM}} = \mathbf{Y}_{gg}^S - \mathbf{Y}_{gg}^S \left( \mathbf{Y}_{gg}^S - \mathbf{Y}_{gg}^\delta \right)^{-1} \mathbf{Y}_{gg}^S \quad (2.100)$$

with the fully extended delta model

$$\mathbf{Y}_{gg, \text{fully ext}}^\delta = \mathbf{Y}_{gg}^R \underbrace{-\mathbf{Y}_{gb}^R (\mathbf{Y}_{bb}^R - \mathbf{Y}_{bb}^E)^{-1} \mathbf{Y}_{bg}^R}_{\text{Reduction on the global DoF}}. \quad (2.101)$$

This delta model can be inserted into the SEMM equation (2.100) using  $\mathbf{Y}_{bb}^R = \mathbf{Y}_{bb}^S$ ,  $\mathbf{Y}_{bg}^R = \mathbf{Y}_{bg}^S$ , and  $\mathbf{Y}_{gb}^R = \mathbf{Y}_{gb}^S$  because the reduction happens not only at the boundaries but also at the global DoF of the start model (see Eq. (2.105)):

$$\mathbf{Y}_{\text{fully ext}}^{\text{SEMM}} = \mathbf{Y}_{gg}^S - \mathbf{Y}_{gg}^S \left( \mathbf{Y}_{gg}^S - \mathbf{Y}_{gg}^S + \mathbf{Y}_{gb}^S (\mathbf{Y}_{bb}^S - \mathbf{Y}_{bb}^E)^{-1} \mathbf{Y}_{bg}^S \right)^{-1} \mathbf{Y}_{gg}^S. \quad (2.102)$$

Simplified:

$$\mathbf{Y}_{\text{fully ext}}^{\text{SEMM}} = \mathbf{Y}_{gg}^S - \mathbf{Y}_{gg}^S \left( \mathbf{Y}_{gb}^S (\mathbf{Y}_{bb}^S - \mathbf{Y}_{bb}^E)^{-1} \mathbf{Y}_{bg}^S \right)^{-1} \mathbf{Y}_{gg}^S \quad (2.103)$$

and resolved:

$$\mathbf{Y}_{\text{fully ext}}^{\text{SEMM}} = \mathbf{Y}_{gg}^S - \mathbf{Y}_{gg}^S (\mathbf{Y}_{bg}^S)^+ (\mathbf{Y}_{bb}^S - \mathbf{Y}_{bb}^E) (\mathbf{Y}_{gb}^S)^+ \mathbf{Y}_{gg}^S. \quad (2.104)$$

By multiplying, the condensation and expansion steps are clarified again:

$$\mathbf{Y}_{\text{fully ext}}^{\text{SEMM}} = \mathbf{Y}_{gg}^S \underbrace{-\mathbf{Y}_{gg}^S (\mathbf{Y}_{bg}^S)^+ \mathbf{Y}_{bb}^S (\mathbf{Y}_{gb}^S)^+ \mathbf{Y}_{gg}^S}_{\text{Condensation}} + \underbrace{\mathbf{Y}_{gg}^S (\mathbf{Y}_{bg}^S)^+ \mathbf{Y}_{bb}^E (\mathbf{Y}_{gb}^S)^+ \mathbf{Y}_{gg}^S}_{\text{Expansion}} \quad (2.105)$$

The inverse becomes a Moore-Penrose pseudoinverse due to non-squareness of the inverse matrices. Within the condensation, we invert on the boundaries using pseudoinverse filtering, whereas the experimental model is expanded to the global set of forces and displacements. The big advantage is now, that there are no fixed interface modes compared with the basic SEMM method. Write it in the same matrix manner as Eq. (2.88):

$$\mathbf{Y}_{\text{fully ext}}^{\text{SEMM}} = \mathbf{Y}_{gg}^S - \begin{bmatrix} \mathbf{Y}_{ike} & \mathbf{Y}_{ib} \\ \mathbf{Y}_{bke} & \mathbf{Y}_{bb} \end{bmatrix}^S \left( \begin{bmatrix} \mathbf{Y}_{bke} & \mathbf{Y}_{bb} \end{bmatrix}^S \right)^+ (\mathbf{Y}_{bb}^S - \mathbf{Y}_{bb}^E) \left( \begin{bmatrix} \mathbf{Y}_{kcb} \\ \mathbf{Y}_{bb} \end{bmatrix}^R \right)^+ \begin{bmatrix} \mathbf{Y}_{kci} & \mathbf{Y}_{kcb} \\ \mathbf{Y}_{bi} & \mathbf{Y}_{bb} \end{bmatrix}^S \quad (2.106)$$

The expansion step of the fully extended interface method (Eq. (2.105)) is similar to the basic SEMM (Eq. (2.87), Fig. 2.6) can be interpreted according to the scheme in Fig. 2.7.

In the next step, we can decide, which global or boundary DoF are kept in the equilibrium or compatibility condition. These are indicated by *ke* and *kc*. Although the boundaries are not fixed anymore, the fully extended Interface method can cause issues concerning this kind of *free* behavior. Therefore, intermediate extension levels as the extended equilibrium or the extended compatibility variant can be preferable.

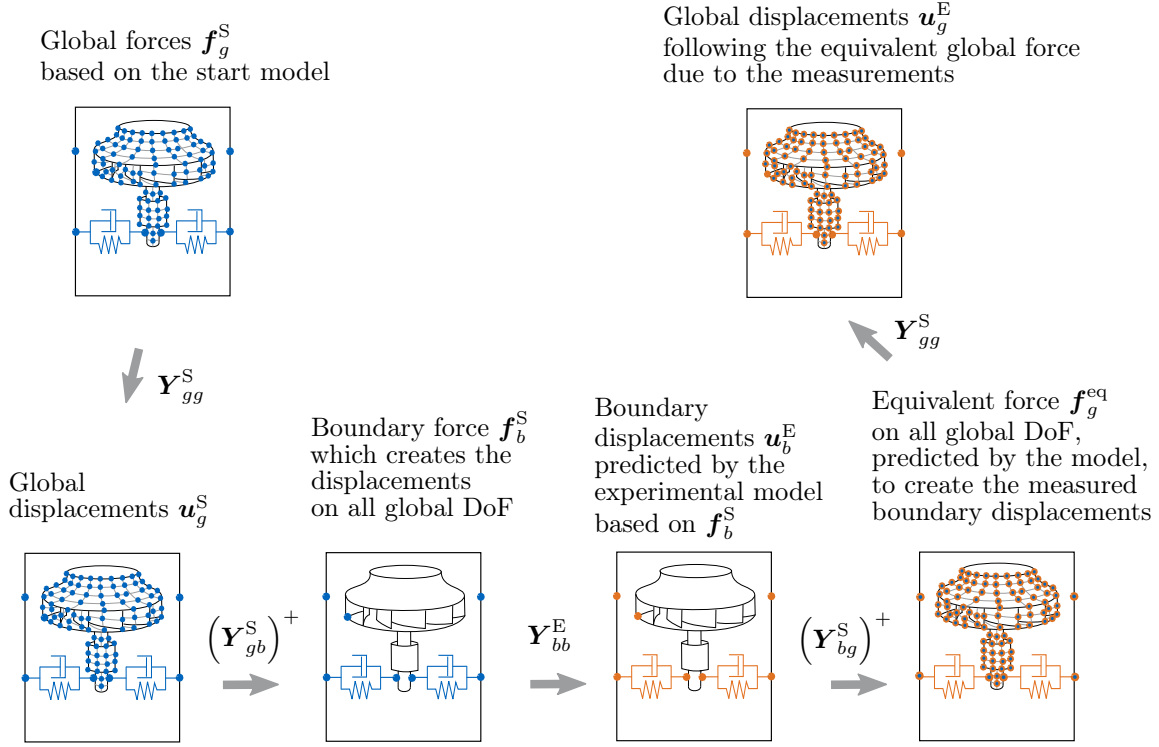


**Figure 2.7:** Fully extended interface SEMM expansion scheme starting from the global forces of a start model and ending with the expanded global displacements of an experimental model.

### 2.4.3 Extended Equilibrium SEMM

Depending on the application, there might be a lack either of controllability or of observability based on the experimental DoF  $\mathbf{Y}_{bb}^E$ . Then, the extended equilibrium or the extended compatibility condition in the condensation step of SEMM might reduce that problem. The extended equilibrium condition is formulated as follows:

$$\mathbf{Y}_{\text{ext eq}}^{\text{SEMM}} = \mathbf{Y}_{gg}^S - \mathbf{Y}_{gg}^S (\mathbf{Y}_{bg}^S - \mathbf{Y}_{bg}^\delta)^+ \mathbf{Y}_{bg}^S. \quad (2.107)$$

Again, the delta model is written as:

$$\mathbf{Y}_{bg, \text{ext eq}}^\delta = \mathbf{Y}_{bg}^R \underbrace{-\mathbf{Y}_{bb}^R (\mathbf{Y}_{bb}^R - \mathbf{Y}_{bb}^E)^{-1} \mathbf{Y}_{bg}^R}_{\text{Reduction on the global DoF within the equilibrium condition}} \quad (2.108)$$

Here, the reduction occurs on the global system, but only within the equilibrium condition. Afterwards, the delta model is put into the SEMM equation again with  $\mathbf{Y}_{bb}^R = \mathbf{Y}_{bb}^S$  and  $\mathbf{Y}_{bg}^R = \mathbf{Y}_{bg}^S$ :

$$\mathbf{Y}_{\text{ext eq}}^{\text{SEMM}} = \mathbf{Y}_{gg}^S - \mathbf{Y}_{gg}^S (\mathbf{Y}_{bg}^S)^+ (\mathbf{Y}_{bb}^S - \mathbf{Y}_{bb}^E) (\mathbf{Y}_{bb}^S)^{-1} \mathbf{Y}_{bg}^S \quad (2.109)$$

and multiplied together:

$$\mathbf{Y}_{\text{ext eq}}^{\text{SEMM}} = \mathbf{Y}_{gg}^S \underbrace{-\mathbf{Y}_{gg}^S (\mathbf{Y}_{bg}^S)^+ \mathbf{Y}_{bb}^S (\mathbf{Y}_{bb}^S)^{-1} \mathbf{Y}_{bg}^S}_{\text{Condensation}} + \underbrace{\mathbf{Y}_{gg}^S (\mathbf{Y}_{bg}^S)^+ \mathbf{Y}_{bb}^E (\mathbf{Y}_{bb}^S)^{-1} \mathbf{Y}_{bg}^S}_{\text{Expansion}}. \quad (2.110)$$

After transferring Eq. (2.110) to block-matrix form we get:

$$\mathbf{Y}_{\text{ext eq}}^{\text{SEMM}} = \mathbf{Y}_{gg}^S - \mathbf{Y}_{gg}^S \left( [\mathbf{Y}_{bke} \quad \mathbf{Y}_{bb}]^S \right)^+ (\mathbf{Y}_{bb}^S - \mathbf{Y}_{bb}^E) (\mathbf{Y}_{bb}^S)^{-1} [\mathbf{Y}_{bi} \quad \mathbf{Y}_{bb}]^S \quad (2.111)$$

### 2.4.4 Extended Compatibility SEMM

As mentioned above, we can also extend the decoupling to global DoF within the compatibility condition. On this occasion, the SEMM model is defined as:

$$\mathbf{Y}_{\text{ext comp}}^{\text{SEMM}} = \mathbf{Y}_{gg}^{\text{S}} - \mathbf{Y}_{gb}^{\text{S}} \left( \mathbf{Y}_{gb}^{\text{S}} - \mathbf{Y}_{gb}^{\delta} \right)^{-1} \mathbf{Y}_{gg}^{\text{S}} \quad (2.112)$$

with the correlating delta model:

$$\mathbf{Y}_{gb, \text{ext comp}}^{\delta} = \mathbf{Y}_{gb}^{\text{R}} \underbrace{-\mathbf{Y}_{gb}^{\text{R}} \left( \mathbf{Y}_{bb}^{\text{R}} - \mathbf{Y}_{bb}^{\text{E}} \right)^{-1} \mathbf{Y}_{bb}^{\text{R}}}_{\text{Reduction on the global DoF within the compatibility condition}}. \quad (2.113)$$

The reduction occurs on the global system, but only at the compatibility condition. The delta model is put in the SEMM equation again with  $\mathbf{Y}_{bb}^{\text{R}} = \mathbf{Y}_{bb}^{\text{S}}$  and  $\mathbf{Y}_{gb}^{\text{R}} = \mathbf{Y}_{gb}^{\text{S}}$ :

$$\mathbf{Y}_{\text{ext comp}}^{\text{SEMM}} = \mathbf{Y}_{gg}^{\text{S}} - \mathbf{Y}_{gb}^{\text{S}} \left( \mathbf{Y}_{bb}^{\text{S}} \right)^{-1} \left( \mathbf{Y}_{bb}^{\text{S}} - \mathbf{Y}_{bb}^{\text{E}} \right) \left( \mathbf{Y}_{gb}^{\text{S}} \right)^+ \mathbf{Y}_{bb}^{\text{S}} \quad (2.114)$$

and multiply it together:

$$\mathbf{Y}_{\text{ext eq}}^{\text{SEMM}} = \mathbf{Y}_{gg}^{\text{S}} \underbrace{-\mathbf{Y}_{gb}^{\text{S}} \left( \mathbf{Y}_{bb}^{\text{S}} \right)^{-1} \mathbf{Y}_{bb}^{\text{S}} \left( \mathbf{Y}_{gb}^{\text{S}} \right)^+ \mathbf{Y}_{gg}^{\text{S}}}_{\text{Condensation}} + \underbrace{\mathbf{Y}_{gb}^{\text{S}} \left( \mathbf{Y}_{bb}^{\text{S}} \right)^{-1} \mathbf{Y}_{bb}^{\text{E}} \left( \mathbf{Y}_{gb}^{\text{S}} \right)^+ \mathbf{Y}_{gg}^{\text{S}}}_{\text{Expansion}}. \quad (2.115)$$

The block-matrix form for the selection of specific DoF which are kept in the compatibility condition looks as follows:

$$\mathbf{Y}_{\text{ext comp}}^{\text{SEMM}} = \mathbf{Y}_{gg}^{\text{S}} - \begin{bmatrix} \mathbf{Y}_{ib} \\ \mathbf{Y}_{bb} \end{bmatrix}^{\text{S}} \left( \mathbf{Y}_{bb}^{\text{S}} \right)^{-1} \left( \mathbf{Y}_{bb}^{\text{S}} - \mathbf{Y}_{bb}^{\text{E}} \right) \left( \begin{bmatrix} \mathbf{Y}_{kcb} \\ \mathbf{Y}_{bb} \end{bmatrix}^{\text{S}} \right)^+ \mathbf{Y}_{gg}^{\text{S}}. \quad (2.116)$$

The SEMM techniques presented now serve as a framework for modal expansion. All four variants are evaluated with respect to the modeling of the presented industrial blower example in Sec. 5.2.2.



## Chapter 3

# Vibration Monitoring Methods

Vibration Monitoring with respect to continuous state observation of rotating machinery has specific requirements within this thesis. We focus offline on snapshot observation and do not develop a real-time system. This perspective on monitoring mainly stems from the target of wireless, industrial sensor networks. Here, continuous streaming of sensor data with real-time post-processing is mostly not practicable due to restricted resources of micro-controlled systems. Also, the condition decision is not time-sensitive within the regarded examples, since operational forces due to faults inside rotor systems increase slowly. Thus, sensor data post-processing can last from several minutes up to hours. In this case, discrete data snapshots are favorable. These are collected during steady-state operation and are evaluated retrospectively. In this chapter, methods for extracting the desired information from vibration signals are introduced in order to combine them with hybrid models for quantitative fault diagnosis. Essentially, a distinction is made between two exemplary fault types. On the one hand, these are faults which express themselves within an increased amplitude at the fundamental rotational frequency. In this context, unbalance in the form of harmonic vibration excitation is considered as a representative example of bearing load in section 3.3. On the other hand, there are faults which manifest within small impact forces. These are amplitude-modulated in high frequency bands. The frequency position of these bands complies with resonances of the rotor system, such as the bearings. In section 3.4, an exemplary condition indicator is shown based on the presented bearing diagnosis methods.

In general, there are two common model-based approaches which can help in observing these fault types. They will be presented next.

## 3.1 State-Space Observer Approach

A common approach to set up the model for vibration monitoring is the integration of a finite element (FE) model which is often anyway created during the development process. Though, these FE-models need some operational data to adapt themselves to real boundary conditions [48]. This adjustment can for example be implemented by a controller which measures the deviation between simulation and the monitored system. Some parameters of the model are selected and adjusted based on the measurement. Therefore, the healthy state must be well known. A classical approach for model-based monitoring is realized by the first order form of the mechanical equation of motion. For this occasion, the state space *ABCD*-representation using the state vector  $\boldsymbol{x}$  and external loads within the input vector  $\boldsymbol{v}(t) \hat{=} \boldsymbol{f}(t)$  is used for model description<sup>1</sup>. Here, a feedback matrix  $\boldsymbol{H}$  is assembled which contains the difference between reality and model. Referring to the equations 2.10-2.16, a representative model-based monitoring method by Gasch et al. [48] is described as follows:

---

<sup>1</sup>Details concerning assembling of the state-space matrices are described in Sec. 2.1.3

The internal dynamics are represented by the first time derivative of  $\boldsymbol{x}(t)$  containing the displacements  $\boldsymbol{u}(t)$  and velocities  $\dot{\boldsymbol{u}}(t)$ :

$$\dot{\boldsymbol{x}}(t) = \boldsymbol{A}\boldsymbol{x}(t) + \boldsymbol{B}\boldsymbol{v}(t); \quad \boldsymbol{x} \in \mathbb{R}^{2n}. \quad (3.1)$$

According to Eq. (2.1), the dimension  $2n$  refers to the duplication of  $n$  DoF within the second order form. These dynamics are further described by the state transition matrix  $\boldsymbol{A}$  and the state influence matrix  $\boldsymbol{B}$  which capture the mass, stiffness and damping matrices of the observed structure. The external loads are characterized by  $\boldsymbol{v}(t)$ . The difference between reality and the observed system is defined as

$$\Delta\boldsymbol{y}(t) = \boldsymbol{P}(\boldsymbol{x}(t) - \hat{\boldsymbol{x}}(t)) \quad (3.2)$$

where  $\boldsymbol{P}$  characterizes a Boolean matrix which selects accessible degrees of freedom for system output measurements.  $\hat{\boldsymbol{x}}(t)$  is the observed counterpart to  $\boldsymbol{x}(t)$ . Generally, the hat  $\hat{\star}$  designates the observed estimate in this context.

The observer itself consists of the matrix  $\hat{\boldsymbol{A}}$  to be corrected by measurements and  $\boldsymbol{H}$  amplifying the difference between these measurements and the model. Eq. (3.1) and Eq. (3.2) can be combined for the observed state as

$$\dot{\hat{\boldsymbol{x}}}(t) = \hat{\boldsymbol{A}}\hat{\boldsymbol{x}}(t) + \boldsymbol{H}\boldsymbol{P}(\boldsymbol{x}(t) - \hat{\boldsymbol{x}}(t)) + \boldsymbol{B}\boldsymbol{v}(t) \quad (3.3)$$

By subtraction of Eq. (3.3) from Eq. (3.1), we get the differential equation of faults:

$$\Delta\dot{\boldsymbol{x}}(t) = (\hat{\boldsymbol{A}} - \boldsymbol{H}\boldsymbol{P})\Delta\hat{\boldsymbol{x}}(t) + \Delta\boldsymbol{A}\boldsymbol{x}(t) \quad (3.4)$$

containing the state vector error  $\Delta\boldsymbol{x}(t) = \boldsymbol{x}(t) - \hat{\boldsymbol{x}}(t)$  and the error within the system matrices  $\Delta\boldsymbol{A} = \boldsymbol{A} - \hat{\boldsymbol{A}}$ . The feedback matrix (observer matrix)  $\boldsymbol{H}$  must be well chosen so that Eq. (3.4) has proper solutions. This can be done by pole specification [48] or by a Kalman filter approach (see Sec. 3.2.) Further details concerning the assembly of the state-space matrices are described in Sec. 2.1.3. Often, they are big and therefore computationally expensive for the operating system. Thus, model order reduction is required, especially when the monitoring system should decide about the state during operation. Ludwig et al. [81, 82] divided the numerical model into substructures (rotor and bearings) and reduced the model's degrees of freedom based on the Craig-Bampton method [17, 108]. The extended Kalman filter was then used to estimate magnitude and position of a rotor unbalance [82] and to detect changed rotor stiffness properties [81] by measuring shaft displacements.

## 3.2 Kalman Filter

In the context of monitoring using numerical models based on reduced DoF, the state-space observer approach is often combined with a Kalman filter [65]. Due to its usability for fault force estimation [90] and the important role of fault force quantification within this thesis (see Sec.6.1.1), the technique is briefly outlined based on [18]. The Kalman filter notation is based on the state-space domain representation. All underlying equations are explained in Sec. 2.1.3. We show the technique based on time-dependent states but leave out the time-dependence in the notation here for clarity reasons.

The entire Kalman filter iteration scheme is depicted in Fig. 3.1 to get a first overview.

It utilizes a time-discrete state space model based on the solution of Eq. (3.1) for a certain time sample:

$$\boldsymbol{x}_{k+1} = \boldsymbol{A}_k\boldsymbol{x}_k + \boldsymbol{B}_k\boldsymbol{v}_k; \quad \boldsymbol{x} \in \mathbb{R}^{2n}. \quad (3.5)$$

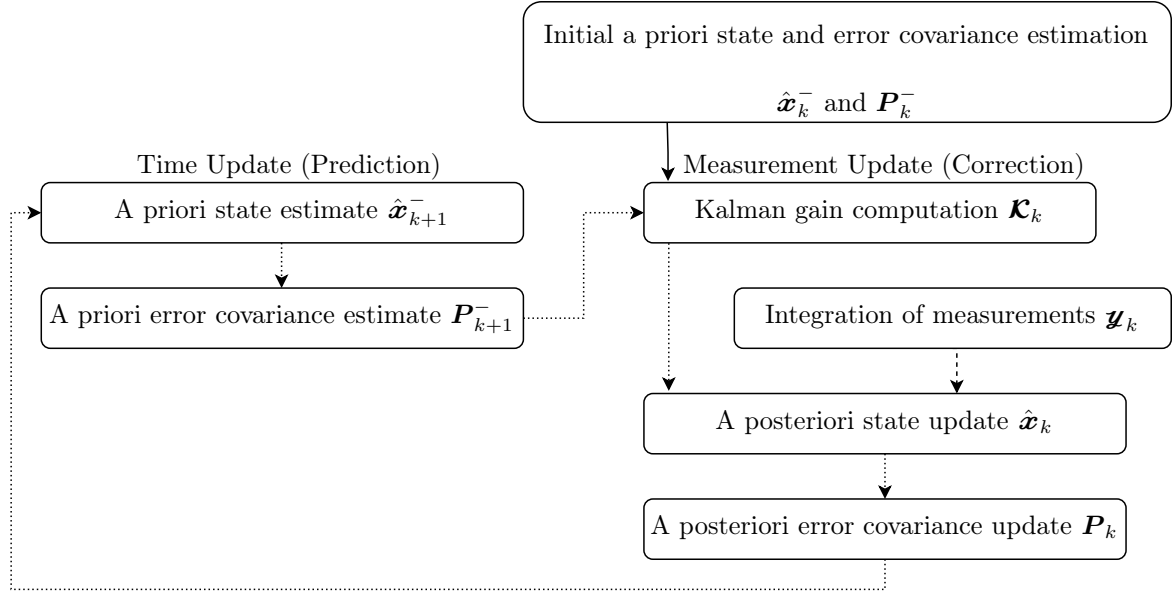


**Figure 3.1:** Kalman filter iteration scheme. Initially, an a priori state and an error covariance must be estimated. Subsequently, the estimates are updated by measurements. Based on these corrections, the state and error covariance are updated and further corrected until the state converges. Solid lines represent unique steps. All iteratively updated values are delineated by dotted lines. The integrated measurements can differ from each other and are therefore linked with the a posteriori state update by a dashed line.

The state is subject to a random process uncertainty  $\mathbf{w}_k \sim N(\mathbf{0}, \mathbf{I})$  with the state error covariance  $\mathbf{Q}$ :

$$\mathbf{x}_{k+1} = \mathbf{A}_k \mathbf{x}_k + \mathbf{B}_k \mathbf{v}_k + \mathbf{Q} \mathbf{w}_k. \quad (3.6)$$

Furthermore, we utilize  $m$  measurements<sup>2</sup> in form of the output vector  $\mathbf{y}_k$  superimposed with noise  $\mathbf{v}_k \sim N(\mathbf{0}, \mathbf{I})$  and the measurement error covariance  $\mathbf{R}$  under the assumption that the direct link matrix  $\mathbf{D}$  is zero<sup>3</sup>:

$$\mathbf{y}_k = \mathbf{C}_k \mathbf{x}_k + \mathbf{R} \mathbf{v}_k; \quad \mathbf{y} \in \mathbb{R}^m. \quad (3.7)$$

For  $\mathbf{v}_k$  and  $\mathbf{w}_k$  the assumption is made that they correspond to uncorrelated, white noise. The filter bases on a model-based a priori state assumption  $\hat{\mathbf{x}}_{k+1}^-$ . In this context, the *minus superscript* stands for an initial (a priori) guess of the predicted state:

$$\hat{\mathbf{x}}_{k+1}^- = \mathbf{A}_k \hat{\mathbf{x}}_k + \mathbf{B}_k \mathbf{v}_k. \quad (3.8)$$

An initial prediction must also be estimated for an a priori error covariance matrix

$$\mathbf{P}_k^- = E \begin{bmatrix} \mathbf{e}_k^- & \mathbf{e}_k^{-T} \end{bmatrix} \quad \text{with the a priori error estimate } \mathbf{e}_k^- \hat{=} \mathbf{x}_k - \hat{\mathbf{x}}_k^- \quad (3.9)$$

and the expectation  $E$ . Further, we need the corresponding a posteriori covariance matrix

$$\mathbf{P}_k = E \begin{bmatrix} \mathbf{e}_k & \mathbf{e}_k^T \end{bmatrix} \quad \text{with the a posteriori error estimate } \mathbf{e}_k \hat{=} \mathbf{x}_k - \hat{\mathbf{x}}_k. \quad (3.10)$$

<sup>2</sup>Usually, the size of the numerical model significantly exceeds the measurement degrees of freedom since only some measurement points are used for model correction ( $m < n$  DoF)

<sup>3</sup>see Sec. 2.1.3 for details

Now, we come to the Kalman filter's task. Its state prediction  $\hat{\boldsymbol{x}}_k$  at any time step  $k$  is computed, based on the previous state estimate  $\hat{\boldsymbol{x}}_k^-$  and the actual measurements  $\boldsymbol{y}_k$  as well as the model-based measurement estimate  $\boldsymbol{C}_k \hat{\boldsymbol{x}}_k^-$ :

$$\hat{\boldsymbol{x}}_k = \hat{\boldsymbol{x}}_k^- + \boldsymbol{K}_k \underbrace{(\boldsymbol{y}_k - \boldsymbol{C}_k \hat{\boldsymbol{x}}_k^-)}_{\text{residual}}. \quad (3.11)$$

In Eq. (3.11), the Kalman gain  $\boldsymbol{K}$  tries to minimize the residual  $(\boldsymbol{y}_k - \boldsymbol{C}_k \hat{\boldsymbol{x}}_k^-)$ . This is done indirectly by minimizing the error covariance  $\boldsymbol{P}_k$  (see Eq. (3.10)). A popular form of the Kalman gain is defined as:

$$\boldsymbol{K}_k = \boldsymbol{P}_k^- \boldsymbol{C}_k^T (\boldsymbol{C}_k \boldsymbol{P}_k^- \boldsymbol{C}_k^T + \boldsymbol{R}_k)^{-1}. \quad (3.12)$$

Here, the Kalman gain weighs the residual to a greater or lesser extent depending on the measurement noise. The smaller the measurement error covariance  $\boldsymbol{R}$  the less the predicted measurement  $\boldsymbol{C}_k \hat{\boldsymbol{x}}_k^-$  is trusted. In the opposite case, the smaller the error covariance  $\boldsymbol{P}_k^-$ , the less the measurement is trusted as  $\boldsymbol{K}$  approaches zero.

In terms of implementation, the filter is constructed as a feedback control loop. Initially, the a priori state is estimated and the feedback is obtained as computed, noisy "measurement". Subsequently, the feedback is corrected by real measurements. Therefore, the discrete Kalman filter is structured into two steps: The *time update* (measurement prediction) and *measurement update* (correction). These are defined as follows:

$$\begin{array}{l} \text{Time} \\ \text{Update} \end{array} \quad \left\{ \begin{array}{l} \hat{\boldsymbol{x}}_{k+1}^- = \boldsymbol{A}_k \hat{\boldsymbol{x}}_k + \boldsymbol{B}_k \boldsymbol{v}_k \quad \text{a priori state estimate} \\ \boldsymbol{P}_{k+1}^- = \boldsymbol{A}_k \boldsymbol{P}_k \boldsymbol{A}_k^T + \boldsymbol{Q}_k \quad \text{a priori error covariance estimate} \end{array} \right. \quad (3.13)$$

and

$$\begin{array}{l} \text{Measurement} \\ \text{Update} \end{array} \quad \left\{ \begin{array}{l} \boldsymbol{K}_k = \boldsymbol{P}_k^- \boldsymbol{C}_k^T (\boldsymbol{C}_k \boldsymbol{P}_k^- \boldsymbol{C}_k^T + \boldsymbol{R}_k)^{-1} \quad \text{Kalman gain computation,} \\ \hat{\boldsymbol{x}}_k = \hat{\boldsymbol{x}}_k^- + \boldsymbol{K}_k (\boldsymbol{y}_k - \boldsymbol{C}_k \hat{\boldsymbol{x}}_k^-) \quad \text{new state estimate} \\ \boldsymbol{P}_k = (\boldsymbol{I} - \boldsymbol{K}_k \boldsymbol{C}_k) \boldsymbol{P}_k^- \quad \text{a posteriori error covariance estimate} \end{array} \right. \quad (3.14)$$

Based on the converged state, an accurate estimation of the real dynamic behavior can be made. For detailed information about the initial guesses for  $\hat{\boldsymbol{x}}_k^-$  and  $\boldsymbol{P}_k^-$  and and the extended Kalman filter for nonlinear problems, please find [18]. For condition monitoring of rotating machinery, the *extended* Kalman filter is usually required since estimated fault forces strongly depend on the rotational frequency. Here, a linearization must be made at the operating speed of interest [81].

Referring to further research in this context, condition monitoring up to remaining life time estimation already succeeded building on the Kalman filter methodology. In that sense, fault force identification using iterative state estimation was successfully implemented in [80].<sup>4</sup> In roller bearing diagnostics, the Kalman filter has already been used to estimate the remaining life of bearings [117]. The advantage of the Kalman filter lies in its ability to correct state models by measurements. Nevertheless, we must not forget that the filter is applied under the assumption of eliminating white, uncorrelated noise. This assumption is not necessarily fulfilled when changes in structural dynamic properties are involved, such as resonance shifts due to varying boundary conditions.

<sup>4</sup>Fault force quantification will play an important role within this thesis (see Sec.6.1.1). Roller bearing diagnosis will also be an issue in Sec. 3.4.

### 3.3 Frequency Modulated Fault Extraction of Rotor Unbalance

Within unbalance identification, we have to track frequency-modulated excitation. This can be done via different approaches. One example is the Fourier-fit [1], when knowing exactly at which frequency the excitation occurs. Alternatively, the signal can be specifically filtered within a band of interest, where the excited frequency due to the unbalance is expected. Here, we have to wait until a complete time-snapshot of the sensor data is acquired. Additionally, the signal must be filtered in forward and backward direction, when the phase information is of interest. The big advantage of this method is the flexibility with respect to varying excitation frequencies. We do not have to know it exactly - the bandpass filter excuses inaccuracies. These inaccuracies can especially occur within industrial target applications since the exciting frequency is usually not directly measurable. Here, additional sensors are utilized which exemplarily observe the magnetic field to estimate the rotational frequency indirectly. However, the magnetic field frequency does not exactly match the mechanical rotor speed, which is pivotal for unbalance excitation. In this thesis, the type of filtering is used on a blower test rig to observe the rotor fundamental frequency with and without unbalance for test rig characterization and model validation.

### 3.4 Amplitude Modulated Fault Diagnosis of Roller Bearings

Vibration-based roller bearing fault diagnosis implies a huge field of techniques especially concerning signal-based methods [116]. Here, we have to distinguish between methods which build on physically-based feature extraction and purely learning-based techniques. Data-based learning approaches can be Neural Networks or classical machine learning solutions such as Support Vector Machines gain importance [27, 66, 102, 128]. The big advantage is that there is no knowledge about fault models needed. On the other hand, huge training data sets are potentially required - especially in case of deep learning approaches as within the neural networks. Especially in the context of development processes of condition monitoring systems, where applications and boundary conditions can change again and again, huge data sets are often not available. These variations preclude learning-based approaches since new conditions require new training data with healthy and faulty conditions.

Hence, we focus on physical-supported methods within this thesis. In this section, the most important techniques to extract the bearing fault information from raw vibration signals, in a physical manner, specified for MEMS-based sensor systems, is shown. All explained *filtering* processes try to extract small impacts from the signal.

These impacts are caused by the bearing balls rolling over irregularities on their own surface or on the inner/outer raceway. An example is shown in Fig. 3.2. Here, the three lower balls are impinged with a radial load and pass an outer ring fault. When the ball enters the pit, it is temporarily unloaded (see area within green dotted circle at the left side of Fig. 3.2). After passing the pit, it excites the enclosed structure by an impact force since it is suddenly loaded again. These impacts occur in a regular manner depending on geometry and rotational frequency of the bearing (green marked area at the right side of Fig. 3.2). The aim is to extract these impacts. Within this section, we will present several exemplary results in order to compare the underlying methodology. All examples are based on the proposed final sensor system (specified in Chap. 7) based on a wireless MEMS sensor device (STMicroelectronics LSM6DSL [125]) at the pump test rig<sup>5</sup> with a rotational frequency of  $f_n = 58.3$  Hz.

<sup>5</sup>See Sec. 4.13 for the measurement setup. In this chapter, the axial z-direction is observed. Thus, we see in the results that the axial direction is affected by the impact responses even with a horizontally aligned fault.

The measurements were performed by Röhrl [113].

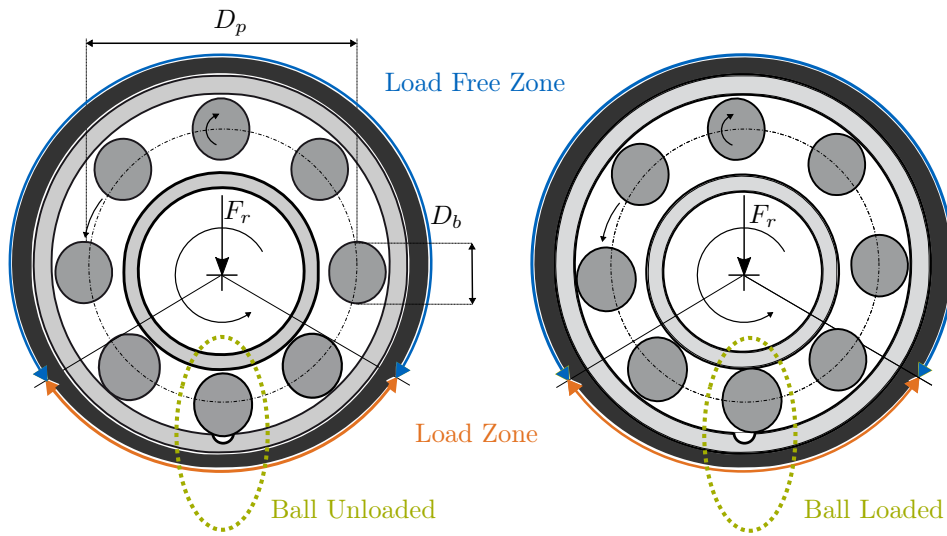


**Figure 3.2:** Faulty roller bearing kinematic with rotating inner ring and resting outer ring treated with a vertical radial force  $F_r$ , referring to [46]. Three balls are situated in the load zone due to radial load. Left: scenario with ball in an exemplary outer ring fault (see Fig. 4.14) The ball is unloaded due to the space between inner ring and ball. Right: scenario  $\Delta t$  later, the ball has passed the pit and it is suddenly loaded again.

The fault frequencies which depend on geometry and kinematic roller bearing are defined as follows:

- Frequency of a fault at the outer ring

$$f_O = \frac{1}{2}f_n \cdot Z \cdot \left[ 1 - \frac{D_b \cdot \cos \alpha}{D_p} \right], \quad (3.15)$$

- Frequency of a fault at the inner ring

$$f_I = \frac{1}{2}f_n \cdot Z \cdot \left[ 1 + \frac{D_b \cdot \cos \alpha}{D_p} \right], \quad (3.16)$$

- Frequency of a fault at the rolling element

$$f_B = \frac{f_n \cdot D_p}{D_b} \cdot \left[ 1 - \left( \frac{D_b \cdot \cos \alpha}{D_p} \right)^2 \right]. \quad (3.17)$$

---

This is reasoned by the axial operating force in the axial flow conveying direction.

These three characteristic bearing fault frequency types depend on the following parameters (see Fig. 3.2 and Fig. 3.3):

- $f_n$ : Rotor operational frequency,
- $Z$ : Number of rolling elements,
- $D_b$ : Rolling element diameter,
- $D_p$ : Pitch diameter,
- $\alpha$ : Contact angle.

The above mentioned contact angle  $\alpha$  is depicted in Fig. 3.3 which depends on an axial force  $F_A$ . This load issues from operational forces or static boundary conditions.

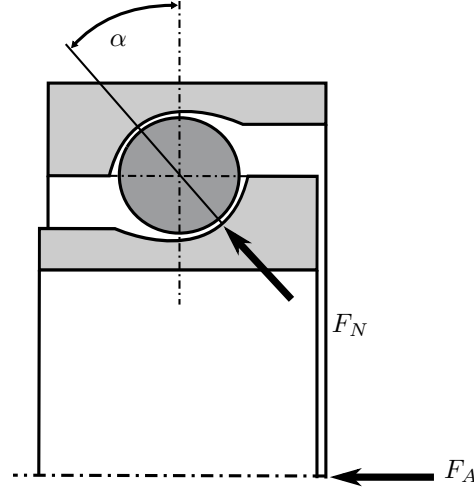


**Figure 3.3:** Visualization of the contact angle  $\alpha$  depending on an axial load  $F_A$ . The exemplary ball bearing transmits the normal force  $F_N$  between inner and outer ring.

### 3.4.1 Statistical Indicators

We start with statistical indicators which are representative for the bearing state usually in a broad frequency range, although we pointed out the importance of discrete defect frequencies above. These indicators are easy to implement and often provide proper information about the bearing state since they can capture a bundle of raceway irregularities within a scalar value. Statistical indicators according to VDI3832 [140] regard the collective vibration level over a period of time. The subsequently mentioned properties are called *statistical central moments*:

- *Root Mean Square Value (Effective Value)*:  $x_{\text{rms}} = \frac{1}{T} \int_0^T x(t)^2 dt$  usually increases due to signal peaks based on fault force impacts,
- *Maximum Value*:  $x_{\text{max}} = \max|x(t)|$ . Impact forces evoke increased peak values.
- *Crest Factor*:  $cr = \frac{|x_{\text{max}}|}{x_{\text{RMS}}}$ . Measure for impact content of the signal, complies with the quotient of maximum value and root mean square value.
- *Kurtosis*:  $k = \frac{1}{n} \sum_{i=1}^n \left(\frac{x_i - \bar{x}}{s}\right)^4$ : The curvature of the signal describes the peakedness within normal distribution. It is characterized by the mean value  $\bar{x}$  of  $n$  samples  $x_i$  containing a standard deviation  $s$ . The Gaussian normal distribution is specified by three. In case of bearing defects, this value is exceeded.
- *K(t)-Value*: Relation of the product of peak and effective value at two different time snapshots.

### 3.4.2 Envelope Analysis

As we introduced the discreteness of impacts caused by bearing faults, broadband indicators are often not suitable to characterize them properly. These impacts are usually measured indirectly regarding decay processes of the entire system. Now, the frequency of these abating

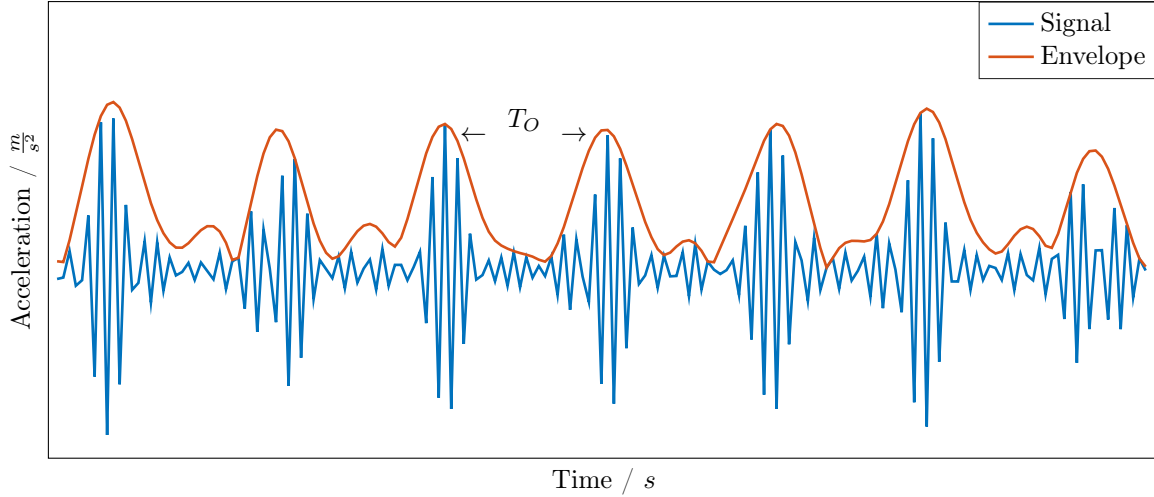


**Figure 3.4:** Exemplary ball bearing outer ring fault signal (blue) with associated envelope (orange). Specific impacts due to the fault appear within the time interval  $T_O$  - inverse to the frequency  $f_O$ . The underlying bearing defect can be found in Fig. 4.14

vibrations must be captured. To solve this problem, the envelope (Fig. 3.4) is regarded as discussed by [113].

We can determine the envelope of a signal  $x(t)$  in an number of ways. The process can be imagined for example as a rectifier in combination with low-pass filter to remove the carrier signal. A very popular option is the utilization of Hilbert Transformation  $x_H(t)$ . It is applied within this thesis referring to [58], defined for a considered time sequence  $\tau$  :

$$x_H(t) = \mathcal{H}\{x\} = \frac{1}{\pi} \int_{-\infty}^{+\infty} \frac{x(\tau)}{t - \tau} d\tau = x(t) * \frac{1}{\pi t}. \quad (3.18)$$

Based on the Hilbert-Transformation we get the complex, analytical signal from a real signal:

$$x_a(t) = x(t) + ix_H(t). \quad (3.19)$$

with real part  $x(t)$  equal to the original signal and imaginary part  $ix_H(t)$  containing the Hilbert-Transformation. The Hilbert Transform as imaginary part is equivalent to a  $90^\circ$  phase shifted original signal. When envisaging this signal comprising sines and cosines, they are converted into each another by the Hilbert Transform. In order to compute the envelope curve, the basic signal's mean value  $\bar{x}$  is subtracted to get rid of static offsets. Resting upon this adjusted base, the analytical signal is calculated:

$$x_a(t) = (x(t) - \bar{x}) + i\mathcal{H}\{(x(t) - \bar{x})\}. \quad (3.20)$$

Afterwards, the upper ( $x^+$ ) and lower ( $x^-$ ) envelopes are obtained by the mean value summed up or subtracted by the absolute value of the analytical signal:

$$x^+(t) = \bar{x} + |x_a(t)| \quad (3.21)$$

$$x^-(t) = \bar{x} - |x_a(t)| \quad (3.22)$$

$$(3.23)$$

In terms of bearing diagnosis, the upper envelope is usually further analyzed in the frequency domain representation. Especially within this work, the Hilbert implementation by MathWorks

is utilized according to [85]. A more efficient realization of the envelope computation can be implemented for example by a correlation operation in the frequency domain representation [45]. This can be very helpful for implementations on constrained sensor systems, but the method has drawbacks as filtering in the frequency domain representation. Here, the envelope's resolution can be reduced. However, since we do not have big post-processing resource constraints, efficiency in envelope calculation does not matter that much to us.

### 3.4.3 Optimal Filter Design

As mentioned in Sec. 3.4.2, the impacts can only be measured indirectly and they might be superimposed by interfering signals due to operational conditions such as excitation by the fluid conveyed by the pump for example - or simply by the rotational frequency harmonics. In order to extract the blank acceleration responses to these impact forces, some filtering is helpful. The art consists in figuring out the frequency range, where the impacts are amplitude-modulated. When the perfect frequency band is known, it can be extracted with a simple band-pass filter, but there are a bundle of methods to pull out the desired information from measured vibrations. Some of them will be presented here.

#### Spectral Kurtosis and Kurtogram

The Spectral Kurtosis  $SK(f)$  emphasizes non normal distribution or non-stationary behavior within an inspected frequency area. The main feature lies in the ability to separate frequency ranges including peaks as evoked by the bearing fault force impacts from rather Gaussian areas. Thus, transient events can be found in noisy signals [7, 10, 113]. It is a statistical tool and defined as

$$SK(f) = \frac{\langle |X(t, f)|^4 \rangle}{\langle |X(t, f)|^2 \rangle^2} - 2. \quad (3.24)$$

Here, we have a short time Fourier transformed (STFT) signal  $X(t, f)$  as input. The frequency resolution depends on the length of the STFT-blocks, which are exponentiated and averaged over time defined by the brackets  $\langle \cdot \rangle$ . The correlation between STFT block length and frequency resolution of a given signal  $X(t, f)$  depending on the sampling rate  $f_s$  is depicted in Fig. 3.5. If a time frame of  $2/f_s$  is chosen as block length, the frequency resolution would be  $f_s/2$  since the maximum frequency is  $f_s/2$ . In order to calculate the first Spectral Kurtosis value, a STFT block length of at least  $4/f_s$  is needed. In this example, a single scalar Spectral Kurtosis value  $SK(f)$  would be calculated over the entire frequency range up to  $2/f_s$  by exponentiating and averaging over the two frequency bins ( $0 - f_s/4$  and  $f_s/4 - f_s/2$ ). The center frequency in this case would be  $f_s/4$ . Here, the Spectral Kurtosis cannot distinguish between signal content in different frequency ranges. Due to the averaging between two adjacent frequency bins, the frequency decomposition level (see Fig. 3.6) must be at least two (STFT block length  $4/f_s$ ). The longer the STFT time frame, the higher the frequency resolution. If the STFT-frame is chosen as long as the entire signal  $X(t, f)$ , the frequency resolution would be maximal but it would be hard to find the best frequency range because of the narrowness of the frequency ranges.

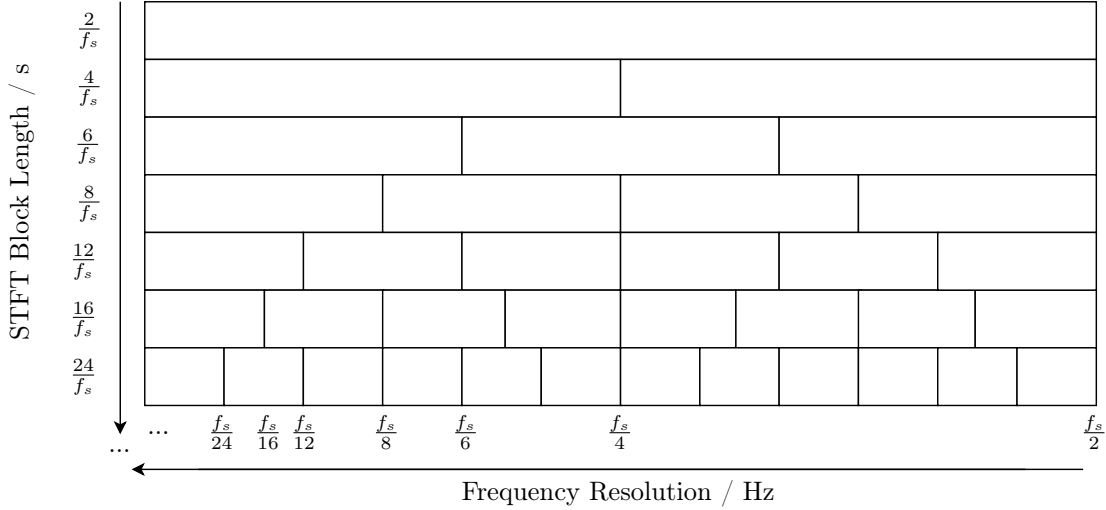


**Figure 3.5:** Correlation between the STFT block length and frequency resolution for the calculation of scalar Spectral Kurtosis values.

Essentially, the Spectral Kurtosis can distinguish between three scenarios:

- White noise:  $SK(f) = 0$ ,
- Harmonic signals:  $SK(f) < 0$ ,
- Impact signals:  $SK(f) > 0$ .

This ability figures out frequency ranges of interest, where the impacts provoked by the bearing faults are present. Therefore, the Kurtogram was established to find the frequency band with maximum Kurtosis by evaluating a frequency/frequency resolution dyad. The Kurtogram regards the spectrum in predefined frequency blocks by using a decomposition in form of a frequency/frequency resolution plane representation. This plane is depicted in Fig. 3.7. The frequency blocks are defined by breaking down the entire spectrum by a defined decomposition index  $k$  in  $2^k$  frequency blocks. The index  $k$  is chosen depending on the type of a binary tree of filter banks (for example 1/2 or 1/3 binary tree [8]). The higher the number of frequency blocks, the smaller the block size and the higher the resolution at a certain index. In case of a 1/2 binary tree, the index counts up in a way of  $k = [1; 2; 3; \dots]$ . In case of a 1/3 binary tree, the index counts up in a way of  $k = [1; 1.6; 2; 2.6; 3; 3.6; \dots]$ . Therefore, the 1/3 binary tree expansion contains an additional intermediate stage of kurtosis evaluation due to the index count and thus shows a finer resolution than the 1/2 binary tree.

For all frequency blocks at a given index, the spectral kurtosis is determined. In order to pick these frequency blocks, the center frequency of each block is needed by the algorithm. By using the center frequency, low-pass and high-pass filters are applied through the filterbank to cut out the frequency blocks with the center frequencies in their respective centers. Consequently, the frequency decomposition level must be twice as high as the amount of frequency blocks. This level is defined by  $k$  in  $2^{k+1}$ . By searching for the band with maximum spectral kurtosis, it is possible to find out how narrow the frequency block, and thus how high the degree of decomposition, must be in order to identify a frequency range where the bearing fault impacts are located. Fig. 3.7 shows an example measured at the pump test rig with built-in roller bearing (see Fig. 4.14). The figure was generated based on the MATLAB<sup>®</sup> function by Antoni [8, 9] utilizing the 1/3 binary tree. Here, the maximum Kurtosis  $SK_{\max} = 4.06$  is reached at a decomposition level of six (note the brightest, yellow frequency block). This results in a center frequency of 1388 Hz and a frequency band of 278 Hz to the left and right

## Frequency Decomposition

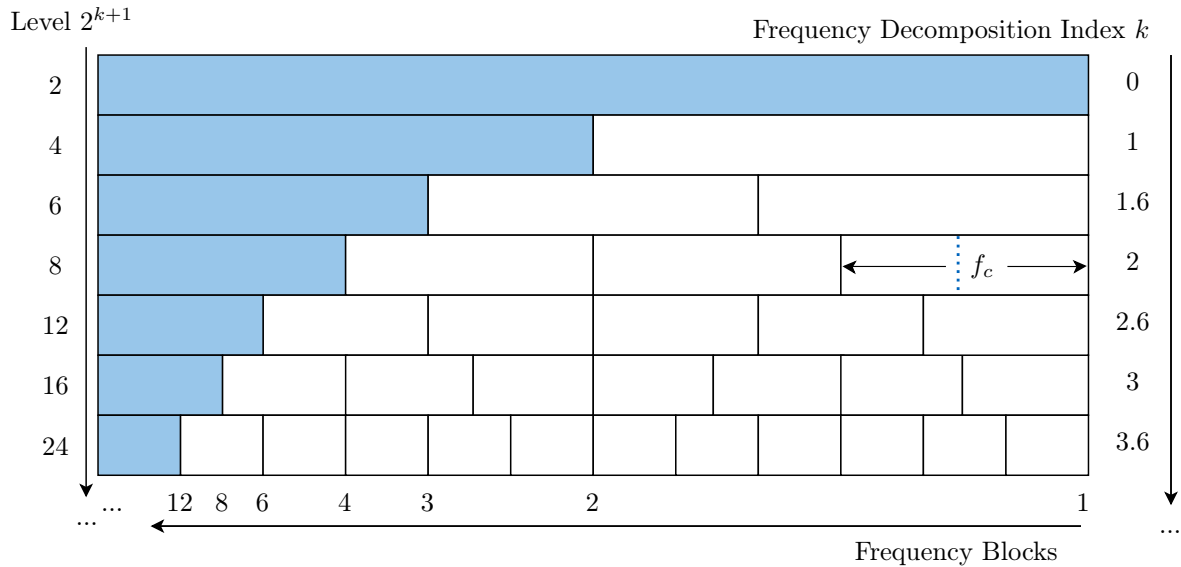


**Figure 3.6:** Schematic representation of the Kurtogram frequency/frequency resolution plane with example decomposition levels of 2-24 and a frequency block decomposition of 1-12 (highlighted in blue) based on the 1/3-binary tree Kurtogram estimator in [8]. An exemplary frequency block at decomposition index 2 is picked and divided into two sub-blocks by the center frequency  $f_c$  (blue dotted line) according to frequency decomposition level 8. The filter bank would select this block with a high-pass and a low-pass filter to the left and right of the center frequency.

of the center frequency. Thus, referring to a frequency resolution of 1.6 Hz, the band pass filter specification optimum would be situated from 1093 Hz up to the maximum of 1666 Hz. The sensor's bandwidth is limited to this maximum in the presented example. Therefore, the Kurtogram just leads to a high-pass filter. Based on this filter, we have a look at the resulting envelope spectra. The post-processed signal based on same test conditions as in Fig. 3.7 is depicted in Fig. 3.8. Here, the mean envelope spectrum of 55 snapshots (0.615 s measurement time each in axial z-direction) is observed. The unfiltered acceleration envelope magnitude contains higher amplitudes at the fundamental rotational frequency  $f_n$  and its fourth harmonic  $4 \cdot f_n$ . These signal parts stem from the basic rotor imbalance and harmonic flow processes within the pump housing. Due to the large amount of snapshots, non-stationary rotational speed can amplify or lower these peaks on average. Especially the frequency line of the mean value can differ from the expected basic rotor frequency due to time-variant load of the built-in asynchronous motor, provoked by the pump medium. Regarding the high-pass filtered envelope magnitude, these peaks are almost damped out - especially the protrusion at  $4 \cdot f_n$ . Contrary to that, the over-rolling impact at the fault frequency line  $F_O$  emerges significantly. Conclusively, a Kurtogram-based filter can clearly improve the visibility of bearing faults within the vibration envelope signal.

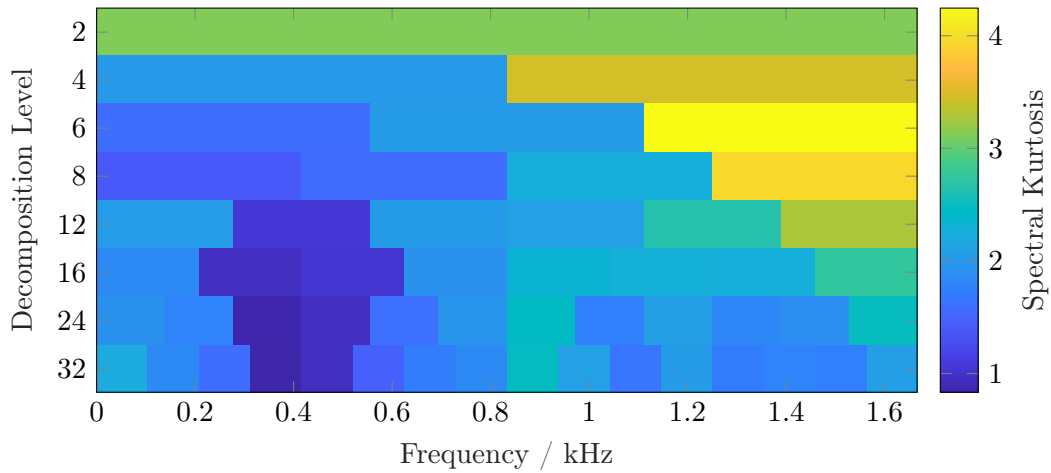


**Figure 3.7:** Exemplary Kurtogram structure based on an outer ring fault (see Fig. 4.14), measured with a wireless MEMS sensor device (LSM6DSL) at the pump test rig in axial z-direction referring to [113] based on [9].

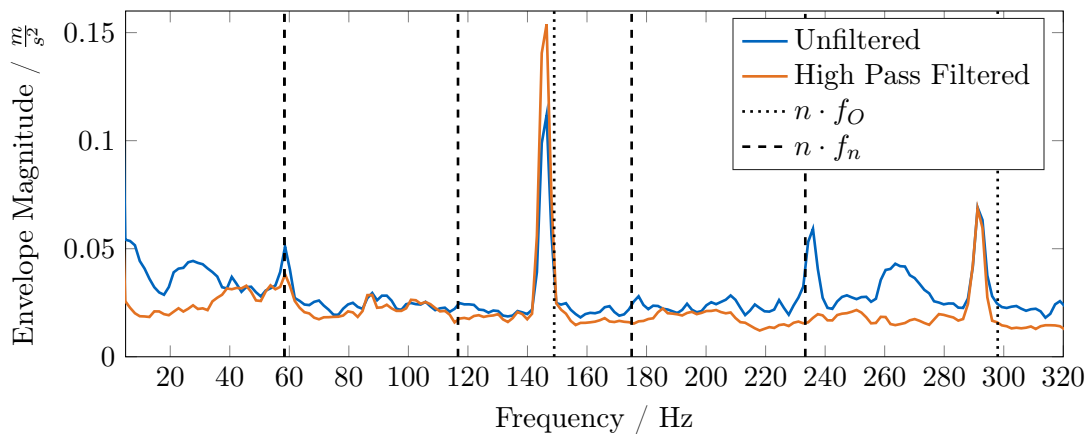


**Figure 3.8:** Averaged envelope spectrum of an exemplary outer ring fault (see Fig. 4.14). Measurement performed with a wireless MEMS sensor device (LSM6DSL) at the pump test rig in axial z-direction (Sec. 4.13) by [113]. Rotational frequency  $f_n = 58.3$  Hz, outer ring rollover frequency  $f_O = 149$  Hz at  $n$  harmonics.

### Empirical Mode Decomposition

Another data filtering method targeting the extraction of transient events within vibration signals is the Empirical Mode Decomposition (EMD) [107, 129, 145] or its extension - the Ensemble Empirical Mode Decomposition (EEMD) [147]. Both methods perform in the time domain representation and try to find so called *Intrinsic Mode Functions* (IMFs), which build an orthogonal basis for the original signal. The only difference introduced by the EEMD compared with the standard EMD can be an enhanced decoupling of the IMFs. The EMD's idea is essentially that every signal  $x(t)$  comprises an individual amount of IMFs and a residual. Based on [107, 113], the technique to find these IMFs via an iterative scheme is defined as follows:

1. Calculation of the upper and lower envelope  $x^+(t)$  and  $x^-(t)$  of a time signal  $x(t)$  as described in Sec. 3.4.2,
2. Mean value  $\bar{x}_{k,i}(t)$  computation of both envelopes within the iteration  $i$ :

$$\bar{x}_{k,i}(t) = \frac{1}{2} [x^+(t) + x^-(t)], \quad (3.25)$$

3. Utilizing  $s_k(t) = x(t)$  as start signal with subtraction of the mean envelope at each iteration

$$s_k(t) = s_k(t) - \bar{x}_{k,i}(t). \quad (3.26)$$

Here, we get a new signal  $s_k(t)$  at every iteration step. Note that the signal  $s_k(t)$  will not change anymore if the signal is symmetric to the time axis because in this case the mean value  $\bar{x}_{k,i}(t)$  of the upper and lower envelope would be zero. An initial stop criterion must be introduced depending on the definition of an Intrinsic Mode Function. As assessment for an IMF we utilized the criterion proposed in [144] using the scalar relative tolerance specification:

$$\frac{\|s(t)_{i-1} - s(t)_i\|^2}{\|s(t)_i\|^2} < 0.2 \quad (3.27)$$

If  $s_k(t)$  does not correspond with an IMF, step four is skipped and  $s_k(t)$  is utilized as a new start signal for the envelope computation in step one.

4. If the assessment criterion is fulfilled,  $s_k(t)$  complies with an IMF and a new start signal (or leftover residual)  $l_k(t)$  is calculated by subtracting the IMF from the original start signal  $x(t)$ . After finding the first IMF, we get a new residual  $l_k(t)$  after every new identified IMF. Thus, the subsequent *start* signal is defined as

$$l_k(t) = l_{k-1}(t) - s_k(t) \quad (3.28)$$

Afterwards, we go back to step one again, replacing  $x(t)$  by  $l_k(t)$  and computing the envelopes. Finally, every  $s_k(t)$  in Eq. (3.28) is stored as a IMF.

Conversely, the original signal  $x(t)$  is reassembled by the sum of all IMFs together with the final residual. Defining  $N$  IMFs, we get the origin based on

$$x(t) = \sum_{i=1}^N s_i(t) + l_N(t). \quad (3.29)$$

The following example in Fig. 3.9 shows the first four IMFs of the same exemplary bearing vibration signal as considered in Sec. 3.4.3 within the Kurtogram evaluation. When evaluating these four Intrinsic Mode Functions, the decreasing content of high frequency parts from IMF 1 to IMF 4 is obvious. In the presented example, only the first IMF implies information about the high-frequency amplitude modulated fault impacts. Comparing it with Fig. 3.10, the impacts become visible within the first IMF. It works a bit like the presented high pass filter. Although the stopping criterion is not reached, the fourth IMF does not contain any expedient components anymore. The frequencies would further decrease with higher IMFs. Hence, no more Intrinsic Mode Functions are plotted here.

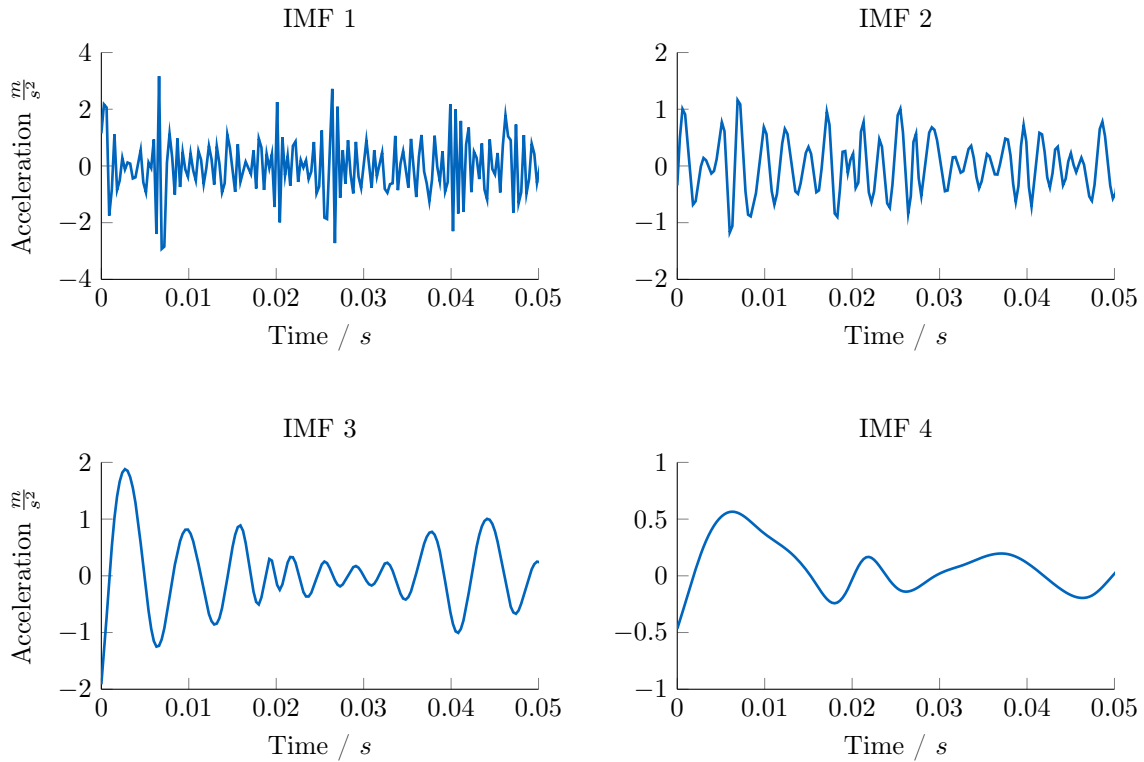


**Figure 3.9:** Exemplary Empirical Mode Decomposition of an outer ring fault (implemented defect see Fig. 4.14). Measurement performed with a wireless MEMS sensor device (LSM6DSL) at the pump test rig in axial z-direction at 58.3 Hz rotational speed (Sec. 4.13) based on [113].

As discussed in the previous paragraph, the bearing faults are rather visible within the first IMFs. Thus, the envelope spectra of the first and second IMF and a comparison with the raw envelope spectrum are depicted in Fig. 3.10. Here, a slight enhancement of the first over-rolling frequency peak at 149 Hz at the first IMF is observed by contrast with the raw signal. However, the second IMF does not contain any information about the bearing fault impacts. In this example, we can even stop the Empirical Mode Decomposition after the first Intrinsic Mode Function.

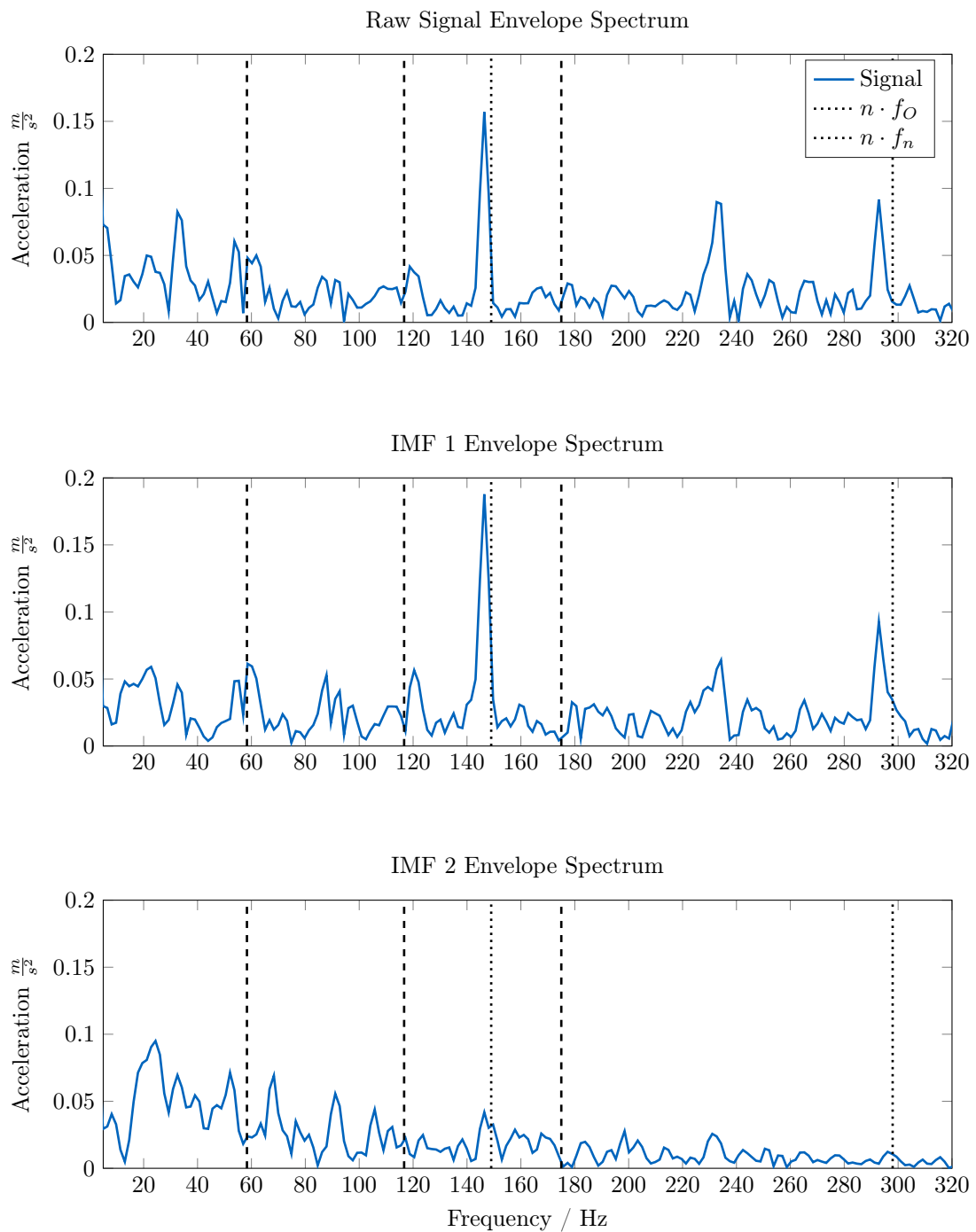


**Figure 3.10:** Envelope spectra of the first two IMFs with an exemplary outer ring fault (see Fig. 4.14). Data snapshot (0.615 s) acquired with a wireless MEMS sensor device (LSM6DSL) at the pump test rig in axial  $z$ -direction at 58.3 Hz rotational speed referring to [113].

### Multipoint Optimal Minimum Entropy Deconvolution Adjusted Filtering

Another filtering method in order to extract bearing fault signal properly from interfering vibrating components is the Multipoint Optimal Minimum Entropy Deconvolution Adjusted (MOMEDA) signal processing technique [86]. Here, the filtered signal is not utilized as input for an envelope spectral analysis as in the previous examples. The MOMEDA essentially consists of a Fourier spectrum in a particularly specified frequency range. This range is defined according to the expected frequency location of impacts. We just define a time interval containing impacts at multiples of time  $t$  referring to the bearing fault frequencies. The timing of the impacts due to the expected bearing fault is known based on the rotational frequency and the bearing kinematics. For an exemplary rollover impact at the times  $t = 3$  and  $t = 6$ , the target vector would look as follows:

$$\mathbf{t} = [ 0 \ 0 \ 1 \ 0 \ 0 \ 1 \ 0 \ 0 ]^T. \quad (3.30)$$

Within this target vector, we search for a filter  $\mathbf{f}$

$$\mathbf{f} = (\mathbf{X}_0 \mathbf{X}_0^T)^{-1} \mathbf{X}_0 \mathbf{t} \quad (3.31)$$

which best extracts the impacts from a time signal  $X$ :

$$\mathbf{X}_0 = \begin{bmatrix} X_L & X_{L+1} & X_{L+2} & \cdots & \cdots & X_N \\ X_{L-1} & X_L & X_{L+1} & \cdots & \cdots & X_{N-1} \\ X_{L-2} & X_{L-1} & X_L & \cdots & \cdots & X_{N-2} \\ \vdots & \vdots & \vdots & \ddots & \cdots & \vdots \\ X_1 & X_2 & X_3 & \cdots & \cdots & X_{N-L+1} \end{bmatrix} \quad (3.32)$$

with filter length  $L$  and  $N$  samples of the measured signal. The filter length must be higher than the calculated impulse period of the bearing fault in order to maintain a tolerance. As tested by [46, 113, 143], 1.4 times the impulse period is an empirically proven value for that length. Finally, to find the best combination of filter length  $L$  and number of samples  $N$  based on the Kurtosis values,  $m$  different target vectors  $\mathbf{t}$  are evaluated. Therefore, we get  $s_m$  impact sequences in the frequency domain representation for further evaluation by the Kurtosis:

$$\mathbf{S} = [ \mathbf{s}_1 \ \mathbf{s}_2 \ \cdots \ \mathbf{s}_m ] = \mathbf{X}_0^T \mathcal{F} \quad (3.33)$$

with

$$\mathcal{F} = [ \mathbf{f}_1 \ \mathbf{f}_2 \ \cdots \ \mathbf{f}_m ] = (\mathbf{X}_0 \mathbf{X}_0^T)^{-1} \mathbf{X}_0 [ \mathbf{t}_1 \ \mathbf{t}_2 \ \cdots \ \mathbf{t}_m ]. \quad (3.34)$$

In order to determine a sequence which best describes the over-rolling fault impacts, a Multipoint-Kurtosis  $\mathcal{K}_m$  is calculated:

$$\mathcal{K}_m = \frac{\left( \sum_{n=1}^{N-L} \mathbf{t}_n^2 \right)^2 \sum_{n=1}^{N-L} (\mathbf{t}_n \mathbf{s}_n)^4}{\sum_{n=1}^{N-L} \mathbf{t}_n^8 \left( \sum_{n=1}^{N-L} \mathbf{s}_n^2 \right)^2}. \quad (3.35)$$

The highest Multipoint-Kurtosis value is utilized to find the best combination of  $L$  and  $N$ . In order to use this method to filter out the frequency ranges containing the fault impacts, the frequency resolution of the signal must be high enough. If the frequency resolution is not high enough, too few multiples of the rollover frequency may be included in the time sequence  $\mathbf{t}$ . A low bandwidth can lead to the same effect. In this cases the impulses are not

contained in the impact sequence  $\mathbf{s}$  and the corresponding Multipoint-Kurtosis is low. If the regarded time signal  $\mathbf{X}_0$  is a time-limited snapshot and thus has low frequency resolution as well as limited bandwidth, the method is not suitable for finding the bearing fault indicators [113]. Despite the high performance of MOMEDA to detect bearing faults, the method is not evaluated in detail here due to the bandwidth and frequency resolution restrictions. The target application in the scope of this thesis are MEMS-based sensor systems, which have low frequency resolutions and limited bandwidths.

### Cepstrum Prewhitening

A further helpful method to emphasize peaks at the bearing defect rollover frequencies is the cepstrum prewhitening technique. It was also discussed by [113] and is primary based on the complex cepstrum. This description was initially defined by Oppenheim and Schaffer [103]. The complex cepstrum  $\mathcal{C}_{(c)}$  is defined as inverse Fourier transformation of the logarithmic spectrum:

$$\mathcal{C}(c) = \mathcal{F}^{-1}(\log(X(\mathcal{f}))) = \mathcal{F}^{-1}(\ln(A(\mathcal{f})) + i\varphi(\mathcal{f})); \quad \mathcal{C} \in \mathbb{C} \quad (3.36)$$

with  $X(\mathcal{f})$  as the Fourier transformed time signal  $\mathcal{F}(x(t))$  and the so-called *quefrequency*  $c$ . [29]. We get the so-called *real cepstrum* by setting the phase component in Eq. (3.36) to zero:

$$\mathcal{C}(c) = \mathcal{F}^{-1}(\ln(A(\mathcal{f}))); \quad \mathcal{C} \in \mathbb{R}. \quad (3.37)$$

A peak within the cepstrum at a certain quefrequency can be imagined as the inverse period of harmonics in a spectrum.

The prewhitened cepstrum is calculated in two steps: In the first step, the entire cepstrum is set to zero, except for the zero-quefrequency line. In the second step, the zero-quefrequency line is transformed back into the time domain representation, taking into account the phase information. The effect of this procedure corresponds to a cancellation of discrete frequencies by deterministic excitations. Resonances of the entire system can also be filtered out by this technique [20, 104]. In contrast to that, harmonic excitations such as the bearing fault impacts can therefore be amplified. The prewhitened cepstrum is obtained by dividing the complex spectrum by its absolute value:

$$x_{CPW} = \mathcal{F}^{-1}\left(\frac{X(\mathcal{f})}{|X(\mathcal{f})|}\right). \quad (3.38)$$

We target an amplification of the defect rollover-frequency and its harmonics based on the theory of deleted discrete frequencies. The exemplary outer ring fault signal is threatened with that method and the result is depicted in Fig. 3.11.

Here, the cepstral prewhitened envelope spectrum is averaged over 55 snapshots (0.615 s measurement time each) and normalized with the unfiltered standard envelope spectrum for better comparability. The peaks which are not associated with the fundamental rotor frequency or the defect frequencies are erased by the cepstrum prewhitening. Moreover, both amplitudes at the outer ring rollover frequency and its harmonic slightly increase. Thus, the positive effect of this method is visible.

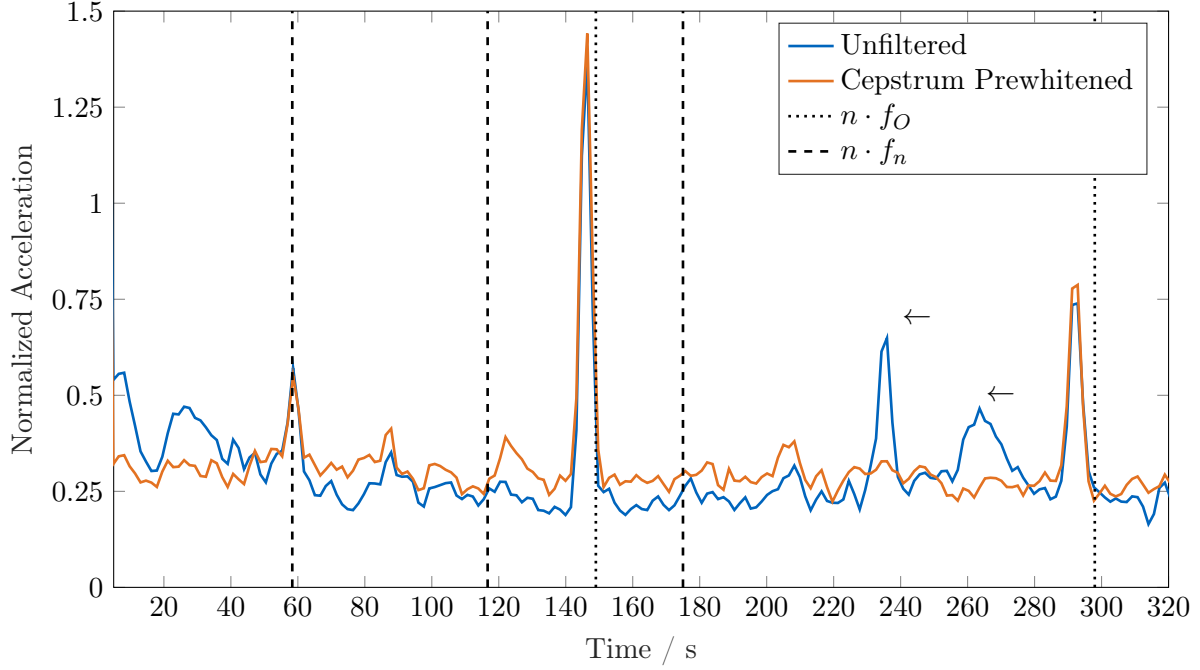


**Figure 3.11:** Unfiltered, but averaged (blue) and cepstrum prewhitened (orange) envelope spectra of an exemplary outer ring fault (depicted in Fig. 4.14). Measurement snapshot acquired with a wireless MEMS sensor device (LSM6DSL) at the pump test rig in axial z-direction by [113]. Rotational frequency  $f_n = 58.3$  Hz, outer ring rolover frequency  $f_O = 149$  Hz at  $n$  harmonics.

### 3.4.4 Concluding Signal-Based Condition Indicator

Now, the different methods presented in this section are compared. Considering only reasonable techniques which turned out to be suitable for a wireless sensor node application, the Kurtogram-based envelope spectrum, the Empirical Mode Decomposition-based envelope spectrum and the Cepstrum prewhitened envelope spectrum have to be taken into account. (compare Fig. 3.8, 3.10 and 3.11). Here, it turns out that the classical bandpass/highpass filtered envelope spectrum provides the best results. The Kurtogram seems to be the best method to design the filter. In cases of low bandwidth and low resolution sensor data, the frequency range has to be analyzed where the amplitude-modulated over-rolling impacts are placed. Based on these findings, a signal-based condition indicator  $I_f$  is defined in order to obtain a scalar assessment criterion.

$$I_f = \sqrt{\frac{1}{N} \sum_{f-6.5 \text{ Hz}}^{f+6.5 \text{ Hz}} X(f)^2} + \sqrt{\frac{1}{N} \sum_{2f-6.5 \text{ Hz}}^{2f+6.5 \text{ Hz}} X(f)^2}, \quad (3.39)$$

using

$$\begin{aligned} X(f) &= \mathcal{F}\{x^+(t)\}, \\ f &= \text{Bearing over-rolling frequency}, \\ x^+(t) &= \text{Highpass-filtered envelope of } x(t), \\ N &= \text{Amount of Samples}. \end{aligned}$$

The indicator calculates the sum of the RMS-values within an exemplary 13 Hz-band around the over-rolling frequency and its twofold harmonic. For this purpose, the raw time signal

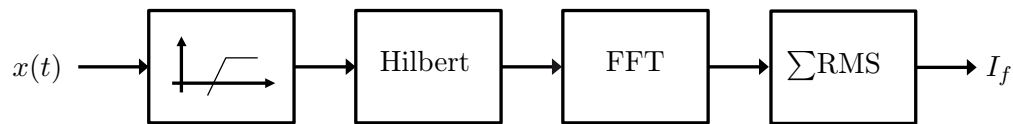


**Figure 3.12:** Condition indicator signal flow chart starting with a highpass-filter, continuing with Hilbert transformation for envelope approximation and finally calculating the RMS-based Indicator inspired by [113].

$x(t)$  is high-pass filtered based on a Kurtogram (Fig. 3.7) and the envelope is computed via Hilbert-Transformation. Fig. 3.12 shows an exemplary signal flow chart for this purpose. A method for vibration monitoring of roller bearings placing a virtual sensor in the bearing center using this condition indicator is discussed in Sec 7.2.1.

### 3.4.5 Summary

All presented techniques aim to detect bearing faults based on physical reasons and are tailored for MEMS accelerometer sensor systems. These physical reasons are small impacts which are the consequence of small defects inside the bearing. These impacts express themselves within an amplitude-modulated impulse over the entire measured vibration signal. *Statistical indicators* allow a first statement to the machine health based on a broad-frequency range since the impacts emphasize these statistical features inside the overall vibration. Differentiating between fault source and fault type, *envelope analysis* is the method of choice. The amplitude-modulated impulse can be well extracted by this technique with subsequent Fourier transformation. Further enhancement is possible by pre-filtering the measured signal before calculating the envelope. Here, the *spectral kurtosis* helps to find a frequency range where the impacts of interest are modulated. On that base, a proper band-pass filter can be found. *Empirical Mode Decomposition* is another tool to extract the bearing fault information from the signal. Here, *Intrinsic Mode Functions (IMFs)* are found which can pull out the bearing fault content from the entire machine vibration. Envelope spectral analysis of these IMFs provide enhanced fault extraction results compared to the unfiltered analysis. Another roller bearing fault peak emphasizing filter can be designed by *cepstrum prewhitening*. This technique enhances the results with respect to MEMS sensor system measurements. Though, *MOMEDA* fails in this context since the frequency resolution of these sensor systems is too low for this method. The best fault detecting results are found by utilizing a filter which is designed on the Spectral Kurtosis base. Subsequent envelope spectral analysis allows to define a *signal-based condition indicator* which provides a scalar value correlating with the fault type and the specific provoked vibration amplitude. This indicator will be used later for a virtual sensing approach in Sec 7.2.1.



## Chapter 4

# Test Rig Characterization

Within this chapter, we present two test rigs which are essential for method development and validation according to the thesis. Both setups comprise industrial rotating machines with a similarly structured rotor implying an overhung impeller. At the outset, we introduce a blower test rig containing a high-dynamic housing as characteristic feature. Moreover, a pump test rig is presented as second example which has, in contrast to the blower, stiff housing properties and a highly damped rotor. Both applications will be used for validation of the hybrid models. Their development will be described in Chap. 5 and 6.

## 4.1 Blower Test Rig

The main application to demonstrate our hybrid modeling approach is an industrial blower test rig. Its task is the cooling of a locomotive drive, which is mounted below. The blower represents a predestined example due to its dynamic properties. The test rig is depicted in Fig. 4.1 in form of a hybrid visualization. In the figure, an insight into the blower is given to highlight the rotor (1). It includes an overhung impeller (2) which is widely used in blowers and centrifugal pumps. The rotor with its impeller sucks the air axially and expels it via a centrifugal principle on a mechanical decoupled steel base (3). Especially the struts (4) and the bearings (5) as coupling points between rotor and housing influence the entire dynamics. The rotor is supported by the bearings inside a relatively stiff motor block (6). The blower constitutes a scenario where a sensor position at the outside housing is required due to wireless sensor data transmission. An exemplary wireless sensor system (7) is mounted on the housing. The transfer path from rotor forces via the two roller bearings to the sensor position is denoted by orange (8).

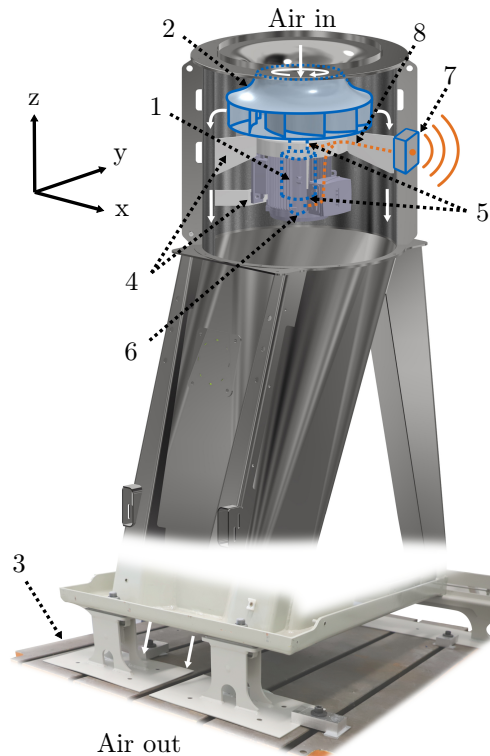


**Figure 4.1:** Locomotive drive cooling blower test rig as exemplary application for hybrid dynamic models. All main features (1-8) are described on the left.

All essential technical information of the blower is specified in Tab. 4.1.

**Table 4.1:** Technical specifications at of the blower at rated operating point.

|                   |                        |                                     |                        |
|-------------------|------------------------|-------------------------------------|------------------------|
| Power $P$         | 7.5 kW                 | Frequency $f$                       | 60 Hz                  |
| Current $I_N$     | 13 A                   | Flow rate $Q$                       | 1.65 m <sup>3</sup> /h |
| Voltage $U$       | Y-440 V                | Temperature range $T$               | -40 °C...40 °C         |
| Rated speed $n_N$ | 3540 min <sup>-1</sup> | Active power factor $\cos(\varphi)$ | 0.85                   |

#### 4.1.1 Housing Dynamics and Their Influence on Unbalance Monitoring

In case of monitoring rotor faults, as for example discussed in [130], we must be aware of the entire systems' structural dynamics. In the following section, rotordynamic effects are presented on the blower test rig. These are caused by an orthotropic rotor support and affect the housing dynamics within unbalance monitoring. The influence of the stiffness orthotropy due to the bracing between motor and housing is particularly emphasized when monitoring the rotor unbalance. All results in this section are based on [73]. In this publication, the measurements are acquired at a roughly similar blower system. The presented application is evaluated in a healthy and in a defined unbalanced state by measurements utilizing horizontally distributed accelerometers to answer two questions:

1. Is an unbalance detectable at different operating conditions by measuring on the outside housing?
2. Which effects have to be considered, when estimating an orthotropically supported rotor?

#### Coupled Effects - Minimal Model

Orthotropic rotor support causes two divergent stiffnesses in the horizontal x-y plane. This can also be seen in the transfer functions between rotor excitation and a housing measurement position. These transfer functions represent the inverse dynamic stiffnesses, differing from each other in x- and y-axis direction (orthotropic rotor support). Fig. 4.2 shows the simplified analogous model of a flying supported rotor with orthotropic bearing stiffnesses and associated FRFs.

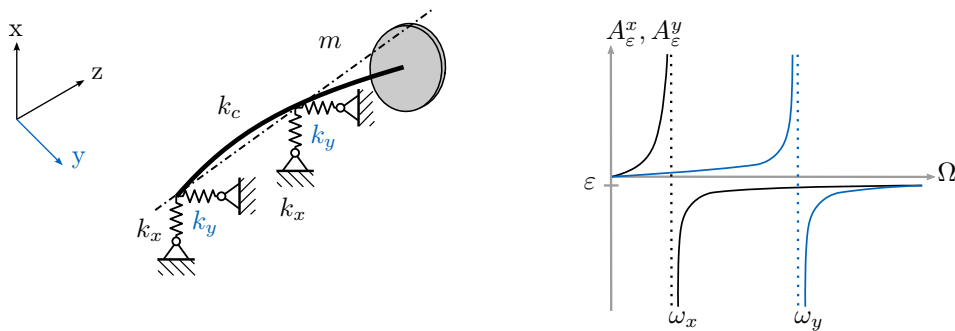


**Figure 4.2:** Left: Flying, orthotropic supported rotor as simplified analogous model related to the blower with shaft stiffness  $k_c$  and bearing stiffness  $k_x \neq k_y$ . Right: FRF of the analogous model with mass unbalance and neglected damping. Gyroscopic effects are also not considered here. Response amplitudes  $A_\varepsilon^x(\Omega)$ ,  $A_\varepsilon^y(\Omega)$  in x-direction (black) and y-direction (blue), excitation frequency  $\Omega$ , two resonances  $\omega_x$ ,  $\omega_y$  and eccentricity  $\varepsilon$  according to [73].

In Fig. 4.2, the rotor orthotropic support is represented by  $k_x$  and  $k_y$ , mainly expressed by the blower's struts and housing. For the outlined minimal model, we assume a homogenous, symmetric shaft (stiffness  $k_c$ ) which is connected with a lumped mass  $m$  as overhung impeller at the rotor end. With respect to the mass position, Fig. 4.2 contains just a schematic depiction concerning the flying rotor support of the real application. By performing an eigenanalysis of the model, the two resonances

$$\omega_x = \sqrt{\frac{k_c}{m} \cdot \frac{2k_x}{2k_x + k_c}} \quad \text{and} \quad \omega_y = \sqrt{\frac{k_c}{m} \cdot \frac{2k_y}{2k_y + k_c}}. \quad (4.1)$$

are obtained. These eigenfrequencies appear as vertical dotted lines in the FRF (see Fig. 4.2). Here, the black line represents the frequency response amplitude  $A_\varepsilon^x(\Omega)$  in x-direction with eigenfrequency  $\omega_x$  whereby the blue line ( $A_\varepsilon^y(\Omega)$ ) depicts the corresponding response in y-direction with resonance  $\omega_y$ . Within the schematic FRF representation, we only regard unbalance excitation (eccentricity  $\varepsilon$ ) and ignore possibly damping effects. Until the  $\omega_x$  line, x- and y-direction respond in phase<sup>1</sup>. Above this first eigenfrequency, a 180 degree phase shift of  $A_\varepsilon^x(\Omega)$  is observed (rotational speed of the application between 19 Hz and 22 Hz). After passing  $\omega_y$  ( $\omega_y = 22$  Hz in the presented example), the amplitudes respond phase-synchronously again. These phase shifts can express themselves within the acceleration signal if measuring at the blower housing in the two horizontal directions. This effect can also be clarified referring to [48]. Here, the phenomenon is explained as increasing and abating of an elliptical motion of the unbalance-excited shaft center involving principal axes x (real part) and y (imaginary part). For that,  $A_\varepsilon^x$  and  $A_\varepsilon^y$  are utilized in the time domain representation. In this case, they imply the elliptical half-axes

$$A_\varepsilon^x = \frac{\varepsilon \cdot \Omega^2}{\omega_x^2 - \Omega^2} \quad \text{and} \quad A_\varepsilon^y = \frac{\varepsilon \cdot \Omega^2(t)}{\omega_y^2 - \Omega^2} \quad (4.2)$$

with the equality of the absolute values of the sum and difference of the two amplitudes:

$$|A_\varepsilon^x + A_\varepsilon^y| = |A_\varepsilon^x - A_\varepsilon^y|. \quad (4.3)$$

In the x-direction resonance,  $A_\varepsilon^y = 0$  and in the y-direction resonance,  $A_\varepsilon^x = 0$ . The motion can be represented in the complex plane by the complex amplitude

$$\boldsymbol{w}_\varepsilon = \boldsymbol{w}_{\varepsilon, re}^x + j\boldsymbol{w}_{\varepsilon, im}^y = A_\varepsilon^x \cos \Omega t + jA_\varepsilon^y \sin \Omega t. \quad (4.4)$$

$\Omega$  constitutes the current operational speed and  $\varepsilon$  the unbalance mass eccentricity. When applying the Euler Equations, we write the shaft center movement as

$$\boldsymbol{w}_\varepsilon = \frac{1}{2} (A_\varepsilon^x + A_\varepsilon^y) e^{j\Omega t} + \frac{1}{2} (A_\varepsilon^x - A_\varepsilon^y) e^{-j\Omega t} = A_{(+)}^w e^{j\Omega t} + A_{(-)}^w e^{-j\Omega t} \quad (4.5)$$

with the elliptical shaft movements  $A_{(+)}^w$  and  $A_{(-)}^w$  in sense and opposed to the rotor turning direction. Depending on these two superimposed orbits, the mode correlated, highest amplitude is responsible for whirling direction: In case of  $|A_{(+)}^w| > |A_{(-)}^w|$ , the shaft orbit shape is elliptical and its rotation direction is orientated in forward whirl. In case of  $|A_{(+)}^w| < |A_{(-)}^w|$ , the shaft moves on an elliptical shape too, but in backward whirl direction. In case of  $|A_{(+)}^w| = |A_{(-)}^w|$ , oscillating linear motion is observable (see Fig. 4.7). Inserting the half-axes (Eq. (4.2)) into Eq. (4.5), we determine both amplitudes of the forward and backward whirling movement ratio:

$$A_{(+)}^w = \frac{\varepsilon \Omega^2}{2} \frac{\omega_y^2 + \omega_x^2 - 2\Omega^2}{(\omega_y^2 - \Omega^2)(\omega_x^2 - \Omega^2)} \quad \text{and} \quad A_{(-)}^w = \frac{\varepsilon \Omega^2}{2} \frac{\omega_x^2 + \omega_y^2}{(\omega_y^2 - \Omega^2)(\omega_x^2 - \Omega^2)}. \quad (4.6)$$

<sup>1</sup>rotational speed of the application below 19 Hz.

## Operational Measurements

To get an idea of the blower's vibration resulting from a unbalanced rotor at the entire operating range, we acquired the system response during a rotor run up. For data acquisition, triaxial Kistler 8688A piezoelectric accelerometers combined with a Siemens LMS Test Lab System<sup>2</sup> were used. Note that triaxial accelerometers are utilized for the measurements but only the horizontal X- and Y-directions are considered here. A waterfall diagram is determined via Fast Fourier Transform<sup>3</sup> and depicted in Fig. 4.3. Looking at the test configuration on the left side of the figure, the circle represents the housing's top ring with centered rotor (not shown) and delineated rotation direction with accelerometer position (black dot). The waterfall diagram results from an y-direction measurement. Regarding the waterfall plot, the first order resonance at 22 Hz is striking. Here, the excitation is realized by a defined, 10 g unbalance mass and 204 mm eccentricity. The speed-dependent amplitude at the 22nd speed multiple is excessive due to eleven impeller blades and their twofold excitation frequency due to a flow channel division in the housing.

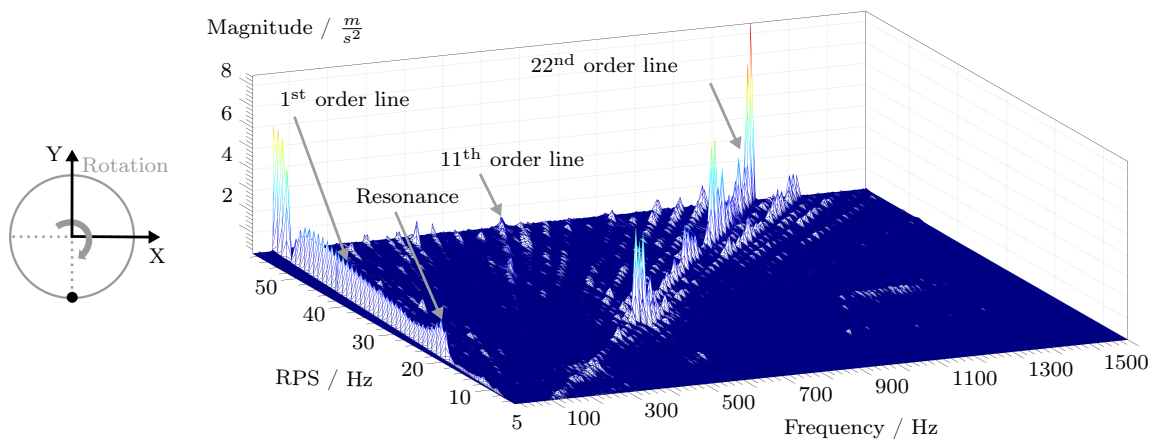


**Figure 4.3:** Y-direction run up waterfall diagram of a blower with an unbalanced rotor (10 g unbalance mass, 204 mm eccentricity). Note the resonance at 22 Hz which is excited by the first order. The 11th and 22nd orders also occur with striking amplitudes.

Here, the orbit is shaped elliptically and the unbalanced rotor just shows an increased amplitude. The rotation direction of the signal is equally aligned compared with the rotor's sense of rotation. We observe forward whirl [48]. The same measurement was subsequently made for further operating speeds. Considering the 20 Hz operational frequency near the resonance of 22 Hz, and compare the result with the 16 Hz plot, two conspicuities were observed: The ellipsis inclination has rotated by 90 degrees and the rotating direction has reversed. Now, the signal is oppositely orientated compared with the rotor's sense of rotation. This specific effect will be discussed in the next subsection.

<sup>2</sup>8192 S/s sampling frequency.

<sup>3</sup>30 s measurement time for each rotational speed frequency, (5 Hz - 60 Hz, 1 Hz step resolution). Note, all written speed frequencies in this section refer to the magnetic field frequency and do not correspond to the exact mechanical rotation speed.

For the subsequent considerations, the sensors were arranged as shown in Fig. 4.4 consisting of two horizontally, orthogonally aligned measurement DoF (black dots). Utilizing that test set-up, we evaluated a healthy reference blower and a blower with unbalanced rotor (10 g unbalance mass, 204 mm eccentricity). As operational speed frequency, 16 Hz were chosen in order to stay far enough away from the first order resonance as depicted in Fig. 4.3. For all subsequent orbit plots, a FIR bandpass filter<sup>a</sup> was used, applying MATLAB®'s *filtfilt* function to the time signals in order to eliminate phase shift errors. The resulting acceleration orbits (black reference rotor, blue unbalanced rotor) are plotted in Fig.4.5 (left).

<sup>a</sup> $\pm 5$  Hz around the considered operational speed frequency, forward and backward filtering.

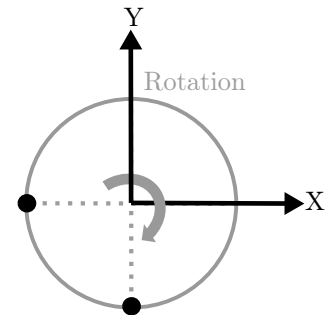


**Figure 4.4:** Measurement set-up (blower top view) with marked sensor positions at the outer housing (black dots).

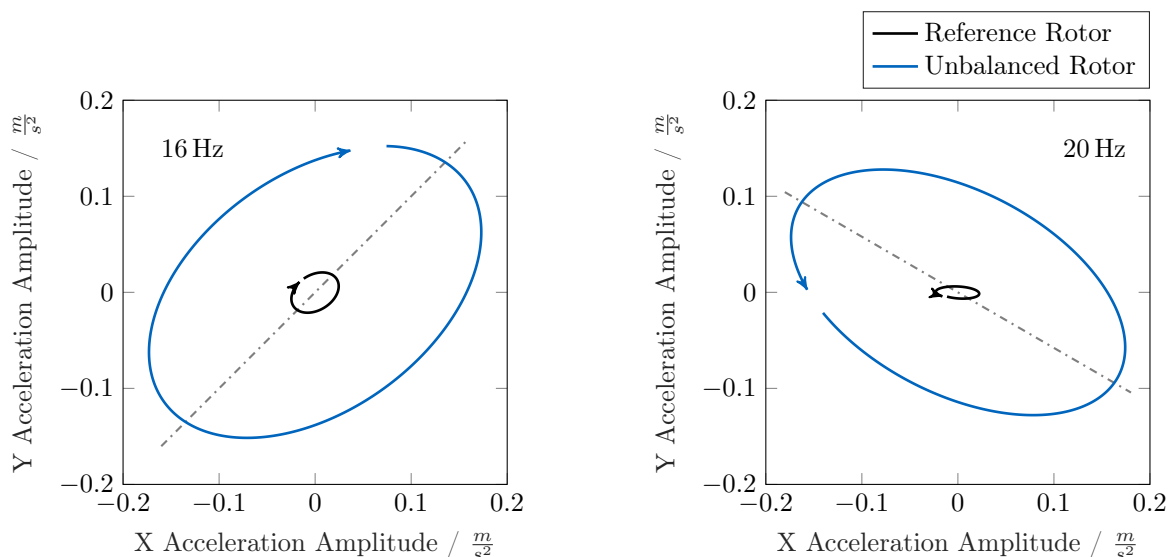


**Figure 4.5:** Acceleration orbits of the blower housing with a reference rotor (black) and an unbalanced rotor (10 g unbalance) at 16 Hz rotational speed with forward whirling rotor (left). Right: backward whirling rotor at 20 Hz rotational speed.

Now, a significantly higher rotational speed at 37 Hz is considered to be far apart from the resonance area. Comparing the resulting acceleration orbit with the correlating plot at 20 Hz rotational speed, we find the same effect that occurs between 16 Hz and 20 Hz. The ellipsis inclination has rotated again by 90 degrees and the signal direction is now again equally aligned to the rotating direction. The ellipses of both reference and unbalanced rotor excitation are now drawn in rotational sense of the rotor. We also observe a strong amplitude increase compared with the lower operating speed measurements due to the unbalance effect. Both directions reversed their phases two times. Hence, a correlation to resonance effects might be obvious. Particularly, the orbit shapes direction of inclination, which alters by about 90 degrees at each regarded operational speed might result from the mode shapes.

We assume that the orbit forms come from the bending mode direction associated to the modes, but an evidence is needed. Therefore, the operational excitation response at the resonance frequency of 22 Hz is observed. The rotational speed was varied around 18 Hz-33 Hz to find a second mode shape, orthogonal to the known y-direction movement at 22 Hz. The associated x-direction mode shape was found with a resonance at 19 Hz. The analysis was performed on the blower with a balanced reference rotor. Both resonances lie very close together (orbits see Fig. 4.7.). The reason for this kind of orthogonal modes are two different stiffnesses of the housing relative to the rotor. These dynamic properties are obvious regarding Fig. 4.1. Here, entire structure's y-direction is much more rigid then the x-form. We have a closer look at these modes with correlation to signal rotation direction, hereinafter.

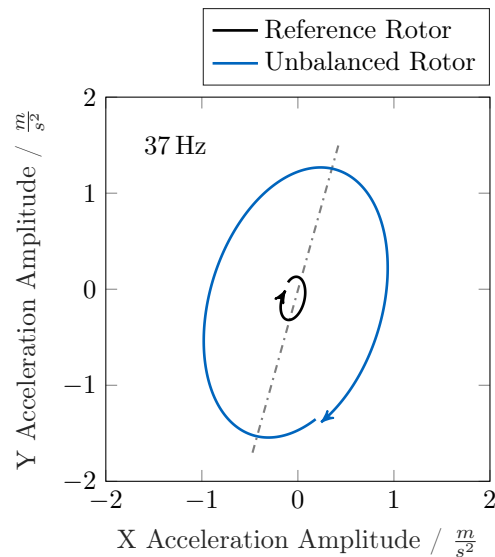


**Figure 4.6:** Acceleration orbits of the blower housing with a reference rotor (black) and an unbalanced rotor (10 g unbalance) at 37 Hz rotational speed. Forward whirling rotor.

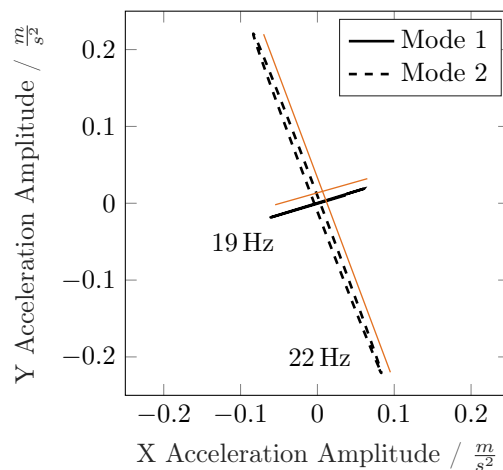


**Figure 4.7:** Acceleration orbits of the two orthogonal mode shapes determined utilizing a balanced reference rotor. Mode 1 at 19 Hz and mode 2 at 22 Hz. The two half axes are plotted in orange.

### Intermediate Summary

In this section, the influence of housing dynamics on unbalance monitoring was investigated, especially with respect to the effect of an orthotropic elastic rotor support. Forward and backward whirls are represented within the rotational frequency of the orthogonally aligned, horizontal measurement DoF. The effect on these horizontally measured acceleration signals when passing through resonances was discussed using the blower test rig. At resonance, the vibration orientation at the outer housing is aligned exclusively with the mode shape direction. Due to these orthogonally aligned mode shapes (Fig. 4.7), an elliptical orbit is no longer visible during operation at the two resonances (19 Hz and 22 Hz). Therefore, a "rotating force" is no longer visible in the measurements and the unbalance force is difficult to determine. In the measurements, the two half axes are visible in the resonant case (orange lines in Fig. 4.7). In an undamped system, the amplitude of the resonating axis would approach infinity, while the amplitude of the axis orthogonal to it would be zero. Due to these effects, the operating frequency range for further investigations in this work was set to a range between 30 Hz and 60 Hz<sup>4</sup> to avoid these resonances.

---

<sup>4</sup>range of the exciting magnetic field rotational speed.

### 4.1.2 Modal Analysis

As seen in Sec. 4.1.1, the blower test rig has some resonances which would affect monitoring strategies if the rotational speed overlaps with them. In order to further become familiar with the system, Mulser [89] performed an experimental modal analysis. For the investigation within this thesis, the entire operating frequency range up to 60 Hz is regarded. Therefore, measurements were carried out utilizing Siemens LMS Test Lab, an electrodynamic shaker (Type Brüel & Kjaer 4809) for radial and tangential excitation. In order to determine the system's response properly, 44 measurement points at ten different heights (Sensor Type 8688A50T) were distributed over the entire blower. The system was excited applying a periodic chirp force signal to the shaker<sup>5</sup>. All measurement and excitation DoF are visualized in Fig. 4.8. Here, the height of the sensors in the left blower overview is marked by dotted lines. Based on the depicted setup, seven modes were found within the operational frequency

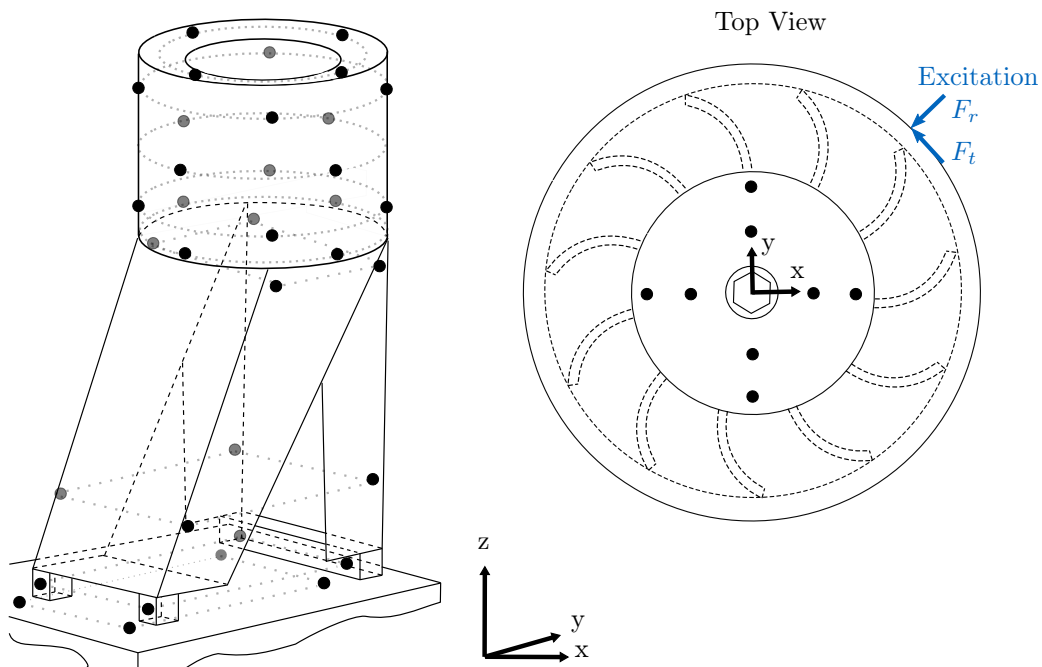


**Figure 4.8:** Experimental modal analysis test setup based on [89]. Left: housing and base measurement points. Sensor grouping according to the height highlighted by dotted lines. Right: rotor disc measurement points, radial and tangential excitation forces  $F_r$ ,  $F_t$ .

range. These are listed in Tab. 4.2. Here, we have two horizontal foundation resonances below the pronounced bending mode shapes in  $x$ - and  $y$ -direction as discussed in Sec. 4.1.1. In this case, only structural properties excluding rotational effects are regarded. Comparing the first resonance frequency (18 Hz) with the preliminary operational measurements, we recognize that it is slightly lower compared to the resonance within operation (19 Hz). On the one hand, this effect could be argued with a centrifugal stiffening due to an axial compressive force on the overhung rotor in the blower in the resonance case [47]. On the other hand, the deviation is only one hertz and thus within the tolerance of the measurement uncertainty. A foundation eigenfrequency at 31 Hz in  $z$ -direction appears beyond the first blower bending mode shapes, but does not cause issues regarding the measurement signals at operation, probably because it is not excited by the rotor unbalance. Modes six and seven also do not affect the output signal in the same way compared to the first two bending modes. For this reason, they are not discussed in detail. Note that modes one to six show high damping ratios. This is probably

<sup>5</sup>measurement time: 5.12s, excitation frequency range: 0-3000 Hz.

caused by the foundation: When looking at the mode shapes (see for example Fig. 4.9), we recognize that the foundation seems to be part of the modes and the decoupling elements (high damping) are part of the shape movements. Following the investigations carried out as part of this work, the elastomeric elements of the foundation were replaced with air bellows to improve decoupling. Now, we have a closer look at the first two bending mode shapes due to

**Table 4.2:** Resonance frequencies  $f_i$ , damping ratio  $\theta$  and mode shapes of the blower test rig within the frequency range of 5 Hz - 60 Hz according to [89]

| Mode | $f_i / \text{Hz}$ | $\theta / \%$ | Shape                          |
|------|-------------------|---------------|--------------------------------|
| 1    | 9                 | 3,5           | Foundation mode in x-direction |
| 2    | 11                | 3,2           | Foundation mode in y-direction |
| 3    | 18                | 3,0           | Bending mode in x-direction    |
| 4    | 22                | 3,6           | Bending mode in y-direction    |
| 5    | 31                | 3,2           | Foundation mode in z-direction |
| 6    | 41                | 3,0           | Bending mode in x-direction    |
| 7    | 52                | 0,5           | Bending mode in y-direction    |

their influence on the system as described in Sec. 4.1.1. These are depicted in Fig. 4.9. Here, a three-panel projection including an isometric view of the blower test rig is depicted. The deformation within both modes is highlighted in orange. On the left hand side, the x-axis shape (18 Hz) is observed whereby the y-direction shape (22 Hz) is depicted on the right. The defined movements with slightly diagonal orientation are conspicuous. These are comparable with the rotor orbit alignments in Fig. 4.7. To sum up, both expected operational modes are validated by the experimental modal analysis.

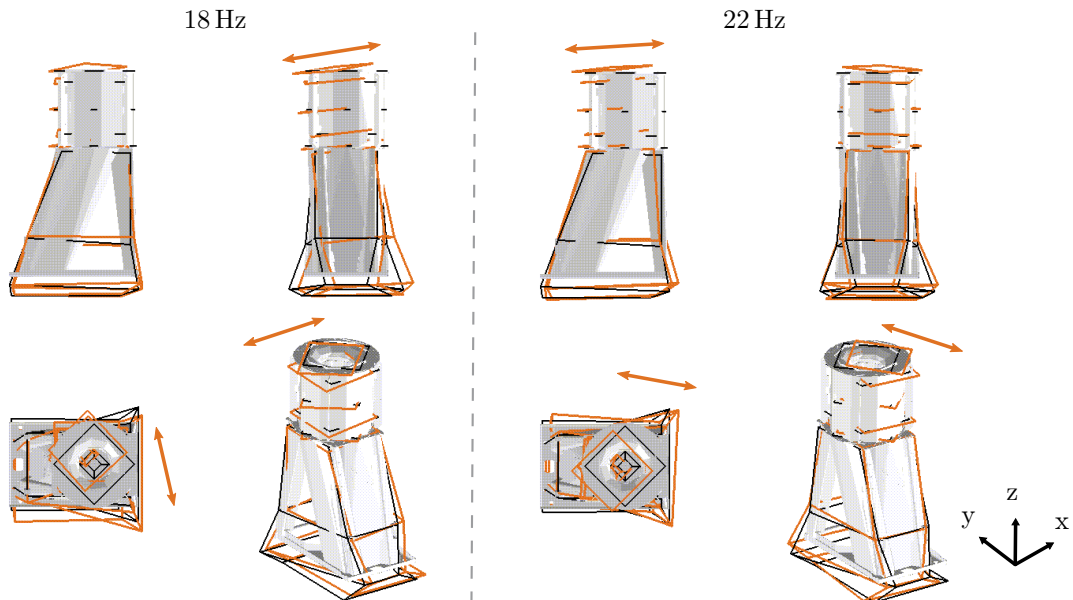


**Figure 4.9:** Experimental modal analysis results based on [89]. Left: Bending mode shape in x-direction at 18 Hz. Right: Bending mode shape in y-direction at 22 Hz.

### 4.1.3 Transfer Function Reciprocity

Besides the knowledge of mode shapes, linearity and reciprocity between housing and rotor is of big interest for the presented modeling approach. As discussed in Sec. 2.3.4, a hint for linearity generally exists, if two admittances  $Y_{ij}$  and  $Y_{ji}$  have the same magnitude. In this case,  $Y_{ij}$  and  $Y_{ji}$  are represented by  $Y_{\text{Housing, Rotor upper shaft end}}$  and  $Y_{\text{Rotor upper shaft end, Housing}}$ . This is justified since different model types must be characterized with respect to operational rotor forces by measuring at the outside housing. The test setup to investigate reciprocity is depicted in Fig. 4.10. Here, the automatic modal hammer AMimpact [83] was utilized. The system responses were gathered by triaxial piezoelectric accelerometers (Kistler 8688A). A Müller-BBM PAK front-end was used for signal acquisition and for building the transfer functions up to 1.6 kHz (0.5 Hz resolution). From this point on, the observed frequency range is restricted to that maximum.

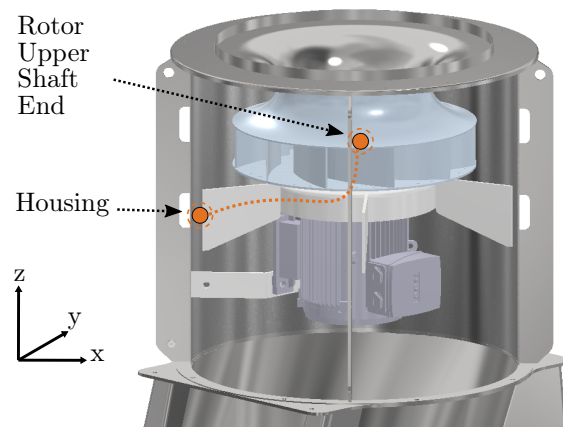


**Figure 4.10:** Test setup for an exemplary reciprocity measurement between the rotor upper shaft end (obscured by flow guiding coverage) and the housing based on [89]. Horizontally aligned excitation and measurement direction.

We chose sensor and impact position at the housing based on a strut connection between motor block and housing. Here, proper structure-borne transfer is ensured. The rotor excitation DoF was selected based on accessibility reasons. Based on that restriction, radial excitation is exclusively possible on the rotor upper shaft end. This shaft end is hidden by the impeller blades in Fig. 4.10 and depicted in Fig. 4.11.

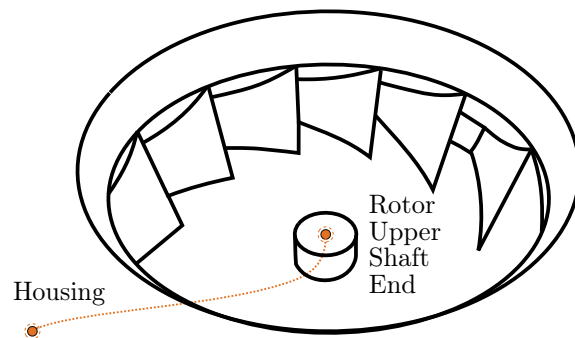


**Figure 4.11:** Top view on the test setup with impeller blades and the transfer path between rotor upper shaft end within the impeller and housing.

For better understanding of this special shaft extension within the impeller, Fig. 4.11 shows a top view of the rotor inside the blower. The upper shaft end of the rotor can be seen as measuring and excitation point. The results of both FRFs<sup>6</sup> are plotted in Fig. 4.12. Comparing them, we notice proper reciprocity for the most part of the observed frequency range. Though, within an area between 100 Hz and 400 Hz, the reciprocity is less satisfactory. This is also represented by the coherence which reaches its maximum at 500 Hz. The range with greater discrepancy between 120 Hz and 200 Hz is discussed in 5.2.3. Here, an advanced model is needed to describe the dynamic behavior between rotor and housing sensor position.

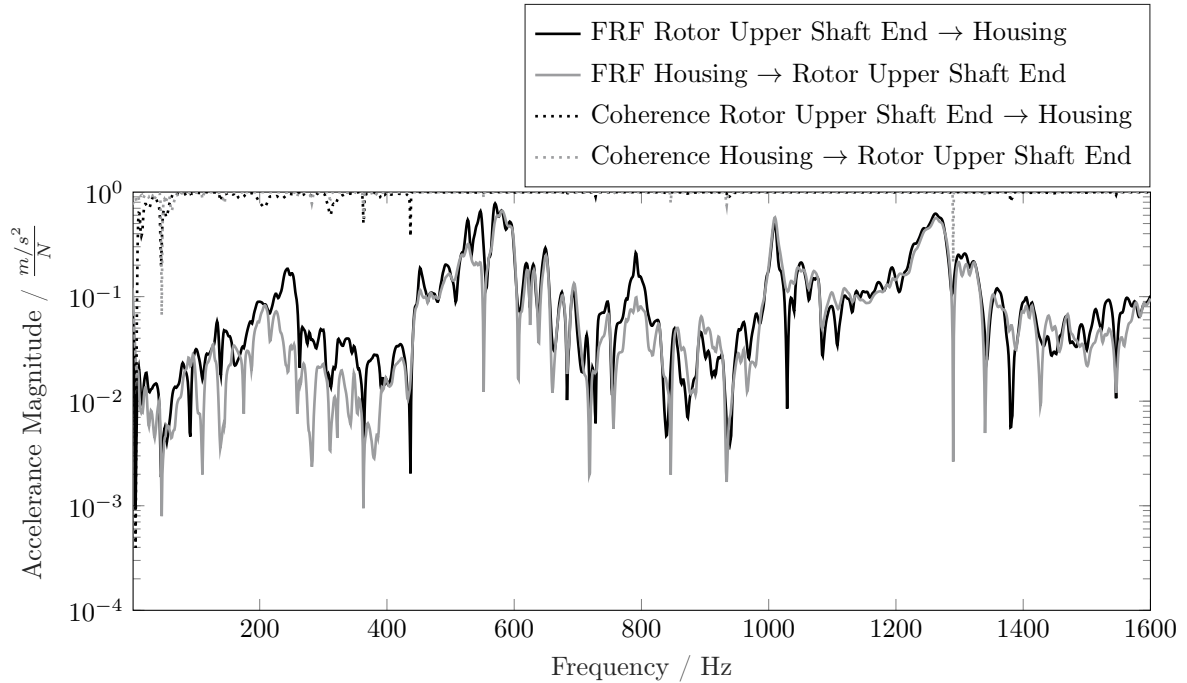


**Figure 4.12:** Frequency response accelerance magnitudes and coherences concerning reciprocity at rotor upper shaft excitation and housing measurement (black) and reversed (gray) based on the setup in Fig. 4.10 referring to measurements of [89].

#### 4.1.4 Summary

The presented blower test rig shows some specific phenomena concerning orthotropic elastic rotor support. Although vibration monitoring in the frequency range below 30 Hz is problematic due to resonances, the specified frequency range (30 Hz - 60 Hz) is in a suitable frequency range for monitoring, especially with the 11th and 22nd harmonic excitations. This is also shown by the transfer function in terms of reciprocity and coherence between rotor and housing over a wide frequency range. All resonances and associated mode shapes within the operating speed area including higher harmonic excitations must be kept in mind for the analyses. This high dynamic content even within the specified speed range qualifies the blower test rig as predestined, complex example for vibration monitoring utilizing hybrid dynamic models.

<sup>6</sup>housing excitation, upper shaft end measurement and upper shaft end excitation with housing measurement.

## 4.2 Pump Test Rig

As introduced in the flow chart (Fig. 1.1) in the beginning of this thesis, different types of methodology are shown at two applications. Our second application besides the blower setup is an oil pump test rig. Essentially, we use it to show a simple virtual force estimation approach for bearing condition monitoring at the end of this thesis (see Sec. 7.2.1). Furthermore, some bearing fault detection algorithms were evaluated utilizing an exemplary MEMS accelerometer (Sec. 3.4). The whole set-up is depicted in Fig. 4.13. Required measurement positions and transfer functions are delineated (1-3). The installed centrifugal pump is responsible for oil circulation within a cooling circuit of a traction transformer<sup>7</sup>. If the pump stands still because of a defect of its roller bearings, the whole train stops. Due to the importance of that component, exact and precise monitoring is essential. The aim is to find the force and the resulting acceleration induced by a roller bearing defect by measuring far away from the bearing - above the electrical junction box (9). Therefore, the MEMS sensor<sup>8</sup> system is built in a customized box (10). In Fig. 4.13, we see the pump and a pipe system which is fed by an oil compensation tank (not on the photo). The pump is driven via an inverter<sup>9</sup> and one can increase the resistance by a throttle (8) in a defined manner. The flow is principally verifiable by an ultrasound flow measurement system (4). Though, this measurand is not employed within this thesis, since focusing on stationary rotational speed is sufficient for the observations. In order to keep an eye on the temperature with a PT100 sensor, a measurement case (5) is integrated into the pipe system. The test rig is connected to the oil compensation tank via a hose (6) and can be deflated at the drain outlet position (7).

The pump rotor is supported by *fixed-free* bearings. Axial forces are transmitted by a double-row angular ball bearing (SKF type 3305 ATN9/C3). Additional radial support is ensured by a single-row deep groove ball bearing (SKF type 6304/C3). Further important information about the test rig is written in Tab. 4.3.

For the measurements, we utilize two types of accelerometers. As reference, the single-axis sensor (Brüel & Kjaer type 4397) is used in combination with a SKF Microlog GX data logger at 25.6 kS/s sampling frequency. This piezoelectric accelerometer is visible twice in Fig. 4.15<sup>10</sup>. Furthermore, a MEMS accelerometer<sup>11</sup> is used for the final application within the presented methodology. This sensor device is integrated in the box above the pump's electrical junction housing. Note, the global coordinate system is actually identical with the MEMS system. This system is rotated around the z-axis by  $-22.5^\circ$  compared with the test rig base plate and the pipe system.

**Table 4.3:** Technical specifications at of the centrifugal oil pump B2/120/80 at rated operating point based on [113].

| Motor Data                          |                        | Hydraulic Data            |   |
|-------------------------------------|------------------------|---------------------------|---|
| Power $P$                           | 2.8 kW                 | Discharge head $H$        | 17.7 m                                      |
| Current $I_N$                       | 4.4 A                  | Flow rate $Q$             | 30 m <sup>3</sup> /h                        |
| Voltage $U$                         | Y-440 V                | Oil temperature range $T$ | $-25^\circ\text{C} \dots 115^\circ\text{C}$ |
| Rated speed $n_N$                   | 3500 min <sup>-1</sup> |                           |   |
| Frequency $f$                       | 60 Hz                  |                           |   |
| Active power factor $\cos(\varphi)$ | 0.83                   |                           |   |

<sup>7</sup>A traction transformer transforms the overhead line voltage of a railroad line to the operating voltage of the locomotive.

<sup>8</sup>evaluated in Sec. 7.1.

<sup>9</sup>SINAMICS G120C, not on the photo.

<sup>10</sup>This sensor is also applied as reference for the MEMS sensor evaluation in Sec. 7.1.

<sup>11</sup>STMicroelectronics LSM6DSL, characterized in Sec. 7.1, 3332 S/s sampling frequency.

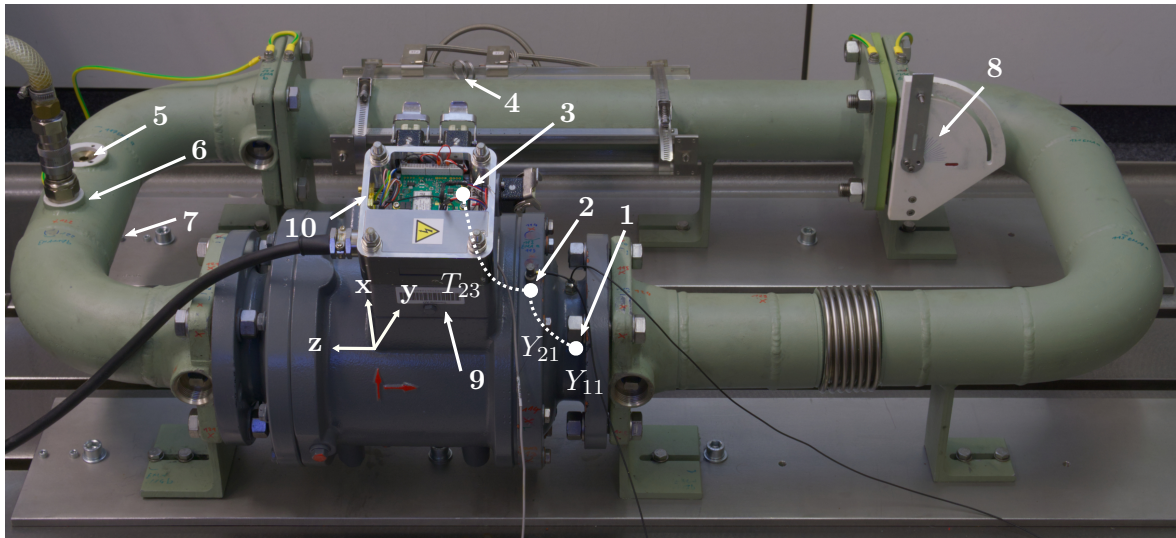


**Figure 4.13:** Oil pump test rig with bearing acceleration measurement position (1), housing acceleration measurement position (2), MEMS sensor and reference acceleration measurement position (3), ultrasound flow sensor (4), temperature measurement position (5), connection to oil compensation tank (6), drain outlet position (7) and throttle (8). Admittances  $Y_{11}$ ,  $Y_{21}$  and the transmissibility  $T_{23}$  are drawn in for future considerations in Sec. 7.2.1. The pump is powered by the electrical junction box (9). On top of its housing, a customized sensor box with wireless data transmission is mounted (10, cover omitted).

In Sec. 3.4, roller bearing fault diagnosis methods were already evaluated. These were investigated with respect to the limitations of an exemplary MEMS sensor system. All measurements concerning bearing faults were performed at the oil pump test rig. The implemented, synthetic outer ring bearing fault is depicted in Fig. 4.14. Although its lack of realism compared with real roller bearing faults, the defect is exactly defined by a groove (1.5 mm width) and definitely over-rolled by the balls. In the presented example, the the single-row ball bearing (SKF type 6304/C3) is prepared. The corresponding bearing seat is visible in Fig. 4.15 below the sensor position (1).

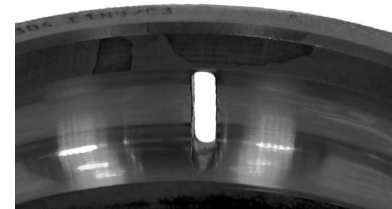


**Figure 4.14:** Exemplary, synthetic outer ring fault with 1.5 mm groove width at the single-row ball bearing (SKF type 6304/C3) prepared by [113]

At the pump test rig, we essentially have three measuring positions regarding operating accelerations and transfer functions. All three locations are depicted in Fig. 4.13. Position (1) is placed directly at the single-row deep groove ball bearing and position (2) is selected at the outside pump housing. Here, the shortest transfer path ( $Y_{21}$ ) to the bearing is ensured. At sensor position (3) we have the MEMS sensor and the same reference accelerometer glued as chosen for locations one and two. Both positions and the transfer function (white dotted line) are depicted in Fig. 4.15. Here, we see the right disassembled flange including the bearing seat below sensor position (1).

Now, the pump test rig's vibration will be evaluated. In order to explain all fundamental frequencies which occur in operation, specific characteristics need to be known.

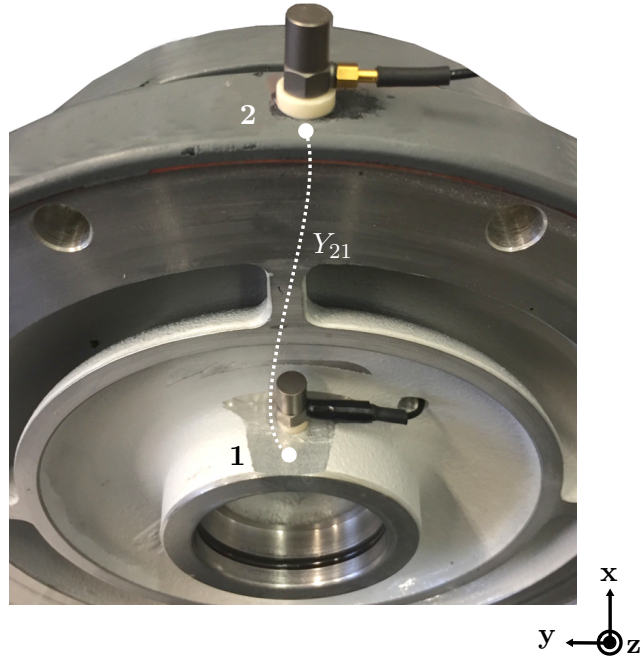


**Figure 4.15:** Disassembled right pump flange of the test rig in Fig. 4.13. Partial view of the single-row deep groove ball bearing location (1) and the housing acceleration measurement position (2). The drawn admittance (white dotted line) and the sensor positions are required in Sec. 7.2.1.

During operation, impulse response frequencies caused by the blades of impeller and flow guiding elements are observable. According to [57], based on hydraulic forces, the *blade pass frequency* ( $f_{\text{BPF}}$ ) appears in the vibration signal of centrifugal pumps:

$$f_{\text{BPF}} = n_{ib} \cdot f_n \quad (4.7)$$

with rotational frequency  $f_n$  and number of impeller blades  $n_{ib}$ . Impulse forces appear due to loading and unloading of the impeller blades. Particularly, they arise when passing stationary components of the housing during each turn of the rotor.

Furthermore, there is the *blade rate frequency* ( $f_{\text{BRF}}$ ):

$$f_{\text{BRF}} = \frac{n_{ib} \cdot n_{fb}}{E} \cdot f_n, \quad (4.8)$$

with number of flow guiding blades  $n_{fb}$  plus  $E$ , the greatest common divisor of impeller blades and flow guiding blades. Usually, the amount either of impeller- or flow guiding blades is odd. If their number were both even, more than one pair of blades would cross at the same time during rotation. This would lead to pronounced pulsation effects and must be absolutely avoided. Due to this context, the factor  $E$  appears in Eq. (4.8). In the presented example, that constellation expressed itself in seven impeller blades and eight flow guiding blades of the housing (see Fig. 4.16 and 4.17). Consequently, the following frequencies can appear at operation:

$$\begin{aligned} f_{\text{BPF}} &= 7 \cdot f_n \\ f_{\text{BRF}} &= \frac{7 \cdot 8}{1} \cdot f_n = 56 \cdot f_n \end{aligned}$$



**Figure 4.16:** Oil pump impeller [113].



**Figure 4.17:** Oil pump housing partial view with flow guiding blades [113].

In Fig. 4.18, a spectrum of the healthy pump state is depicted. Here, the Fourier transformation of the MEMS sensor measurement above the electrical junction box is plotted. In this context, Röhrl [113] measured over a snapshot time block  $(0.615 \text{ s})^{12}$ . Essentially, the pump operated at steady state ( $58.3 \text{ Hz}$  rotational speed  $f_n$ ). Thus, we regard dominant peaks in the spectrum and find correlations between the frequency components and the pump geometry.

To begin with, an amplification can be seen at around  $175 \text{ Hz}$  belonging to a structural resonance<sup>13</sup>. Visible harmonics start with the seven impeller blades as well as the eight flow guiding blades. They are dominant based on multiples of the rotational speed. When going further along the frequency axis, the twofold of both blade peaks are conspicuous ( $14f_n$  and  $16f_n$ ). The oil is divided into the stator winding chamber and a surrounding flow cavity. This partition wall can cause these twofold frequencies. Furthermore, there are four additional chambers at the opposite pump side. These four *boundaries* and their duplicates are modulated around the impeller and flow guiding blade frequencies. As a consequence, additional peaks are visible at  $18f_n$ ,  $20f_n$ ,  $22f_n$  and below the  $14f_n$  (not marked). The frequency band in which the main resonances of the system are located can also be excited by the third harmonic originating from a modulation on the left side of the impeller blade pass frequency.

<sup>12</sup>As it will be discussed in Sec. 7.1, the acquisition time of the MEMS device is restricted to this value of  $0.615 \text{ s}$  due to low power wireless data transmission requirements. By observing a single snapshot, random discrete events are not eliminated by virtue of averaging. Proper averaging is not possible in this case by the MEMS, since all snapshots are recorded at intervals of  $30 \text{ s}$ . Unsteady flow processes would lead to increased noise in the resulting spectrum.

<sup>13</sup>see transfer function plot in Fig. 4.19 for details.

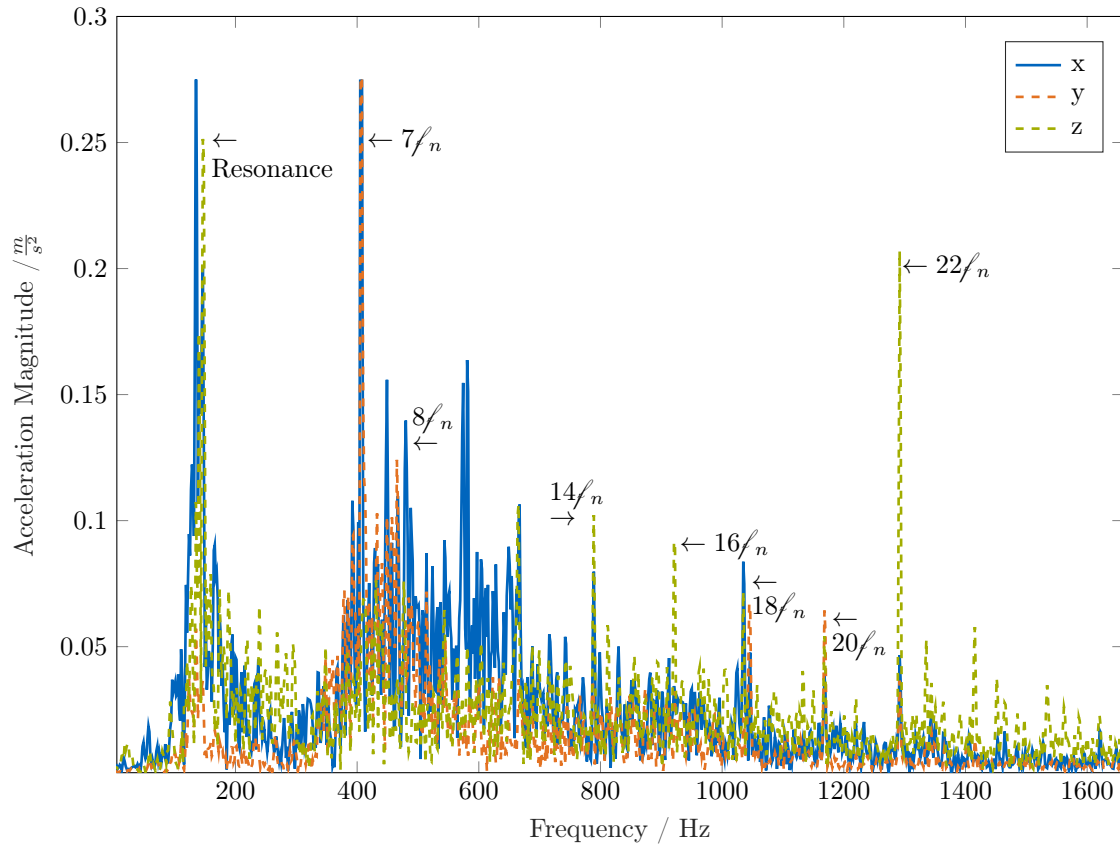


**Figure 4.18:** Vibration spectrum characterizing the healthy pump test rig state. Fourier transformation of a single wireless sensor system snapshot (MEMS accelerometer type LSM6DSL, 0.615 s measurement time at 58.3 Hz pump rotational speed  $f_n$ ). Measurement performed by Röhrl [113].

#### 4.2.1 Transfer Function Reproducibility

Within the scope of rotor system fault monitoring, there is always a transfer path between fault source and measurement position. Since the FRFs are utilized to find virtual forces and accelerations, these FRFs need to be known properly. By virtue of that, three pumps of the same type were investigated with respect to reproducibility of the radial x-direction transfer function. Here, we utilized the build-in pump (filled with oil) and excited the structure at position (3) with an impact hammer (Brüel & Kjaer 8204) and measured the response at the bearing position (1) (see Fig. 4.13, 4.15 for the positions). Comparing the transfer functions in Fig. 4.19, the reproducibility of all three pumps in magnitude and phase is striking. Excepting the frequency range around 700 Hz, the repeatability is more than satisfactory. This is an important outcome, as there is a lot of potential to change the system during dismantling and set-up including a new oil filling process at changing pumps within the test rig. Although all screws were tightened with the same torque<sup>14</sup> and the overall system was vented, small differences can arise concerning the filling degree. These mass changes and possibly stiffness discrepancies after the mounting procedure can be responsible for the visible lacks of reproducibility.

<sup>14</sup>installation information: Tightening torque of bolts between pump ↔ pipe system: 100 N m, tightening torque of bolts between pump flanges ↔ pump housing: 20 N m, tightening torque of bolts between electrical junction box ↔ pump housing: 10 N m.

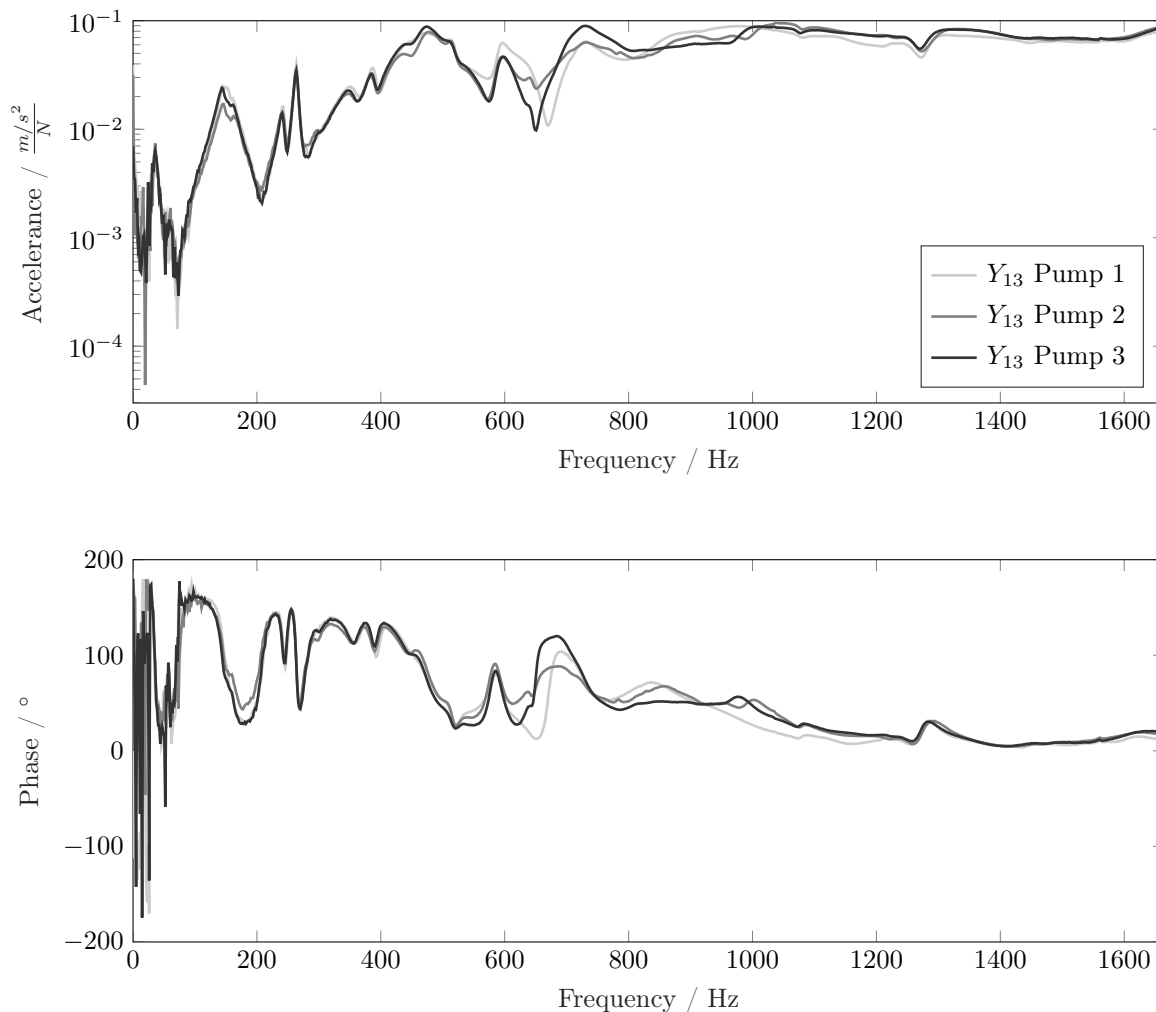


**Figure 4.19:** Radial x-direction transfer functions resulting from excitation at the MEMS sensor position (3) and acceleration response measurement at the oil pump bearing (1). See Fig. 4.13, 4.15 for the positions. The reproducibility is shown at three pump models of the same type.

### 4.2.2 Operational Output Reproducibility

Besides transfer function reproducibility, the influence of disassembling and reassembling the bearings must be evaluated. This is necessary in order to qualify the test rig concerning comparability of healthy and faulty bearing states. The general qualification of the test rig for roller bearing monitoring methods in Sec. 3.4 also required this step. Operational forces mainly occur at the rotor and are transferred over the bearing position. This bearing position is not accessible by utilizing a classical impact hammer. Hence, the comparison of operational vibration signals after a disassembling and reassembling procedure provides an additional statement about transfer function reproducibility. Here, we measured the operational acceleration in all three sensor axes using three monoaxial Brüel & Kjaer 4397 sensors and regarded the space absolute value of these three axes. In this context, we evaluated scalar values according to the statistical indicators of VDI3832 [140]. These indicators were observed at healthy state before and after installation of a defective bearing in the interim. Specifically, we compared Root Mean Square (RMS) value, Crest Factor and kurtosis<sup>15</sup> of these two healthy states over the entire reference sensor bandwidth of 25.6 kHz. The measurements

<sup>15</sup>explanation see Sec. 3.4.1.

were recorded for 30 s and broken down into 10 blocks of 3 s each. We performed the FFT over these blocks and regarded the averaged spectrum of these 10 samples up to a frequency of 500 Hz. This additional frequency spectrum is plotted in Fig. 4.20. The measurements were performed in dry run in order to avoid errors due to differing flow influences at possible venting deviation of the test rig. Furthermore, four days were allowed to elapse between the first and second measurement.

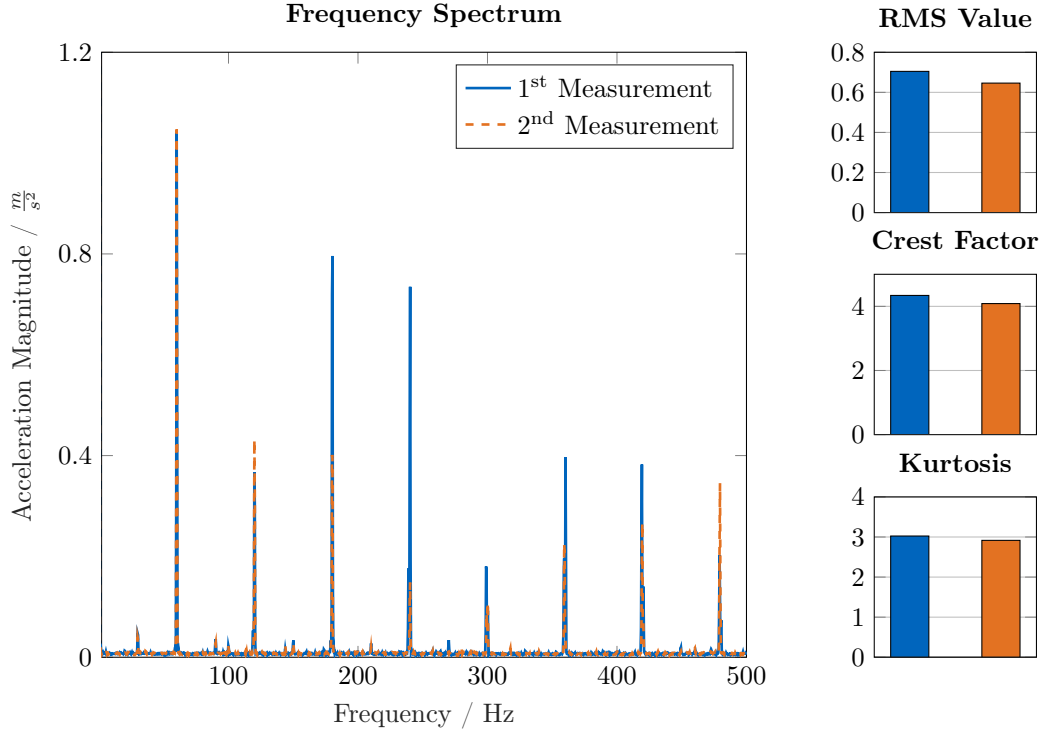


**Figure 4.20:** Comparison of two operational measurements at healthy bearing states concerning reproducibility based on [113]. The measurements were performed before (blue plots) and after (orange plots) installation of a defective bearing in the interim at dry run. Note that the bearing was healthy at both measurements, before and after mounting the defective one. The space absolute value of x, y and z-direction (three times monoaxial sensor type: Brüel & Kjaer 4397, 58.3 Hz rotational speed) was regarded here.

The first and second results of all three scalar values differ from each other by less than 10%. When examining the spectrum, it is difficult to distinguish between both measurements at the fundamental frequency and its first harmonic (first and second peak). Conversely, the higher harmonics show larger differences. Though, the whole investigated frequency range up to 25.6 kHz is captured by the scalar values. Therefore, we attribute additional importance to them and classify the results as reproducible.

### 4.2.3 Temperature Influence

During rated operation of the oil pump test rig, 2.8 kW are consumed by the motor. This power over time is converted into mechanical work with thermal energy. The total amount is divided into flow, kinetic and dissipation work. Due to low flow speed and pressure differences within the pump test rig, the most of consumed power during operation time is converted to dissipative thermal energy. By virtue of this effect, the test rig heats up very fast. In our measurement example, the temperature increases from 36 °C to 82 °C during an operation time

of 30 min. Linear temperature rise by this measurement is not assumed, but the approximated temperature increase speed is known. Based on this information and an acquisition of 60 MEMS sensor snapshots within an operating time of 30 min, a Fourier transformation on every snapshot was performed and the result was plotted in Fig. 4.21. When looking at the plot in detail, we see the magnitude slightly decreasing, especially in the second half of the operation time. This effect mainly occurs in the lower frequency range. The amplitude decrease can be explained by declining oil viscosity at rising oil temperature. The lower oil viscosity reduces the axial pump resistance due to diminished displacement work. Because of this lower resistance, the restoring axial rotor force decreases. Thus, the fixed bearing is pressed less into the seat and consequently impact forces caused by bearing faults are also reduced. Note, the exemplary bearing fault (Fig. 4.14) was implemented to see the temperature effect based on proper excitation at operation. However, within the first ten minutes of pump operation, we ensure quasi-stationary condition concerning the vibration amplitude, although the temperature course was not exactly measured. In this time section, all stationary operational measurements for this thesis are taken. Furthermore, note that temperature sensitivity effects of the applied MEMS sensor are evaluated separately in Sec. 7.1.2. Doubts concerning possibly temperature cross-correlations can be eliminated there.

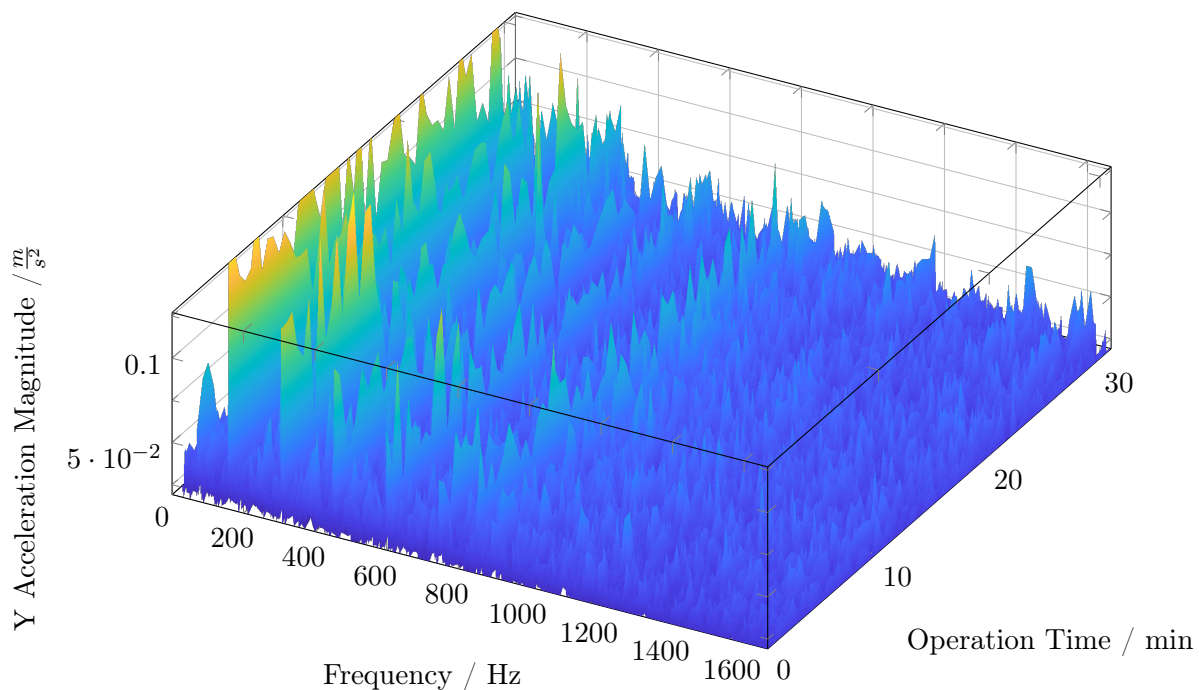


**Figure 4.21:** Envelope spectrum of 60 snapshots at stationary rotational speed performed with a wireless MEMS sensor device (LSM6DSL) at the pump test rig in axial z-direction at 58.3 Hz rotational speed. The measurements were performed by [113] with an exemplary bearing fault (6304-A-II). The temperature increased from 36 °C to 82 °C during the snapshots within 30 min.

#### 4.2.4 Summary

The oil pump test rig is successfully qualified for virtual sensing applications with respect to bearing diagnosis. Therefore, the main peaks within the operational vibration spectrum can be physically justified even when utilizing a MEMS sensor system. The transfer function reproducibility is satisfactory determined at three different pumps of the same type after disassembling and reassembling. Also, broadband indicators as RMS value, crest factor and kurtosis show proper repeatability when measuring at operation. Based on increasing

temperature of the pump medium during operation and the slightly decreasing vibration amplitudes with the operating time, a time window with stationary operating conditions is defined.

## Part II

# Hybrid Dynamic Substructuring and Modal Expansion



## Chapter 5

# Hybrid Dynamic Modeling

Complex systems are not easy to model strictly numerically or experimentally. Our approach to deal with that problem is a hybrid solution. In this chapter, we propose a step-by-step technique which is demonstrated on the exemplary blower application. Therefore, the entire system is divided into the sub-components rotor and housing. Firstly, the rotor is modeled numerically by a reference simulation based on a detailed finite element simulation (Sec 5.1.1). Building on these results and an experimental validation, a rotor model with reduced DoF is created (Sec 5.1.2). We aim to reach an efficient rotor model with a small amount of DoF in order to get it suitable for monitoring applications. The content of Sec 5.1 with the entire rotor modeling technique has been published in [72]. Alongside, the housing is modeled in two ways. A simplified numerical solution as well as an experimental model are created (Sec 5.2.1). In Sec 5.2, the rotor is coupled with both housing types performing the Lagrange Multiplier frequency-based substructuring technique. To correct the resulting overall model estimate, we perform further FRF measurements at some locations of the complete blower set and then expand this dynamic information to the entire DoF set in Sec. 5.2.2. This modal expansion is based on the System Equivalent Model Mixing technique. Conclusively, the hybrid blower model is validated by frequency response measurements.

## 5.1 Rotor Modeling

To begin with the rotor modeling, we need an overview of the rotor type. This component is widely used in applications like blowers and pumps. It is depicted in Fig. 5.1. On the left, the mounted state shows the working principle within the blower, whereby the rotor sucks air from the top and blows it on a motor below. On the right, all main rotor parts are labeled. We see two bearing seats on the shaft, to support the overhanging rotor. Also on the shaft section, there is a bundle of laminations which belongs to the integrated cage motor. The transition between shaft and impeller blades consists of a thin circular disc, which is mainly responsible for the rotor's structural dynamics within the presented application. This blade will be challenging in terms of model set-up within this section. Eleven impeller blades are directly welded on this transition. These are covered by a flow guiding hood.

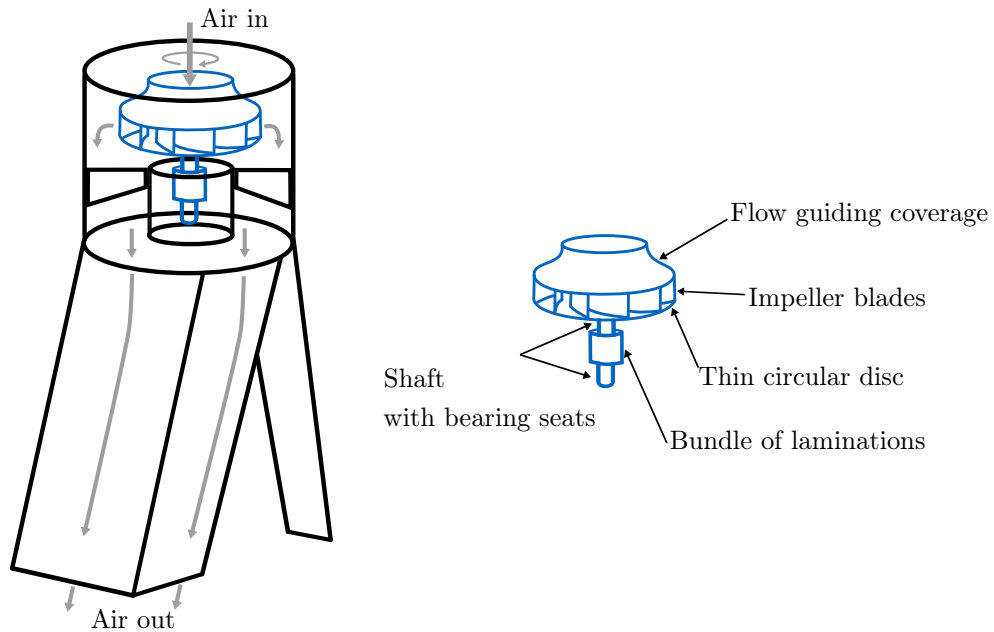


**Figure 5.1:** Blower application (left) with extracted rotor (right) and marked main sections based on [72].

### 5.1.1 Reference Simulation

The modeling is started by a reference finite element simulation (ANSYS<sup>®</sup> SOLID 187 tetrahedral volume elements). Therefore, a very fine mesh structure (575 718 DoF) was chosen. Here, we focus on proper experimental validation possibility. In the given case, boundary conditions are challenging. Due to this problem, the rotor is virtually hung up at the rotor disc during simulation in order to provide approximately *free-free* boundary conditions. In reality, for the experimental validation, elastic bands were utilized to hang up the rotor. The stiffness of these bands is measured and embedded as boundary condition in the simulation (see Sec. 5.1.3). This band support has different stiffnesses in axial and radial direction. These stiffnesses are needed by ANSYS<sup>®</sup> in form of a stiffness per surface to which the stiffness is linked. Therefore, the axial band stiffness is divided by the impeller underside surface in order to approximate the axial rotor support stiffness for ANSYS<sup>®</sup>. This area is assumed as axial *active surface* required by the ANSYS<sup>®</sup> simulation. The radial *active surface* is similarly implemented: For this purpose, the disk is virtually cut horizontally in the center along the rotor axis. The resulting cut surface is used twice as a surface for the connected radial "springs" of ANSYS<sup>®</sup>. These assumptions are made to obtain a base stiffness in the unit N/m<sup>3</sup> for ANSYS<sup>®</sup> to solve the eigenvalues. On these conditions, two first mode shapes were calculated at 81.6 Hz and 795.2 Hz) (Fig. 5.2). Note that the quasi-rigid low-frequency modes due to the support conditions were not regarded here.

Based on the applied boundary conditions, the rotor shows characteristic bending in the impeller disc area. Especially, the first mode bends only at this thin transition. Also within the second mode, we see pronounced deformation of the blade. Here, the upper bearing seat is part of the deflection. Although, the second mode will change significantly in installed condition, it is a structural property of the extracted rotor and will be used for experimental validation. These results serve as an orientation for the subsequent reduced model creation.

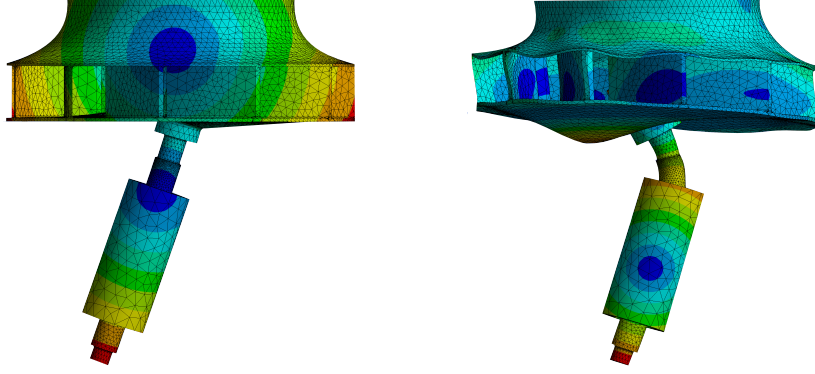


**Figure 5.2:** First two rotor bending mode shapes based on the reference simulation (very low modes due to soft supports not regarded). Left: 81.6 Hz, right: 795.2 Hz based on [72].

### 5.1.2 Reduced Simulation

Now, a rotor model is developed which describes its main dynamic properties along the rotary axis on a minimal DoF set. We are aiming at building a model containing a small number of DoF in order to use it for monitoring purposes. In that case, the model should be small so that it can run fast and with small computation resources for instance on a microprocessor. Hence, we will develop a model based on simple one-dimensional elements having four DoF per node (two horizontal displacements and two bending rotational DoF). Due to the aspired monitoring solution, where the fault forces mainly occur in horizontal direction, we concentrate on four DoF per element. Only two radial displacements and two axial bending DoF are regarded. Therefore, the association of elements is primarily modeled as a one-dimensional Timoshenko beam. Every beam element is structured as

$$\mathbf{u}_e = \begin{bmatrix} u_x \\ \psi_x \\ u_y \\ \psi_y \end{bmatrix} \quad \begin{cases} u_x, u_y : \text{translational DoF} \rightarrow \text{radial displacements} \\ \psi_x, \psi_y : \text{rotational DoF} \rightarrow \text{bending around the rotor axis} \end{cases} \quad (5.1)$$

For this reduced simulation, the rotor is divided into four sections. These sections are selected based on their likewise geometries. Parts should be found, where similar discretization methods are applicable. These belong mainly to three rotor substructures (shaft, disc and adjoining upper impeller part). Here, the upper impeller part is discretised differently concerning rotor blades and flow guiding coverage. In Fig. 5.3, we see the MATLAB<sup>®</sup>-based rotor visualization of the presented blower rotor example. In this figure, the shaft which is based on the beam model as well as the flow guiding coverage are rendered in blue, whereby the thin circular disc is highlighted in orange. Note that the beam elements used to discretize the cylindrical shaft (Fig. 5.3) have different lengths. Although this dimension  $dz$  is initially set to 20 mm, we enforce, an optimal element distribution along the shaft sections and prohibit diameter jumps that overlap elements. Fig. 5.3 shows a schematic side view of the discretized rotor. We begin with the rotor shaft section. The rotor coordinate system starts at the lower shaft end. Here, the z-axis points along the rotor axis, upwards to the impeller. x- and y are radially orientated as depicted in Fig. 5.3. The simulation is performed in MATLAB<sup>®</sup> under the same boundary condition assumptions as in Sec. 5.1.1.

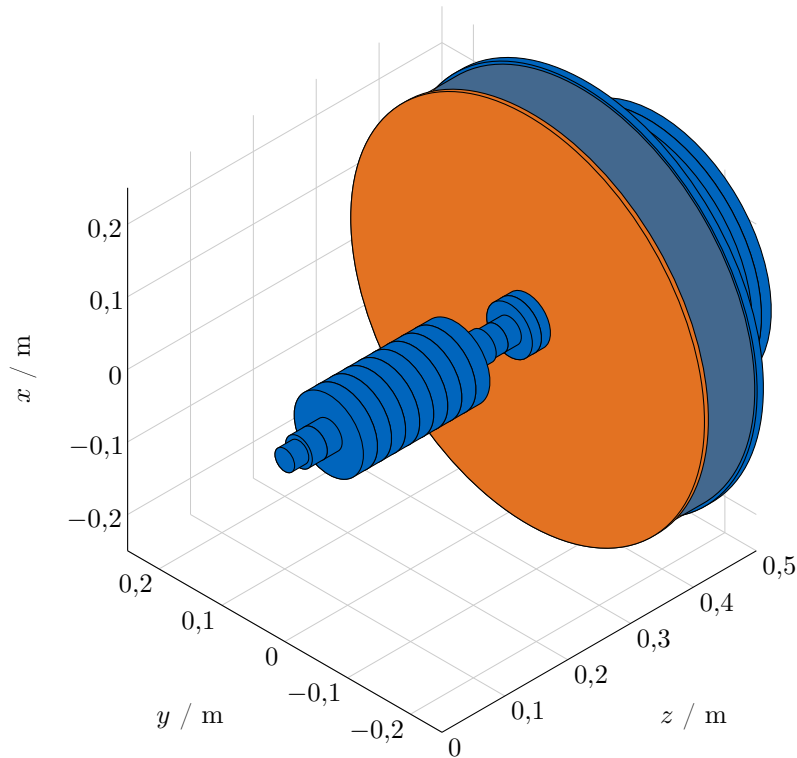


**Figure 5.3:** Isometric blower rotor visualization based on the axial discretization of the reduced model. The underlying cylindrical Timoshenko beam elements (blue) are distinguished from the thin circular disc (orange).

### Rotor Shaft Discretization

We outlined the rotor shaft by Timoshenko beam elements along the rotor axis [131]. This is easily conceivable due to simple cylindrical shaft sections. Therefore, cross-sections and geometrical moments of inertia are decisive. In this context, the general axial ( $\mathbf{I}_x, \mathbf{I}_y$ ), polar ( $\mathbf{I}_p$ ) and mixed ( $\mathbf{I}_{xy}$ ) geometrical moments of inertia [6], are specified as

$$\mathbf{I}_x = \int_A y^2 dx, \quad \mathbf{I}_y = \int_A x^2 dy, \quad \mathbf{I}_p = \mathbf{I}_x + \mathbf{I}_y \quad \text{and} \quad \mathbf{I}_{xy} = - \int_A xy dA. \quad (5.2)$$

Within this section, the geometrical and polar moments of inertia  $\mathbf{I}_x = \mathbf{I}_y$  and  $\mathbf{I}_p$  are represented based on ring and circle sections (outer and inner diameter  $D_a, D_i$ ) as

$$\mathbf{I}_x = \frac{\pi \cdot (D_a^4 - D_i^4)}{64}, \quad \mathbf{I}_p = 2 \cdot \mathbf{I}_x \quad \text{and} \quad \mathbf{I}_{xy} = - \int_A xy dA = 0. \quad (5.3)$$

In case of the shaft:  $D_{i,circle} = 0$ .

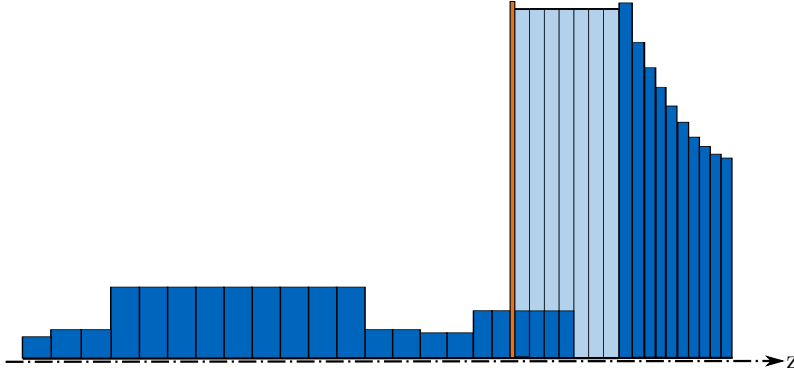


**Figure 5.4:** Schematic sectional view of the axially discretized rotor (partially cut) with impeller disk (orange). The light blue section contains the impeller blades in the area where they are not covered with the flow guiding coverage (dark blue right end of the rotor).

### Impeller Blades Discretization

Regarding the impeller blades, there are sections with constant cross-sectional areas and sections with variable cutting surfaces depending on the  $z$ -coordinate along the rotor axis. We start with the constant interfaces which border on the circular disc (Fig. 5.5). These blades are described by their inner and outer radii  $r_1$ ,  $r_2$ . Essentially, they are ring sections ranging from  $r_{ti}$  to  $r_{vi}$  over the angle  $\varphi$  with circle center  $M_s$ .  $D$  characterizes the intersection point on a virtual line  $\bar{y}$  in the middle between  $r_1$  and  $r_2$ . Considering a single blade, we recognize a coordinate system rotation to the individual blade  $\eta - \xi$  system. In order to calculate the blades' geometrical moments of inertia, their cross-sectional area as well as the distance  $\bar{y}_S$  between their centroid  $S$  and the individual blade radial coordinate system center  $M_S$  are needed. Based on these parameters, the geometrical moments as well as the volumes along the rotor axis are defined. Particularly, they are derived in App. A.1. Note that there is also a section with varying rotor blade cross-sectional area along the rotor axis. The according geometrical correlation is figured out in App. A.2.



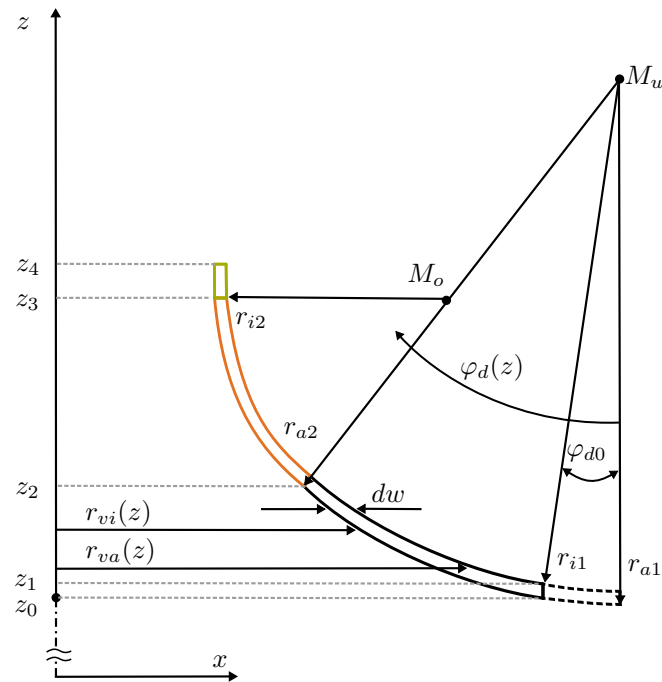


**Figure 5.6:** Partial section view of the rotationally symmetric flow guiding coverage in x-z plane based on [72]. All necessary parameters for the moments of inertia calculation are shown.

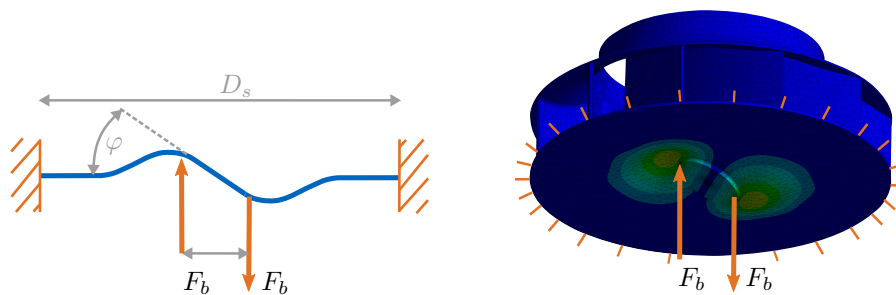


**Figure 5.7:** Load condition set-up according to [72]. Left: Scheme of the deformed impeller disc with circumferential, rigid clamping at the outer diameter  $D_s$ . The axial bending moment generating forces  $F_b$  act at a distance of  $d$  and evoke a bending angle  $\varphi$ . Right: Same presentation as impeller finite element model (ANSYS®) including clamping and bending forces.

focusing the circular plate (Fig. 5.2). Therefore, two oppositely orientated unit forces  $F_b$  are applied at the interface between rotor shaft and impeller at a distance of  $d$ . Meanwhile, the impeller is rigidly clamped circumferential at the outer disc diameter  $D_s$ . We get a resulting bending moment  $M = F_b \cdot d$  and an angle  $\varphi$ . Based on these values, the bending stiffness  $k_b = M/\varphi$  is obtained which is representative for the transition between shaft and impeller - especially relevant for the first two mode shapes. Conversely, the lateral stiffness is assumed to be close to infinity because the plate has almost no shear flexibility. We call its stiffness  $k_{inf}$ . Therefore, the stiffness value of the adjoining shaft element (diameter  $d$ ) is multiplied with  $10^6$  in order to approximate  $k_{inf}$ . This is just an approximation to get an idea of plate's stiffness against lateral force since infinite large values are unfavorable within numerical simulations. To complete the element assembling, we neglect the coupling terms between rotational DoF  $\psi$  and translational DoF  $u$ . Considering the one-dimensional Timoshenko beam approximation, a node between shaft and impeller plate was taken and occupied by these assumed values. Finally, the element lateral forces  $F$  and bending moments  $M$  of this impeller disc element are written as

$$\begin{bmatrix} F_x \\ M_x \\ F_y \\ M_y \end{bmatrix} = \begin{bmatrix} k_{inf} & 0 & -k_{inf} & 0 \\ 0 & k_b & 0 & -k_b \\ -k_{inf} & 0 & k_{inf} & 0 \\ 0 & -k_b & 0 & k_b \end{bmatrix} \begin{bmatrix} u_x \\ \psi_x \\ u_y \\ \psi_y \end{bmatrix}. \quad (5.4)$$

Finally, the adjoining shaft node is connected to the impeller by this element stiffness matrix.

## Results

Using the model described above, the first two bending mode shapes are calculated by using the eigensolver of MATLAB<sup>®</sup>. These are located at 82.1 Hz and 813.0 Hz (Fig. 5.8). As for the orientation of the graphs shown, we see the bottom rotor end on the left<sup>a</sup>. Regarding the mode shapes, we can recognize two characteristic antinodes. In case of the first mode (blue), this bending point is located at the transition between shaft and impeller, evoked by the thin circular disc at 335 mm rotor axis z-coordinate.

<sup>a</sup>Note, only the symmetry line of the rotor is shown for clarity.

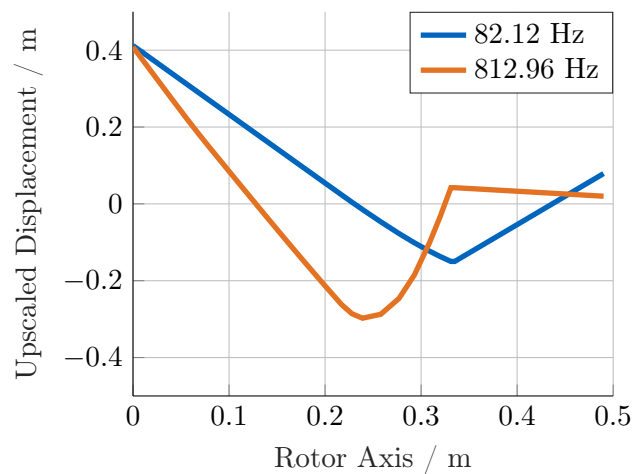


**Figure 5.8:** First (blue) and second (orange) axial bending mode shape of the reduced simulation according to [72]. The rotor axis is aligned horizontally.

The second mode shape antinode (orange graph) appears at the upper bearing seat ( $z = 270$  mm) - of course only within this free-free boundary condition scenario. In comparison with the results of the reference simulation (Fig. 5.2), we qualitatively recognize the same axis deflection. The first natural frequency is 0.6% higher and the second 2.3% higher than the

reference. The element types and sizes of the reduced simulation differ significantly from the reference finite elements net. This can be a justification for the deviations (see [70], p. 316). However, it is only a justification besides which all the approximations described above must nevertheless be taken into account. Despite the approximations, the deviation is still within an acceptable range.

### 5.1.3 Experimental Rotor Validation

In order to validate the simulation, an experimental modal analysis was performed with multiple inputs (x, y, and z-direction) as well as with multiple outputs<sup>1</sup>.

#### Test Set-Up

The excitation force ( $F_e$  in Fig. 5.9) was applied by an impact hammer (Brüel & Kjaer 8204) at the lower rotor end and the response was measured using triaxial piezoelectric accelerometers (Kistler 8688A). All signals were acquired by a Siemens LMS Test Lab System. We carried out the roving accelerometer method (3 sets with 7 accelerometers each) in order to obtain a complete column within the FRF matrix. The driving point FRFs were performed by hitting the shaft on the opposite side of the sensor. Afterwards, we employed the LMS PolyMAX algorithm [95] on behalf of modal parameter estimation.

For the experimental modal analysis, the rotor was supported with four elastic bands to realize *free-free* boundary conditions. The set-in angle  $\varphi_s$  of each band based on impeller maximum radius  $r_a$  and the start length  $l_0$  is depicted in Fig. 5.9. Furthermore, the elongation  $\delta l$  of the elastic bands due to gravity  $F_g$  of the rotor is shown. Thus, we get a set of radial, linearized stiffnesses to  $F_{ax} = F_g$  and  $F_r = F_g \cdot \tan(\varphi_s)$ . These results were also set for the simulation models' boundary conditions as described above.

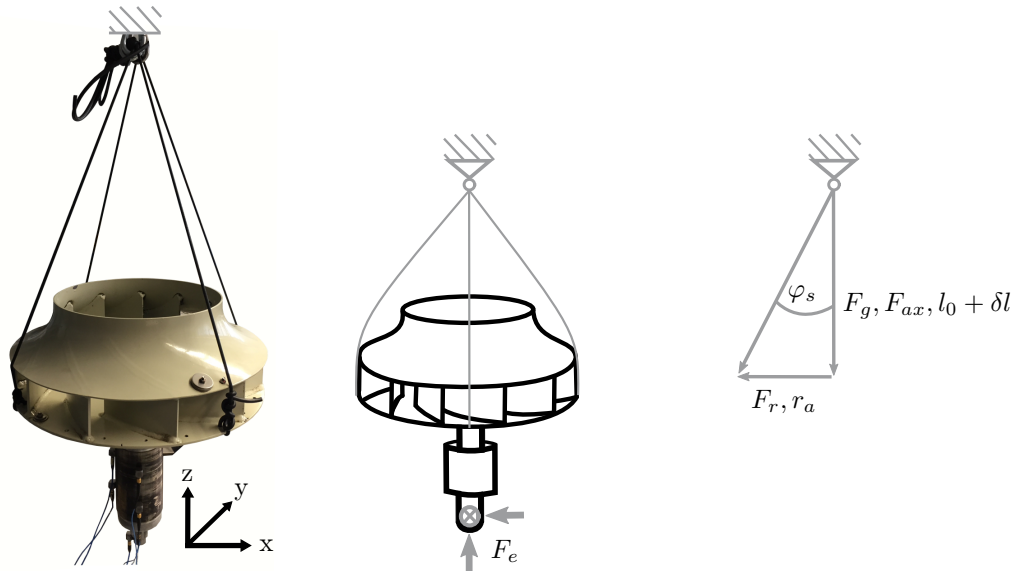


**Figure 5.9:** Left: Hung rotor suspended by means of four bands. The picture contains the first set of seven attached accelerometers. Middle: Schematic rotor drawing with marked position and direction of the impact excitation force  $F_e$ . Right: Sketch of acting forces along the geometry of an elastic band for the stiffness approximation. All figure content is based on [72].

<sup>1</sup>21 measurement DoF, spread over the entire rotor.

## Results

Based on this set-up, we firstly regard the horizontal FRFs. In Fig. 5.10, the constellation is depicted. The same excitation DoF at the lower shaft end are utilized as within the experimental modal analysis setup. As response DoF, we choose the protruding upper shaft end within the impeller (*pin*) to properly capture the expected bending modes. The results are plotted in Fig. 5.11. Here, we can see that the FRFs with respect to x- and y-direction are very similar due to the symmetric rotor properties. The two resonance peaks at  $f_1 = 79.9\text{ Hz}$  and  $f_2 = 810.3\text{ Hz}$  are noticeable. In particular, there is no dynamic in between. Because of a welded steel impeller structure, the damping ration is generally low (0.07 % at  $f_1$  and 0.52 % at  $f_2$ )<sup>a</sup>.

<sup>a</sup>estimation by the Polymax algorithm [95] utilizing all 21 measurement DoF.

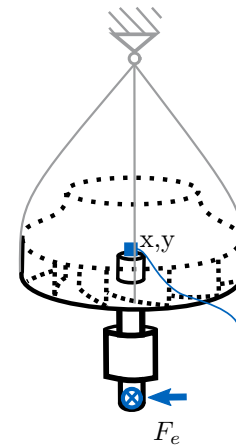


**Figure 5.10:** Test set-up with horizontal x- and y- excitation force  $F_e$  and appropriate measurement DoF concerning the FRF determination for Fig. 5.11.

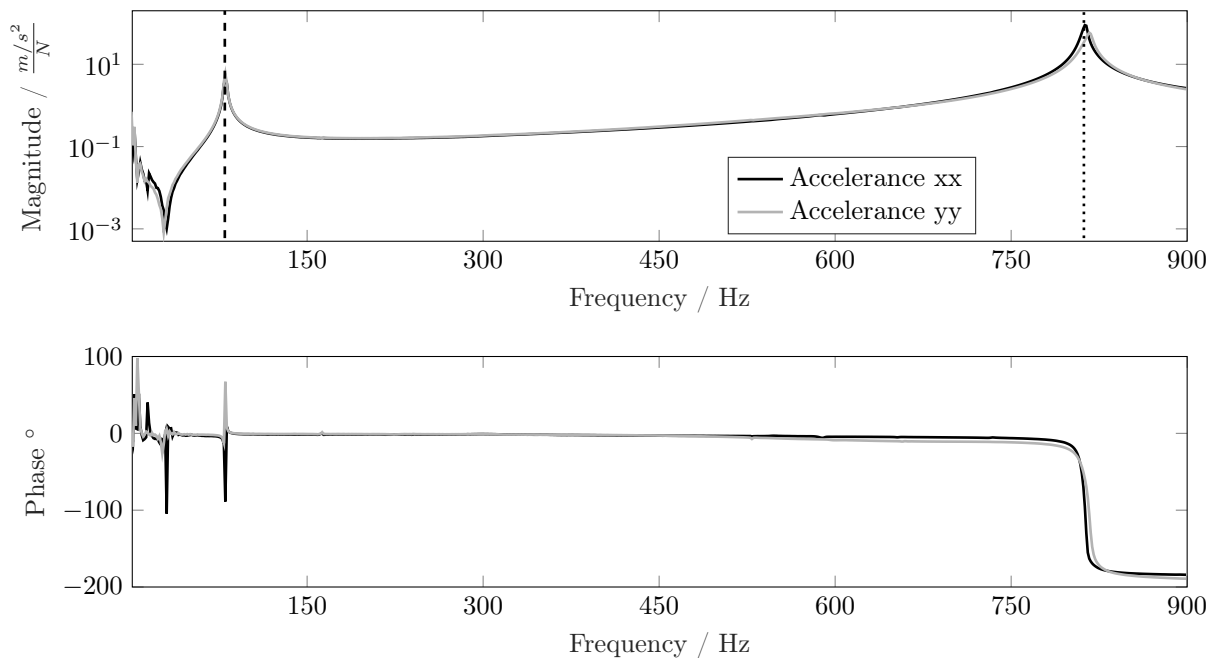


**Figure 5.11:** Frequency response functions in x- and y-direction (measurement set-up see Fig. 5.10). The first resonance at 79.9 Hz (dashed line) and the second resonance at 810.3 Hz (dotted line) are visible.

For the experimental modal analysis, the mode shapes are estimated based on all 21 measurement DoF. The modes are depicted in Fig. 5.12. Here, we can consider the first two mode shapes' x-axis projection. All measurement points are highlighted and the undeformed geometry is drawn in black to illustrate relative displacement. The reason why the measurement points are not placed along a line along the rotor shaft is the possibility of detecting torsional modes.

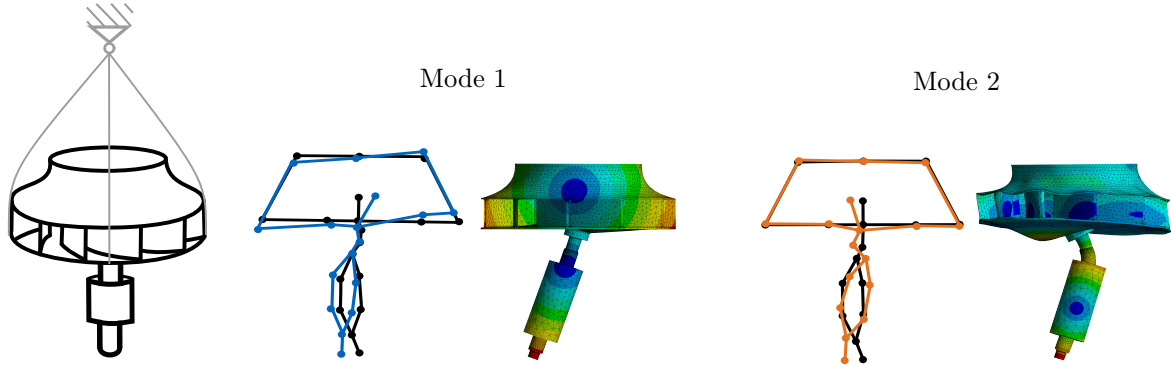


**Figure 5.12:** Experimental determined, axial bending mode shapes at resonance frequencies  $f_1$  (blue) and  $f_2$  (orange) according to [72]. The modes are compared with the reference simulation results.

Comparing the first resonance frequency of the different models with the experimental validation, we observe a deviation to the reference model of 2.2% and 2.8% to the reduced simulation. Basically, the mode shapes are very different (mode shape similarity based on the Modal Assurance Criterion: 7.2%) The mode shapes are only comparable at the transition between shaft and impeller. Here, the impeller tilting is striking. The big difference occurs at the upper bearing. It is rigid at the first mode and shows a pronounced bending at the second mode. The second considered resonance differs 1.9% from the reference and 0.3% from the reduced model. In this case, disc deflection is opposed to the first - in agreement with the simulation results. Furthermore, there is a likely antinode at the upper bearing seat position underneath the impeller.

A possible explanation for the frequency deviations is the mass distribution. Although reference- and reduced model masses were checked and corrected, especially at the bundle of laminations, the mass might be distributed unrealistically.

In addition, the coating is not included in the simulations. Also, the stiffness assumption at the impeller is only an approximation due to numerous reinforcing welding seams.

To sum up, the resonance frequency deviations are low and the mode shapes comparable. Despite the 136 DoF, a small number compared to the 575,718 elements of the reference, the reduced rotor model reflects the first two bending modes very well. The discrepancy is located within a range of 10%, which can be valued as standard deviation according to Klein ([70], p.316).

### 5.1.4 Summary

In this subsection, we created a validated base to set up efficient simulations for a widely used rotor type. The Timoshenko beam theory is combined with an analogous stiffness of a characteristic, circular impeller disc. The resulting small model represents the rotors' structural dynamics utilizing just 136 DoF. The model will be used in the following sections to assemble an entire model of the exemplary blower application. To sum up, all rotor resonances are opposed in Tab. 5.1.

**Table 5.1:** Axial bending resonance frequencies  $f_1$  and  $f_2$  of the reference simulation and the reduced model compared with the experimental validation according to [72]

| Resonance Frequencies | Reference | Reduced  | Experimental |
|-----------------------|-----------|----------|--------------|
| $f_1$                 | 81.6 Hz   | 82.1 Hz  | 79.9 Hz      |
| $f_2$                 | 795.2 Hz  | 813.0 Hz | 810.3 Hz     |

## 5.2 Frequency-Based Model Mixing

In this main section of Chap. 5, we show a hybrid approach for combining rotor and housing models. The basic principle using both numerical rotor and housing is based on [74]. This technique is supplemented by an experimentally determined housing which is coupled with the numerical housing. The coupling procedure is performed in the frequency domain representation, based on Lagrange Multiplier frequency-based substructuring and System Equivalent Model Mixing. The SEMM method is used in Sec. 5.2.2 for further *model updating* of the coupled system. This enhancement is needed since there are applications where the overall system dynamics can not be properly described by standard LM-FBS. Joint dynamics or bearing stiffnesses for example are hardly captured by LM-FBS because ideal compatibility and equilibrium condition is assumed at these interfaces.

The multi-stage technique consists of three parts:

1. A finite element rotor model with a small amount of (DoF) is created based on [72], (see Sec. 5.1.2). All DoF are used in order to calculate the fully occupied Frequency Response Function (FRF) matrix.
2. This entire FRF-matrix is coupled with the transfer functions of the housing. In a first analysis, the assembly is obtained by coupling the numerical submodel of the rotor and a very simplified numerical model of the housing. In a second analysis, the assembly is built by coupling the numerical rotor submodel with an experimental model of the housing.
3. Admittances of a collocated subset DoF of the entire, assembled system are experimentally determined and expanded to the FRF-matrix of the coupled model (numerical rotor submodel coupled with an experimental model of the housing) by all variants of the SEMM framework.

Finally, we get the complete, symmetrical FRF-matrix being full rank and containing structural dynamics of the entire, coupled system. Note, rotordynamic effects are not regarded here. For

the experimental validation, we use an exemplary transfer function, which is not included in the measurements for modal expansion.

### 5.2.1 Housing Model Estimation

The entire model is estimated in two ways. Each approximation consists of two coupled models (rotor and housing). Note that the *housing* consists of the motor block (stator) and the entire surrounding casing. In the first step, the housing is a rough, simplified numerical assumption. This numerical assumption was similarly published in [74]. In the second step, an experimentally determined housing is used for coupling with the rotor.

#### Numerical Housing Model

The numerical housing is approximated by a single-side supported, hollow, cylindrical single-dimensional Timoshenko-beam using 20 nodes with four DoF each (cylindrical component  $B$  at Fig. 5.13). Its wall thickness and clamping stiffness (springs in Fig. 5.13) are tuned to match the first eigenfrequencies and housing mass of the blower test rig. The first two modes stemming from the support stiffness occur at 9 Hz and 11 Hz<sup>2</sup>. By means of this very simplified model, a coarse assumption of the housing FRFs can be made. Based on this experimentally tuned model, the entire  $80 \times 80$  DoF model is coupled at the rotor connection point (lower bearing position node). We assume that the rotor is directly coupled at its two roller bearings ( $b_1$  and  $b_2$ ) with the single-dimensional Timoshenko-beam node at the lower bearing position ( $4 \times 4$  DoF). Generally, the housing is assumed to be fully rigid between  $b_1$  and  $b_2$  due to the massive motor block, which is part of the housing. Bearing- and support-stiffnesses between motor block and housing are neglected. Only displacements along the  $x$ ,  $y$  axis and rotations around the same two axes are considered. Compatibility and equilibrium condition between the lower bearing VP of the housing and the two bearing positions  $b_1$  and  $b_2$  of the rotor are enforced performing the LM-FBS method. The coupling of  $A$  and  $B$  is delineated by gray arrows in Fig. 5.13.

Thus, the solution for the coupled system is formulated with respect to the LM-FBS algorithm (see Eq (2.33)) as:

$$\mathbf{Y}_{\text{coupled}}^{(AB)} = \mathbf{Y} - \mathbf{Y}\mathbf{B}^T(\mathbf{B}\mathbf{Y}\mathbf{B}^T)^{-1}\mathbf{B}\mathbf{Y}. \quad (5.5)$$

In this case, the Boolean matrices for compatibility  $\mathbf{B}_c$  and equilibrium condition  $\mathbf{B}_e$  are the same since we use the same amount of excitation and response DoF. Therefore,  $\mathbf{B}_c$  and  $\mathbf{B}_e$  are simply represented by  $\mathbf{B}$ . Equation 5.5 uses the complex admittances  $\mathbf{Y} = \mathbf{Y}_{\text{uncoupled}}^{(AB)}$  with displacement responses to external forces of the uncoupled subsystems  $A$  and  $B$  in block diagonal form.

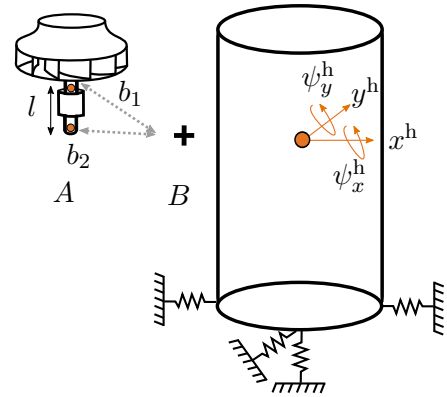


**Figure 5.13:** Numerical rotor model and housing representation as schematic subsystems  $A$  and  $B$  with two displacements and two rotations ( $x$ - and  $y$ -direction). The DoF at the rotor bearings ( $b_1$  and  $b_2$ ) are coupled with the housing at the lower bearing (Timoshenko beam node, orange).

<sup>2</sup>experimental modal analysis reported in 4.1.2.



used and the system responses were sensed by triaxial piezoelectric accelerometers (Kistler 8688A). A Müller-BBM PAK front-end was utilized for data acquisition<sup>3</sup>.

As described in Sec. 2.3, proper selection of impact and measurement DoF is required. In the presented example, we selected 19 impact- and 15 accelerometer-DoF from a set of 26 inputs and 18 outputs on the motor block. An exemplary selection of representative impacts and sensors is depicted in Fig. 5.14. The decision criteria was the specific impact and sensor consistency. The selected subset DoF should best describe the virtual point dynamics. Therefore, both specific and global consistency criteria were evaluated (see Sec. 2.3.4 for explanation). Based on a trade-off between the amount of DoF for proper controllability and observability of the system and sufficient specific consistency, the quality index was set to 68 %. All DoF below were discarded (orange line in Fig. 5.15). An overview over all specific impact and sensor consistencies is given in Fig. 5.14.

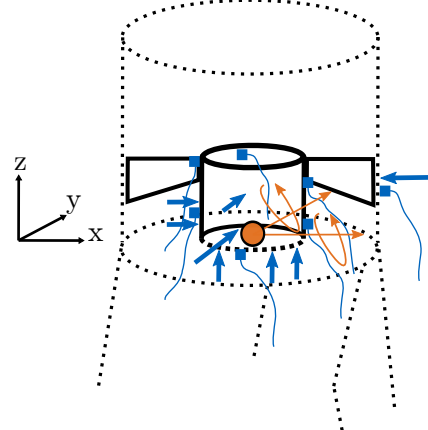


**Figure 5.14:** Blower housing section with a selection of representative, exemplary excitation arrows and accelerometers (blue). These are transformed on the lower bearing virtual point (orange). As shown in orange, in accordance with the rotor model, only horizontal displacements in x- and y-directions and the corresponding axial bending DoF of the virtual point are used for modeling. The  $2 \times 2$  housing DoF are labeled by blue but long arrows and one sensor.

<sup>3</sup>Note, for all frequency-based models, a bandwidth up to 1.6 kHz with 0.5 Hz frequency resolution was used.

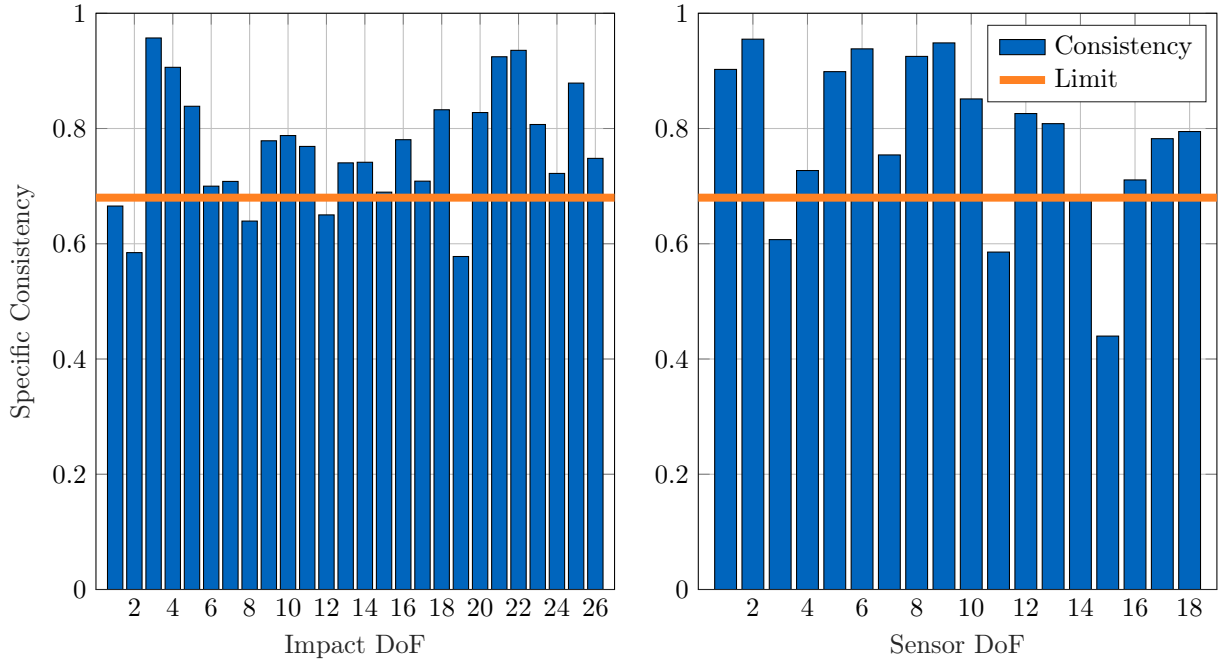


**Figure 5.15:** Specific consistencies of all utilized impact DoF (left) and all acceleration sensors (right). The chosen consistency limit is drawn in form of the orange line.

Besides the specific consistency, we can also observe the global consistency as quality index for evaluating the VPT by a chosen impact and sensor set. Fig. 5.16 shows the global consistency of all DoF before the specific selection for input DoF (left) and output DoF (right). After the selection of DoF for the VPT based on the specific consistency, we get an overall consistency which is depicted in Fig. 5.16. Here, significant improvement is observable especially in the lower frequency range up to 800 Hz. At around 960 Hz, a significant drop is noticeable especially in the overall force consistency. As described in Sec. 2.3.4, this can be an indicator for a flexible interface displacement mode. If the residual displacements

$$\boldsymbol{\mu}_u = \mathbf{u}_{1,2}(\omega) - \tilde{\mathbf{u}}_{1,2}(\omega) \quad \text{and forces} \quad \boldsymbol{\mu}_f = \mathbf{y}_{2,1}(\omega) - \tilde{\mathbf{y}}_{2,1}(\omega) \quad (5.8)$$

within the VPT are considered at this frequency, the residuum increases at two impacts and one sensor DoF. These DoF are all orientated in the same direction, located on a strut between the motor block and the housing directly at the connection between suspension and motor block. They therefore include the flexibility of the strut between motor block and the housing. Despite of this effect, they are kept in the VPT because there are no alternative practically accessible impact and sensor DoF inside the blower to provide proper controllability and observability.

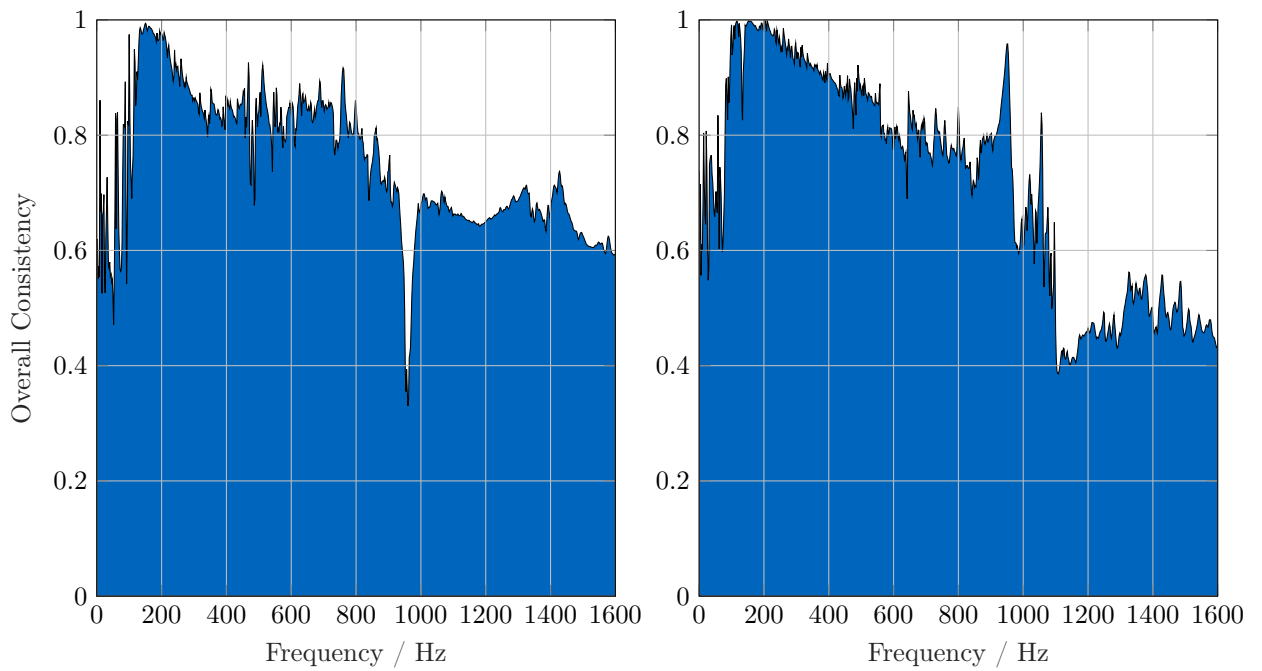


**Figure 5.16:** Overall impact- (left) and sensor consistency (right) of the entire measurement set-up.

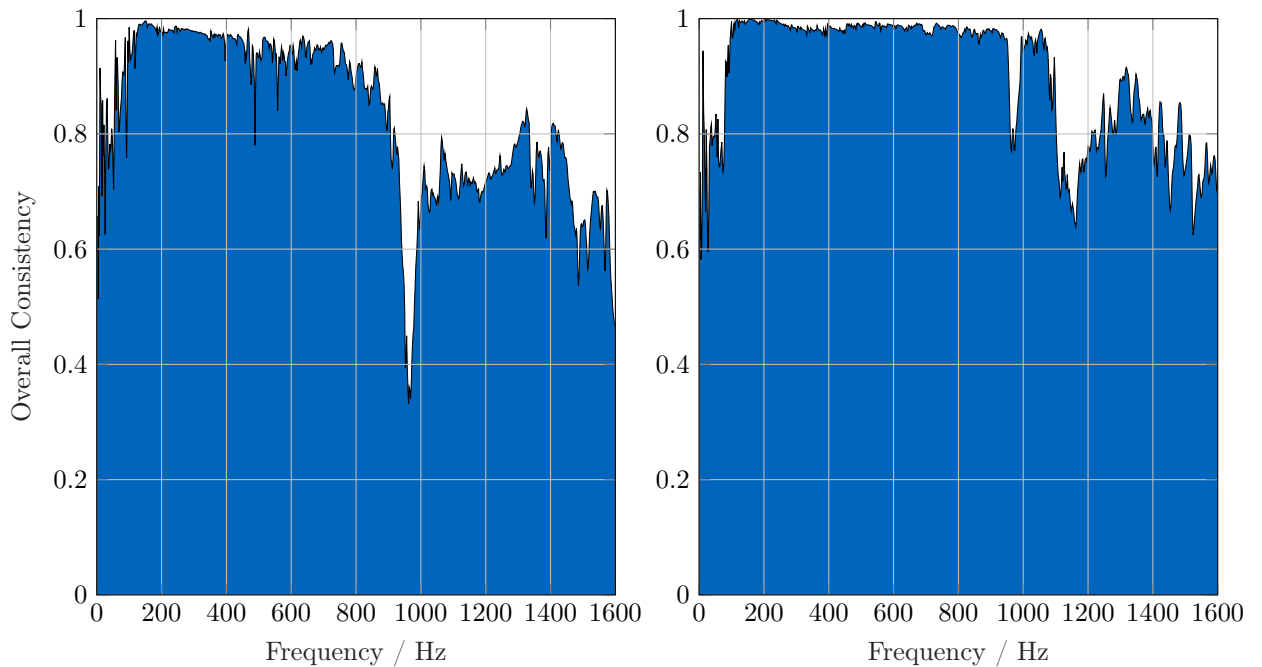


**Figure 5.17:** Overall consistency of the impact DoF (left) and the sensor DoF (right) at a selected subset DoF based on the specific consistencies (see Fig. 5.15).

Based on the selected subset DoF of impacts and sensors, we performed a VPT to each bearing containing radial displacements and axial bending DoF. The result is a  $6 \times 6$  FRF-Matrix implying one  $4 \times 4$  virtual point at the lower bearing seat (VP2) and the  $2 \times 2$  housing DoF. It is assembled as follows:

In order to assemble the experimental housing with the rotor, we perform the LM-FBS algorithm exploiting the Boolean matrix

$$\mathbf{B} = \begin{matrix} & \psi_y^{b1} y^{b1} \psi_x^{b1} x^{b1} & \psi_y^{b2} y^{b2} \psi_x^{b2} x^{b2} & \psi_y^{VP2} y^{VP2} \psi_x^{VP2} x^{VP2} y^h x^h & \\ \left[ \begin{array}{cccccccccccccccc} \dots & 1 & 0 & 0 & 0 & \dots & 0 & 0 & 0 & 0 & \dots & -1 & 0 & 0 & 0 & 0 & 0 \\ \dots & 0 & 1 & 0 & 0 & \dots & 0 & 0 & 0 & 0 & \dots & 0 & -1 & l & 0 & 0 & 0 \\ \dots & 0 & 0 & 1 & 0 & \dots & 0 & 0 & 0 & 0 & \dots & 0 & 0 & -1 & 0 & 0 & 0 \\ \dots & 0 & 0 & 0 & 1 & \dots & 0 & 0 & 0 & 0 & \dots & -l & 0 & 0 & -1 & 0 & 0 \\ \dots & 0 & 0 & 0 & 0 & \dots & 1 & 0 & 0 & 0 & \dots & -1 & 0 & 0 & 0 & 0 & 0 \\ \dots & 0 & 0 & 0 & 0 & \dots & 0 & 1 & 0 & 0 & \dots & 0 & -1 & 0 & 0 & 0 & 0 \\ \dots & 0 & 0 & 0 & 0 & \dots & 0 & 0 & 1 & 0 & \dots & 0 & 0 & -1 & 0 & 0 & 0 \\ \dots & 0 & 0 & 0 & 0 & \dots & 0 & 0 & 0 & 1 & \dots & 0 & 0 & 0 & -1 & 0 & 0 \end{array} \right]. \end{matrix} \quad (5.9)$$

After the coupling process, size  $\left(\mathbf{Y}_{\text{coupled}}^{(AB)}\right) = 142 \times 142$  DoF. One  $4 \times 4$  bearing-VP DoF appears twice. Thus, these duplicate DoF were dropped, so that afterwards size  $\left(\mathbf{Y}_{\text{coupled}}^{(AB)}\right) = 138 \times 138$  DoF.

### 5.2.2 SEMM-Based Modal Expansion

By coupling the rotor with two different housing models, we got a first numerical or hybrid approximation of the entire system dynamics. In this section, it is called *start model*. In order to refine the validity of the start model further on, the model is mixed with additional transfer functions of the entire system. Even when having a perfect start model performing LM-FBS, the bearing stiffnesses are not captured, since ideal transmission is assumed by compatibility and equilibrium condition between rotor and housing. We use the modal expansion technique SEMM (Sec. 2.4) to improve these interface dynamics. The frequency response measurements DoF on the entire system are depicted in Fig. 5.18. Note that all excitation DoF are in-plane with the rotor axis in order to avoid torsional excitation.

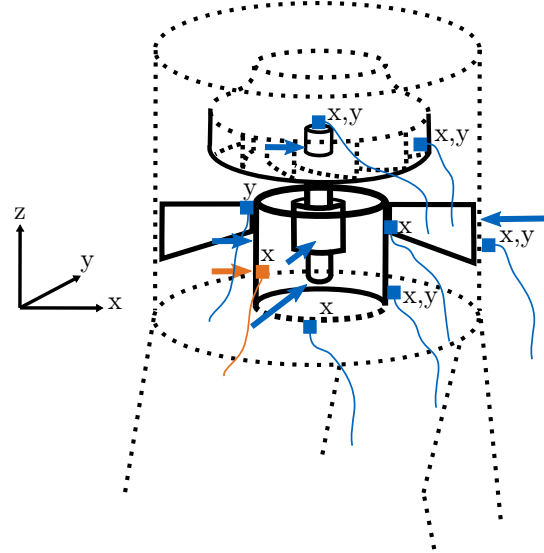


**Figure 5.18:** Partial blower representation with marked measurement set-up. Blue force impacts (arrows) and accelerometers are used for modal expansion. Note that the two longer arrows correspond to the outer housing excitation DoF. These are in-plane with the rotor axis and are at the same  $z$ -position as the accelerometer on the outer housing. All sensor axes incorporated herein are mapped in the figure. The orange set-up (accelerometer and impact arrow) represents the validation measurement point at the motor block center.

We assume that the assembly is very rigid along the radial direction at the location of the sensors and impacts. Therefore, it is expected that the measurements can be assumed to represent the force and displacements for a given position along the vertical axis of the assembly, as if the entire system would be beam-like (see Fig. 5.19). This allows us to impose compatibility conditions between the experimental measurement of the assembly (green string of nodes) and the start models of SEMM (blue and black nodes represent rotor and housing). Hence, the measured inputs and outputs and the DoF in the start model (numerical and hybrid) are *matching*. There is no need for a B matrix because the DoF in the measured FRFs have exact corresponding DoF in the start models (gray arrows).

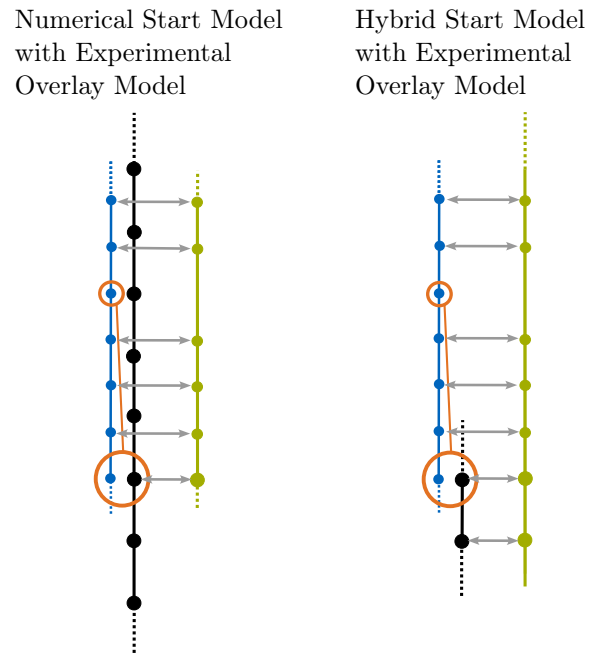


**Figure 5.19:** Scheme of the start models and the overlay model in form of one-dimensional beams (not all DoF depicted). Rotor (blue) and housing (black) are coupled at the orange marked DoF and combined with the green experimental model.

All expanded measurement DoF are outlined in Fig. 5.18 (blue). Note that these measurement DoF correspond to the *overlay* SEMM model. These DoF are a subset of the entire *start* and *parent* model, respectively, and are measured exactly against the corresponding DoF of the start model. The same sensor type and the automatic modal hammer as described in Sec 5.2.1 were utilized for FRF identification. In this case, Siemens LMS Test Lab was used for data acquisition to set up an experimental FRF-matrix with  $11 \times 5$  DoF containing eleven responses and five impacts in x- and y-direction as depicted in Fig. 5.18. This FRF-matrix represents the *overlay* or *experimental* model within the SEMM framework. Therefore, all these measured DoF are considered as boundary DoF for mixing with the start model. One strength of SEMM is the ability to expand the experimental determined dynamics to internal DoF at the rotor, which are not accessible for measurements. Especially in rotating machines, the rotor is often at least partially housed in the motor. The surrounding motor block needs to be stiff in order to transmit the drive torque to further periphery as the housing. Maximum controllability and observability should be reached by the presented experimental overlay model. Thus, we chose the experimental DoF on the motor, based on specific sensor and impact consistency criteria like within the VPT of Sec 5.2.1 but a VPT was not performed for the experimental model. Only output and input DoF possessing specific consistency  $>85\%$  were included in the overlay model. Within these DoF, exclusively horizontal directions (x, y) are picked. On that base, four sensor positions containing three x- and two y- direction measurements were selected on the motor block. One x- and one y-excitation were chosen. To ensure gathering coupling dynamics between the subsystems rotor and housing, two additional sensors are applied on the impeller. These contain two x- and y-directions. In order to enhance observability according to the sensor setup at all components (rotor and housing), two horizontal excitation and measurement DoF (x- and y-direction) were additionally placed at the outside housing. All calculated SEMM models were validated with an exemplary FRF acquired by the orange setup in x-direction (see Fig 5.18).

Generally, there are four primary extension levels to implement the SEMM method referring to [69] which were described in Sec. 2.4. We show the results by implementing all four variants on the presented application. The global SEMM start model is defined as:

$$\mathbf{Y}_{gg}^S = \begin{bmatrix} \mathbf{Y}_{ii} & \mathbf{Y}_{ib} \\ \mathbf{Y}_{bi} & \mathbf{Y}_{bb} \end{bmatrix}^S. \quad (5.10)$$

As mentioned in Sec. 2.4, the sub-admittances  $\mathbf{Y}_{ii}, \mathbf{Y}_{ib}, \mathbf{Y}_{bi}, \mathbf{Y}_{bb}$  do not necessarily have to be symmetric. They can also appear as  $\mathbf{Y}_{i_u i_f}, \mathbf{Y}_{i_u b_f}, \mathbf{Y}_{b_u i_f}, \mathbf{Y}_{b_u b_f}$  if there are different amounts of excitation forces  $f$  and response displacements  $u$  within the internal and boundary DoF. This is now the case. Therefore, the global SEMM start model is defined as:

$$\mathbf{Y}_{gg}^S = \begin{bmatrix} \mathbf{Y}_{i_u i_f} & \mathbf{Y}_{i_u b_f} \\ \mathbf{Y}_{b_u i_f} & \mathbf{Y}_{b_u b_f} \end{bmatrix}^S \quad (5.11)$$

According to the dimensions, we have to separate between the **numerical** and the **hybrid** start model.

The **numerical start model** serves as the parent model according to the SEMM framework with

- $\text{size}(\mathbf{Y}_{gg}) = 212 \times 212$  DoF,
- $\text{size}(\mathbf{Y}_{i_u i_f}) = 201 \times 207$  DoF,
- $\text{size}(\mathbf{Y}_{i_u b_f}) = 201 \times 5$  DoF,
- $\text{size}(\mathbf{Y}_{b_u i_f}) = 11 \times 207$  DoF,

- $\text{size}(\mathbf{Y}_{b_u b_f}) = 11 \times 5$  DoF.

The **hybrid start model** is defined as

- $\text{size}(\mathbf{Y}_{gg}) = 138 \times 138$  DoF,
- $\text{size}(\mathbf{Y}_{i_u i_f}) = 127 \times 133$  DoF,
- $\text{size}(\mathbf{Y}_{i_u b_f}) = 127 \times 5$  DoF,
- $\text{size}(\mathbf{Y}_{b_u i_f}) = 11 \times 133$  DoF,
- $\text{size}(\mathbf{Y}_{b_u b_f}) = 11 \times 5$  DoF

and the **experimental overlay model** is defined as  $\text{size}(\mathbf{Y}_{b_u b_f}) = 11 \times 5$  DoF.

The four implemented SEMM variations are:

**Basic SEMM** with reduction of the experimental dynamic information solely on the interface DoF. Problems due to fixed interface modes can occur. It is written as:

$$\mathbf{Y}_{\text{basic}}^{\text{SEMM}} = \mathbf{Y}_{gg}^{\text{S}} - \begin{bmatrix} \mathbf{Y}_{i_u b_f} \\ \mathbf{Y}_{b_u b_f} \end{bmatrix}^{\text{S}} \left( \mathbf{Y}_{b_u b_f}^{\text{S}} \right)^+ \left( \mathbf{Y}_{b_u b_f}^{\text{S}} - \mathbf{Y}_{b_u b_f}^{\text{E}} \right) \left( \mathbf{Y}_{b_u b_f}^{\text{S}} \right)^+ \begin{bmatrix} \mathbf{Y}_{b_u i_f} & \mathbf{Y}_{b_u b_f} \end{bmatrix}^{\text{S}}. \quad (5.12)$$

**Fully Extended Interface SEMM.** Here, the experimental blower model is decoupled from the numerical or hybrid start model at all global DoF. This full extension with no fixed interfaces promises proper improvement especially of the hybrid start model due to the fact that the hybrid start model already contains measured information about the dynamic behavior. This prevents fixed interface resonances due to potentially high dynamics of both models (start model and experimental model). It is implemented as:

$$\mathbf{Y}_{\text{fully ext}}^{\text{SEMM}} = \mathbf{Y}_{gg}^{\text{S}} - \mathbf{Y}_{gg}^{\text{S}} \left( \begin{bmatrix} \mathbf{Y}_{b_u i_f} & \mathbf{Y}_{b_u b_f} \end{bmatrix}^{\text{S}} \right)^+ \left( \mathbf{Y}_{b_u b_f}^{\text{S}} - \mathbf{Y}_{b_u b_f}^{\text{E}} \right) \left( \begin{bmatrix} \mathbf{Y}_{i_u b_f} \\ \mathbf{Y}_{b_u b_f} \end{bmatrix}^{\text{S}} \right)^+ \mathbf{Y}_{gg}^{\text{S}}. \quad (5.13)$$

**Extended Equilibrium SEMM.** In case of better controllability of the experimental model compared with the start model, this extension of the standard method can enhance the significance of the SEMM model. This can be achieved by a large set of independent force action DoF. Although this is not the case in the presented application, the results are shown for a comparison of the methods. The equation is defined as:

$$\mathbf{Y}_{\text{ext eq}}^{\text{SEMM}} = \mathbf{Y}_{gg}^{\text{S}} - \mathbf{Y}_{gg}^{\text{S}} \left( \begin{bmatrix} \mathbf{Y}_{b_u i_f} & \mathbf{Y}_{b_u b_f} \end{bmatrix}^{\text{S}} \right)^+ \left( \mathbf{Y}_{b_u b_f}^{\text{S}} - \mathbf{Y}_{b_u b_f}^{\text{E}} \right) \left( \mathbf{Y}_{b_u b_f}^{\text{S}} \right)^{-1} \begin{bmatrix} \mathbf{Y}_{b_u i_f} & \mathbf{Y}_{b_u b_f} \end{bmatrix}^{\text{S}}. \quad (5.14)$$

**Extended Compatibility SEMM.** This extension of the standard method is preferred in case of extraordinary observability of the experimental model by a large set of sensor DoF. In fact, the experimental model includes many more distributed sensor DoF than excitations points and suggests promising results according to an enhancement of the start model. It is written as:

$$\mathbf{Y}_{\text{ext comp}}^{\text{SEMM}} = \mathbf{Y}_{gg}^{\text{S}} - \begin{bmatrix} \mathbf{Y}_{gb} \\ \mathbf{Y}_{b_u b_f} \end{bmatrix}^{\text{S}} \left( \mathbf{Y}_{b_u b_f}^{\text{S}} \right)^{-1} \left( \mathbf{Y}_{b_u b_f}^{\text{S}} - \mathbf{Y}_{b_u b_f}^{\text{E}} \right) \left( \begin{bmatrix} \mathbf{Y}_{i_u b_f} \\ \mathbf{Y}_{b_u b_f} \end{bmatrix}^{\text{S}} \right)^+ \mathbf{Y}_{gg}^{\text{S}}. \quad (5.15)$$

### 5.2.3 Results

The described SEMM methods are tested via predicting an exemplary driving point FRF at the blower test rig (see orange markers in Fig. 5.18). The figures (5.21 and 5.22) show a comparison between the presented two LM-FBS start models<sup>4</sup>, all four SEMM implementations and the experimental validation. Both figures are divided into three parts. Each part shows a frequency range extract. The whole regarded range is depicted on the top, whereby zoomed sections are arranged below. Here, we give an overview and show specifically two frequency areas of interest. In the whole frequency range, significant deviations between the models can be observed. Especially, the purely numerical solution seems almost static along the regarded frequency range, except the first foundation mode. None of the SEMM solutions can represent the measurement in the higher frequency range properly. Here, the best approximation is given by the fully extended interface SEMM. Although, some of the hybrid models come close to the validation measurement at some frequencies. The bad reproduction of the experimental high frequency FRF does not need to be necessarily a problem. Particularly, the observed frequency range of interest, concerning unbalance estimation for example, is related to the lower frequency range.

Therefore, we consider the middle figure which includes a frequency range with dynamics between about 120 Hz and 200 Hz. These dynamics stem from local resonances between motor block and housing including bearings and struts. The specific mode shapes, based on the test setup in Fig. 4.8, are depicted in Fig. 5.20. Here, the top view of a mode shape of the blower test rig at 143 Hz is depicted - directly within the discussed medium frequency range. The resting system is plotted in black, whereby the moving contour is marked in orange. Regarding the motion of the rotor (small circle) and the blower housing (wide circle), we observe relative movement between both components. Conclusively, the mode shape of the bearings - coupled with struts between rotor and housing is notable.

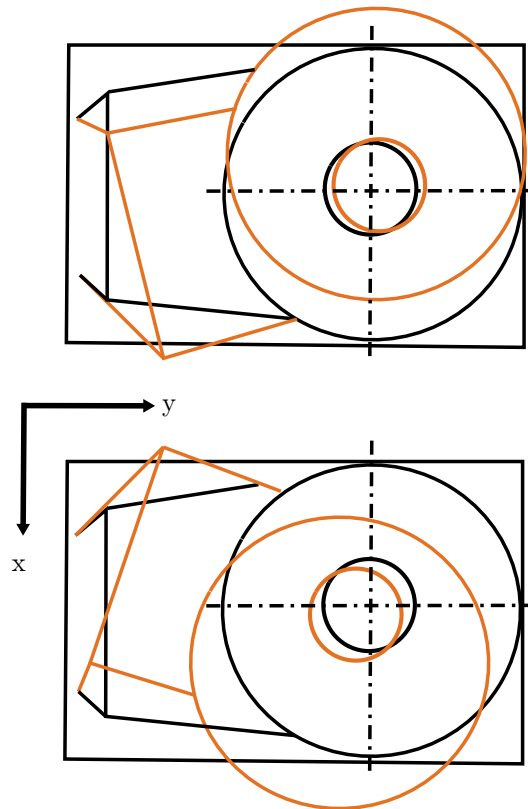


**Figure 5.20:** Top view at the mode shape of the blower test rig at 143 Hz. Initial contour (black) and moving shape (orange). Figure of the two maximum relative deflections between rotor (small circle) and housing (wide circle). Visualization of the coupled bearing-struts mode between rotor and housing.

Concerning the different SEMM models - at the numerical start model based approximation (Fig. 5.21), the basic SEMM best describes the dynamics. This can be justified by the non

<sup>4</sup>Strictly numerical SEMM results are depicted in Fig. 5.21 and SEMM results of the combination of an experimental housing and a numerical rotor model are delineated in Fig. 5.22.

existing dynamics inside the fully numerical parent model. The interface resonances are best introduced by the basic SEMM since they are able to force the static parent to its unique behavior without needing to extend the compatibility or equilibrium condition. There is no extension needed due to non existing interface resonances. An extension rather leads to *free* behavior [69] and static offsets of the three further SEMM variations. This effect is also observable at the blower operational frequency range (bottom part of the figure). To sum up, the basic SEMM model with the numerical start model approximates the experimental solution very well in the low and mid-frequency range, but the number of DoF is significantly higher than when using the hybrid start model (212 numerical vs. 138 DoF hybrid).

Fig. 5.22 looks somewhat different with the fully hybrid approximations. Each solution - even the start model shows dynamic behavior. The whole frequency range overview at the top is confusing, especially in the higher frequency area, the FRFs are hardly separable. Therefore, we zoom in the middle and lower range. Here we observe a better adaption of the main dynamics at the mode depicted in Fig. 5.20 compared with the hybrid start model. The correlating resonance is adapted by most of the SEMM models but missed by the LM-FBS start model. Here, the inclusion of support dynamics by the SEMM models become clear. These are missing due to the strict compatibility and equilibrium conditions at the interfaces of LM-FBS. Even the lower blower operating speed frequency range shows proper results respecting the SEMM approximations. Here, the basic SEMM and the extended compatibility SEMM yield the best outcomes. This might be justified by the extended measurement setup compared with the excitations, which results in improved observability. This extended observation is introduced by the additional accelerometers at the rotor compared with the setup within experimental housing modeling in Sec. 5.2.1. The input force DoF at the modal expansion step does not introduce much additional information compared with the housing system identification. This might be a reason for failing of the extended equilibrium SEMM model. The amount of force DoF in the experimental overlay model is too less for better controlling the entire system. This information is already implemented in the hybrid start (parent) model. With respect to the extended compatibility condition, the results look different. Here, the extension to all output DoF within the decoupling step enhances the FRF quality. In this case, the parent as well as the overlay model embody different information about the dynamic behavior in form of the displacements. Considering the approximation of the 143 Hz resonance between motor block and housing and the performance in the operational and in the entire frequency range, the basic SEMM model constitutes the best choice. Nevertheless, there will be further enhancement in the subsequent section.

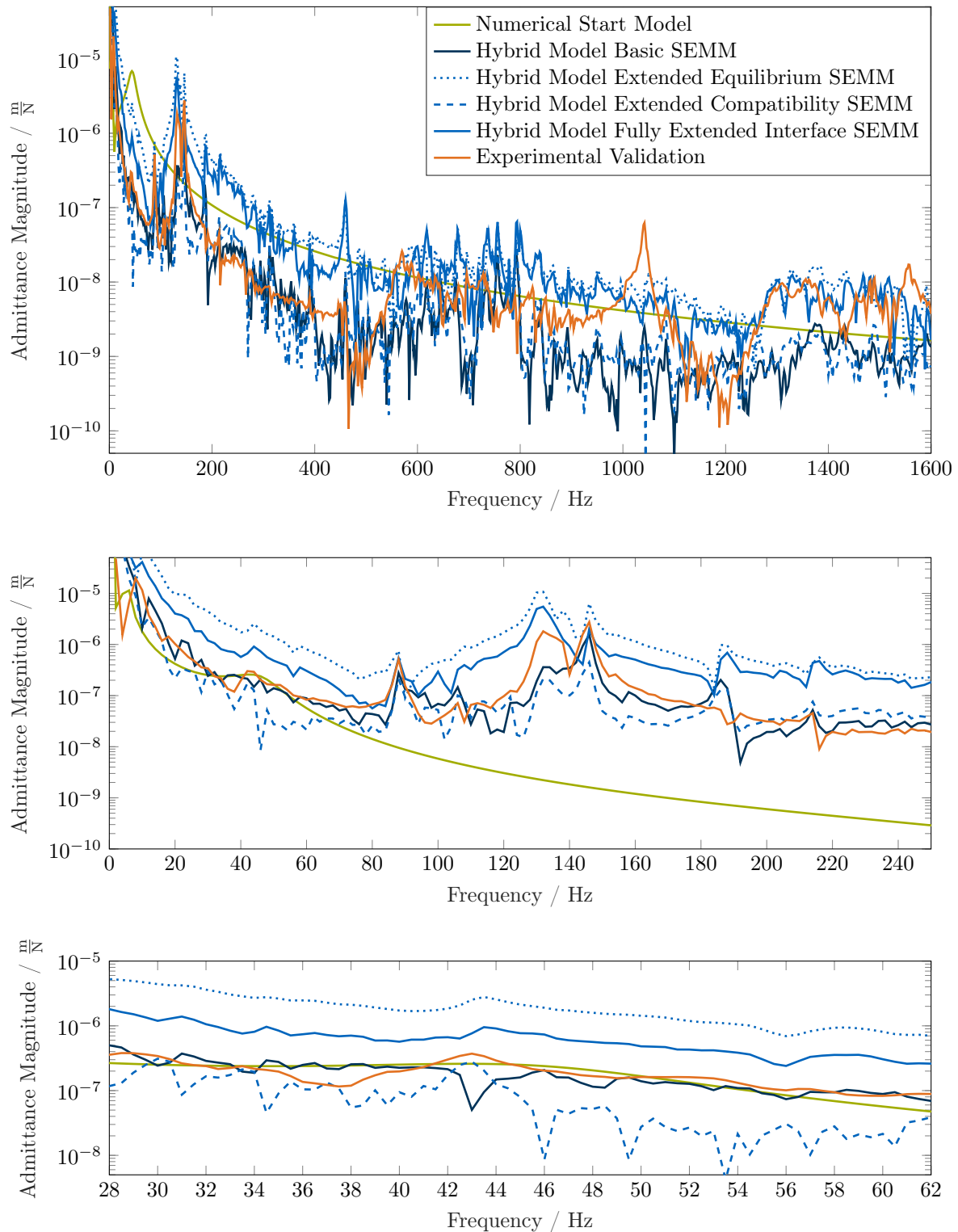


**Figure 5.21:** Admittance Comparison of the **numerical start model** with four SEMM methods and experimental validation. Driving point admittance magnitudes in x-direction based on impact excitation on the motor block. Green: hybrid start model (numerical rotor model coupled with numerical housing (4 DoF) the lower bearing-VP), blue: FRF-prediction by the hybrid SEMM model variants, orange: experimental validation. Top: full bandwidth up to 1.6 kHz, center: lower frequency range, bottom: blower operational frequency range (30 Hz - 60 Hz).

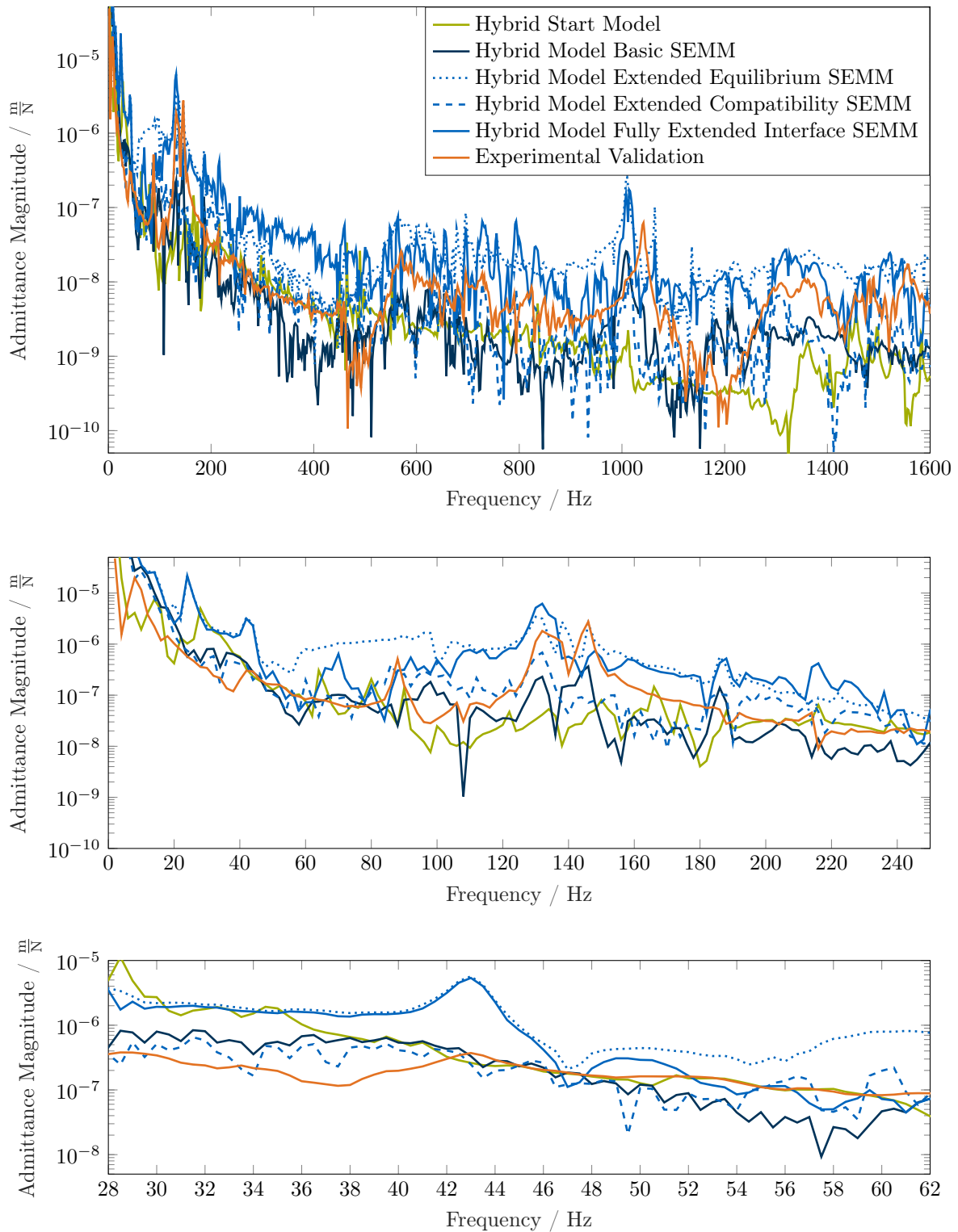


**Figure 5.22:** Admittance Comparison of the **hybrid start model** (experimental housing, numerical rotor) with four SEMM models and experimental validation. Driving point admittance magnitudes in x-direction based on impact excitation on the motor block. Green: hybrid start model (numerical rotor model coupled with experimental housing (6 DoF) at the two rotor bearing positions), blue: FRF-prediction by the hybrid SEMM model variants, orange: experimental validation. Top: full bandwidth up to 1.6kHz, center: lower frequency range, bottom: blower operational frequency range (30 Hz - 60 Hz).

### 5.3 Summary

In this chapter, a hybrid modeling strategy for rotating machinery was evaluated at a blower test rig. Firstly, a numerical rotor model with reduced DoF was created and experimentally as well as numerically validated. Furthermore, the housing model was established as counterpart both numerically and experimentally. These two housing models were subsequently coupled with the rotor utilizing the Lagrange Multiplier Frequency-Based Substructuring algorithm. The coupling was performed at the virtual bearing degrees of freedom. Therefore, a virtual point transformation was implemented and enhanced based on excitation and response consistency criteria. Finally, the two coupled systems were adapted using the SEMM method at the entire structure in order to introduce interface dynamics at the roller bearing coupling points. Main differences concerning a validation FRF were discussed with additional aid of an experimental modal analysis of the entire blower test rig.

## Chapter 6

# Iterative SEMM-Based Model Adaption

A proper model description including the interaction between rotor and housing is essential to estimate operational forces of rotating machinery from measurements at the housing. In most instances, the rotor is not directly accessible for the application of a monitoring system. Hybrid models can solve this problem. In Chap. 5, we built up structural dynamic models of the exemplary blower application. A method for adaption of those models to operational conditions and varying boundary conditions is shown in this chapter. The associated changes of dynamic properties are supposed to be captured by the proposed technique utilizing a minimal sensor setup and a start model with minimum degrees of freedom (Basic SEMM start model resting upon the hybrid start model of Sec. 5.2.2)

## 6.1 Model Adaption to Operating Conditions

In order to evaluate the operational forces, the horizontal transfer functions between rotor disc and housing according to the global coordinate system are considered. These FRFs can not be measured directly due to inaccessibility of the plate for excitation. Nevertheless, the exciting forces can be validated during operation, since we are able to attach a defined unbalance mass to the plate. Exemplary horizontal forces during operation are shown in Fig. 6.1. The transfer functions from the plate (1), which connect the upper and lower roller bearing (2) with the housing measurement position (3), are also delineated (gray dotted lines). An informative outline over the admittances based on the hybrid start model is given in Fig 6.2.

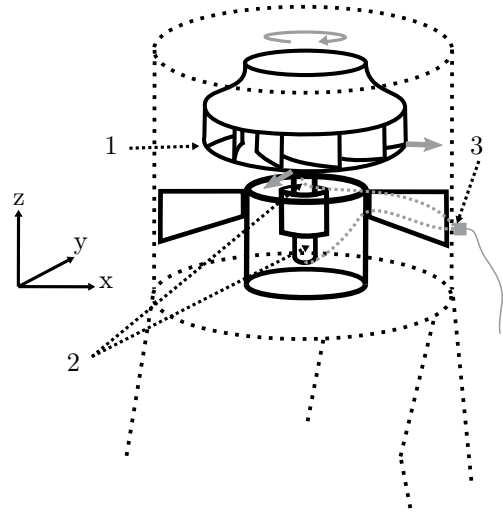


**Figure 6.1:** Blower sectional view with virtual excitation forces (arrows) at the rotor plate (1) and transfer paths (dotted lines) from the bearings (2) to an exemplary accelerometer at the housing (3).

In this preceding context, all future SEMM models are build on the hybrid start model utilizing the setup of Fig. 5.18. Now, these hybrid models are fed with measurements at all operational speed frequencies (30 Hz - 60 Hz, steady state, 1 Hz increment) by an advanced SEMM-based iteration procedure.

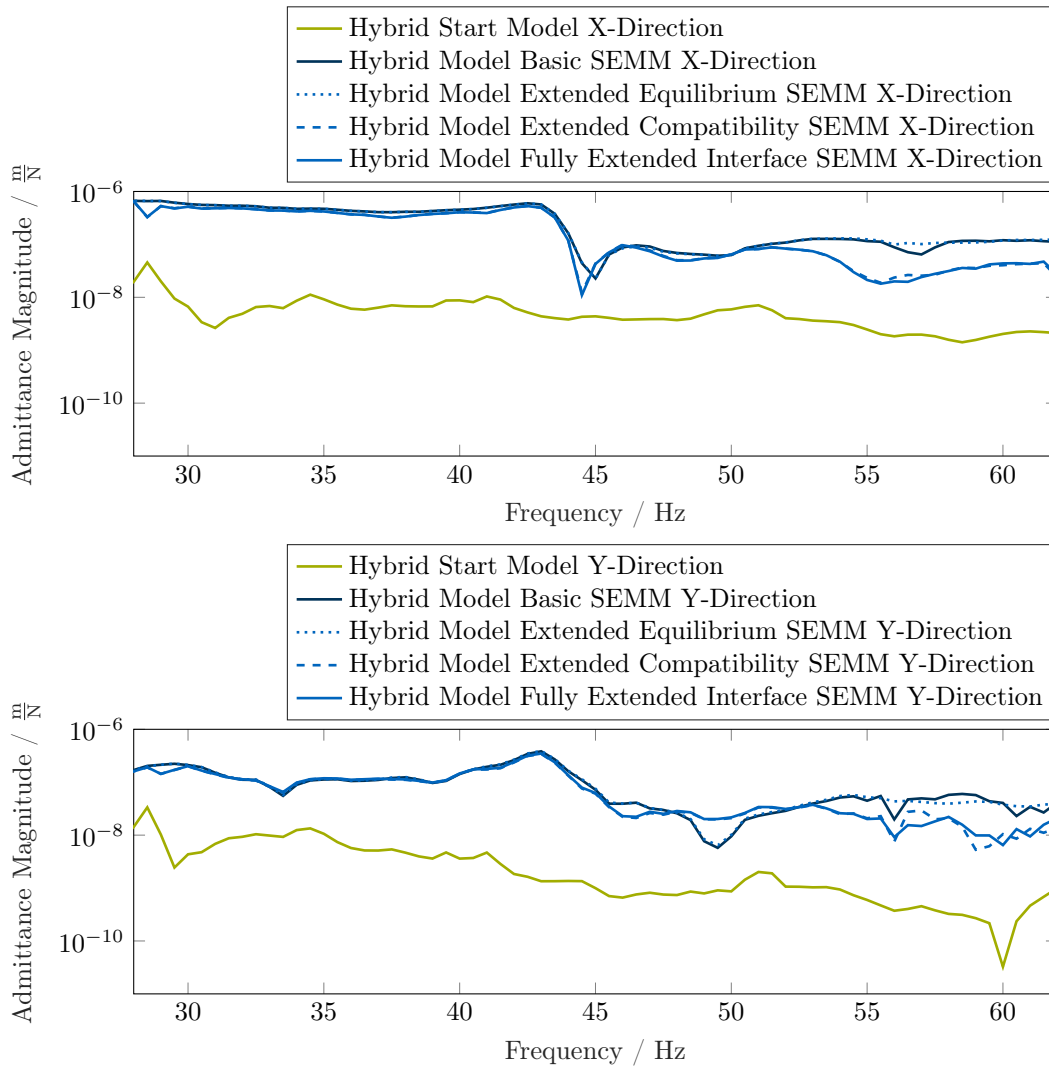


**Figure 6.2:** Admittance magnitudes for virtual rotor blade excitation and housing measurement at the blower operational frequency range (30 Hz - 60 Hz). Upper figure: x-direction, lower figure: y-direction.

The underlying measurement setup for this modal expansion optimization is depicted in Fig. 6.3. Two virtual forces at a motor block sensor position, close to the lower bearing, are calculated based on horizontal acceleration outputs. These virtual forces can be considered as *in-situ* forces as initially introduced by Moorhouse & Elliot [42, 88] and further explained by Van der Seijs [139]. The assembly consisting of rotor and housing is considered in-situ, with the exciting rotor (active component A) coupled to the surrounding motor block with outer housing (passive component B). Note that the motor block can also be considered as an active component, as it is stiff, receives the rotor’s dynamics transmitted through the bearings, and generates the driving magnetic field for the rotor. In contrast, the connection to the outer housing is relatively soft.

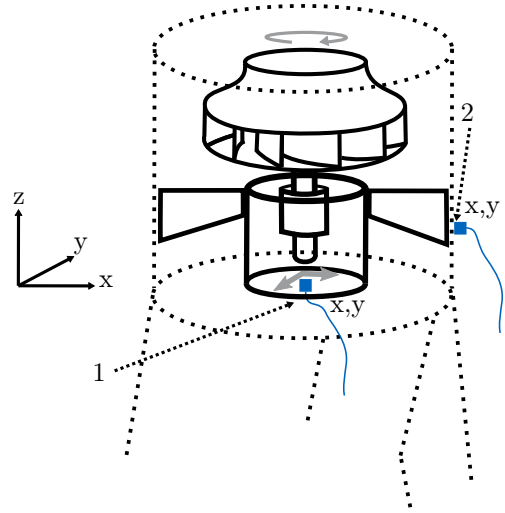


**Figure 6.3:** Measurement setup with virtual excitation forces at lower motor block end (gray arrows) and triaxial accelerometers at motor block (1) and outer housing (2).

Note that the mass unbalance is not an uncorrelated excitation in the both measured, horizontal directions and it is not the only excitation force at operation (additional electromagnetic excitation, bearing forces,...). Hence, it is helpful to estimate these virtual forces to update the model. The measurements for the modal expansion were performed on component B. Therefore, two triaxial accelerometers were applied, placed at the virtual force position at the motor block (1) and at the outer housing (2). Note that only the horizontal measurement directions of the accelerometers (x,y) were utilized because the z-direction does not appear in the models. The hybrid basic SEMM model resting upon on the hybrid start model (see Sec. 5.2.3) will be updated by these measurements due to the reduced model size compared with the numerical start model. This start model therefore serves as “parent model” for the subsequent SEMM-updating. In this context, according to (Eq. (5.12)) the parent start model  $\mathbf{Y}_{\text{basic}}^{\text{SEMM}}$  is structured as:

$$\mathbf{Y}_{gg}^k = \begin{bmatrix} \mathbf{Y}_{i_u i_f}^k & \mathbf{Y}_{i_u b_f}^k \\ \mathbf{Y}_{b_u i_f}^k & \mathbf{Y}_{b_u b_f}^k \end{bmatrix}. \quad (6.1)$$

Here, the modal expansion becomes an iterative procedure. For iteration  $k = 1 \dots n$ ,  $\mathbf{Y}_{gg}^k$  is recalculated for each loop pass. In the presented example, its sub-dimensions are defined as:

- $\text{size}(\mathbf{Y}_{gg}^k) = 138 \times 138$  DoF,
- $\text{size}(\mathbf{Y}_{i_u i_f}^k) = 134 \times 136$  DoF,
- $\text{size}(\mathbf{Y}_{i_u b_f}^k) = 134 \times 2$  DoF,
- $\text{size}(\mathbf{Y}_{b_u i_f}^k) = 4 \times 136$  DoF,
- $\text{size}(\mathbf{Y}_{b_u b_f}^k) = 4 \times 2$  DoF.

The boundaries are now allocated to a new experimental model including the operational acceleration measurements indicated in Fig. 6.3. To establish  $\mathbf{Y}_{b_ub_f}$ , we need the operational excitation forces. The problem is that they are unknown. Thus, we assume two virtual, horizontal forces at the lower motor block end. They are marked by gray arrows in Fig. 6.3. The force location was selected because of the presence of the triaxial accelerometer at this position, and because they allow good observability for the exemplary minimal number of sensors.

Hereinafter, we explain the model optimization loop, building on this operational measurement data and the hybrid start model:

Based on the four acceleration outputs, a virtual boundary load matrix (x- and y- forces at the lower motor block end) is calculated iteratively. For iteration  $k = 1 \dots n$ , this force estimation is obtained from

$$\mathbf{F}_b^k = \left( \mathbf{Y}_{b_ub_f}^k \right)^+ \mathbf{U}_b^k. \quad (6.2)$$

with the displacement matrix  $\mathbf{U}_b^k$  and the boundary admittance matrix  $\mathbf{Y}_{b_ub_f}^k$ . In the presented example, the new experimental model matrices have the dimensions:

- $\text{size}(\mathbf{F}_b^k) = 2 \times 1$  DoF,
- $\text{size}(\mathbf{U}_b^k) = 4 \times 1$  DoF,
- $\text{size}(\mathbf{Y}_{b_ub_f}^k) = 4 \times 2$  DoF.

The estimated excitation force  $\mathbf{F}_b^k$  is utilized to calculate a new experimental model  $\mathbf{Y}_{b_ub_f}^{k+1}$ :

$$\mathbf{Y}_{b_ub_f}^{k+1} = \mathbf{U}_b^k \left( \mathbf{F}_b^k \right)^+. \quad (6.3)$$

This experimental model is implemented in the SEMM expansions (Eq. (5.12) - 5.15) in every iteration step. After that expansion, we get a new SEMM model  $\mathbf{Y}_{gg}^{\text{SEMM},k}$  for each SEMM technique. From this global model description, we take the boundary admittance subset  $\left( \mathbf{Y}_{b_ub_f}^k \right)$  and start again at Eq. (6.2). Within the loop, the hybrid solution converges to an iterative SEMM-model  $\mathbf{Y}_{gg}^{\text{SEMM},n}$  for each of the four SEMM methods. Note, the entire procedure is applied for each SEMM method separately. The overall technique from model setup to iterative model adaption is represented by the flowchart in Fig 6.4. Here, the iterative determination of  $\mathbf{Y}_{b_ub_f}^k$  is explained as follows:

During the iterative SEMM model updating, we search for two virtual forces at the lower motor block end which best describe four displacements at the housing. Here, the assumption is made that the motor block is relatively stiff. This approximation is justified given the sensor consistency within the virtual point measurements at the motor block (Sec. 5.2.1). The position of forces is chosen based on observability condition, since these loads are estimated at the same DoF as the accelerometer is set. In order to identify these forces, we apply a second sensor at the outside housing, away from the accelerometer on the motor, to capture maximum information about the operational dynamics between rotor and housing although using a minimal sensor setup. By utilizing four displacement outputs and the Moore–Penrose pseudoinverse of a  $4 \times 2$  DoF admittance subset within Eq. (6.2), the forces are estimated. These two forces have to justify four outputs, so the row-rank four of the  $4 \times 1$  DoF displacements is reduced to rank two of the forces which equals to column rank two of the admittance subset matrix. Here, a projection  $4 \rightarrow 2$  is performed. After determination of these forces within the iterative SEMM loop, they are applied to estimate the  $4 \times 2$  DoF admittance matrix by performing the pseudoinverse multiplication in Eq. (6.3). The resulting  $4 \times 2$  DoF admittance

matrix has rank one, since we apply the same acceleration measurement as already utilized for the previous force identification. These steps are necessary to find the iterative admittance  $\mathbf{Y}_{b_u b_f}^k$  as overlay model for the SEMM. We substitute Eq. (6.2) in Eq. (6.3) and write it as follows:

$$\mathbf{Y}_{b_u b_f}^{k+1} = \mathbf{U}_b^k \left( \left( \mathbf{Y}_{b_u b_f}^k \right)^+ \mathbf{U}_b^k \right)^+ . \quad (6.4)$$

Note that in the presented case:

$$\mathbf{Y}_{b_u b_f}^{k+1} \neq \mathbf{U}_b^k \mathbf{Y}_{b_u b_f}^k \left( \mathbf{U}_b^k \right)^+ \quad (6.5)$$

because  $\left( \mathbf{Y}_{b_u b_f}^k \right)^+$  in Eq. (6.4) has column-rank two, but  $\mathbf{U}_b^k$  owns only column-rank one. Consequently, the necessary and sufficient condition for this simplification is not given [52]. For the presented example, the acceleration response was measured at steady state for all operational frequencies, 34 s acquisition time each. It was transformed into frequency domain representation (sample rate = 8192 S/s). The time data was split into snapshots (two seconds each) with 0.5 Hz resolution up to a frequency of 1.6 kHz in order to deal with the same dimensions as we utilized within the previous FRF measurements (see for example Sec. 5.2.2). A Kaiser window ( $\beta = 20$ ) was applied prior to the FFT in order to avoid leakage effects. Subsequently, all 34 snapshots were averaged in the frequency domain representation at steady state operational speed condition to get a smooth result for each sensor DoF.

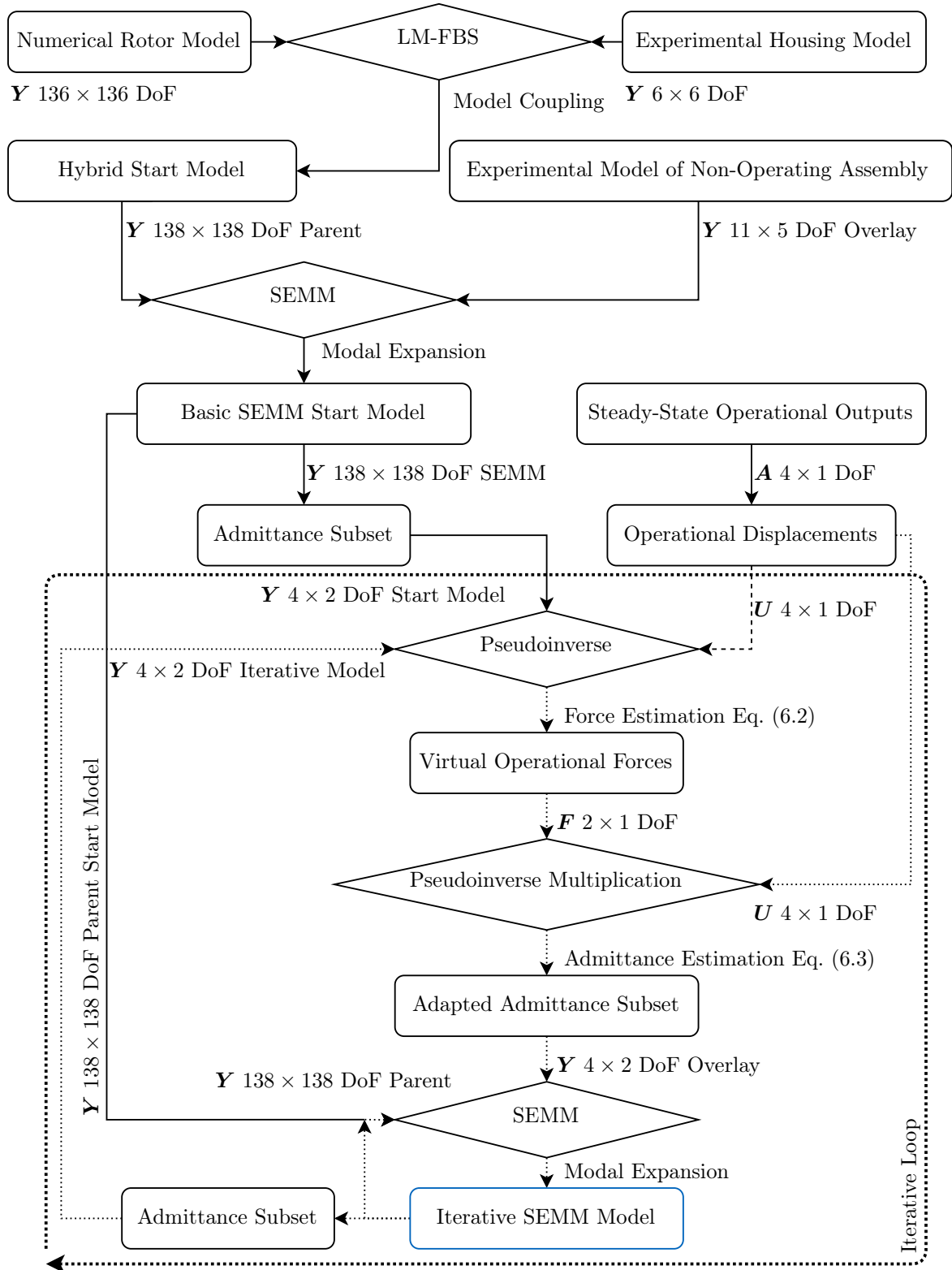


**Figure 6.4:** Model assembling and iterative updating. It starts with the *Hybrid Basic SEMM Start Model* and the *Steady-State Operational Outputs*. All underlying models were previously developed in Chap. 5. Solid lines represent unique steps. Some of them are replaced by iterative models within the loop (dotted lines). The operational displacements interact with the start models and with the iterative model inside the loop (dashed line). Finally, we obtain an iteratively adapted hybrid entire system model (blue).

### 6.1.1 Operational Force Estimation

Starting from the non-operating model obtained by applying the four different variants of SEMM to the initial hybrid assembly model (see Chap 5), four in-operation models were obtained after applying the SEMM-iterations just explained and summarized in Fig. 6.4. The procedure was applied separately for each rotation speed, so that we obtained four in-operation models per operation speed. Using then these updated in-operation models, we try to identify the operational forces by using a final updated admittance matrix between the impeller of the rotor and the outer housing. In order to validate the model for this admittance and to get an impression about the linearity of the system, we sequentially attached two exemplary unbalance masses  $m_u$  to the impeller disc (10 g and 20 g). The test setup is depicted in Fig. 6.5. Here, the unbalance mass attached to the outer edge of the circular plate is shown.

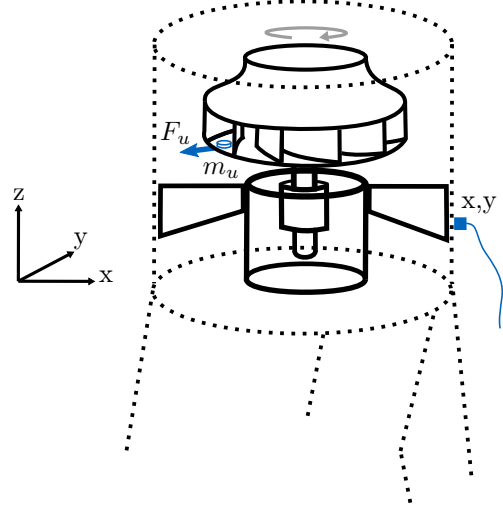


**Figure 6.5:** Test setup for acceleration output measurements due to a defined unbalance force  $F_u$  based on different masses  $m_u$  (small blue disc at the rotor blade). Only two horizontal directions (x, y) of a single, triaxial accelerometer at the outside housing are considered as responses to the unbalance during operation.

During operation, a defined radial unbalance force  $F_u$  acts on the rotor plate DoF in global x and y direction. With the applied mass  $m_u$ , radial vector  $e_r(t)$  with eccentricity  $r$  and operational speed  $\Omega(t)$ , the validation force is defined as

$$\mathbf{F}_u(t) = m_u \mathbf{e}_r(t) \Omega^2(t) \quad (6.6)$$

We utilize  $\mathbf{F}_u(t)$  to compare it with the resulting force from the presented SEMM models and measured acceleration at the housing position marked in Fig. 6.5 for each unbalance. Therefore, we pick the two horizontal transfer paths between plate and housing and write them into an admittance matrix  $\mathbf{Y}_{hur_f}^k$ . This admittance characterizes the path of forces on the rotor plate  $r$  to the housing  $h$ . The operational force is estimated by the iterative SEMM model during iteration  $k$  by

$$\mathbf{F}_r^k = \mathbf{U}_h^k \left( \mathbf{Y}_{hur_f}^k \right)^{-1}. \quad (6.7)$$

Note that the iterative process of Fig. 6.4 is meant and that no further iterative updating is carried out here. Thus, we investigate the estimated operational force (unbalance) as function of the rotation speed:

$$\mathbf{F}_r^k = \begin{bmatrix} F_x \\ F_y \end{bmatrix}^k \quad (6.8)$$

with

$$\mathbf{U}_h^k = \begin{bmatrix} U_x \\ U_y \end{bmatrix}^k \quad \text{and} \quad (6.9)$$

$$\mathbf{Y}_{h_u r_f}^k = \begin{bmatrix} Y_{xx} & Y_{xy} \\ Y_{yx} & Y_{yy} \end{bmatrix}^k. \quad (6.10)$$

After all, a scalar unbalance force is estimated:

$$F_u^k = \sqrt{(F_x^k)^2 + (F_y^k)^2}. \quad (6.11)$$

This unbalance force is now compared with the result of Eq. (6.6). The iterative force estimation is depicted in Fig. 6.6 and also compared with the basic SEMM start model before the first SEMM adaption (see Fig. 6.4). The rated/maximum mechanical rotational speed (59 Hz) is regarded as representative scenario.

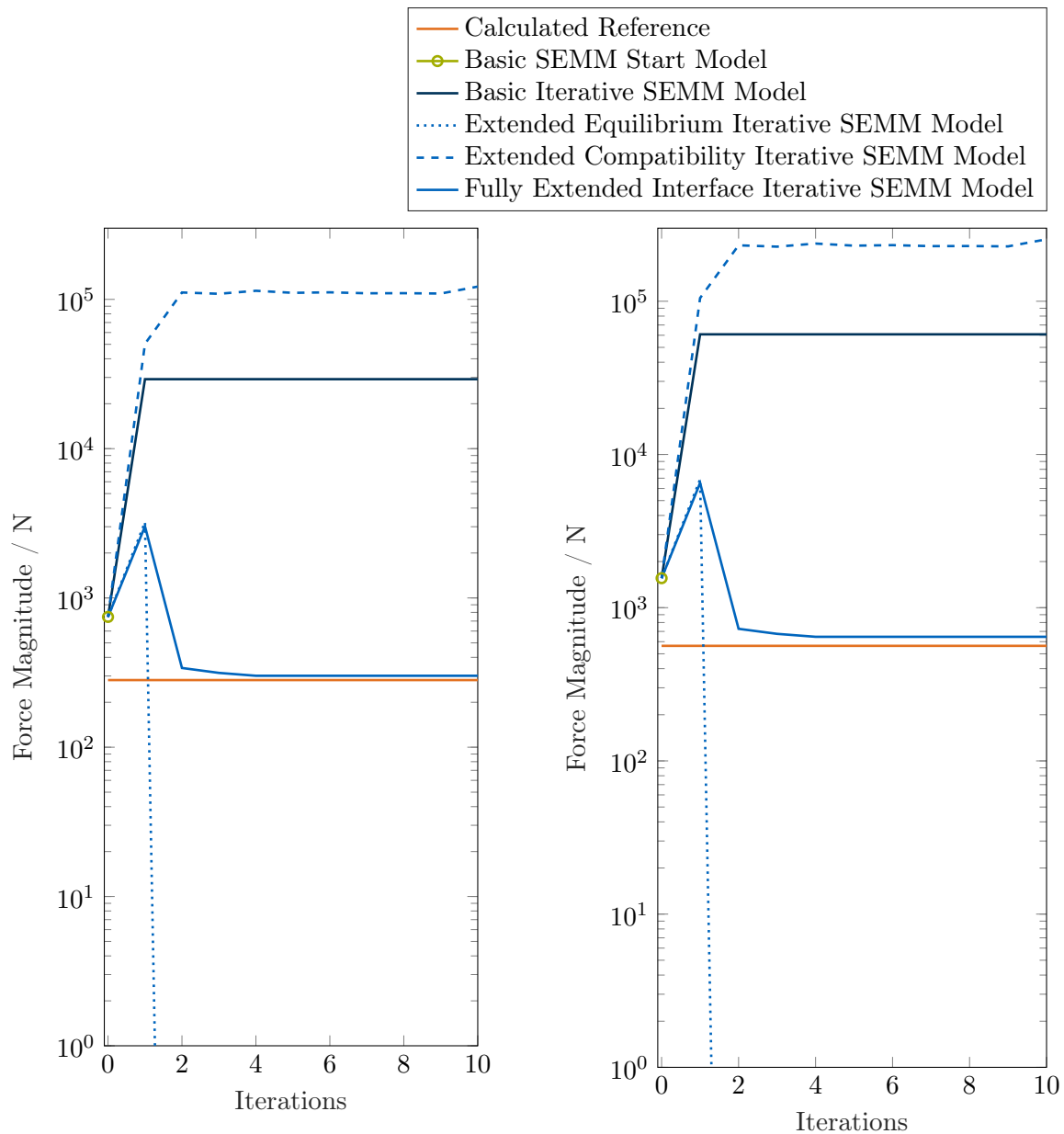


**Figure 6.6:** Unbalance force estimation based on the basic SEMM start model and the four iterative SEMM models at rated 59Hz mechanical rotation speed. Left: 10g unbalance mass, right: 20g unbalance mass.

Comparing the different approximations, they converge to a constant force within ten iterations except the extended compatibility SEMM model. Here, a slight decrease after eight iterations is observable. Compared with the reference, the force is far too high. Conversely, the extended equilibrium method underestimates the force by 10 orders of magnitude (plot cut at 1 N). These two techniques seem to be inappropriate. Even the hybrid start model provides better outcomes. The basic method does not show any changes after the first iteration and we observe almost perfect convergence of the fully extended interface SEMM model. Note that the whole iteration progress is passed through for every operational speed separately. Based on the outlined results and efficiency reasons, the loop termination criterion is set after five iterations. The results of both unbalance masses are plotted to show the linearity in this respect. For further considerations, the focus is set to the 20g unbalance mass measurements.

Due to greatly varying force estimations depending on the chosen SEMM method (Fig. 6.6), an extended frequency range around the operational speed is evaluated in Fig. 6.7 and Fig. 6.8 for all SEMM models. In the upper two sub-figures, the admittances between applied unbalance mass location and the housing's measurement position are depicted in the two horizontal directions  $x$  and  $y$ . Below, the estimated unbalance force based on these admittances<sup>1</sup> is plotted before and in the course of five iterations.

Within the iterations, the curves seem to become spiky. The evaluation at 59 Hz rated rotational speed shows these effects in all SEMM models. Although, the fully extended interface keeps the smoothest shape without offset. Keeping in mind the multiple decoupling and coupling within the SEMM loop, local resonances can be introduced [68, 109]. Thus, these introduced peaks seem to be unphysical.

Regarding the basic SEMM model, spikes arise with certain regularity and the SEMM loop can not improve the model. The iteratively extended compatibility force shape offset is quite higher and the extended equilibrium's offset is crucial. Extending the decoupling step on the equilibrium seems not to be an appropriate assumption, since in this case, an equilibrium of two virtual force DoF is extended to 138 degrees of freedom. Note, these forces are found based on only four measurement DoF. Extending the equilibrium of these filtered forces to all remaining DoF can therefore lead to this bad issue.

Also extending the compatibility based on the four measurement DoF does not work. The reason for restriction of the three methods (basic, extended equilibrium, extended compatibility) can be found in the concentration of information about changing dynamics within operation. This information is accumulated in Eq. (6.4) and is expanded within the loop in every SEMM expansion.

Due to the best results provided by the fully extended interface method, henceforth, we focus on that technique. Hereinafter, all outlined SEMM models are assembled by this procedure.

---

<sup>1</sup>see Eq. (6.11) with 59 Hz rotational speed and 20 g unbalance mass

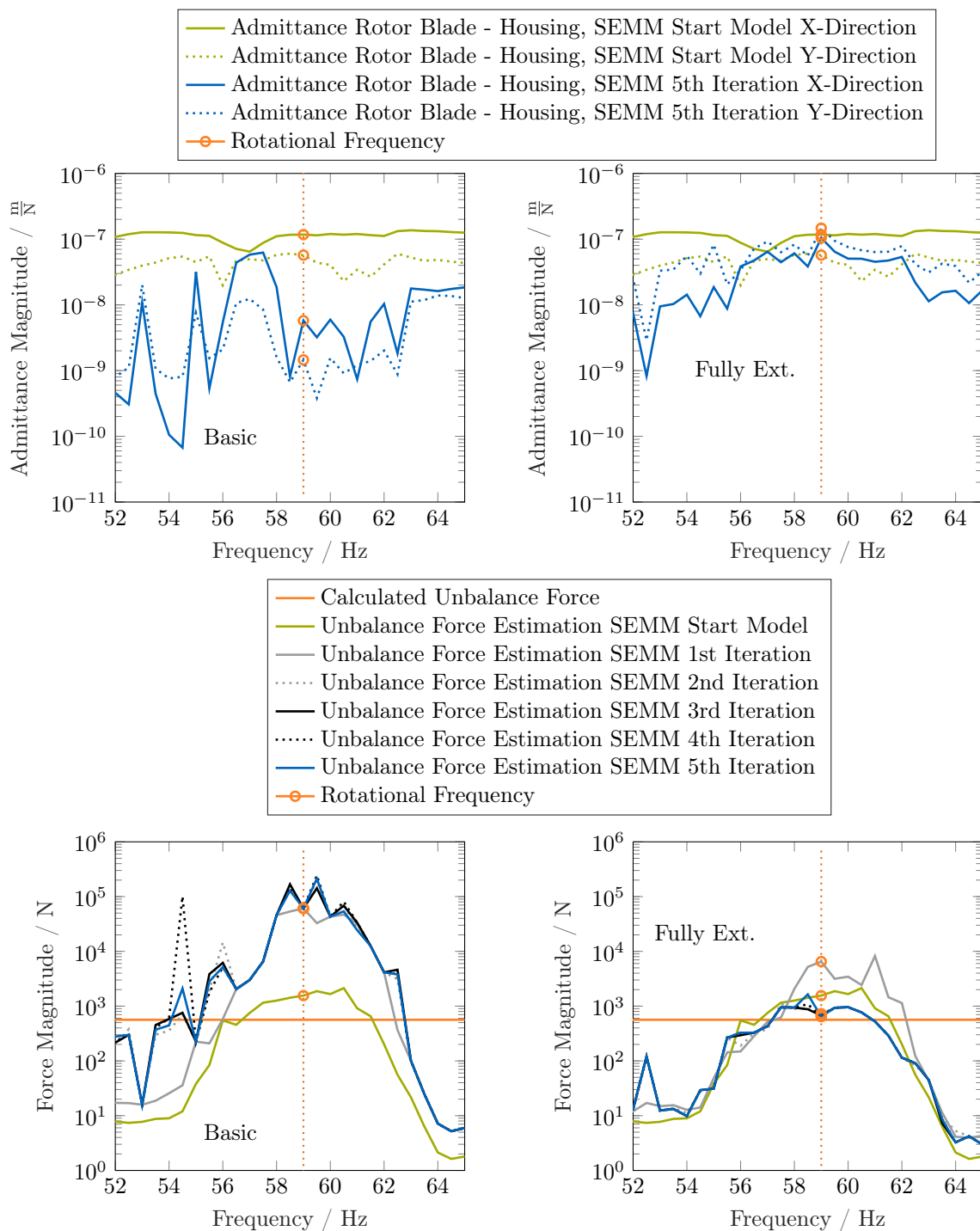


**Figure 6.7:** Admittances and force magnitudes estimated with operational measurements at a given rotational speed ( $\Omega = 59$  Hz). Left top: **basic SEMM** start and iterative SEMM admittance after five loop passes. Right top: **fully extended interface SEMM** start and iteratively determined admittance. Bottom left: force estimation based on the **basic SEMM** start model and iterations one to five. Bottom right: force estimation based on the **fully extended interface SEMM** start and iterative models one to five. The calculated unbalance force depending on the rotational speed of 59 Hz and 20 g unbalance mass is depicted in form of an orange horizontal line.

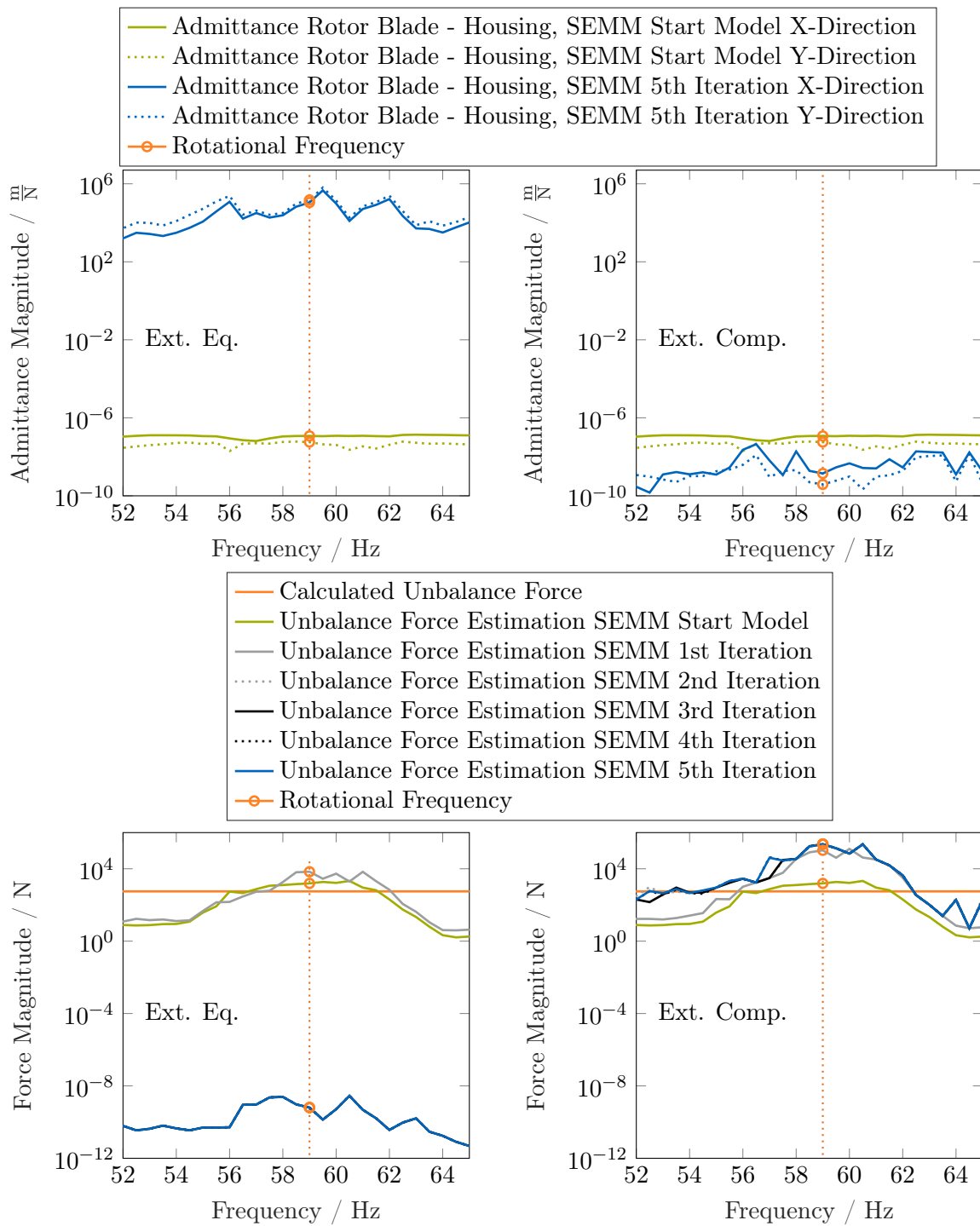


**Figure 6.8:** Similar figure as Fig. 6.7 but with applied extended equilibrium SEMM and extended compatibility SEMM.

Although the spikes of the fully extended interface model do not arise directly on the operational frequency line in Fig. 6.7, conditions might occur, where this is not the case. Now, another operating speed (44.5 Hz) is regarded (Fig. 6.9). Here, we see that the shape degradation in form of a local peak can occur directly on the operational frequency line. Due to these effects, we developed an autonomous solution to filter out the peaks, which is presented in Sec. 6.1.2.

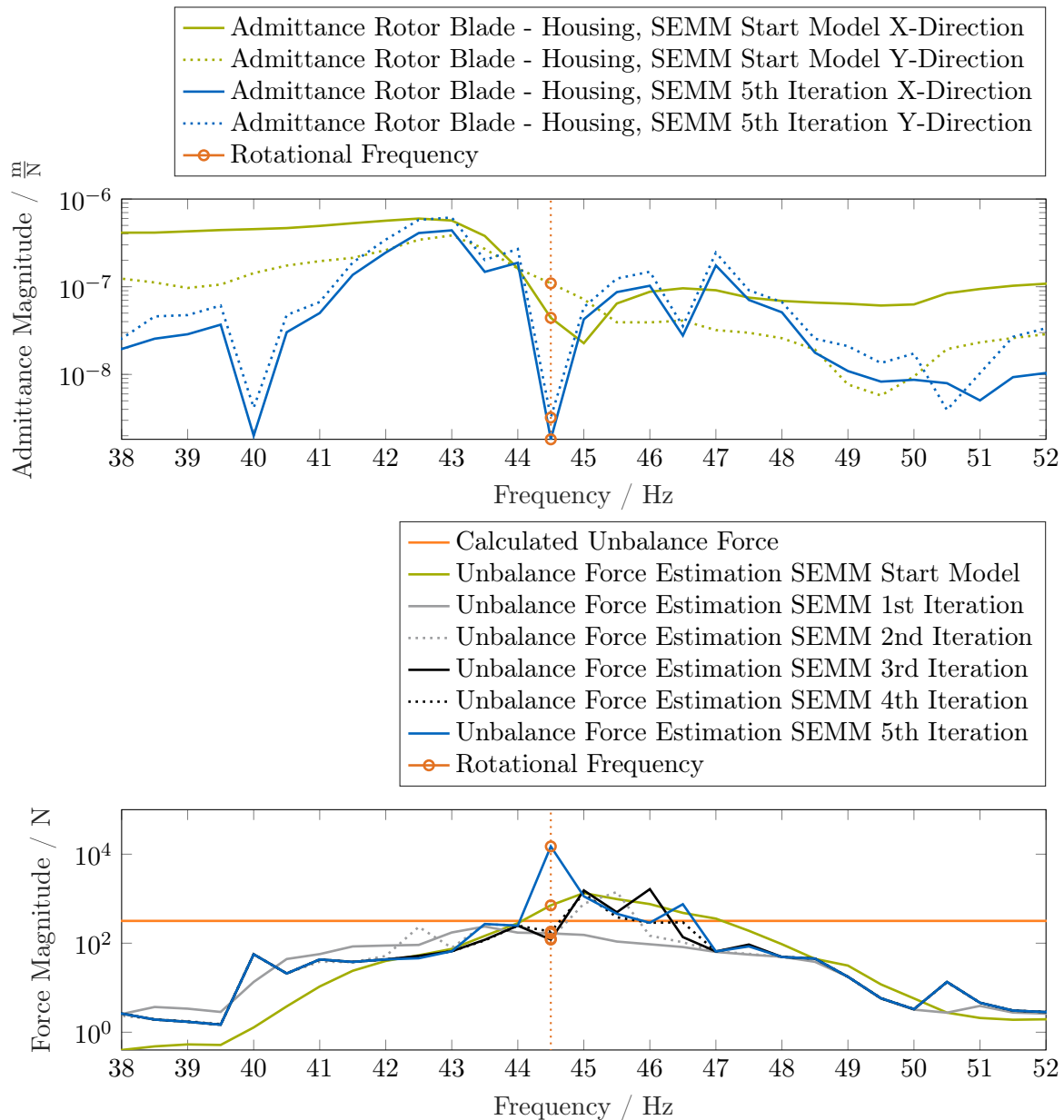


**Figure 6.9:** Similar figure as Fig. 6.7 but only for the **fully extended interface SEMM** method and SEMM adaption at  $\Omega = 44.5$  Hz.

### 6.1.2 Adaptive Force Shaping

The objective of this section is a brief introduction of a robust algorithm which adaptively shapes the iterative SEMM force estimation to the SEMM start model force curve in order to eliminate the unphysical spikes. This procedure will be shortly explained based on Fig 6.10. More details can be looked up in App. B. The smoothing of the iterative SEMM force magnitude is done using a spline fit. Basically, the start model (green curve in Fig 6.10) and the iterative SEMM model (gray curve in Fig 6.10) are considered as physical bases for defining the fit. This basis should still remain after smoothing. For this purpose, scalar values, such as the force-magnitude RMS value in a frequency band around the rotational frequency are determined. After the first spline fit is placed over the iterative SEMM model (dotted blue curve in Fig 6.10), the scalar values of this spline fit curve are determined and compared with the base values. If they are outside an acceptable deviation from the base values, the sample with the highest magnitude of the iterative SEMM model is deleted (top orange bubble in Fig 6.10). A spline fit is then formed again and the deletion of spike samples is repeated until the scalar values of the spline fit are within an acceptable deviation from the base values. The force magnitude of the final spline fit at the rotational speed frequency is finally taken as the smoothed, scalar force value<sup>2</sup>.

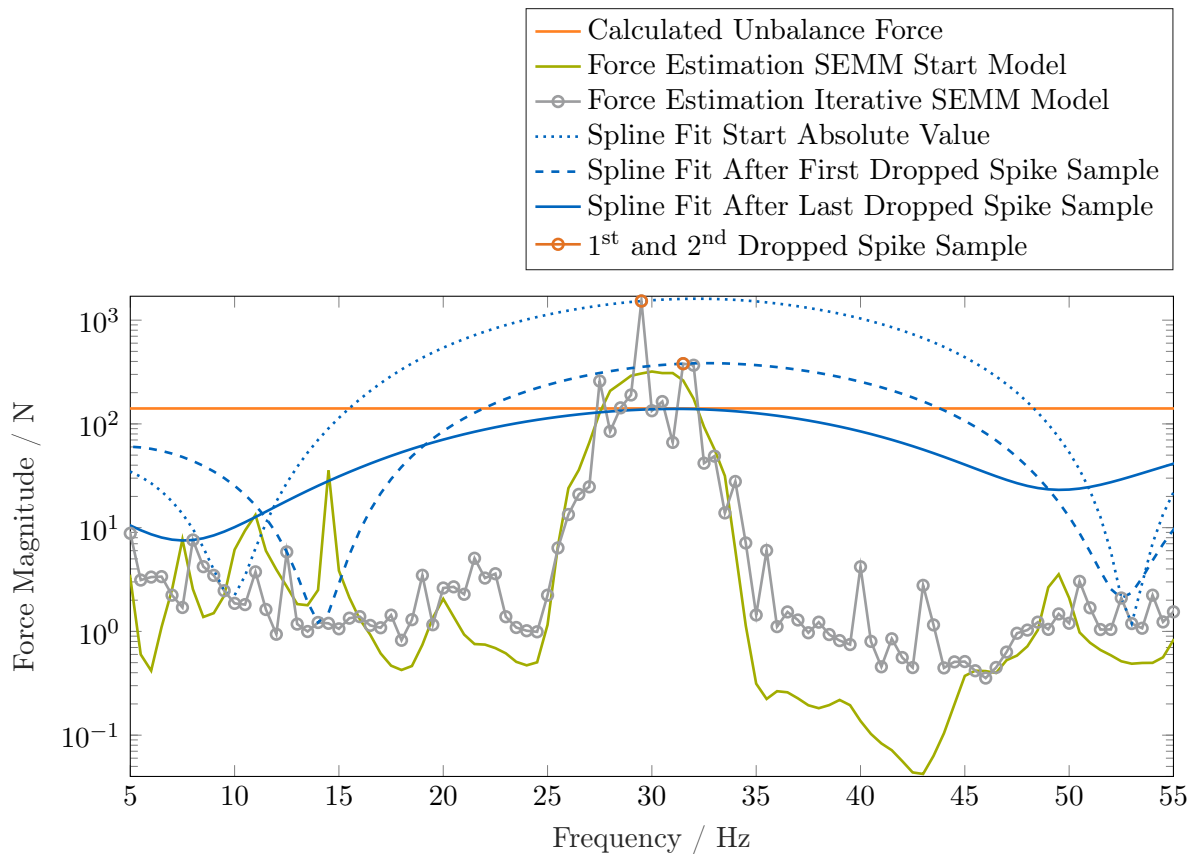


**Figure 6.10:** Force estimation at 30 Hz rotational speed with main force peak at the fundamental frequency. Adaptive spline fit with depicted first two dropped spike samples within seven fit iterations. First fit iteration: blue dotted curve, second fit iteration: blue dashed curve, last fit iteration: blue solid curve.

<sup>2</sup>In case the reader wondered at the beginning of this thesis what the point of the cover picture is: The cover picture corresponds to a top view of a three-dimensional representation of the iteratively formed force estimation. It starts at the bottom with the spiky, iterative SEMM model and is shaped toward the center at the top. The center corresponds to the final, estimated force.

The presented technique is nonlinear with respect to the operational condition. Therefore, we linearized it for certain operating speeds over the entire rotational frequency range (magnetic field frequencies 30 Hz to 60 Hz). Thus, the two iterative procedures (Fig. 6.4 and Fig B.1) have to be passed through for every rotational speed condition separately. The result is depicted in Fig. 6.11. We see the calculated unbalance force as reference (orange) and the force estimation via three models<sup>3</sup>. The force estimation technique should provide robust results. The robustness can be evaluated regarding the entire operating speed range as well as different unbalance masses (Fig. 6.6). Generally, the presented method is very robust concerning varying unbalances. In contrast to that, the unbalance force is not approximated with the same quality at all operational speeds. However, the shaped force estimation can increase the robustness compared with the raw iterative SEMM solution (see for example the estimations at 30 Hz and 44.5 Hz in Fig. 6.11) but it does not significantly improve the result over the entire frequency range. Generally, the iterative SEMM mostly provides better force assumptions than the SEMM start model.

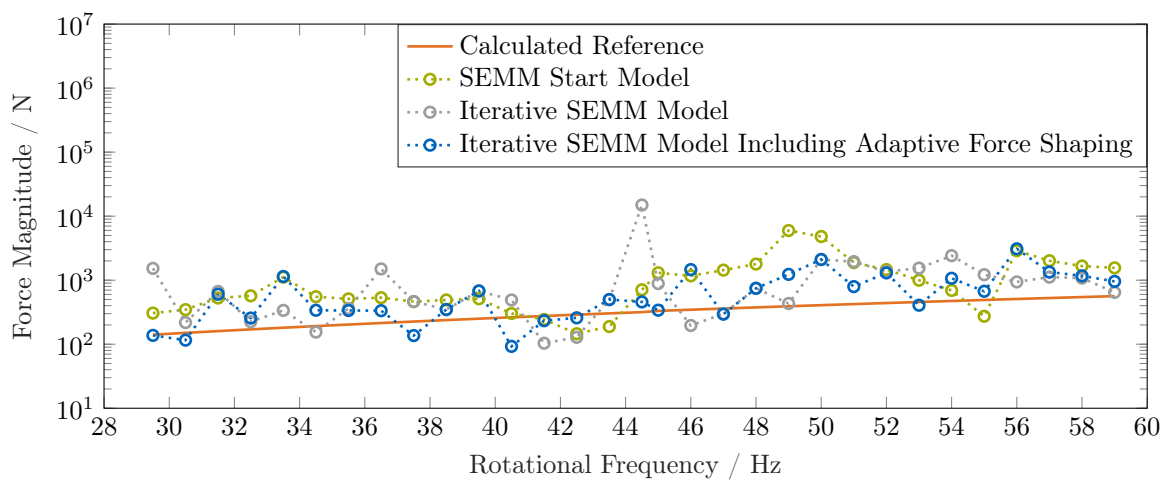


**Figure 6.11:** Entire frequency range unbalance force estimation (20 g unbalance) strictly at operational speed frequency lines based on the SEMM start model, the iterative SEMM model and the iterative SEMM model including the adaptive force shaping technique.

<sup>3</sup>SEMM start model (green), iterative SEMM model without force shaping (gray) and iterative SEMM approximation including iterative force shaping (blue).

## 6.2 Model Adaption to Varying Boundary Conditions

Due to promising results of the iterative SEMM expansion in Sec. 6.1, a likewise approach for system adaption to varying boundary conditions is evaluated. The objective is an adaption of the rotating machine to field peripheries. Therefore, we rely on a single measurement position at the outside housing. Note that the procedure is similar as in Sec. 6.1 (see Fig. 6.3 for the measurement setup) but only two outputs instead of four were used. The single measurement position with the two outputs represents the two DoF of a future, triaxial monitoring sensor. In the presented example, regarding horizontal accelerations only, there are two outputs to describe the excitation forces. These two outputs should capture information about changing transfer functions due to varying boundary conditions. These boundary condition changes are simulated by an additionally attached mass at the outside housing.

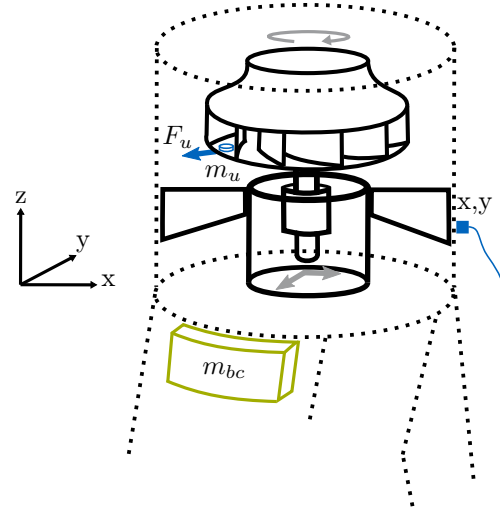


**Figure 6.12:** Measurement setup for adaption to varying boundary conditions (additionally attached mass  $m_{bc}$ ). Virtual excitation forces at the lower motor block end (gray) and one triaxial accelerometer at the housing (only radial directions considered). For the validation, two different unbalance masses (blue disc,  $m_u$  10 g and 20 g ) are sequentially attached to the rotor blade, evoking a defined unbalance force  $F_u$ .

In the particular example, we attached 37 kg ( $m_{bc}$  in Fig. 6.12). This mass represents a realistic system detuning due to heavy tool bracket purpose of the locomotive motor blower. The measurement setup is depicted in Fig. 6.12. Now, the two acceleration outputs at the housing for determining two virtual forces at the motor block in a similar manner as described in Sec. 6.1 are used. These forces are utilized in order to construct a  $2 \times 2$  DoF admittance matrix ( $\mathbf{Y}_{b_u b_f}$ ), which is expanded to the entire system subsequently. Here, this expansion step is applied only once. Again, we have a couple of different models for the SEMM adaption: The parent model with global structure

$$\mathbf{Y}_{gg} = \begin{bmatrix} \mathbf{Y}_{i_u i_f} & \mathbf{Y}_{i_u b_f} \\ \mathbf{Y}_{b_u i_f} & \mathbf{Y}_{b_u b_f} \end{bmatrix} \quad (6.12)$$

implies the dimensions:

- $\text{size}(\mathbf{Y}_{gg}) = 138 \times 138$  DoF,
- $\text{size}(\mathbf{Y}_{i_u i_f}) = 136 \times 136$  DoF,
- $\text{size}(\mathbf{Y}_{i_u b_f}) = 136 \times 2$  DoF,
- $\text{size}(\mathbf{Y}_{b_u i_f}) = 2 \times 136$  DoF,
- $\text{size}(\mathbf{Y}_{b_u b_f}) = 2 \times 2$  DoF.

The estimation of two virtual forces at the motor block is defined as

$$\mathbf{F}_b = (\mathbf{Y}_{b_u b_f})^+ \mathbf{U}_b \quad (6.13)$$

containing the displacements  $\mathbf{U}_b$  based on outputs with changed boundary conditions and the admittance matrix  $\mathbf{Y}_{b_u b_f}$  between the motor forces and housing displacements. Now, they simply hold the dimensions

- $\text{size}(\mathbf{F}_b) = 2 \times 1$  DoF,
- $\text{size}(\mathbf{U}_b) = 2 \times 1$  DoF,
- $\text{size}(\mathbf{Y}_{b_u b_f}) = 2 \times 2$  DoF.

The approximated virtual excitation force  $\mathbf{F}_b$  is utilized to assemble a second experimental model  $\mathbf{Y}_{b_u b_f}^{(2)}$ :

$$\mathbf{Y}_{b_u b_f}^{(2)} = \mathbf{U}_b (\mathbf{F}_b)^+ . \quad (6.14)$$

This new experimental model is now implemented in the fully extended interface SEMM expansion. Here, no iterative approach is chosen, since we have no force filtering possibility as within the iterative adaption to operational conditions. The system is not over-determined so pseudoinverse filtering is not possible in the same way as in Eq. (6.4). Though, putting Eq. (6.13) and Eq. (6.14) together, we write:

$$\mathbf{Y}_{b_u b_f}^{(2)} = \mathbf{U}_b \left( (\mathbf{Y}_{b_u b_f})^+ \mathbf{U}_b \right)^+ . \quad (6.15)$$

Note that

$$\mathbf{Y}_{b_u b_f}^{(2)} \neq \mathbf{U}_b \mathbf{Y}_{b_u b_f} (\mathbf{U}_b)^+ \quad (6.16)$$

since  $(\mathbf{Y}_{b_u b_f})^+$  in Eq. (6.15) has column-rank two, but  $\mathbf{U}_b$  only column-rank one. As already mentioned in Sec. 6.1, the necessary and sufficient condition for the simplification of Eq. (6.16) is not given in the presented case [52].

An overview flow chart of the entire technique of periphery adaption is depicted in Fig 6.13. The whole procedure is passed through for every operational speed frequency separately. Now, we utilize the adapted iterative SEMM model to determine the unbalance force at varied boundary conditions. The procedure is similar to the force estimation process in Sec. 6.1.1<sup>4</sup>. Based on the unbalance force vector

$$\mathbf{F}_u = \mathbf{U}_h \left( \mathbf{Y}_{h_u r_f}^n \right)^+ \quad (6.17)$$

we get the scalar unbalance force

$$F_u = \sqrt{(F_x)^2 + (F_y^k)^2} . \quad (6.18)$$

This unbalance force is now calculated for each frequency line. Here, unphysical spikes might occur again. Due to that, we perform the same evaluation method as in Sec. 6.1. Hence, we strictly select the operational frequency line and perform the adaptive force shaping algorithm (see Fig. B.1) on the adapted iterative SEMM model to get rid of possible unphysical spikes. The outcome is depicted in Fig. 6.14. The iterative SEMM model including adaption and force shaping (black) increases the accuracy of force estimation almost at the entire frequency range except in an area between 36 Hz and 42 Hz compared with the SEMM start model (green). Also the iterative SEMM model without adaption to changed boundary conditions (gray) slightly enhances the force estimation at most operational frequencies but note that there are exceptions at 30 Hz and 44.5 Hz operational speed as discussed in Sec. 6.1.

<sup>4</sup>see Eq. (6.7) up to Eq. (6.11).

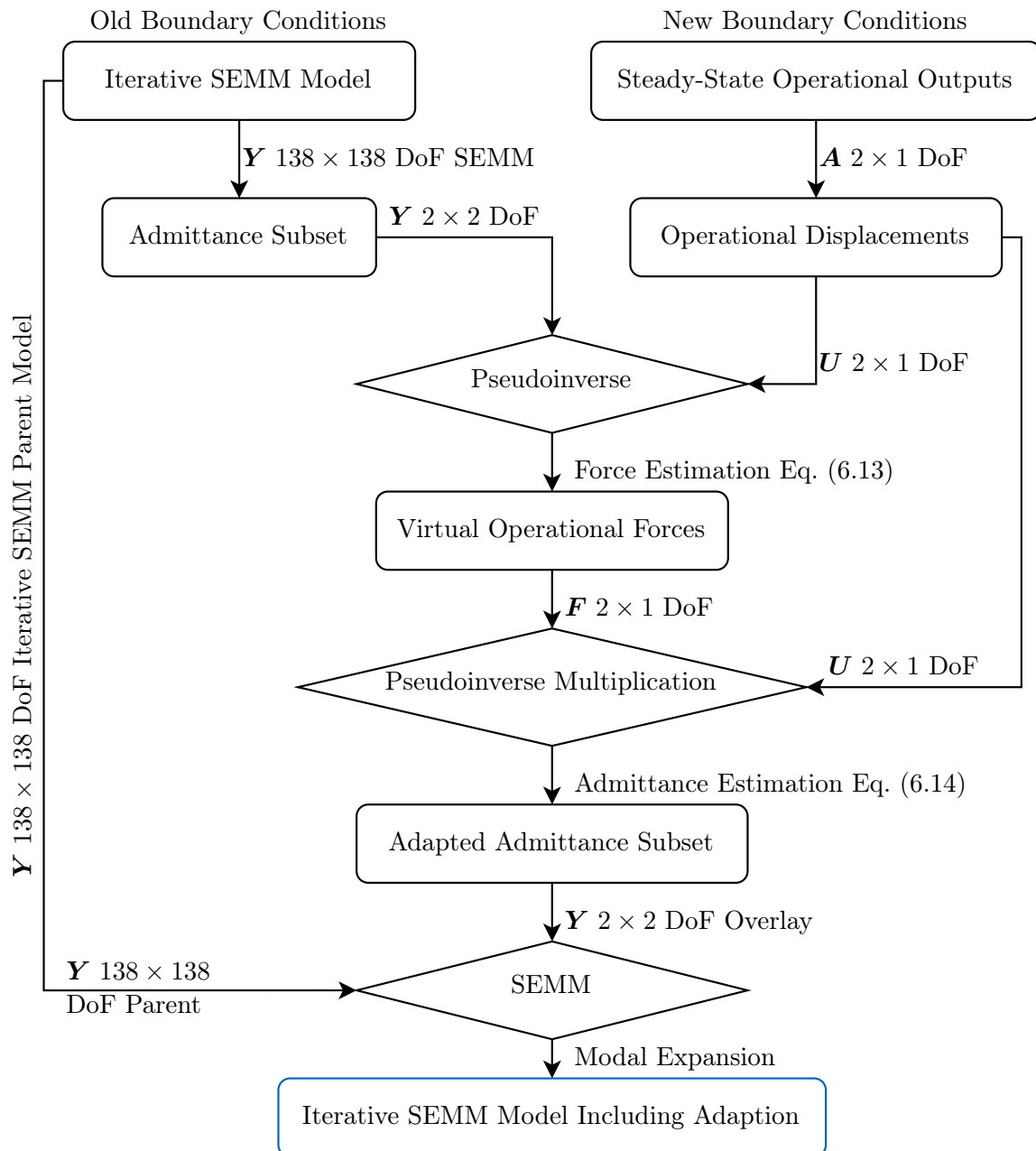


**Figure 6.13:** Model adaption to varying boundary conditions via unique SEMM expansion. The operational outputs are extracted from measurements at an application with boundary conditions different to the iterative SEMM model. This SEMM model is updated by these measurements containing information about the system modification. In the end, we get an iterative SEMM model including the new boundary conditions due to the adaption process (blue).

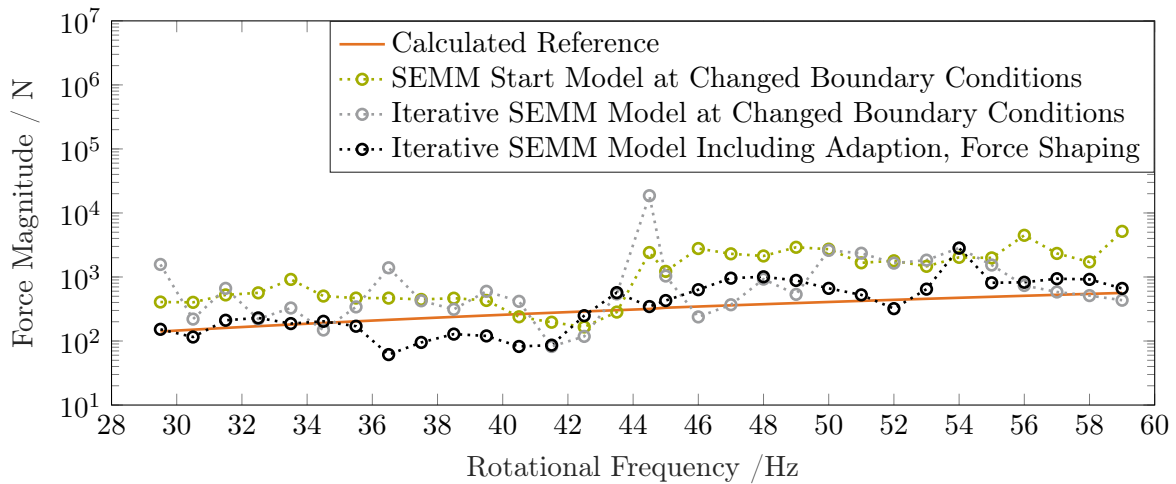


**Figure 6.14:** Unbalance force estimation over the entire operational speed range strictly at the operational speed frequency lines at 20 g unbalance. The results are based on the SEMM start model (green), the iterative SEMM model (gray) and the iterative SEMM model including one-step adaption to the changed boundary conditions and adaptive force shaping (black).

### 6.3 Summary

Within this chapter, an iterative modal expansion method was presented based on a minimal sensor setup containing two accelerometers for model adaption to operational conditions. Furthermore, a single triaxial accelerometer was used for a model adaption to changed boundary conditions. The method behind builds on the System Equivalent Model Mixing technique. In the presented methodology, the “magic” happens within an iterative Moore-Penrose pseudoinverse filtering on virtual operational forces. These forces were subsequently smoothed by an iterative spline fitting technique. This method was introduced since at some operational speed frequencies, the resulting force spectrum showed pronounced, unphysical spikes. Proper robustness of the final force estimation was shown at the overall operational frequency range. Furthermore, the entire process was applied to changed boundary conditions of the exemplary test rig. In this context, the sensor setup was further reduced to a single accelerometer at the housing. Here, the force shaping robustness fails at some operational frequencies. Though, the technique can properly adapt the hybrid model to changed boundary conditions. All estimated forces along the operating frequency range were experimentally validated by implementing an exemplary unbalance on the blower test rig. Due to varying operational conditions at different rotational frequencies, the entire process was gone through for each rotational speed frequency separately.



**Part III**

**Industrial Applications**



# Application of a Final Sensor System

In this chapter, we propose a possible solution for a final sensor system as exemplary application for the presented hybrid models. Our condition monitoring strategy targets constrained devices as industrial, wireless sensor nodes. In the first section, we show a case study for an experimental sensor characterization based on a MEMS sensor, which was already utilized within Sec. 3.4 for the comparison of roller bearing diagnosis methods. The subsequent evaluation concerning frequency response and temperature sensitivity is based on a condition indicator. This tracer was described in Sec. 3.4.4 and has emerged as suitable criterion for bearing fault diagnosis based on wireless MEMS sensor systems. Also on that foundation, the proposed sensor system is evaluated on a virtual sensing technique, whereby the virtual sensor is placed in the inaccessible bearing center. Finally, the same device is applied to the scenario of adapting the sensor system to varying boundary conditions on the blower test rig example in Sec. 7.3.

## 7.1 Experimental Sensor Characterization

MEMS sensors often imply interdependent drawbacks as noise, limited bandwidth and acceleration range or sensitivity [31, 79]. Despite of these problems, they can reach high bandwidth, high acceleration range [53] or rather high resolution [151]. However, their significant benefit of having a digital output can be destroyed by internal filtering, which cannot be modified. These specific filter characteristics are often not disclosed by manufacturers. In order to ensure proper transfer quality, the sensor's individual transfer function must be evaluated experimentally. A reasonable approach to improve the measured signals from MEMS accelerometers was already shown in [12]. Here, the authors determined a characteristic filter function to enhance the linearity. In the presented case, we regard the sensor system as an additional transmissibility, which can be added to the presented hybrid model in the frequency domain representation. Furthermore, the sensor's transfer behavior itself is evaluated by applying different references and varying temperature conditions.

### 7.1.1 Frequency Response Linearity Evaluation

A test rig was set up for an experimental MEMS accelerometer characterization. A LabView-based control unit was used, which was essentially constructed by Pejic in [96]. He assembled an electrodynamic shaker (Brüel & Kjaer 4809) on a decoupled basis and controlled it based on a National Instrument NI PXIE-1062Q Chassis. Therefore, a piezoelectric reference accelerometer was mounted on the shaker. This vibration exciter is supplied with a test voltage signal which is defined in the LabView program, created by a waveform generator and boosted by a shaker power amplifier. The reference sensor measures the resulting acceleration

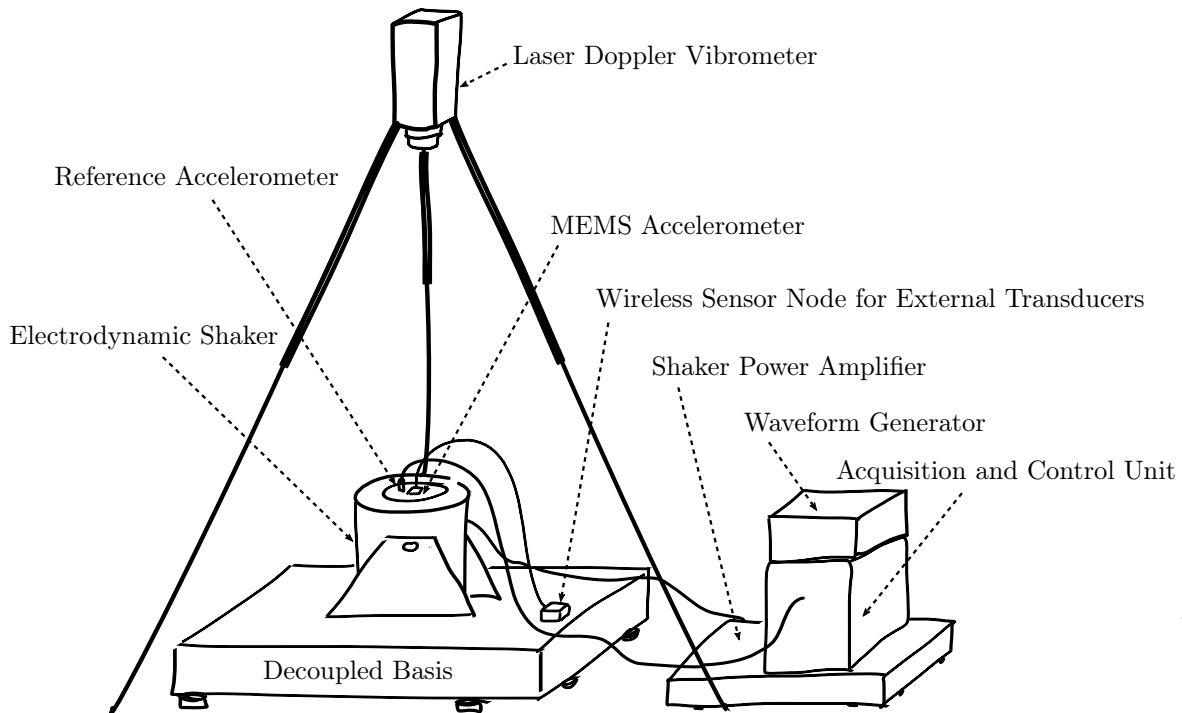


**Figure 7.1:** MEMS accelerometer amplitude response characterization test rig. The set-up is depicted including both reference sensors (piezoelectric accelerometer and a laser doppler vibrometer).

on the shaker's table. This signal is fed into the NI chassis again and checked in terms of deviation from the nominal value. The shaker voltage is then adapted and the reference acceleration is measured again. Based on that groundwork, we developed a software for test automation and integrated a laser doppler vibrometer for signal acquisition to get a non-intrusive, high-quality reference vibration signal. Utilizing the laser vibrometer, drawbacks as additional mass on the shaker and distortion due to inconvenient sensor mounting or specific resonances within the reference measurement chain are eliminated. An overview over the test rig is depicted in Fig. 7.1. Instead of characterizing the entire node, we characterized only the MEMS built in the node. Hence, we utilized an external MEMS accelerometer without any disturbances by structural dynamics of circuit boards or housing of the sensor node. Therefore, the accelerometer is connected via an external cable with the wireless sensor node. This box contains a micro-controlled digital signal processing unit including wireless connectivity infrastructure. The main characteristic properties of the evaluated accelerometer (LSM6DSL by STMicroelectronics) associated with the sensor box are:

- Output data rate (sampling rate): 3332 S/s,
- Measurement range:  $\pm 20 \text{ m s}^{-2}$
- Sensitivity:  $0.61 \text{ mm s}^{-2}/\text{LSB}$ ,
- Noise density:  $800 \mu\text{s}^2/\sqrt{\text{Hz}}$ ,
- Snapshot measurement time: 0.615 s,
- Samples per snapshot: 2048,
- Ambient temperature:  $20^\circ\text{C}$  (unless otherwise specified).

Based on the MEMS sensor Nyquist frequency, we desire sharp low-pass filtering at 1666 Hz evoked by the internal anti-alias filtering. This specific filter characteristic is evaluated with the presented test rig. Therefore, a logarithmic 200-point frequency vector for the shaker input was defined from 10 Hz up to 10 kHz using an excitation amplitude of  $\pm 5 \text{ m s}^{-2}$ . This amplitude was selected to ensure a sufficient signal-to-noise ratio within the low frequency area. Furthermore, we needed to stay properly within the measurement range keeping in mind the  $9.81 \text{ m s}^{-2}$  static acceleration of gravity. The measurement time of 0.615 s was repeated every 30 s. Due to the use-case envisioned for this method will later require low power consumption, the time was set that short. All snapshots were sent to a gateway (Siemens IOT 2040) via Wireless-LAN. The snapshots were downloaded from there in order to evaluate them offline. Within the snapshot measurements, stationary excitation is required. We must not measure within switching between two frequencies. Therefore, the hold time at every frequency step was set to 45 s to ensure stationary snapshots within all 200 frequency steps. In that time slot, the Root Mean Square (RMS) amplitude was measured by the reference and the MEMS sensor. We used a laser doppler vibrometer (Polytec OFV-525/-5000-S) and a monoaxial piezoelectric accelerometer (Brüel & Kjaer 4397) at 100 kS/s sampling rate as references. The MEMS RMS amplitude is calculated for every snapshot. This value divided by the reference RMS amplitude is written for every frequency line. Thus, we get an amplitude response function. An example is depicted in Fig. 7.2. Here, the results are shown for a triaxial MEMS sensor (STMicroelectronics LSM6DSL) utilizing the piezoelectric accelerometer as well as the laser doppler vibrometer. Note that only the sensor z-axis is observed here because it is most used within the exemplary applications here. We observe an almost linear transfer transmission behavior up to a frequency of nearly 500 Hz. Here, a small peak is visible, which is more pronounced in the transmissibility utilizing the piezoelectric reference. The mass removal when using the laser vibrometer instead of the piezoelectric accelerometer in this frequency area might be a reason for that. Thus, we expect a test setup specific phenomena which has probably nothing to do with sensor specific properties. On the other hand, this peak can come from digital filtering ripple. This leads to the transfer performance around the Nyquist frequency. The roll-off starts beyond 2 kHz, which is far too late. The range from the Nyquist frequency at 1666 Hz up to that value can be mirrored at the Nyquist line. Thus, this aliasing renders an important frequency range of the measurement unusable. The internal filtering is too weak. The subsequent amplitude amplification increase starts again above 3 kHz but remains somewhat better low-pass filtered.

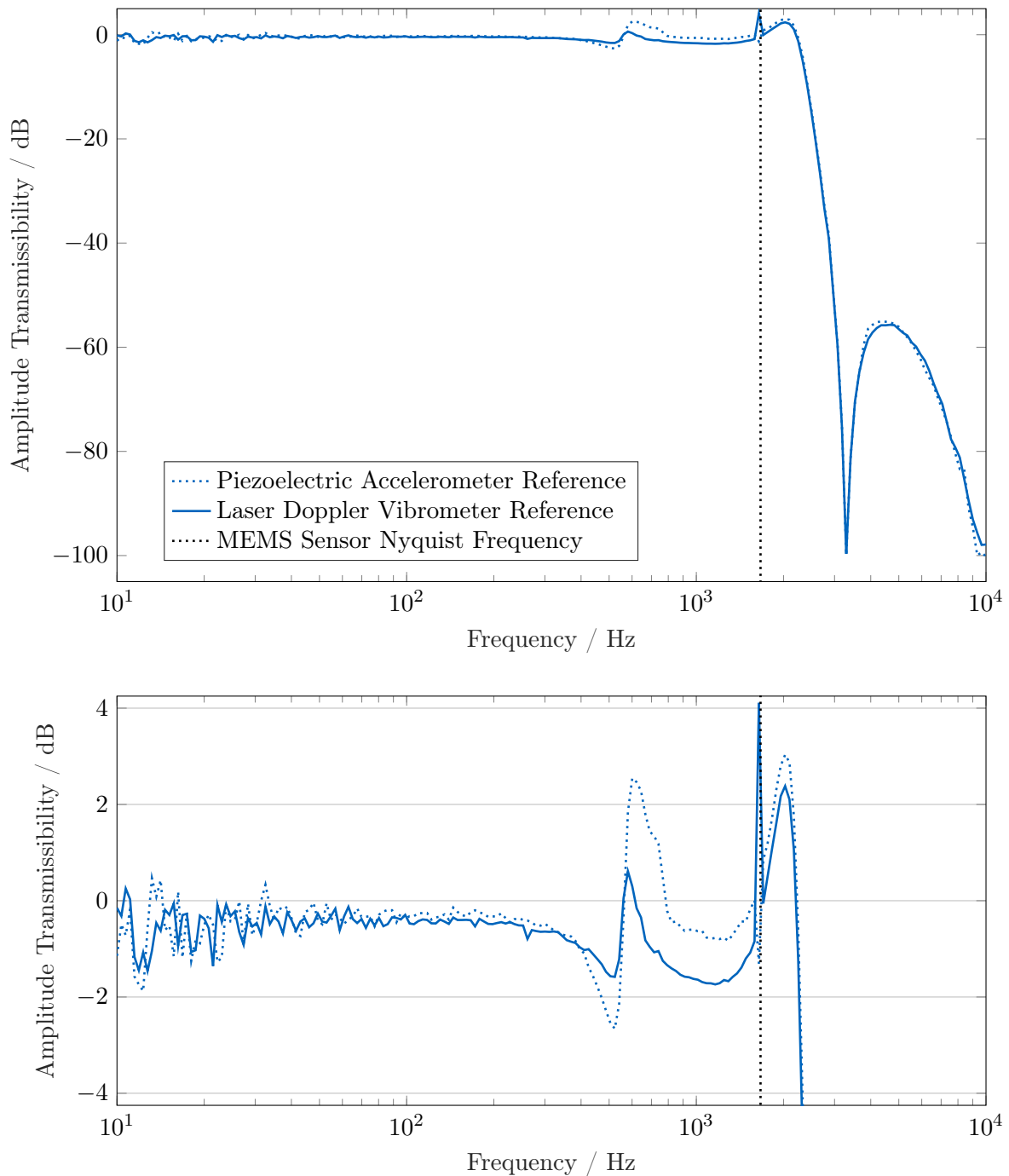


**Figure 7.2:** Evaluation of the applied MEMS sensor (STMicroelectronics LSM6DSL generation 2017) concerning the amplitude response function. The sensor is evaluated utilizing a piezoelectric accelerometer as reference (dotted line) and a laser doppler vibrometer (solid line). Entire transmissibility range (top) and zoomed transmissibility up to the Nyquist frequency area (bottom).

### 7.1.2 Temperature Sensitivity Characterization

Temperature-specific sensitivity and temperature dependent sampling frequency drift are common disadvantages of various MEMS sensor types [56]. These changes express themselves within the specific frequency response. Hence, the same single-sine excitation test as in Sec. 7.1.1 was performed to evaluate the amplitude frequency response. In this case, a piezoelectric accelerometer was utilized as reference (Brüel & Kjaer type 4309) since the test rig needs to be placed inside a climatic chamber in which there is not enough space for a laser doppler vibrometer. The experimental test set-up is depicted in Fig. 7.3.

The MEMS sensor and the piezoelectric reference are placed on the electrodynamic shaker described in Sec. 7.1.1. The surrounding air temperature is measured by two thermocouples (National Instruments type K). Essentially, the temperature is controlled by the climatic chamber (Völtch type VCL 7010) using a PT100 transducer and cross-checked by the thermocouple measurement. The amplitude response measurements were performed at four different temperature steps from  $0^{\circ}\text{C}$  up to  $60^{\circ}\text{C}$ .

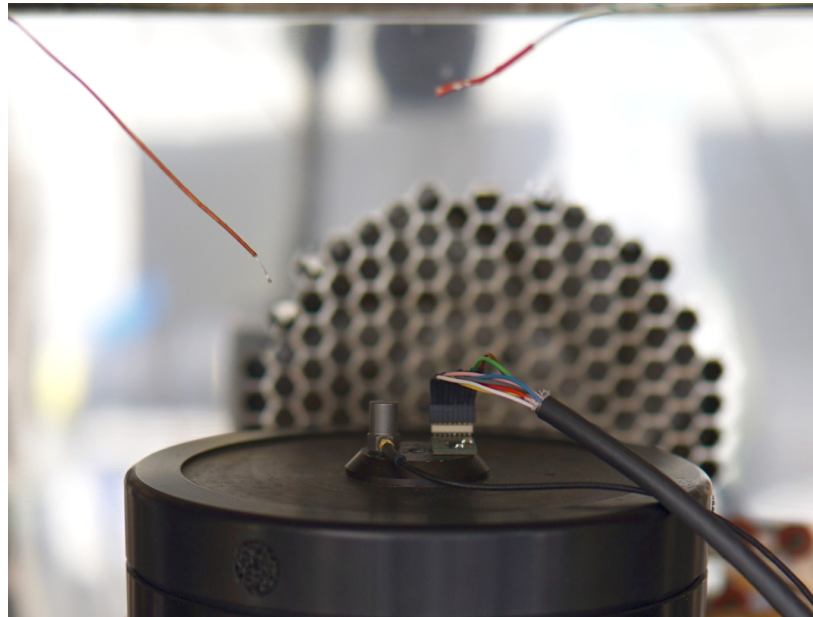


**Figure 7.3:** Climatic chamber interior with electrodynamic shaker, piezoelectric reference accelerometer (left) and MEMS sensor as device under test (right). The two red wires rising into the surrounding air represent thermocouples for temperature monitoring during the amplitude frequency response measurements.

For each temperature stage, steady state was ensued by a hold time of half an hour, before the test from 10 Hz to 10 kHz at 200 logarithmic frequency steps was performed. The result is depicted in Fig. 7.4. Here, a slight transmissibility decrease with rising temperature is observable. This effect remains within one decibel below the Nyquist frequency. At the amplitude response increase shortly after that, the temperature impact is a little bit higher (approximately two decibel). Nevertheless, the temperature sensitivity keeps in acceptable limits.

Even though the temperature sensitivity seems insignificant, we need to check if the small observed effect does not issue from inadequate repeatability. In order to examine that potential manifestation, the same test as depicted in Fig. 7.4 was repeated at constant temperature of  $20^{\circ}\text{C}$ . The result is depicted in Fig. 7.5. Here, proper reproducibility is visible over the entire tested frequency range except for an outlier at the Nyquist frequency. When comparing the temperature sensitivity with reproducibility measurements (Fig. 7.4 and Fig. 7.5), irregularities around 700 Hz also seem to result from a lack of repeatability. Overall, however, the reproducibility is to be classified as satisfactory.

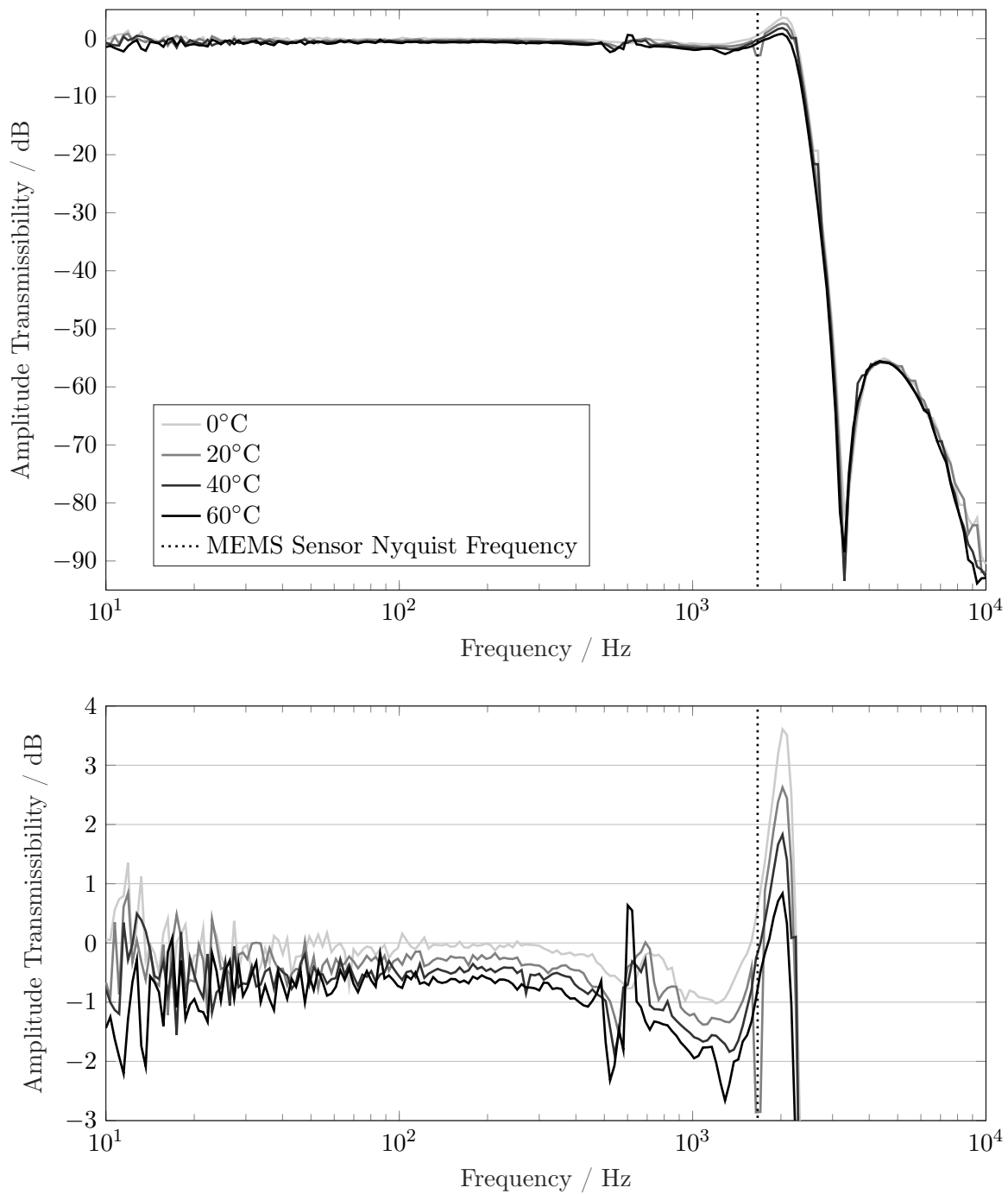


**Figure 7.4:** Temperature sensitivity consideration of a MEMS accelerometer (STMicroelectronics LSM6DSL generation 2017) at four different temperature levels. Whole transmissibility dynamic (top) and zoomed range up to shortly above the Nyquist frequency (bottom).

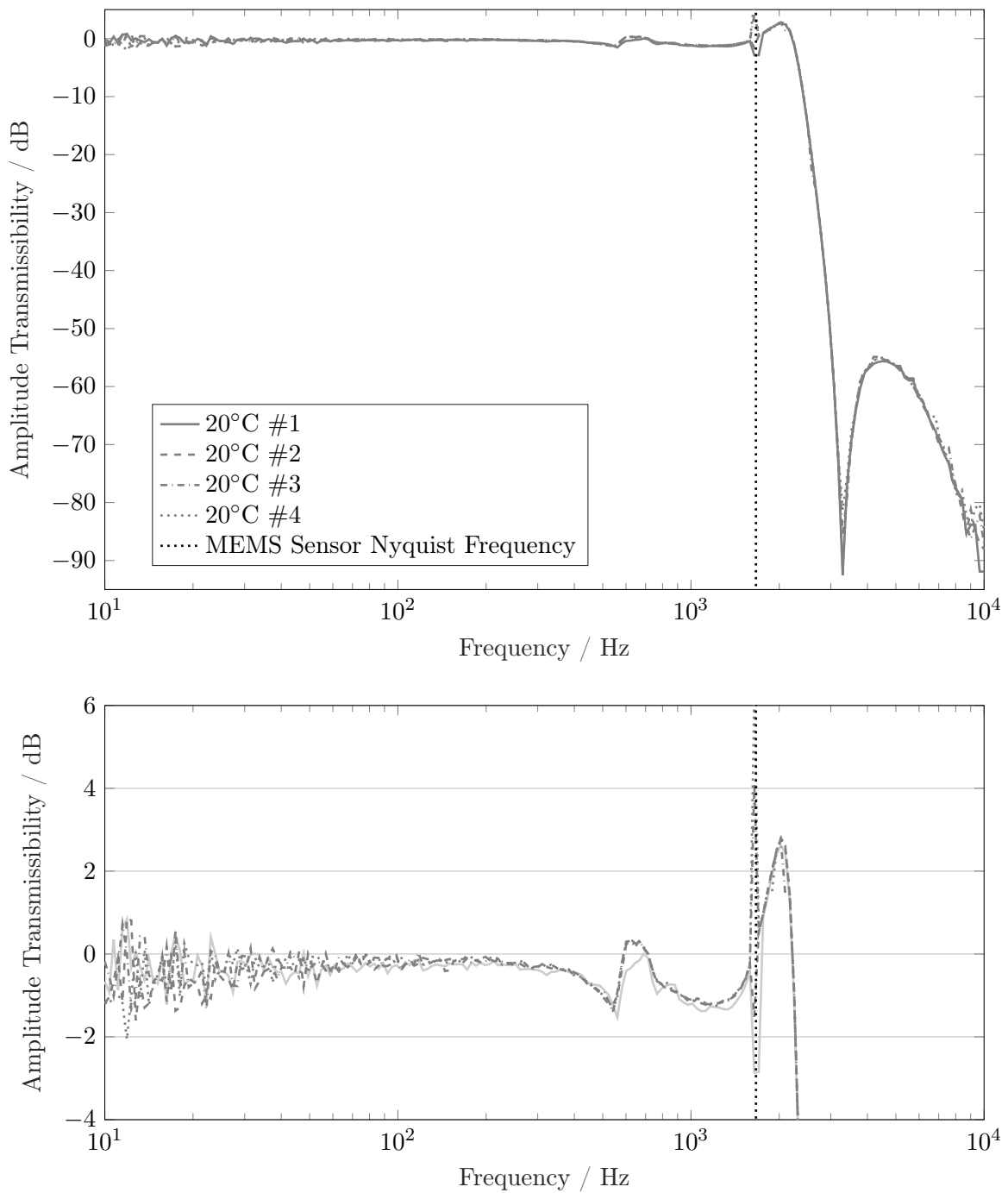


**Figure 7.5:** Amplitude response reproducibility check at a constant temperature of 20 °C regarding the exemplary MEMS accelerometer (STMicroelectronics LSM6DSL generation 2017). Whole transmissibility dynamic (top) and zoomed range up to shortly above the Nyquist frequency (bottom).

### 7.1.3 Summary

In this section, an exemplary MEMS accelerometer was qualified for a final sensor system concerning its frequency response linearity, reproducibility and temperature sensitivity. The evaluated sensor showed deficiencies referring to filtering around the Nyquist frequency. The transmissibility slightly decreases with higher temperatures but stays in an acceptable range. Even the reproducibility within four samples was classified as satisfactory.

## 7.2 Virtual Sensing for Bearing Fault Diagnosis

In this section, an exemplary scenario is shown where the presented constrained sensor system is applied to calculate virtual vibrations at inaccessible measurement positions. The approach is based on a virtual force assumption [87, 88]. Essentially, the idea of the virtual force consists in accounting for the fact that the measurement for the diagnosis is not performed directly at the inaccessible location of the force related to the fault, but is observed away from it at a location that can be accessed. Therefore, coupled transfer functions in combination with a transmissibility function at operation of the pump test rig are applied. With the proposed technique, we are able to estimate the fault impact forces directly at the bearing utilizing a virtual sensor there. These forces are converted to accelerations using an adequate frequency response to validate it with a piezoelectric reference accelerometer. Finally, industrial usability is observed by calculating the dispersion of results based on the transfer functions of three pumps within the presented test rig.

### 7.2.1 Virtual Sensing and Validation

In the presented case study, we placed a piezoelectric reference sensor at an exemplary, *inaccessible* point at the bearing seat to validate the predicted acceleration. The setup including preprocessing of the transfer functions is demonstrated at the pump test rig. The final observation is made using the previously introduced MEMS sensor system to calculate the exact acceleration at a faulty bearing<sup>1</sup>. The reference accelerometer is mounted directly at this bearing to validate the results<sup>2</sup>.

In the presented example, we roughly estimate the transfer behavior by considering only one single axis. In reality, the fault impacts excite the structure more or less in all six degrees of freedom. We just pick out the radially orientated x-direction and observe the system concerning that single axis. This radical approximation drastically simplifies the preprocessing test effort in order to get the required FRFs within industrial requirements. These FRFs can be determined by different partners in the industrial environment. Hence, preprocessing effort must be minimized. Specifically, the following assumed transfer-/transmissibility functions are required for the presented method<sup>3</sup>:

- The bearing driving point admittance  $\mathbf{Y}_{11}$  (not accessible for an impact hammer or shaker) is roughly approximated by the driving point FRF  $\mathbf{Y}_{22}$ .
- The transfer function  $\mathbf{Y}_{21}$  between bearing excitation position (1) and housing response measurement position 2 is estimated under reciprocity assumption by  $\mathbf{Y}_{12}$ .

<sup>1</sup>see Fig. 4.14 for the implemented, exemplary bearing defect.

<sup>2</sup>sensor position (1) in Fig. 4.15.

<sup>3</sup>see descriptions in Fig. 4.13 and Fig. 4.15.

- The transmissibility function  $\mathbf{T}_{23}$  between housing measurement location (2) and MEMS sensor position (3) is additionally required to implement further information about the transfer behavior at operation.

In this context, rough assumptions are needed. These are reasonable because of some investigations, we made within the test rig characterization (Sec. 4.2). In Sec. 4.2.1, the reproducibility of three pump samples in radial direction was proven. On this basis, and because of the rigid axial flange design, the estimation is made that the radial FRFs  $\mathbf{Y}_{11}$  and  $\mathbf{Y}_{22}$  are not too different. The hope is to reduce resulting errors by including a transmissibility function at pump operation. Hereby, the transmissibility  $\mathbf{T}_{23}$  is integrated between the well accessible housing position (2) and MEMS sensor location (3). Using that information, dynamics are captured which are missed by the FRF assumptions. In detail, a measurement at these two locations was performed within steady-state pump operation (58.3 Hz rotational speed). In terms of measurement equipment, a Brüel & Kjaer piezoelectric reference accelerometer type 4397 in combination with a SKF Microlog GX<sup>®</sup> data logger at 25.6 kS/s sampling frequency was used. We measured for 30 s and performed the FFT over two second blocks. The resulting 15 magnitude spectra with 0.5 Hz frequency resolution were averaged in the frequency domain to eliminate time-variant peaks. In order to calculate the *transmissibility*  $\mathbf{T}_{23}$ , the quotient of these spectral absolute values concerning the results at measurement locations (2) and (3) was formed.

The set-up to generate these operational output spectra for transmissibility computation contained a defective bearing. The defective bearing was chosen due to an impact-like excitation of the entire system by the fault at the bearing position (1). Note, this excitation does not constitute a perfect, broadband, uniformly distributed noise and - to be precise because of that -  $\mathbf{T}_{23}$  captures not a real transmissibility function. Though, we utilized a large bearing defect (similar to Fig. 4.14 but with 3 mm groove fault width) and applied this kind of *oscillating impact excitation*.

Now, a relation between the functions explained above and the virtual bearing vibration  $\mathbf{a}_1$  is established. The transfer behavior  $\mathbf{Y}_{21}$  between housing and bearing is initially needed to get the force on the bearing as

$$\mathbf{F}_1 = (\mathbf{Y}_{21})^{-1} \cdot \mathbf{a}_2. \quad (7.1)$$

Therefore, the housing acceleration  $\mathbf{a}_2$  at operation is indirectly calculated by the transmissibility function  $\mathbf{T}_{23}$  and a snapshot of operational acceleration  $\mathbf{a}_3$  is obtained by the MEMS sensor system<sup>4</sup>:

$$\mathbf{a}_2 = \mathbf{T}_{23} \cdot \mathbf{a}_3. \quad (7.2)$$

To sum up, we get

$$\mathbf{a}_1 = \underbrace{\mathbf{Y}_{11} (\mathbf{Y}_{21})^{-1} \mathbf{T}_{23}}_{\mathbf{T}_{13}} \cdot \mathbf{a}_3 \quad (7.3)$$

for the virtual bearing acceleration.

In order to validate the results via an accelerometer due to immeasurability of the force  $\mathbf{F}_1$  directly at the bearing, we calculated the resulting acceleration by the estimated driving point admittance  $\mathbf{Y}_{11}$ . Finally, the results were cross-checked by MEMS-snapshots which were taken within operation using the large bearing fault as well as the smaller bearing defect. These snapshots were utilized as  $\mathbf{a}_3$  to feed Eq. (7.3) aiming to calculate the virtual bearing acceleration  $\mathbf{a}_1$

---

<sup>4</sup>measurement time: 0.651 s.

This acceleration was subsequently compared with the real measured accelerations at bearing (1), housing (2) and the MEMS position (3). The real bearing vibration was taken to validate the result of Eq. (7.3). Fig. 7.6 shows the coupled transfer function  $\mathbf{T}_{13}$ . The approx-

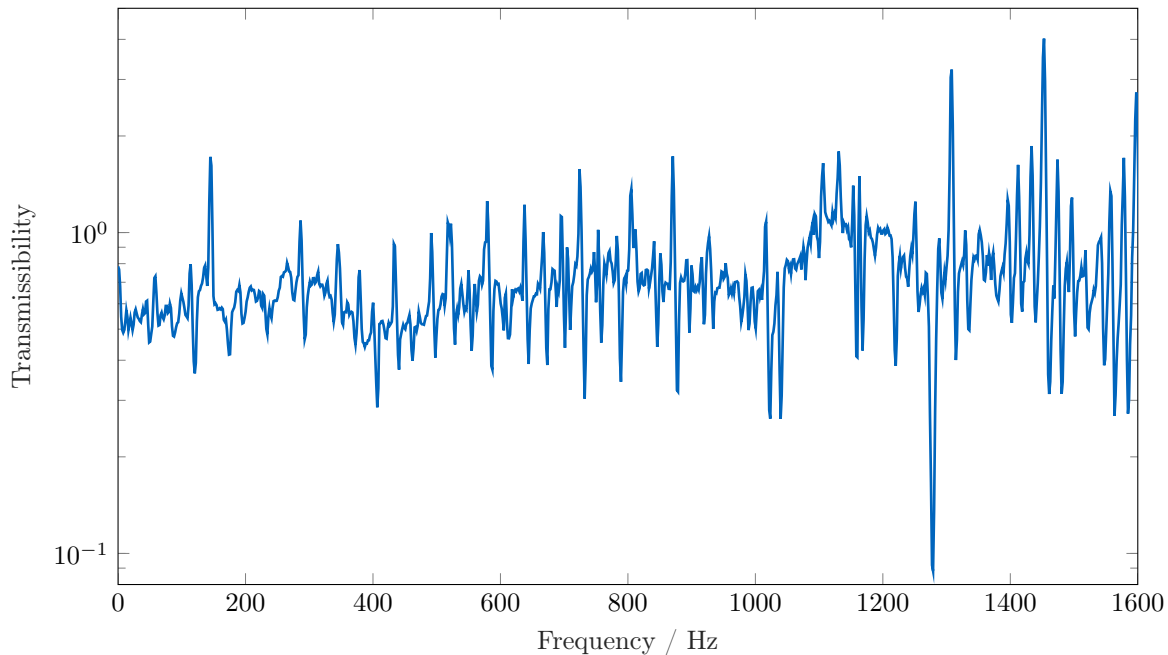


**Figure 7.6:** Transmissibility function  $\mathbf{T}_{13}$  resulting from Eq. (7.3) between the MEMS sensor position (3) and a virtual bearing location (1) in radial x-direction of the oil pump test rig.

imated transmissibility implies pronounced dynamics over the whole frequency range. It will significantly influence future considerations regarding  $\mathbf{a}_1$ . Note that most of the recurring peaks stem from the excitation at operation. They are related to the operational speed and seem not to come only from the housing dynamics.

Considering possibly temperature influence as discussed in 4.2.3, we picked a measurement at approximately constant 20 °C oil temperature<sup>5</sup>. In order to properly evaluate the validity of the procedure, we considered the signal-based condition indicator  $\mathcal{I}_f$ <sup>6</sup> to obtain a scalar assessment criterion. Therefore, the Hilbert spectrum of the low-pass filtered virtual snapshot  $\mathbf{a}_1$  was calculated. In Fig. 7.7, the Hilbert spectrum result of the real measured MEMS snapshot at position (3) is shown, which is strongly dampened at the over-rolling frequency compared with the results at observed locations (1) and (2). Looking at the housing measurement (orange), the amplitude at bearing fault specific frequencies is much higher than at the MEMS position. Though, it deviates sharply from the original bearing acceleration (gray). However, the virtual calculated bearing acceleration at the bearing (blue) properly maps the real measured bearing vibration. The result with smaller bearing fault<sup>7</sup> also shows very good approximation although the integrated transmissibility  $\mathbf{T}_{23}$  was *trained* with the big fault. This kind of validation shows that the method including monitoring algorithm can be applied to existing (probably already defective) systems.

<sup>5</sup>oil temperature measured by a PT100 sensor at position (5) of the pump test rig.

<sup>6</sup>introduction see Sec. 3.4.4.

<sup>7</sup>see bottom parts of Fig. 7.7 and Fig. 7.8.

Now, the condition indicator was calculated for all measurement positions (1-3) including the virtual vibration snapshot. Referring to the indicator, with use of the Hilbert spectrum absolute values, we took a 13 Hz frequency band around the over-rolling frequency and its twofold harmonic. Subsequently, the summed RMS-value of these two bands was formed. In order to compare the results by scalar values, we calculated the *errors* which were made by the reference sensor at the housing, by the MEMS in the sensor box and by the MEMS including the coupled transmissibility  $T_{13}$  - namely the virtual bearing vibration. These errors  $\sigma$  were referenced to the real measured bearing vibration based on the condition indicator. Thus, we get for the large bearing fault (errors in relation to the actual measured bearing vibrations as reference):

- MEMS sensorbox measurement at position (3) in relation to the real value at position (1):  $\sigma_3 = 50\%$ ,
- Housing measurement at position (2) in relation to the real value at position (1):  $\sigma_2 = 29\%$ ,
- Virtual bearing vibration measurement at position (1) in relation to the real value at position (1):  $\sigma_1 = 8\%$ .

This means up to 42% error reduction by integrating the coupled transmissibility  $T_{13}$  in the MEMS measurement compared with the standard MEMS measurement at position (3). The MEMS sensorbox position is compared with the virtual bearing measurement position (1). For the smaller bearing fault, we get:

- MEMS sensorbox measurement at position (3) in relation to the real value at position (1):  $\sigma_3 = 50\%$ ,
- Housing measurement at position (2) in relation to the real value at position (1):  $\sigma_2 = 23\%$ ,
- Virtual bearing vibration measurement at position (1) in relation to the real value at position (1):  $\sigma_1 = 28\%$ .

Analogously, for the smaller fault, up to 22% error minimization is reached comparing the MEMS result with and without the virtual bearing position transformation.

Furthermore, the variation of the results for three pump samples was investigated. In detail, we determined the FRFs of three pump samples considering  $Y_{11}$  and  $Y_{21}$ . These affect the entire transmissibility  $T_{23}$  in Eq. (7.3). With respect to error calculation, the standard deviation utilizing a  $k$ -factor of 3.3 for the expanded uncertainty was computed referring to [62]. This factor was chosen based on selected 95% coverage probability. Summarized, this implies that all coupled admittances yield the averaged depicted peak values in Fig. 7.8 with 3.3-fold standard deviation. This standard divergence can be that high due to the small amount of tested pumps and the desired 95% coverage probability. In Fig. 7.8, the averaged virtual vibrations are depicted including error bars. Here, the over-rolling frequency Hilbert spectra maxima (fundamental frequency and first harmonic) are visualized again considering the large and the small bearing fault (top and bottom part of the figure). The error bars are shifted 3 Hz to the left from the peak for better visibility. At the large bearing defect (top of Fig. 7.8), we get:

- $1.00 \text{ m s}^{-2} \pm 0.07 \text{ m s}^{-2}$  concerning the over-rolling frequency peak,
- $0.18 \text{ m s}^{-2} \pm 0.01 \text{ m s}^{-2}$  at its harmonic

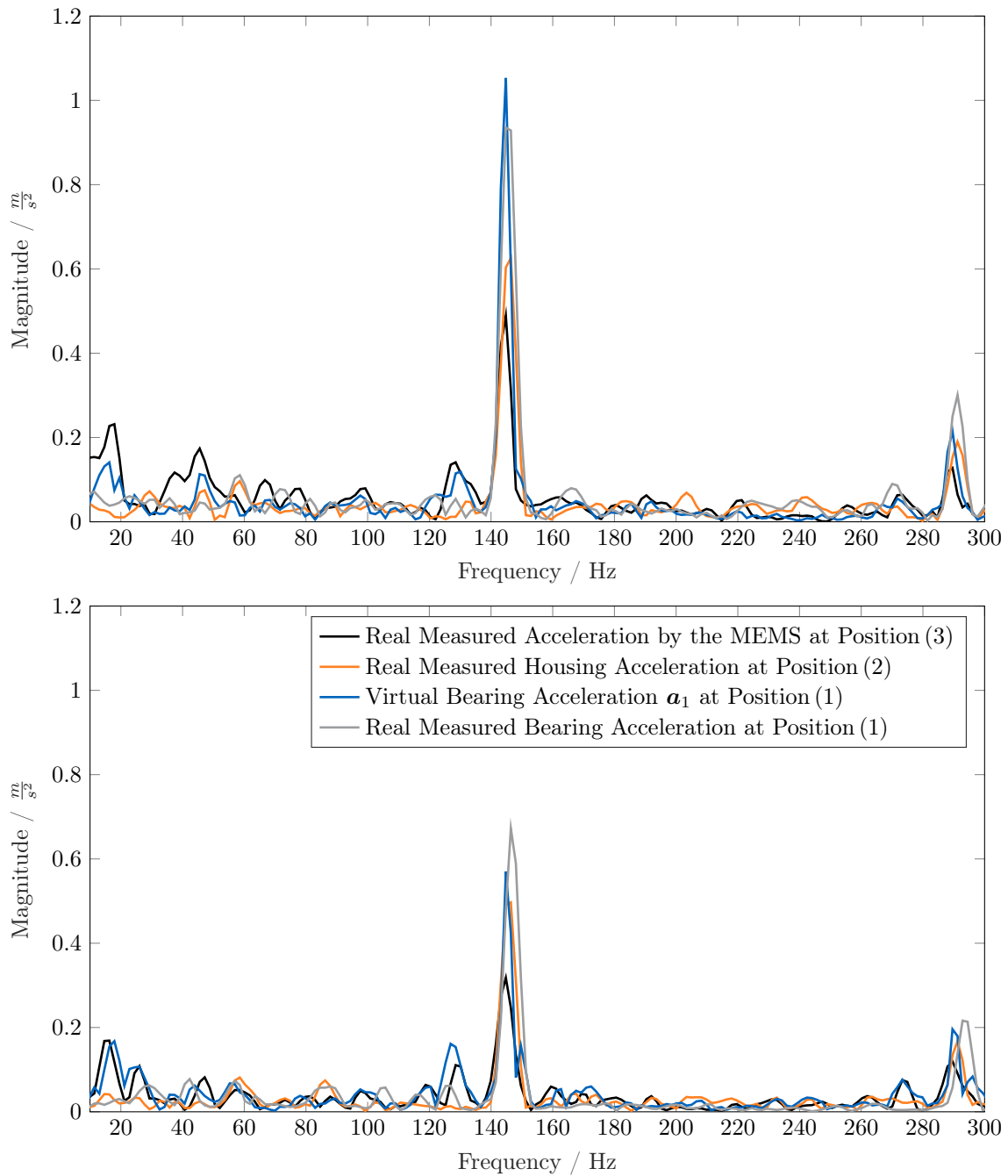


**Figure 7.7:** Hilbert spectra of the pump acceleration at stationary 58.3 Hz operational speed in radial x-direction. Comparison of the pump test rig measurement points (1-3). Bottom: Observation of the bearing fault of Fig. 4.14. Top: Results based on a bearing fault with twice fault groove width.

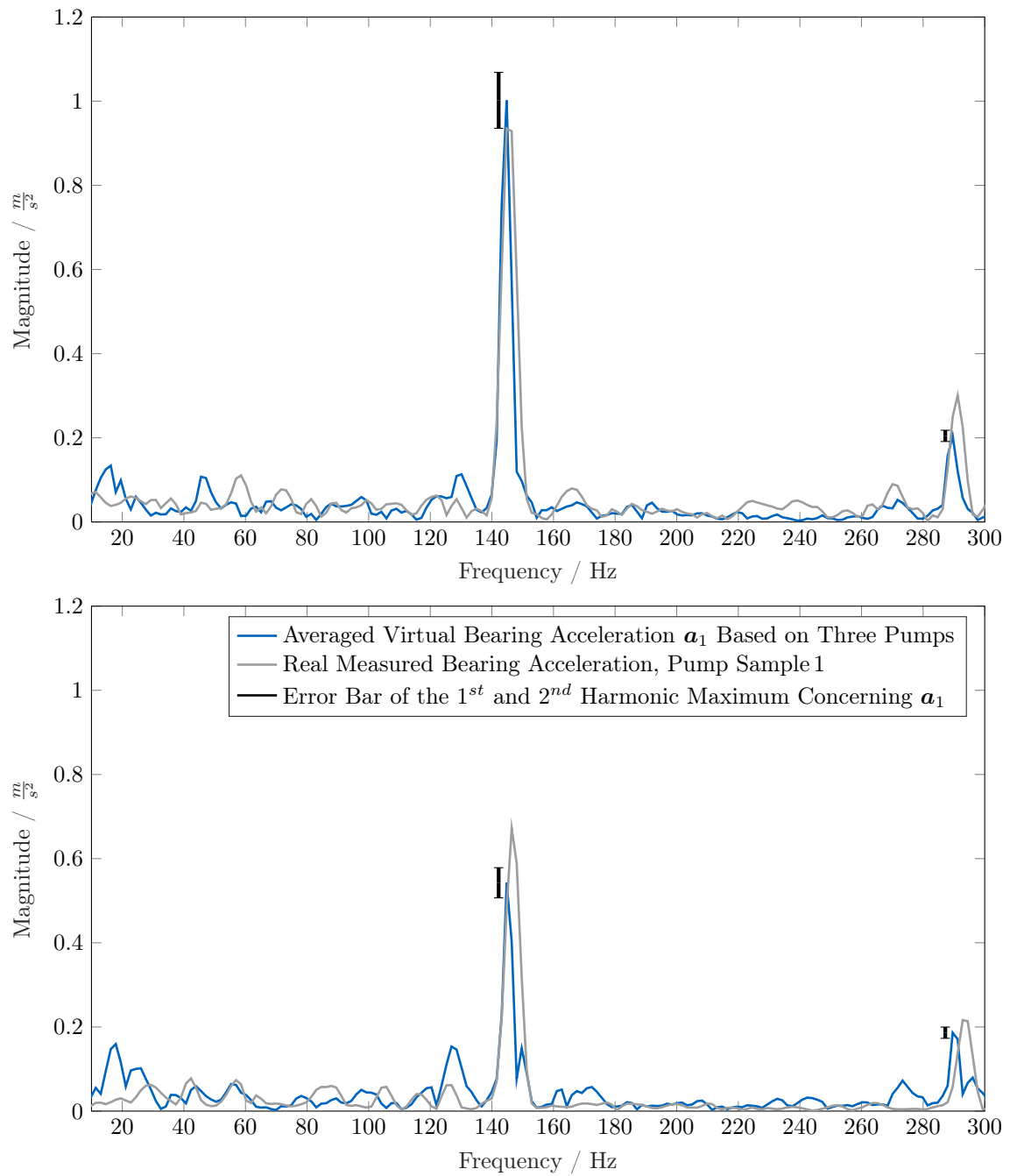


**Figure 7.8:** Hilbert spectra at the bearing measurement point (1). Error analysis at stationary 58.3 Hz operational speed in radial x-direction concerning the virtual vibration. The real measured bearing acceleration of the first pump sample is delineated as reference (gray). Bottom: Observation of the bearing fault of Fig. 4.14. Top: Results based on a bearing fault with twice fault groove width. The error bars (95 % coverage probability) are shifted to the left for better visibility of the peaks.

and the following values for the measurements at the smaller bearing defect:

- $0.56 \text{ m s}^{-2} \pm 0.04 \text{ m s}^{-2}$  again at the first peak and
- $0.19 \text{ m s}^{-2} \pm 0.01 \text{ m s}^{-2}$  at its harmonic.

In summary, this means relatively low dispersion and demonstrates independence from a single pump sample. Hence, the method is applicable within a series of the exemplary pump type since the dispersion is below 10% for the considered small and large bearing fault dependent peaks within the Hilbert spectra.

### 7.2.2 Concluding Summary

A case study with application of a virtual sensing technique for bearing fault diagnosis was shown. The error which is made when measurements are recorded far away from the vibration source can be significantly reduced by this method. Here, a coupled transmissibility function between a wireless sensor system and the bearing position showed proper results although only one measurement direction was observed. Based on the presented technique, the operational force and the vibration directly at the bearing can be determined. All FRFs show small dispersion within three tested pumps. The virtual bearing vibration allows early condition decisions due to accurate and precise diagnosis. Early condition decisions can lead to extension of required service intervals and cost reduction as long-term consequence within the final application.

## 7.3 Application of an Industrial Sensor System to the Blower SEMM Model

In this section, we apply the exemplary industrial MEMS sensor system to the blower test rig under the same, modified boundary conditions as in Sec. 6.2. In this case, the additional mass that was used to change the boundary conditions (see Fig. 7.9) changes the dynamics of the system and thus also the transfer path between an applied unbalance force and the sensor. The sensor system itself introduces system dynamics by its circuit board and housing. Note that these dynamics are not included in the model so far - unlike the experimental model in Sec. 7.2.1, where these dynamics were accounted for by the measured transmissibility. The MEMS accelerometer is mounted directly on this board, where all electronic devices of the system are placed. An experimental modal analysis of the mounted circuit board yielded a first resonance at 900 Hz. This resonance of the sensor system's antenna on the board directly falls into the measurement range of the MEMS sensor. Note, these board vibrations are not reproducible due to manufacturing tolerances and mounting variations. Thus, individual sensor box dynamics can be regarded as part of the transfer path between fault and measurement position.

With the presented method, the dynamics of the sensor box are handled by counting them as an element of varied boundary conditions of the entire monitored system. Before starting with the presentation of our findings, we look back to Sec. 6.2. Here, a proper validated hybrid model of the blower test rig was adapted to changed boundary conditions. The motivation was an adjustment of an existing model to a varied field periphery. This modified *field periphery* was represented by an attached extra mass of 37 kg<sup>8</sup>. Now, the blower is observed by the sensor box containing the previously tested MEMS sensor.

<sup>8</sup>see  $m_{bc}$  in Fig. 7.9.

The MEMS sensor box is glued on the blower housing as schematically depicted in Fig. 7.9 utilizing adhesive wax. We only regard the two horizontal operational output DoF of the triaxial MEMS sensor  $\mathbf{U}_b$  to estimate two virtual motor block forces  $\mathbf{F}_b$

$$\mathbf{F}_b = (\mathbf{Y}_{b_u b_f})^+ \mathbf{U}_b. \quad (7.4)$$

with the same dimensions of  $\mathbf{F}_b$ ,  $\mathbf{U}_b$  and  $\mathbf{Y}_{b_u b_f}$  as we had within the reference measurements in Sec. 6.2. These forces are not directly used for fault estimation but applied to assemble a new, small experimental model  $\mathbf{Y}_{b_u b_f}^{(2)}$ :

$$\mathbf{Y}_{b_u b_f}^{(2)} = \mathbf{U}_b (\mathbf{F}_b)^+. \quad (7.5)$$

This admittance is subsequently implemented into the fully extended interface SEMM. The objective is the introduction of information about the changed boundary conditions as well as the sensor box dynamics by this single SEMM expansion step. We summarize the procedure again as follows:

$$\mathbf{Y}_{b_u b_f}^{(2)} = \mathbf{U}_b \left( (\mathbf{Y}_{b_u b_f})^+ \mathbf{U}_b \right)^+. \quad (7.6)$$

$\mathbf{Y}_{b_u b_f}^{(2)}$  is fed into the fully extended interface SEMM method as shown in the flow chart of Fig 6.13. Subsequently, the unbalance force vector is estimated as

$$\mathbf{F}_u = \mathbf{U}_h (\mathbf{Y}_{h_u r_f})^+ \quad (7.7)$$

based on the admittance matrix  $\mathbf{Y}_{h_u r_f}$  between operational unbalance forces at the rotor plate DoF  $r$  and responses at the housing DoF  $h$ . Hence, again we get the scalar unbalance force  $F_u$  according to Eq. (6.11). This force is validated by the unbalance excitation of Eq. (6.6). In this example, an unbalance mass  $m_u$  of 20 g is applied at rated 59 Hz mechanical operational speed<sup>9</sup>.

The force is estimated by different models. We obtained the preliminary unbalance force estimation by the SEMM start model without the iterative updating to operational conditions (green line). By including the expansion loop for adaption to operational conditions as described in Fig. 6.4, we get the gray curve which is much more spiky than the green basis estimation. Though, the force would be approximated better when these peaks were eliminated. However, the adaption to changed boundary conditions was integrated by Eq. (7.6) to obtain  $\mathbf{Y}_{b_u b_f}^{(2)}$ . Herewith, the black force line in Fig. 7.10 was obtained. We can see a slightly better force estimation compared with the gray one except a high peak near to the operational frequency line. In order to minimize the peakedness, the spline fit-based iterative force shaping was applied according to Sec. 6.1.2. Finally, we got the blue force line as resulting estimation.

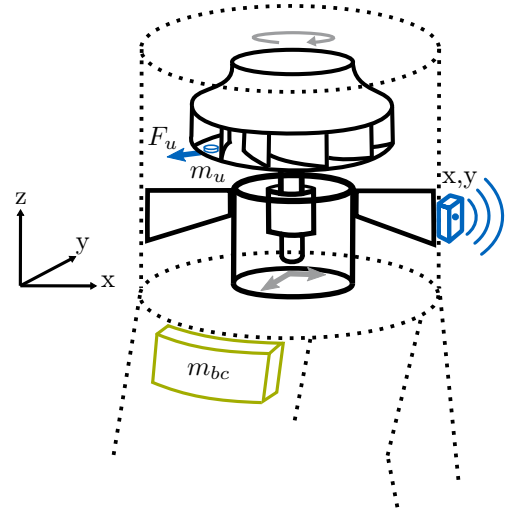


**Figure 7.9:** Setup of an exemplary final sensor system for model adaption to varying boundary conditions (additionally attached mass  $m_{bc}$ ). The same virtual excitation forces as in Sec. 6.2 at the lower motor block end (gray arrows) are used to adapt the model. A defined unbalance mass (blue disc,  $m_u = 20$  g) is attached to the rotor blade, evoking a defined unbalance force  $F_u$ . The model is adapted and validated by measurements at the outside housing utilizing an exemplary wireless sensor node (blue) including an onboard triaxial MEMS-accelerometer. Only horizontal directions are considered.

<sup>9</sup>This scalar represents the reference in form of an orange line in Fig .7.10.

The force shaping worsens the estimation of the iterative SEMM model including adaption to the varied boundary conditions in this example although it is better than the estimation by the SEMM start model. The result before the force shaping comes pretty close to the calculated reference force and can be valued as satisfactory.

### **Concluding Summary**

The force magnitude at rated operational speed frequency approaches the calculated reference force well. By using the iterative SEMM model including adaption to varied boundary conditions, we have a deviation of 7%. In this case, the adaptive force shaping worsens the result. Nevertheless, the estimation is still in the same order of magnitude afterwards. However, the results can be valued as satisfactory, keeping these complex, coupled transfer paths between fault source and measurement position in mind. Generally, an accurate statement concerning the operational forces is not easy due to pronounced, spiky dynamics along the frequency axis around the rotational frequency. Although, the final force estimation at the rotational frequency line is difficult to quantify exactly, the final outcome delivered an improved result of more than 500% compared with the SEMM start model. The underlying, iteratively adapted SEMM technique can therefore serve as a helpful tool for operational force estimations even for industrial MEMS sensor systems.

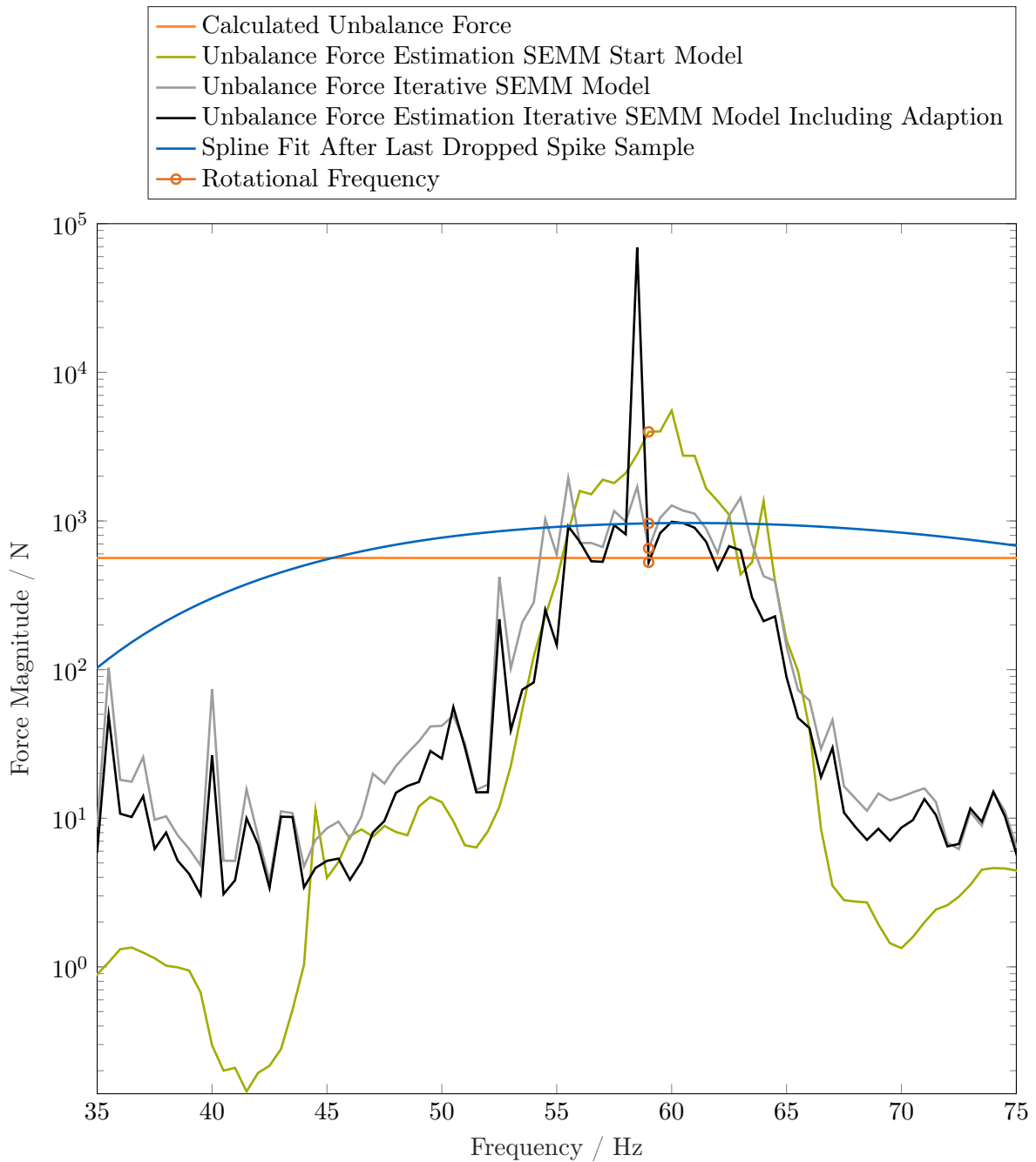


**Figure 7.10:** Force estimation by an exemplary onboard MEMS sensor at rated 59 Hz rotational speed and applied 20 g unbalance mass. The main force peak is visible near the fundamental frequency. An extended frequency range is depicted to show a spline fit's curve progression. Representation of force estimations based on three different SEMM models: start model, iterative model and iterative model with further adaption to modified boundary conditions due to 37 kg additional mass at the outside housing. Dynamics of the sensor circuit are also part of these boundary conditions. On the black curve, adaptive force shaping is applied. The spline fit after two dropped spike samples within three shaping loop runs (blue) is shown.



## Chapter 8

# Conclusion and Perspective

In this thesis, a methodology for condition monitoring approaches was developed based on hybrid dynamic models. Therefore, some of the latest methods in the context of structural dynamics were further adapted and extended to the application of fault quantification of rotating machinery. This chapter summarizes the main findings and provides a perspective for future research to tackle remaining challenges.

## 8.1 Concluding Summary

In the context of answering the research questions, how to develop hybrid dynamic models for industrial condition monitoring requirements, we found:

**Orthotropic elastic rotor support can reduce condition monitoring flexibility in case of measuring at the housing.**

Industrial rotor systems can be supported by bearings with orthotropic bearing stiffnesses. Here, forward and backward whirl occur within the rotor orbit when measured by two orthogonally aligned DoF at the housing. When the operational speed frequency merges with one of the support resonances, the vibration orientation at the outer housing can be solely aligned towards mode shape direction. These modes dominate the measured accelerations and can limit the frequency range for condition monitoring to a range excluding the associated resonances (see Sec. 4.1.1).

**Overhung impellers can be connected by equivalent stiffnesses to beam element shafts.**

Overhung impellers are often part of rotor systems in pump or blower systems containing abrupt, huge diameter changes. A common shaft modeling approach uses Timoshenko beam elements. This technique can not be applied to thin, circular discs which are often the base element of impellers. Here, an analogous stiffness element which connects the shaft with the impeller can solve the problem. This stiffness can be computed by an exemplary load scenario within a reference simulation. Based on the bending angle and the bending moment, the stiffness can be implemented in the element matrix in order to assemble a rotor model with only few degrees of freedom (see Sec. 5.1.2).

**System Equivalent Model Mixing can add missing interface dynamics of Lagrange Multiplier frequency-based substructuring but it can also introduce static offsets.**

In a perfect interface scenario, the Lagrange Multiplier frequency-based substructuring coupling constructs all system dynamics from the subsystems to a coupled, entire model which contains

the real structural dynamic properties. When the method is to be used on rotating machines where the rotor and housing are separate sub-components, the coupling must often be implemented at the bearings. The interface dynamics are usually unknown and not considered in this approach. Modal expansion using System Equivalent Model Mixing can add the information of the lacking interface dynamics. This effect was shown at a certain mode shape between rotor and housing. Although these dynamics are captured by almost all SEMM methods in the presented example, static offsets can occur for an extended frequency range. If the SEMM start model appears to be static but has enough DoF to be adaptive, a highly dynamic experimental model can adequately fit it to real dynamics, especially through the basic SEMM method (see Sec. 5.2.2).

**Pseudoinverse filtering can find virtual operational forces by iterative estimations using a small set of accelerometers.**

The Moore-Penrose pseudoinverse is a powerful method to filter core information from an overdetermined system. The structural dynamic changes due to operational conditions of a rotating machine can be implemented by a minimal sensor set. Here, one triaxial accelerometer close to the acting rotor force (for example the motor block) and one further sensor at the final monitoring system location (typically at the outside housing) can suffice to find an operational rotor force. This load is detected by filtering the displacement information in combination with pre-determined admittances. The technique is based on a hybrid model in the frequency domain representation and finds the virtual, desired force in an iterative, fast converging process. Due to varying operational conditions at different rotational speeds, the entire process was successfully implemented for each speed frequency line separately (see Chap. 6).

**Lack of observability and controllability due to a small set of accelerometers can lead to unphysical spikes within the System Equivalent Model Mixing.**

The problem that SEMM modal expansion can lead to spurious peaks due to fixed boundary modes is well known. When the experimental model consists of a really small subset of DoF<sup>1</sup>, the entire system dynamics can neither be controlled by the two virtual forces nor observed by these four DoF of the reaction measurement<sup>2</sup>. We can eliminate these peaks in a defined frequency range by shaping the spectrum with a cubic spline fit (see Sec. 6.1.1 and Sec. 6.1.2).

**The mechanical fault information manifests in modulation.**

The fault modulation has to be filtered out by the monitoring method which has to be tailored for the mechanical vibration source. Impacts as produced by bearing faults have to be filtered out by amplitude-modulation extracting methods and harmonic excitations can simply be characterized at the exciting frequency line. Amplitude-modulated impacts have just to be inside the bandwidth and resolution of the sensor system. This sensor system must be sensitive enough. If one assumes that MEMS sensor systems fulfill these requirements, they are the applications of choice due to their proper integrability and low price. Envelope spectral analysis in combination with appropriate filtering based on the spectral kurtosis provided the best results within an exemplary MEMS sensor system case study within this work (see Sec. 3.3 and Sec. 3.4).

<sup>1</sup>four DoF vs. 138 DoF in the presented example.

<sup>2</sup>four horizontal DoF based on two triaxial accelerometers at two measurement positions.

**Temperature can influence both load scenarios and the performance of Micro-Electro Mechanical sensor systems.**

When condition monitoring is established on the base of a Micro-Electro Mechanical sensor system (MEMS), the holistic system has to be kept in mind. Temperature can change the dynamic properties of the rotating machine and the MEMS accelerometer sensitivity. The oil pump medium viscosity decreases with temperature and results in less axial force on the rotor. This leads to smaller bearing fault impacts and erroneously, artificially improves the condition of the machine. When high accuracy and precision is required, the surrounding conditions should be observed by additional sensors in order to uphold the quality of sensing (see Sec. 4.2.3 and Sec. 7.1.2).

**Virtual sensors based on mixed transfer functions can significantly increase the accuracy of industrial condition monitoring systems.**

Industrial sensor systems are typically not located directly at the fault source. They are rather mounted at the outside housing, some distance away from the rotor. On the base of coupled frequency response functions and transmissibility measurements, a virtual accelerometer can be placed directly inside the bearing. The virtual bearing acceleration was experimentally validated and assessed on the basis of an envelope spectrum-based condition indicator. This indicator was applied to the virtual bearing vibration at an exemplary fault and showed to enhance accuracy by 50 % compared to the standard MEMS measurement on the housing. In case of three pump samples, the dispersion of FRFs was determined below 10 % (see Sec. 7.2.1).

**Varying boundary conditions including circuit board dynamics can be observed as change in the entire admittance and adapted by Pseudoinverse filtering based on a single accelerometer.**

Changing boundary conditions for example due to extra masses at the housing of rotating machinery can lead to inaccurate fault quantification since the entire system's admittance changes. The influence of these modifications can be captured by a single, triaxial accelerometer at the outside housing. Here, the Moore-Penrose Pseudoinverse helps again to find a virtual force based on the two horizontal acceleration response DoF and the transfer paths to this force. In case of applying a MEMS sensor system, the accelerometer is typically located directly on the circuit board due to cost-efficiency reasons. The circuit board dynamics can be considered as part of the changing boundary conditions, as it is directly related to the transfer function between the operating force and the monitoring accelerometer. In the presented example, the effect of changing boundary conditions did express itself within the operational force estimation of a reference sensor and also within the prediction by an industrial MEMS sensor system. In this final example, the Pseudoinverse filtering was able to enhance the force estimation accuracy up to 7 % (see Sec. 7.3).

## 8.2 Recommendations and Future Work

In this thesis, experimental, numerical and hybrid modeling approaches showed proper results concerning fault quantification at exemplary, industrial test rigs. Nevertheless, significant improvements and further developments can still be achieved in terms of methodology, usability, industrial practicability and automation. The following recommendations are discussed for future research.

**Extend the hybrid modeling approach to all six DoF per element.**

The hybrid modeling method was only implemented for horizontal displacements and bending rotations DoF due to requirements of minimal model size. This led to  $4 \times 4$  element matrices. Though, axial fault forces can definitely occur during operation of rotating machinery. The centrifugal pump example even showed significant bearing fault excitation responses in this direction due to the axial operating force in the axial flow conveying direction. In this case, all six DoF per element should be included in a model. A first approach was pursued by Benkler [15]. Here, a Timoshenko beam rotor model was created including all six DoF per element. In that case study, the influence of high damping was evaluated and the impeller modeling was also generalized without the need to implement an analogous stiffness. The approach of Benkler has not been applied to operational measurements, so its suitability for condition monitoring requires further research.

**Create a fault model library.**

This thesis focuses on structural dynamic modeling methods and does not pay attention to fault models. When the structural dynamic model is validated and possible fault scenarios are known, a fault library can serve as a base for condition decision algorithms. A first step into this direction was developed in [16]. Here, some roller bearing fault scenarios were implemented utilizing a multi-body simulation. In case of roller bearing fault modeling, assumptions concerning the shaft and outer ring must be well thought of. Also the frequency response functions from the bearing impacts to a sensor on the housing should be ensured by placing a virtual six DoF point in the bearing and a triaxial sensor on the housing.

**Enhance the DoF selection for modal expansion.**

The offsets of some FRFs after the application of SEMM (see Fig. 5.21, 5.22) and their ability of mapping the correct dynamics can be further enhanced especially in the higher frequency range. When there were much more DoF included in the experimental model, an optimization scheme for the best impact and sensor DoF selection can be created. Of course, the desired optimization criteria must be chosen based on the frequency range where the machine faults are expected. Also the appearance of unphysical spikes within the adaption to operational conditions (Sec. 6.1) could be reduced by choosing the best sensor setup with respect to controllability and observability.

**Improve and extend the estimation of operational forces.**

The estimation of operational forces in Sec. 6.1.1 is restricted to unbalances. When observing a whole fault library, the force estimation can not be implemented with the shown procedure. Also the cubic spline-based shaping of the force spectrum may not be compatible with all fault types. Therefore, an enhanced filtering technique should be developed to get rid of possible unphysical spikes. Of course, the best solution would be avoiding them by improving the iterative modal expansion. Furthermore, a comparison of the iterative SEMM expansion with a Kalman filter-based approach to estimate the operational forces can be interesting. Moreover, the virtual accelerations in Sec. 7.2 are based on fault forces. Their estimation could be improved by including all six DoF of the virtual bearing point in the coupled transfer paths. Note, virtual point transformations would be necessary which can lead to bad industrial practicability.

**Implement hybrid models including fault selection and quantification on a constrained sensor system.**

The presented methods were all implemented in MATLAB<sup>®</sup> and are based on an offline evaluation. In order to improve the industrial relevance, these methods should be exported to a constrained MEMS sensor system. Although, some matrix multiplications are not a big deal for these micro-controlled systems, the final condition decision algorithm must be well evaluated concerning computational and storage efforts. A possible solution would be the preprocessing of key property indicators as simple filtered Fourier spectra of measured snapshots with subsequent transmission to a cloud service. All further calculations, online adaptations of the model as well as the final fault classification and quantification can be implemented there.



## Appendix A

# Impeller Specific Parameters for Geometrical Moments of Inertia Calculation

In this chapter, we derive the geometrical moments of inertia, which are specific for the blower rotor type regarded within the thesis. All equations are based on [72].

## A.1 Rotor Blades with Constant Cross-Sectional Area

Here, we have a look at the impeller section, depicted in Fig. 5.5. The angle  $\varphi$  can split a single blade into two circle segments (radii  $r_1$ ,  $r_2$ ) due to symmetry. The distances to the individual centroids of each blade  $\bar{y}_{S1/2}$  span the areas  $A_{1/2}$  based on [54]. Imagine that the two circle segments are subtracted from each other to get the blade geometry. We write

$$\bar{y}_{S1/2} = \frac{4 \cdot \sin\left(\frac{\varphi}{2}\right) \cdot r_{1/2}}{3 \cdot \varphi} \quad \text{and} \quad A_{1/2} = r_{1/2}^2 \cdot \frac{\varphi}{2}. \quad (\text{A.1})$$

Based on these values, the  $\bar{y}_S$ -distance to the blade centroid according to [54] is calculated as

$$\bar{y}_S = \frac{\bar{y}_{S2} \cdot A_2 - \bar{y}_{S1} \cdot A_1}{A_2 - A_1} = \frac{4 \cdot \sin\left(\frac{\varphi}{2}\right) \cdot (r_2^3 - r_1^3)}{r_2^2 - r_1^2}. \quad (\text{A.2})$$

The geometrical moments of inertia  $\mathbf{I}_{\bar{x}_s}$ ,  $\mathbf{I}_{\bar{y}_s}$  as well as  $\mathbf{I}_{\bar{x}_s \bar{y}_s}$  relating to the blade section centroid  $S$  are determined by integrating over the blades based on [6, 54]:

$$\mathbf{I}_{\bar{x}_s} = \frac{\left(\sin\left(\frac{\varphi}{2}\right)\right)^3}{3} \cdot \left((r_2 - \bar{y}_s)^3 - (r_1 - \bar{y}_s)^3\right) \cdot \cos\left(\frac{\varphi}{2}\right) \cdot (r_1 + r_2), \quad (\text{A.3})$$

$$\mathbf{I}_{\bar{y}_s} = \frac{\left(\cos\left(\frac{\varphi}{2}\right)\right)^3}{3} \cdot (r_1^3 + r_2^3) \cdot \sin\left(\frac{\varphi}{2}\right) \cdot (r_2 - r_1 - 2\bar{y}_s), \quad \text{and} \quad (\text{A.4})$$

$$\mathbf{I}_{\bar{x}_s \bar{y}_s} = -\frac{\left(\sin\left(\frac{\varphi}{2}\right)\right)^2}{2} \cdot \left((r_2 - \bar{y}_s)^2 - (r_1 - \bar{y}_s)^2\right) \cdot \frac{\left(\cos\left(\frac{\varphi}{2}\right)\right)^2}{2} \cdot (r_1^2 + r_2^2). \quad (\text{A.5})$$

Now, the blade is rotated to the  $\eta$  -  $\xi$  coordinate system around the centroid  $S$ . The emerging geometrical moments of inertia  $\mathbf{I}_\eta$  and  $\mathbf{I}_\xi$  are

$$\mathbf{I}_\eta = \frac{1}{2} (\mathbf{I}_{\bar{x}_s} + \mathbf{I}_{\bar{y}_s}) + \frac{1}{2} (\mathbf{I}_{\bar{x}_s} - \mathbf{I}_{\bar{y}_s}) \cdot \cos(2\varphi_n) + \mathbf{I}_{\bar{x}_s \bar{y}_s} \cdot \sin(2\varphi_n), \quad \text{and} \quad (\text{A.6})$$

$$\mathbf{I}_\xi = \frac{1}{2} (\mathbf{I}_{\bar{x}_s} + \mathbf{I}_{\bar{y}_s}) - \frac{1}{2} (\mathbf{I}_{\bar{x}_s} - \mathbf{I}_{\bar{y}_s}) \cdot \cos(2\varphi_n) - \mathbf{I}_{\bar{x}_s \bar{y}_s} \cdot \sin(2\varphi_n) \quad \text{with} \quad (\text{A.7})$$

$$\varphi_n = \varphi_{n0} + n \cdot \frac{2 \cdot \pi}{N}, \quad (\text{A.8})$$

where  $\varphi_{n0}$  represents the start angle for a first regarded blade referred to  $\eta$ - $\xi$ -axes,  $n = 0 \dots N-1$  constitutes the respective blade index and  $N$  outlines the total amount of blades. Finally, the rotated moments of inertia are shifted via  $\eta$  and  $\xi$  into rotor coordinates  $x$  and  $y$ . Thus, we get

$$\mathcal{I}_x = \mathcal{I}_\eta + y_s^2 \cdot A \quad \text{and} \quad \mathcal{I}_y = \mathcal{I}_\xi + x_s^2 \cdot A \quad \text{using} \quad A = (r_2^2 - r_1^2) \cdot \frac{\varphi}{2} \quad \text{and} \quad (\text{A.9})$$

$$x_s = a \cdot \sin\left(\frac{\varphi}{2}\right), \quad y_s = \frac{r_{vi} + r_{ti}}{2} - a + a \cdot \left(1 - \cos\left(\frac{\varphi}{2}\right)\right), \quad a = r_1 - \bar{y}_s + \frac{r_2 - r_1}{2}. \quad (\text{A.10})$$

## A.2 Rotor Blades with Varying Cross-Sectional Area

In this section, the blade discretization within the impeller sector is considered, which is directly adjacent to the flow-guiding coverage. Here, the cross-sectional surface shrinks from outside to inside with increasing  $z$ -coordinate. Therefore, a *variable reduced* angle  $\varphi_{vr}(z)$  is introduced and deducted from  $\varphi$ . The parameters are illustrated in Fig. A.1. As a consequence, we get the *variable* angle  $\varphi_v(z)$  in exchange for  $\varphi$ . To calculate this variable, a geometrical approximation based on angular relationships is used. Firstly, we get  $d(z)$  due to the marked right-angled triangle by  $d(z) = \sin(\gamma) \cdot (r_{vi0} - r_{vi}(z))$  (see Fig. 5.6 for the radius  $r_{vi}$ ). Afterwards,  $\varphi_{vr}(z)$  is estimated based on this length and the radii  $r_1$  and  $r_2$  by  $\varphi_{vr}(z) = \arctan\left(\frac{2 \cdot d(z)}{r_1 + r_2}\right)$ .

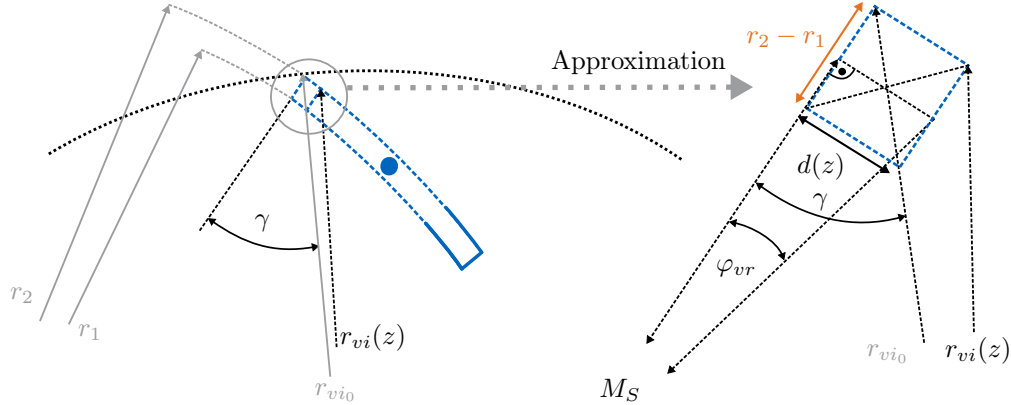


**Figure A.1:** Single impeller blade representation with decreasing cross-sectional area (blue) and geometrical simplifications for  $\varphi_{vr}$  approximation based on [72].  $\varphi_{vr}$  is needed for the calculation of varying cross-sectional area and the geometrical moment of inertia (Sec. A.1 - A.2).

Within the flow guiding coverage adjoining blades' sector, the angle  $\varphi_v(z)$  depends on the  $z$ -coordinate. We utilize the reducing part  $\varphi_{vn}(z)$  linked to the length  $d(z)$ . Applying the additional parameters which are depicted in Fig. A.1, we get

$$\varphi_v(z) = \varphi - \varphi_{vr}(z) \quad \text{with} \quad \varphi_{vr}(z) = \arctan\left(\frac{2 \cdot d(z)}{r_1 + r_2}\right) \quad \text{and} \quad d(z) = \sin(\gamma) \cdot (r_{vi0} - r_{vi}(z)). \quad (\text{A.11})$$

### A.3 Flow Guiding Coverage

The segments of the flow guiding coverage are depicted in Fig 5.6. Here, the equations for the outer radius  $r_{va}(z)$  are noted. Within the first section (dashed black),  $r_{va}$  is approximated to be constant. The radius for the second segment (black) is defined as

$$r_{va}(z) = r_{va}(z_0) - r_{a1} \cdot (\sin\varphi_d(z) - \sin\varphi_{d0}) \quad \text{with} \quad (\text{A.12})$$

$$\varphi_d(z) = \arccos\left(\frac{z_0 - z}{r_{i1}} + \cos(\varphi_{d0})\right) - \varphi_{d0}. \quad (\text{A.13})$$

Regarding the third segment (orange), we write

$$r_{va}(z) = r_{va}(z_2) - r_{a2} \cdot (\sin\varphi_d(z) - \sin\varphi_d(z_2) - \sin\varphi_{d0}) \quad \text{with} \quad (\text{A.14})$$

$$\varphi_d(z) = \arccos\left(\frac{z_2 - z}{r_{i2}} + \cos(\varphi_d(z_2))\right) - \varphi_d(z_2). \quad (\text{A.15})$$

Concerning the last segment (green), we simplify again  $r_{va}$  to be constant.



## Appendix B

# Adaptive Force Shaping Conditions

In order to shape the spiky iterative SEMM force approximation, a physical based reference is needed. This reference is built on scalar values of the force magnitude in a frequency range around the rotational frequency. Examples for such indicators can be found in bearing diagnosis [140]. Here, these scalars are utilized to gain information about roller bearing faults. Generally, they provide knowledge about the shape of a signal within a scalar value. In this context, the features are extracted from the SEMM start model, the final iterative SEMM model and additionally from an iterative cubic spline fit function which is fitted to the final iterative SEMM force magnitude. Particularly, we calculate the subsequent scalars:

- Root mean square value

$$f_{\text{rms}} = \sqrt{\frac{1}{n} \sum_{i=1}^n f_i^2}, \quad (\text{B.1})$$

- Force Maximum  $f_{\text{max}}$ , force minimum  $f_{\text{min}}$ ,
- Crest factor

$$cr = \frac{|f_{\text{max}}|}{f_{\text{rms}}} \quad \text{and} \quad (\text{B.2})$$

- Force kurtosis factor

$$\mathcal{K} = \frac{1}{n} \sum_{i=1}^n \left( \frac{f_i - \bar{f}}{s} \right)^4 \quad (\text{B.3})$$

within a range around the operational speed frequency line of  $\pm 10$  Hz ( $i=1\dots 20$  samples).  $\bar{f}$  represents the force mean value and  $s$  denotes the standard deviation within the specified frequency band.

The root mean square value is utilized as general level of the force hill, whereby the minimum and maximum is used for more specific significance within the iterative force adaption. The crest factor describes the ratio between peak and root mean square value and well characterizes the shape of a smooth signal. More specific information is provided by the kurtosis factor. It is defined by the fourth standardized moment of a signal and properly describes tails of a sample distribution. These tails can be outliers or spikes in the presented case.

The question arises how to define a spike. We decided between different feature types according to the introduced scalar values. Some of them are unique for the SEMM start model (superscript *start*). Properties with superscript *tolstart* are computed only for the final iterative SEMM model, before the iterative force shaping starts. They represent a start deviation between the SEMM start force magnitude and the iterative SEMM force magnitude.

We put together a linked condition which takes effect to keep this deviation within a physically justified tolerance ( $-5\%$  to  $250\%$  deviation). All features comprising superscript *tol* are not unique and replaced by iterative values within the loop. The entire shaping technique is depicted in Fig. B.1 within a flow chart.

At the beginning, the listed force signal scalars of the iterative and of the start model were calculated. Next, we design a start force envelope utilizing a cubic spline fit function. This curve fit is based on the Shape Language Modeling toolbox [33]. It is specified for our signals using Hermite boundary conditions. The required knots are set to an amount of only 100 over the entire frequency range. This decision is made based on weighting the accuracy of peak fitting ability, a generic approach and computation time. In the next step, the loop starts by extracting the fit features  $f_{\text{rms}}^{\text{tol}}$  and  $cr^{\text{tol}}$ . These are compared with the properties of the SEMM starting force estimate and with those of the iterative SEMM model, which includes potential unphysical spikes.

When the linked condition decision results in true, the sample point of maximum amplitude is dropped. This sample must be located within the same frequency range around the rotational frequency ( $\pm 10$  Hz which is utilized for calculating the scalars. After dropping the spike samples, we get a *shaped*, truncated unbalance force vector of the iterative SEMM approximation. The technique of canceling spikes involves eliminating the sample either to the left or right of the rotational frequency. Depending on this, the considered frequency range is shortened with respect to the feature extraction for the subsequent iteration step in the corresponding direction to the left or right of the rotation frequency. Now, the spline is fitted to the shaped force vector and features are extracted both from the adapted force vector as well from the appropriate new fit function. All dynamic properties (superscript *tol*) are now replaced within the iteration. The linked condition decides again, if a spike sample occurs and drops it in case of condition fulfillment. Unless the prerequisite is true, the loop terminates. Finally, the rotational speed frequency line of the final iterative force envelope is taken as scalar force value.

As depicted in the flow chart (see Fig. B.1), the assessment criteria for spike removal distinguish between fitted envelopes and “raw” force signals. Particularly this affects four features ( $f_{\text{rms}}^{\text{tol}}$ ,  $cr^{\text{tol}}$ ,  $f_{\text{max}}^{\text{tol}}$  and  $k^{\text{tol}}$ ).  $f_{\text{rms}}^{\text{tol}}$  and  $cr^{\text{tol}}$  are taken from the fit function, since their force shape is smooth but either too high or too low. For example, when having a spike at the beginning of the loop, the fit covers it with a wide, large hill. This hill is characterized properly by its root mean square value and crest factor. Another extremum might occur, if too many samples are dropped. As a consequence, we get a jagged signal with low amplitude. This is also wrapped by a smooth fit, but with much lower root mean square value and crest factor compared with the SEMM start model. By this choice, we get rid of outliers but keep robust against too many dropped samples.

As further iterative feature, there is the kurtosis factor  $k^{\text{tol}}$  describing steepness and peakedness of the force curve. If these differ too strong from the SEMM start model, the peak is removed. In order to keep robustness,  $f_{\text{max}}^{\text{tol}}$  is regarded. Here, the iteratively shaped maximum must exceed the minimum of the SEMM start model. These two assessment criteria are only reasonable within the unfitted force vectors since the envelope smoothing would distort the feature’s significance.





# Bibliography

- [1] Abuelma'atti, M. T. "A simple algorithm for fitting measured data to Fourier-series models". In: *International Journal of Mathematical Education in Science and Technology* 24.1 (1993), pp. 107–112. DOI: 10.1080/0020739930240114.
- [2] Ahmed, H. and Tahir, M. "Terrain-Based Vehicle Localization Using Low Cost MEMS-IMU Sensors". In: *2016 IEEE 83rd Vehicular Technology Conference (VTC Spring)*. 2016, pp. 1–5. DOI: 10.1109/VTCspring.2016.7504502.
- [3] Albarbar, A., Badri, A., Sinha, J. K., and Starr, A. "Performance evaluation of MEMS accelerometers". In: *Measurement* 42.5 (2009), pp. 790–795.
- [4] Allemang, R. J. "The modal assurance criterion - twenty years of use and abuse". In: *Journal of Sound and Vibration* 37.8 (2003), pp. 14–23.
- [5] Allen, M. S., Rixen, D. J., van der Seijs, M., Tiso, P., Abrahamsson, T., and Mayes, R. L. *Substructuring in engineering dynamics*. Springer, 2020.
- [6] Altenbach, H., Meyer, H., and Schumpich, G. *Technische Mechanik Festigkeitslehre*. Springer, 2016. DOI: DOI:10.1007/978-3-658-22854-5.
- [7] Antoni, J. "The spectral kurtosis: A useful tool for characterising non-stationary signals". In: *Mechanical Systems and Signal Processing* 20.2 (2006), pp. 282–307. ISSN: 08883270. DOI: 10.1016/j.ymsp.2004.09.001.
- [8] Antoni, J. "Fast computation of the kurtogram for the detection of transient faults". In: *Mechanical Systems and Signal Processing* 21.1 (2007), pp. 108–124.
- [9] Antoni, J. *Fast Kurtogram (Version 1.0)*. MathWorks. 2015.
- [10] Antoni, J. and Randall, R. B. "The spectral kurtosis: application to the vibratory surveillance and diagnostics of rotating machines". In: *Mechanical Systems and Signal Processing* 20.2 (2006), pp. 308–331. ISSN: 08883270. DOI: 10.1016/j.ymsp.2004.09.002.
- [11] Avitabile, P. "Model reduction and model expansion and their applications - part 1 theory". In: *Proceedings of the 23th International Modal Analysis Conference, Orlando, Florida, USA. Society for Experimental Mechanics*. 2005.
- [12] Badri, A. E., Sinha, J. K., and Albarbar, A. "A typical filter design to improve the measured signals from MEMS accelerometer". In: *Measurement* 43.10 (2010), pp. 1425–1430.
- [13] Baydar, N. and Ball, A. "A comparative study of acoustic and vibration signals in detection of gear failures using Wigner–Ville distribution". In: *Mechanical Systems and Signal Processing* 15.6 (2001), pp. 1091–1107.
- [14] Bendjama, H., Bouhouche, S., and Moussaoui, A. "Wavelet transform for bearing faults diagnosis". In: *Advances in Control Engineering (ACE)* (2013), pp. 85–88.
- [15] Benkler, K. "FE-Simulation und Validierung dynamischer Lagersteifigkeiten am Beispiel der Kreiselpumpe". Semesterarbeit. Technische Universität München, 2019.

- [16] Benkler, K. “Simulation und experimentelle Validierung von Wälzlagerschadenszenarien”. Master Thesis. Technische Universität München, 2020.
- [17] Besselink, B., Tabak, U., Lutowska, A., van de Wouw, N., Nijmeijer, H., Rixen, D. J., Hochstenbach, M., and Schilders, W. “A comparison of model reduction techniques from structural dynamics, numerical mathematics and systems and control”. In: *Journal of Sound and Vibration* 332.19 (2013), pp. 4403–4422. DOI: DOI:10.1016/j.jsv.2013.03.025.
- [18] Bishop, G., Welch, G., et al. “An introduction to the kalman filter”. In: *Proceedings of SIGGRAPH, Course 8.27599-23175* (2001), p. 41.
- [19] Bohn, P. “Wechselwirkungen von Schwingungen zwischen Motor-Getriebe-Verbund und Kurbeltrieb als Grundlage für Körperschallanalysen”. PhD thesis. Technische Universität Berlin, 2007.
- [20] Borghesani, P., Pennacchi, P., Randall, R. B., Sawalhi, N., and Ricci, R. “Application of cepstrum pre-whitening for the diagnosis of bearing faults under variable speed conditions”. In: *Mechanical Systems and Signal Processing* 36.2 (2013), pp. 370–384. ISSN: 08883270. DOI: 10.1016/j.ymsp.2012.11.001.
- [21] Boudiaf, A., Djebala, A., Bendjma, H., Balaska, A., and Dahane, A. “A summary of vibration analysis techniques for fault detection and diagnosis in bearing”. In: *International Conference on Modelling, Identification and Control (ICMIC)*. IEEE, 2016, pp. 37–42.
- [22] Bregar, T., El Mahmoudi, A., Čepon, G., Rixen, D. J., and Boltežar, M. “Performance of the Expanded Virtual Point Transformation on a Complex Test Structure”. In: *Experimental Techniques* 45.1 (2021), pp. 83–93.
- [23] Bregar, T., Holeček, N., Čepon, G., Rixen, D. J., and Boltežar, M. “Including directly measured rotations in the virtual point transformation”. In: *Mechanical Systems and Signal Processing* 141 (2020), p. 106440. ISSN: 0888-3270. DOI: <https://doi.org/10.1016/j.ymsp.2019.106440>. URL: <https://www.sciencedirect.com/science/article/pii/S0888327019306612>.
- [24] Brumat, M., Slavič, J., and Boltežar, M. “Spatial damping identification in the frequency domain—A theoretical and experimental comparison”. In: *Journal of Sound and Vibration* 376 (2016), pp. 182–193. ISSN: 0022-460X. DOI: <https://doi.org/10.1016/j.jsv.2016.04.006>. URL: <https://www.sciencedirect.com/science/article/pii/S0022460X16300402>.
- [25] Buono, D., Siano, D., Frosina, E., and Senatore, A. “Gerotor pump cavitation monitoring and fault diagnosis using vibration analysis through the employment of auto-regressive-moving-average technique”. In: *Simulation Modelling Practice and Theory* 71 (2017), pp. 61–82.
- [26] Cakir, M., Guvenc, M. A., and Mistikoglu, S. “The experimental application of popular machine learning algorithms on predictive maintenance and the design of IIoT based condition monitoring system”. In: *Computers & Industrial Engineering* 151 (2021), p. 106948.
- [27] Cerrada, M., Sánchez, R. V., Li, C., Pacheco, F., Cabrera, D., Valente de Oliveira, J., and Vásquez, R. E. “A review on data-driven fault severity assessment in rolling bearings”. In: *Mechanical Systems and Signal Processing* (2018). ISSN: 10961216. DOI: 10.1016/j.ymsp.2017.06.012.
- [28] Cheng, Y., Chen, B., and Zhang, W. “Adaptive multipoint optimal minimum entropy deconvolution adjusted and application to fault diagnosis of rolling element bearings”. In: *IEEE Sensors Journal* 19.24 (2019), pp. 12153–12164.

- [29] Childers, D., Skinner, D., and Kemerait, R. "The cepstrum: A guide to processing". In: *Proceedings of the IEEE* 65.10 (1977), pp. 1428–1443. DOI: 10.1109/PROC.1977.10747.
- [30] Cohen, I. B. and Whitman, A. *Isaac Newton. The Principia. Mathematical principles of natural philosophy. A new translation.* 1999.
- [31] Cole, J., Cunningham, A., MacDonald, R., McGimpsey, S., McQuaide, S., and McShain, D. "Optimizing noise and stability of MEMS accelerometers for various applications". In: *Position, Location and Navigation Symposium (PLANS)*. IEEE. 2016, pp. 9–14.
- [32] Craig Jr, R. R. and Bampton, M. C. "Coupling of substructures for dynamic analyses." In: *AIAA journal* 6.7 (1968), pp. 1313–1319.
- [33] D’Errico, J. *SLM - Shape Language Modeling (Version 1.14)*. MathWorks. 2017.
- [34] D’Ambrogio, W. and Fregolent, A. "Decoupling procedures in the general framework of frequency based substructuring". In: *Proceedings of the 27th International Modal Analysis Conference, Orlando, USA. Society for Experimental Mechanics* (2009).
- [35] de Klerk, D., Rixen, D. J., and Voormeeren, S. "General framework for dynamic substructuring: history, review and classification of techniques". In: *AIAA journal* 46.5 (2008), pp. 1169–1181. DOI: 10.2514/1.33274.
- [36] de Klerk, D., Rixen, D. J., and de Jong, J. "The frequency based substructuring (FBS) method reformulated according to the dual domain decomposition method". In: *Proceedings of the 24th International Modal Analysis Conference, St. Louis, Missouri, USA. Society for Experimental Mechanics.* 2006.
- [37] de Klerk, D., Rixen, D. J., Voormeeren, S., and Pasteuning, F. "Solving the RDoF problem in experimental dynamic substructuring". In: *Proceedings of the 26th International Modal Analysis Conference, Orlando, USA. Society for Experimental Mechanics.* 2008.
- [38] Deckers, J. *Entwicklung einer Low-Cost-Körperschallsensorik zur Überwachung des Verschleißverhaltens von wälz- und gleitgelagerten Kreiselpumpen kleiner Leistung.* VDI-Verlag, 2001.
- [39] *20816-1: Mechanische Schwingungen - Messung und Bewertung der Schwingungen von Maschinen - Teil 1: Allgemeine Anleitungen.* Standard. Deutsches Institut für Normung, 2017.
- [40] Dong, X., Huang, Q., Xu, W., Tang, B., Yang, S., Zhu, J., and En, Y. "Research on temperature characteristic of parasitic capacitance in MEMS capacitive accelerometer". In: *Sensors and Actuators A: Physical* 285 (2019), pp. 581–587.
- [41] Du, W., Wang, Z., Gong, X., Wang, L., and Luo, G. "Optimum IMFs selection based envelope analysis of bearing fault diagnosis in plunger pump". In: *Shock and Vibration* 2016 (2015).
- [42] Elliott, A. and Moorhouse, A. T. "Characterisation of structure borne sound sources from measurement in-situ". In: *Journal of the Acoustical Society of America* 123.5 (2008), p. 3176.
- [43] Elnady, M., Sinha, J., and Oyadiji, S. "Condition monitoring of rotating machines using on-shaft vibration measurement". In: *10th International Conference on Vibrations in Rotating Machinery.* Woodhead Publishing, 2012, pp. 669–678. ISBN: 978-0-85709-452-0. DOI: <https://doi.org/10.1533/9780857094537.10.669>. URL: <https://www.sciencedirect.com/science/article/pii/B978085709452050058X>.
- [44] Feldman, M. "Hilbert transform in vibration analysis". In: *Mechanical Systems and Signal Processing* 25.3 (2011), pp. 735–802.

- [45] Feng, G., Zhao, H., Gu, F., Needham, P., and Ball, A. “Efficient implementation of envelope analysis on resources limited wireless sensor nodes for accurate bearing fault diagnosis”. In: *Measurement* 110 (2017), pp. 307–318.
- [46] Fricke, J. G. “Schadensdiagnose und Zustandsüberwachung von wälzgelagerten Rotorsystemen”. Master Thesis. Technische Universität München, 2018.
- [47] Fung, E. and Yau, D. “Effects of centrifugal stiffening on the vibration frequencies of a constrained flexible arm”. In: *Journal of Sound and Vibration* 224.5 (1999), pp. 809–841.
- [48] Gasch, R., Nordmann, R., and Pfützner, H. *Rotordynamik*. Springer-Verlag, 2006. DOI: DOI:10.1007/3-540-33884-5.
- [49] Géradin, M. and Rixen, D. J. *Mechanical vibrations: theory and application to structural dynamics (3rd ed.)* John Wiley & Sons, 2014.
- [50] Gibanica, M. “Experimental-analytical dynamic substructuring: a state-space approach”. Master Thesis. Chalmers University of Technology, Göteborg, Sweden, 2013.
- [51] Gimpl, V. “Untersuchung der Systemeigenschaften additiv gefertigter Komponenten mittels experimenteller Substrukturierung”. Semester Thesis. Technische Universität München, 2018.
- [52] Greville, T. N. E. “Note on the generalized inverse of a matrix product”. In: *Siam Review* 8.4 (1966), pp. 518–521. DOI: DOI:10.1137/1008107.
- [53] Grinberg, B., Feingold, A., Furman, L., and Wolfson, R. “High precision open-loop and closed-loop MEMS accelerometers with wide sensing range”. In: *Position, Location and Navigation Symposium (PLANS)*. IEEE. 2016, pp. 924–931.
- [54] Gross, D., Ehlers, W., Wriggers, P., Schröder, J., and Müller, R. *Formeln und Aufgaben zur technischen Mechanik 1 Statik*. 12th ed. Springer, 2016.
- [55] Häußler, M. and Rixen, D. J. “Optimal transformation of frequency response functions on interface deformation modes”. In: *Dynamics of Coupled Structures, Volume 4*. Springer, 2017, pp. 225–237.
- [56] He, J., Xie, J., He, X., Du, L., and Zhou, W. “Analytical study and compensation for temperature drifts of a bulk silicon MEMS capacitive accelerometer”. In: *Sensors and Actuators A: Physical* 239 (2016), pp. 174–184.
- [57] Hewlett Packard. “Effective machinery measurements using dynamic signal analyzers”. In: *Application Note 243-1* (1997), p. 88.
- [58] Hoffmann, R. and Wolff, M. *Intelligente Signalverarbeitung 1: Signalanalyse*. Springer-Verlag, 2014.
- [59] Hurty, W. C. “Vibrations of structural systems by component mode synthesis”. In: *Journal of the Engineering Mechanics Division* 86.4 (1960), pp. 51–69.
- [60] Isermann, R. “Model-based fault-detection and diagnosis—status and applications”. In: *Annual Reviews in control* 29.1 (2005), pp. 71–85.
- [61] Isermann, R. *Fault-diagnosis applications: model-based condition monitoring: actuators, drives, machinery, plants, sensors, and fault-tolerant systems*. Springer Science & Business Media, 2011.
- [62] *ISO Guide 98-3:2008-9: Uncertainty of measurement - Part 3: Guide to the expression of uncertainty in measurement (GUM)*. Standard. Berlin: International Organization for Standardization, 2008.

- [63] Jetmundsen, B., Bielawa, R. L., and Flannelly, W. G. “Generalized frequency domain substructure synthesis”. In: *Journal of the American Helicopter Society* 33.1 (1988), pp. 55–64.
- [64] Jiménez, S., Cole, M. O., and Keogh, P. S. “Vibration sensing in smart machine rotors using internal MEMS accelerometers”. In: *Journal of Sound and Vibration* 377 (2016), pp. 58–75.
- [65] Kalman, R. E. “A new approach to linear filtering and prediction problems”. In: *Journal of Basic Engineering* 82.1 (1960), pp. 35–45.
- [66] Kankar, P., Sharma, S. C., and Harsha, S. “Fault diagnosis of ball bearings using machine learning methods”. In: *Expert Systems with Applications* 38.3 (2011), pp. 1876–1886. ISSN: 09574174. DOI: 10.1016/j.eswa.2010.07.119.
- [67] Kavitha, S., Daniel, R. J., and Sumangala, K. “High performance MEMS accelerometers for concrete SHM applications and comparison with COTS accelerometers”. In: *Mechanical Systems and Signal Processing* 66 (2016), pp. 410–424.
- [68] Klaassen, S. W. B. and Rixen, D. J. “Using SEMM to Identify the Joint Dynamics in Multiple Degrees of Freedom Without Measuring Interfaces”. In: *Dynamic Substructures, Volume 4*. Ed. by Linderholt, A., Allen, M. S., Mayes, R. L., and Rixen, D. Cham: Springer International Publishing, 2020, pp. 87–99. ISBN: 978-3-030-12184-6.
- [69] Klaassen, S. W., van der Seijs, M. V., and de Klerk, D. “System equivalent model mixing”. In: *Mechanical Systems and Signal Processing* 105 (2018), pp. 90–112. DOI: 10.1016/j.ymsp.2017.12.003.
- [70] Klein, B. *FEM: Grundlagen und Anwendungen der Finite-Elemente-Methode*. Springer-Verlag, 2015. DOI: DOI:10.1007/978-3-658-06054-1.
- [71] Korkua, S., Jain, H., Lee, W.-J., and Kwan, C. “Wireless health monitoring system for vibration detection of induction motors”. In: *Industrial and Commercial Power Systems Technical Conference (I&CPS)*. IEEE. 2010, pp. 1–6.
- [72] Krügel, S., Maierhofer, J., Thümmel, T., and Rixen, D. J. “Rotor Model Reduction for Wireless Sensor Node Based Monitoring Systems”. In: *SIRM 2019 - 13th International Conference on Dynamics of Rotating Machines*. Ed. by Santos, I. Vol. 13. Copenhagen, Denmark: DTU Mechanical Engineering, 2019, pp. 78–87. DOI: 10.13140/RG.2.2.33454.05444. URL: [https://orbit.dtu.dk/files/194456755/SIRM\\_Conference\\_Proceedings\\_ISBN\\_udgave.pdf](https://orbit.dtu.dk/files/194456755/SIRM_Conference_Proceedings_ISBN_udgave.pdf).
- [73] Krügel, S., Maierhofer, J., Wagner, C., Thümmel, T., and Rixen, D. J. “How Housing Dynamics Affect the Monitoring of Rotor Unbalance: A Case Study”. In: *PAMM* 19.1 (2019). DOI: 10.1002/pamm.201900250.
- [74] Krügel, S. and Rixen, D. J. “Frequency Based Model Mixing for Machine Condition Monitoring”. In: *Dynamic Substructures, Volume 4: Proceedings of the 38th International Modal Analysis Conference, A Conference and Exposition on Structural Dynamics. Society for Experimental Mechanics*. Springer Nature. 2020, pp. 157–161. DOI: 10.1007/978-3-030-47630-4\_15.
- [75] Kullaa, J. “Virtual sensing of structural vibrations using dynamic substructuring”. In: *Mechanical Systems and Signal Processing* 79 (2016), pp. 203–224.
- [76] Lahdelma, S. and Juuso, E. K. “Vibration analysis of cavitation in Kaplan water turbines”. In: *IFAC Proceedings Volumes* 41.2 (2008), pp. 13420–13425.

- [77] Li, W., Huang, Z., Lin, H., and Ding, K. “Envelope analysis by wavelet-filter based spectral kurtosis for bearing health monitoring”. In: *Instrumentation and Measurement Technology Conference (I2MTC), 2013 IEEE International*. IEEE. 2013, pp. 1721–1724.
- [78] Liu, J., Zhu, W., Lu, Q., and Ren, G. “An efficient iterative algorithm for accurately calculating impulse response functions in modal testing”. In: *Journal of vibration and acoustics* 133.6 (2011).
- [79] Liu, Y.-T., Wang, Y., and Shao, L. “Quantization noise consideration and characterization in Sigma-Delta MEMS accelerometer”. In: *Microelectronics Journal* 47 (2016), pp. 53–60.
- [80] Lourens, E., Reynders, E., De Roeck, G., Degrande, G., and Lombaert, G. “An augmented Kalman filter for force identification in structural dynamics”. In: *Mechanical Systems and Signal Processing* 27 (2012), pp. 446–460.
- [81] Ludwig, C., Junge, O., and Wever, U. “Online parameter identification methods for oscillatory systems: Estimation of changes in stiffness properties”. In: *Journal of Vibration and Control* 25.4 (2019), pp. 725–738.
- [82] Ludwig Wever, U. “Online fault identification for rotating machinery”. In: *International Conference on Noise and Vibration Engineering, ISMA*. 2018, pp. 881–883.
- [83] Maierhofer, J., El Mahmoudi, A., and Rixen, D. J. “Development of a low cost automatic modal hammer for applications in substructuring”. In: *Dynamic Substructures, Volume 4*. Springer, 2020, pp. 77–86.
- [84] Manikandan, K. G., Pannirselvam, K., Kenned, J. J., and Kumar, C. S. “Investigations on suitability of MEMS based accelerometer for vibration measurements”. In: *Materials Today: Proceedings* (2020).
- [85] Marple L., J. “Computing the discrete-time analytic signal via FFT”. In: *IEEE Transactions on Signal Processing* 47.9 (1999), pp. 2600–2603. ISSN: 1053-587X. DOI: 10.1109/78.782222.
- [86] McDonald, G. L. and Zhao, Q. “Multipoint optimal minimum entropy deconvolution and convolution fix: Application to vibration fault detection”. In: *Mechanical Systems and Signal Processing* 82 (2017), pp. 461–477. ISSN: 10961216. DOI: 10.1016/j.ymssp.2016.05.036.
- [87] Meggitt, J., Elliott, A., Moorhouse, A., Jalibert, A., and Franks, G. “Component Replacement TPA: a transmissibility-based structural modification method for in-situ transfer path analysis”. In: *Journal of Sound and Vibration* (2021), p. 115991.
- [88] Moorhouse, A., Elliott, A., and Evans, T. “In situ measurement of the blocked force of structure-borne sound sources”. In: *Journal of Sound and Vibration* 325.4-5 (2009), pp. 679–685.
- [89] Mulser, T. “Experimentelle Transferpfadanalyse und Substrukturierung am Fahrmotorlüfterprüfstand”. Master Thesis. Technische Universität München, 2019.
- [90] Naets, F., Cuadrado, J., and Desmet, W. “Stable force identification in structural dynamics using Kalman filtering and dummy-measurements”. In: *Mechanical Systems and Signal Processing* 50 (2015), pp. 235–248.
- [91] Newton, I. *Philosophiae naturalis principia mathematica*. London, 1687.
- [92] o’Sullivan, M. “Systematic machine-condition monitoring - a case study from Parenco paper mill in Holland”. In: *Engineering costs and production economics* 21.3 (1991), pp. 277–293.

- [93] Oertel, O. “Evaluation und Weiterentwicklung eines Integrierten Sensorrings”. Bachelor Thesis. Technische Universität München, 2019.
- [94] Pasma, E. “Towards a Robust Component Transfer Path Analysis Method: Application and Validation in Automotive Research”. Master Thesis. Mechanical, Maritime, Materials Engineering - Precision, and Microsystems Engineering - TU Delft, 2014.
- [95] Peeters, B. and van der Auweraer, H. “PolyMax: a revolution in operational modal analysis”. In: *Proceedings of the 1st International Operational Modal Analysis Conference* (2005).
- [96] Pejic, D. “Aufbau und Qualifizierung eines Versuchsstands zur Validierung von intelligenten Zustandsüberwachungssystemen”. Master Thesis. Friedrich-Alexander Universität Erlangen-Nürnberg, 2015.
- [97] Peng, Z. and Chu, F. “Application of the wavelet transform in machine condition monitoring and fault diagnostics: a review with bibliography”. In: *Mechanical Systems and Signal Processing* 18.2 (2004), pp. 199–221.
- [98] Peng, Z., Peter, W. T., and Chu, F. “A comparison study of improved Hilbert–Huang transform and wavelet transform: application to fault diagnosis for rolling bearing”. In: *Mechanical Systems and Signal Processing* 19.5 (2005), pp. 974–988.
- [99] Pogačar, M., Ocepek, D., Trainotti, F., Čepon, G., and Boltežar, M. “System equivalent model mixing: A modal domain formulation”. In: *Mechanical Systems and Signal Processing* 177 (2022), p. 109239. ISSN: 0888-3270. DOI: <https://doi.org/10.1016/j.ymsp.2022.109239>. URL: <https://www.sciencedirect.com/science/article/pii/S0888327022003879>.
- [100] Pourciau, B. “Newton’s interpretation of Newton’s second law”. In: *Archive for history of exact sciences* 60.2 (2006), pp. 157–207.
- [101] Radecker, P. “Entwicklung eines drahtlosen Sensorrings für Rotorsysteme”. Bachelor Thesis. Technische Universität München, 2018.
- [102] Rai, A. and Upadhyay, S. “A review on signal processing techniques utilized in the fault diagnosis of rolling element bearings”. In: *Tribology International* 96 (2016), pp. 289–306. ISSN: 0301679X. DOI: 10.1016/j.triboint.2015.12.037.
- [103] Randall, R. B. “A history of cepstrum analysis and its application to mechanical problems”. In: *Mechanical Systems and Signal Processing* 97 (2017), pp. 3–19. ISSN: 08883270. DOI: 10.1016/j.ymsp.2016.12.026.
- [104] Randall, R. B., Sawalhi, N., and Coats, M. “A comparison of methods for separation of deterministic and random signals”. In: *International Journal of Condition Monitoring* 1.1 (2011), pp. 11–19.
- [105] Randall, R. B. *Vibration-based condition monitoring: industrial, aerospace and automotive applications*. John Wiley & Sons, 2011.
- [106] Rathbone, T. e. a. “Vibration tolerance”. In: *Power Plant Engineering* 43.1939 (1939), pp. 721–724.
- [107] Rilling, G., Flandrin, P., and Es, P. “On empirical mode decomposition and its algorithms”. In: *IEEE-EURASIP workshop on nonlinear signal and image processing 3* (2003), pp. 8–11. ISSN: 15206149. DOI: 10.1109/ICASSP.2008.4518437.
- [108] Rixen, D. J. “A dual Craig–Bampton method for dynamic substructuring”. In: *Journal of Computational and applied mathematics* 168.1-2 (2004), pp. 383–391.

- [109] Rixen, D. J. “How measurement inaccuracies induce spurious peaks in frequency based substructuring”. In: *Proceedings of the 26th International Modal Analysis Conference, Orlando, Florida. Society for Experimental Mechanics*. 2008.
- [110] Rixen, D. J. *A Substructuring Technique Based on Measured and Computed Impulse Response Functions of Components*. 2010.
- [111] Rixen, D. J. “Substructuring using impulse response functions for impact analysis”. In: *Structural Dynamics, Volume 3*. Springer, 2011, pp. 637–646.
- [112] Rixen, D. J. and van der Valk, P. L. “An impulse based substructuring approach for impact analysis and load case simulations”. In: *Journal of Sound and Vibration* 332.26 (2013), pp. 7174–7190.
- [113] Röhr, M. “Automatisierte Lagerdiagnose an Kreiselpumpen”. Master Thesis. Technische Universität München, 2018.
- [114] Roßner, M. “Modellbasiertes Monitoring von Rotoren mit mehreren gleichzeitigen Fehlern”. PhD thesis. Technische Universität München, 2015. ISBN: 9783843923965.
- [115] S., V., D., d., and J., R. D. “Uncertainty Quantification in Experimental Frequency Based Substructuring”. In: *Mechanical Systems and Signal Processing* (2010). DOI: 10.1016/j.ymsp.2009.01.016.
- [116] Saufi, M., Ahmad, Z., Lim, M., and Leong, M. “A review on signal processing techniques for bearing diagnostics”. In: *International Journal of Mechanical Engineering and Technology* 8.6 (2017), pp. 327–337.
- [117] Singleton, R. K., Strangas, E. G., and Aviyente, S. “Extended Kalman filtering for remaining-useful-life estimation of bearings”. In: *IEEE Transactions on Industrial Electronics* 62.3 (2014), pp. 1781–1790.
- [118] Sjövall, P. and Abrahamsson, T. “Component system identification and state-space model synthesis”. In: *Mechanical Systems and Signal Processing* 21.7 (2007), pp. 2697–2714.
- [119] Sjövall, P. and Abrahamsson, T. “State-space model identification for component synthesis”. In: *Proceedings of the 25th International Modal Analysis Conference, Orlando, Florida. Society for Experimental Mechanics*. 2007.
- [120] Sjövall, P. and Abrahamsson, T. “Substructure system identification from coupled system test data”. In: *Mechanical Systems and Signal Processing* 22.1 (2008), pp. 15–33.
- [121] Sjövall, P., McKelvey, T., and Abrahamsson, T. “Constrained state-space system identification with application to structural dynamics”. In: *Automatica* 42.9 (2006), pp. 1539–1546.
- [122] Son, J.-D., Ahn, B.-H., Ha, J.-M., and Choi, B.-K. “An availability of MEMS-based accelerometers and current sensors in machinery fault diagnosis”. In: *Measurement* 94 (2016), pp. 680–691.
- [123] Souza, R. M., Nascimento, E. G., Miranda, U. A., Silva, W. J., and Lepikson, H. A. “Deep learning for diagnosis and classification of faults in industrial rotating machinery”. In: *Computers & Industrial Engineering* 153 (2021), p. 107060.
- [124] Stetco, A., Dinmohammadi, F., Zhao, X., Robu, V., Flynn, D., Barnes, M., Keane, J., and Nenadic, G. “Machine learning methods for wind turbine condition monitoring: A review”. In: *Renewable energy* 133 (2019), pp. 620–635.

- [125] STMicroelectronics. *LSM6DSL iNEMO inertial module: always-on 3D accelerometer and 3D gyroscope*. <https://www.st.com/resource/en/datasheet/lsm6dsl.pdf>. Datasheet - production data, accessed June 5th, 2021. 2017.
- [126] Su, T.-J. and Juang, J.-N. “Substructure system identification and synthesis”. In: *Journal of Guidance, Control, and Dynamics* 17.5 (1994), pp. 1087–1095. DOI: 10.2514/3.21314.
- [127] Swathy, L. and Abraham, L. “Analysis of vibration and acoustic sensors for machine health monitoring and its wireless implementation for low cost space applications”. In: *First International Conference on Computational Systems and Communications (ICCS)*. IEEE. 2014, pp. 80–85.
- [128] Tandon, N. and Choudhury, A. “A review of vibration and acoustic measurement methods for the detection of defects in rolling element bearings”. In: *Tribology International* 32 (1999), pp. 469–480.
- [129] “The empirical mode decomposition and the Hilbert spectrum for nonlinear and non-stationary time series analysis”. In: *Proceedings of the Royal Society a-Mathematical Physical and Engineering Sciences* 454.1971 (1998), pp. 903–995. ISSN: 1364-5021. DOI: 10.1098/rspa.1998.0193.
- [130] Thümmel, T., Rossner, M., Wagner, C., Maierhofer, J., and Rixen, D. J. “Rotor Orbits at Operation Speed and Model-Based Diagnosis of Multiple Errors”. In: *Proceedings of the 10th International Conference on Rotor Dynamics – IFToMM*. Ed. by Cavalca, K. L. and Weber, H. I. Cham: Springer International Publishing, 2019, pp. 222–237. ISBN: 978-3-319-99268-6. DOI: DOI:10.1007/978-3-319-99268-6\_16.
- [131] Timoshenko, S. P. “LXVI. On the correction for shear of the differential equation for transverse vibrations of prismatic bars”. In: *The London, Edinburgh, and Dublin Philosophical Magazine and Journal of Science* 41.245 (1921), pp. 744–746. DOI: DOI:10.1080/14786442108636264.
- [132] Trainotti, F., Haeussler, M., and Rixen, D. J. “A practical handling of measurement uncertainties in frequency based substructuring”. In: *Mechanical Systems and Signal Processing* 144 (2020), p. 106846.
- [133] Trainotti, F. “Development of a proper FRF acquisition procedure for Experimental Dynamic Substructuring”. Semester Thesis. Technische Universität München, 2018.
- [134] Trainotti, F. “Frequency Based Substructuring: Uncertainty Quantification and Regularization of Error Propagation”. Master Thesis. Technische Universität München, 2018.
- [135] Tyagi, S. “Wavelet Analysis And Envelope Detection For Rolling Element Bearing Fault Diagnosis, A Comparative Study”. In: *Proceedings of the 11th National Conference on Machines and Mechanisms*. 2003.
- [136] van der Seijs, M. V. and Rixen, D. J. “Efficient impulse based substructuring using truncated impulse response functions and mode superposition”. In: *International Conference on Noise and Vibration Engineering, ISMA*. 2012, pp. 17–19.
- [137] van der Seijs, M. V., van den Bosch, D. D., Rixen, D. J., and de Klerk, D. “An improved methodology for the virtual point transformation of measured frequency response functions in dynamic substructuring”. In: *4th ECCOMAS Thematic Conference on Computational Methods in Structural Dynamics and Earthquake Engineering*. 4. 2013. DOI: 10.7712/120113.4816.C1539.

- [138] van der Seijs, M. V., van der Valk, P. L., van der Horst, T., and Rixen, D. J. “Towards dynamic substructuring using measured impulse response functions”. In: *Dynamics of Coupled Structures, Volume 1*. Springer, 2014, pp. 73–82.
- [139] van der Seijs, M. “Experimental dynamic substructuring: Analysis and design strategies for vehicle development”. PhD thesis. Delft University of Technology, 2016. DOI: 10.4233/uuid:28b31294-8d53-49eb-b108-284b63edf670.
- [140] *VDI 3832: Measurement of structure-borne sound of rolling element bearings in machines and plants for evaluation of condition*. Standard. Verein Deutscher Ingenieure, 2013.
- [141] Voormeeren, S. “Improvement of Coupling Procedures and Quantification of Uncertainty in Experimental Dynamic Substructuring Analysis; Application and Validation in Automotive Research”. PhD thesis. Master Thesis, TU Delft, 2007.
- [142] Voormeeren, S. N. and Rixen, D. J. “A Dual Approach to Substructure Decoupling Techniques”. In: *Proceedings of the 28th International Modal analysis Conference, Jacksonville, Florida. Society for Experimental Mechanics* (2010).
- [143] Wagner, C. “Dynamic Modeling of Turbopumps-Rotordynamics, Bearings and Contactless Seals”. PhD thesis. Technische Universität München, 2020.
- [144] Wang, G., Chen, X.-Y., Qiao, F.-L., Wu, Z., and Hunag, N. E. “On intrinsic mode functions”. In: *Advances in Adaptive Data Analysis* 02.03 (2010), pp. 277–293. ISSN: 1793-5369. DOI: 10.1142/S1793536910000549.
- [145] Wang, Y.-H., Yeh, C.-H., Young, H.-W. V., Hu, K., and Lo, M.-T. “On the computational complexity of the empirical mode decomposition algorithm”. In: *Physica A: Statistical Mechanics and its Applications* 400 (2014), pp. 159–167.
- [146] Woodhouse, J. “LINEAR DAMPING MODELS FOR STRUCTURAL VIBRATION”. In: *Journal of Sound and Vibration* 215.3 (1998), pp. 547–569. ISSN: 0022-460X. DOI: <https://doi.org/10.1006/jsvi.1998.1709>. URL: <https://www.sciencedirect.com/science/article/pii/S0022460X98917096>.
- [147] Wu, Z. and Huang, N. E. “Ensemble empirical mode decomposition: a noise-assisted data analysis method”. In: *Advances in adaptive data analysis* 1.01 (2009), pp. 1–41. DOI: 10.1142/S1793536909000047.
- [148] Wüstling, S. “Hochintegriertes triaxiales Beschleunigungssensorsystem”. PhD thesis. Karlsruher Institut für Technologie, 1997.
- [149] Xie, Y., Zhifei, G., Ke, T., Mingjie, Z., and Yonghai, W. “Wind turbine gearbox condition monitoring system based on vibration signal”. In: *12th International Conference on Electronic Measurement & Instruments (ICEMI)*. Vol. 1. IEEE. 2015, pp. 159–163.
- [150] Yu, D., Cheng, J., and Yang, Y. “Application of EMD method and Hilbert spectrum to the fault diagnosis of roller bearings”. In: *Mechanical Systems and Signal Processing* 19.2 (2005), pp. 259–270.
- [151] Zou, X. and Seshia, A. A. “A high-resolution resonant MEMS accelerometer”. In: *18th International Conference on Solid-State Sensors, Actuators and Microsystems (TRANSDUCERS)*. 2015, pp. 1247–1250. DOI: 10.1109/TRANSDUCERS.2015.7181156.